Optical models for predicting the color of dental composite materials

Vincent Duveiller

To cite this version:

Vincent Duveiller. Optical models for predicting the color of dental composite materials. Optics / Photonic. Université Jean Monnet - Saint-Etienne, 2023. English. NNT : 2023STET0037 . tel-04556152

HAL Id: tel-04556152
https://theses.hal.science/tel-04556152v1

Submitted on 23 Apr 2024

N° d'ordre NNT : 2023STET037

THÈSE de DOCTORAT
DE L'UNIVERSITÉ JEAN MONNET SAINT-ÉTIENNE

Membre de l'Université de LYON

École Doctorale N° 488
Sciences Ingénierie Santé

Spécialité / discipline de doctorat :
Optique, Photonique, Hyperfréquences

Soutenue publiquement le 26/10/2023, par :
Vincent Duveiller

Optical models for predicting the color of dental composite materials

---

Devant le jury composé de :

ANDRAUD Christine	Professeure des Universités	Muséum National d'Histoire Naturelle	Présidente
GHINEA Razvan	Professeur des Universités	University of Granada, Facultad de Ciencia	Rapporteur
PILLONNET Anne	Professeure des Universités	Université Claude Bernard Lyon 1, ILM	Rapporteure
PACANOWSKI Romain	Chargé de recherche, HDR	INRIA Bordeaux	Examinateur
VYNCK Kevin	Chargé de recherche, HDR	Université Claude Bernard Lyon 1, ILM	Examinateur
HEBERT Mathieu	Professeur des Universités	Université Jean Monnet, IOGS	Directeur de thèse
CLERC Raphaël	Professeur des Universités	Université Jean Monnet, IOGS	Co-directeur de thèse
SALOMON Jean-Pierre	Maître de conférences	Université de Lorraine, Faculté de Nancy	Invité
JOST Sophie	Maître de conférences	ENTPE	Invitée

Funding

This work has been funded by a public grant from the French National Research Agency (ANR) under the “France 2030” investment plan, which has the reference EUR MANUTECH SLEIGHT - ANR-17-EURE-0026.

Remerciements

Mathieu, Raphaël, merci de m'avoir accompagné à travers cette aventure scientifique et humaine. Votre rigueur scientifique dans les expérimentations et la restitution des résultats m'ont profondément aspiré. Merci de m'avoir transmis votre passion pour la recherche, et de m'avoir fait confiance autant dans la conduite de mon travail scientifique que pour les enseignements dispensés aux étudiants en Master et à l'IOGS. Merci Jean-Pierre de m'avoir fait découvrir le monde des restaurations dentaires et pour ton enthousiasme communicatif.

Merci aux membres du jury d'avoir accepté d'évaluer ma défense, et particulièrement aux rapporteurs Anne Pillonnet et Razvan Ghinea, pour leurs retours approfondis et exhaustifs sur ce manuscrit.

J'ai eu la chance de réaliser ce travail de thèse entouré de nombreux collègues et amis dont l'interaction m'a permis de nourrir ce travail de recherche. Ainsi, merci Arthur pour ta contribution importante à ce travail, nos échanges amicaux et nos réflexions fructueuses. Merci Lionel pour nos échanges enrichissants à propos des modèles optiques et des interprétations physiques. Ta précision dans l'analyse est un exemple dont je souhaiterai toujours m'inspirer. Merci Anthony pour ton aide lors de la réalisation des bancs de mesure. Thank you, Maria, for welcoming me so warmly in Granada, for our exchanges on our respective works. I look forward to collaborating with you in the future! Sorry no hablo español.

Merci à mes collègues du laboratoire Hubert Curien, et en particulier à Thierry et Loïc pour vos retours bienveillants sur mon travail, Dylan et Cyril pour leur animation de la vie d'équipe, et Anne-Laure et Patrick grâce à qui les démarches administratives deviennent presque agréables. Merci à Cécile, Aurélie et Elise pour ces nombreux bons moments, en conférence et tout au long de l'année.

Je tiens à remercier mes amis et ma famille pour les moments de complicité et de détente qui ont parsemé ce parcours. Merci à mes amis de Supop Sainté pour tous les bons moments passés ensemble, votre réactivité sans faille pour s'organiser un week-end entre amis. À quand le prochain ?! Merci également à mes amis du JDR, pour ces aventures dans l'aventure. Merci Fanny pour nos appels et nos discussions à toutes les étapes de cette thèse. Ton écoute, tes conseils et ton amitié me sont très chers. Les moments partagés lors des conférences font partis des meilleurs moments de cette aventure. Merci à mes parents : pour votre curiosité à comprendre mon travail, vos encouragements et votre soutien indéfectible tout au long de mon parcours académique. Merci pour tout ce que vous m'avez transmis.

Enfin, merci Alice, de m’avoir accompagné dans cette voie. Merci d’être ma source constante de rires, de joie et de tendresse. Ton soutien tout au long de ce parcours est inestimable, et je suis infiniment reconnaissant de t’avoir à mes côtés.

À vous tous, je vous adresse mes plus sincères remerciements pour avoir rendu ce parcours enrichissant et mémorable. Vos contributions, chacune à sa manière, ont façonné cette réussite. Merci du fond du cœur.

Abstract

Although their main function is mastication, teeth also play a major role in the aesthetics of our face. Dental restorations therefore aim to restore this mechanical functionality, while preserving the aesthetic role as much as possible. Research into dental materials is increasingly driven by this need for aesthetic appeal. The tooth is a complex organ whose appearance is the result of the different optical properties of its constituent tissues, mainly enamel and dentine. To guarantee the aesthetic success of dental restorations, it is necessary to perfectly reproduce the appearance of natural teeth using composite materials. For dental material manufacturers, characterizing the optical properties of materials enables them to better control the visual attributes of the resins developed, converging more rapidly towards a targeted attribute. For practitioners, the shade matching process, *i.e.* the process of selecting the material(s) to be used in a repair, represents a crucial step in the aesthetic success of a dental restoration. This process is, for most practitioners, carried out with the naked eye, and its outcome depends largely on the practitioner's training and the acuity of his or her visual system.

Optical models describing the interactions between light and matter are promising, since they both can be used to characterize the intrinsic optical properties of materials, and to predict physical quantities such as the reflectance spectrum - the physical signal contributing to color - as a function of macroscopic parameters such as material shape or thickness. In the dental domain, the most widely used model is the *Kubelka-Munk* model, which is simple to implement and is based on basic optical instrumentation, but it relies on strong simplifying assumptions that are not suitable with highly translucent materials like dental resin composites. The aim of this thesis is therefore to revisit the Kubelka-Munk model and implement more advanced *two-flux* and *four-flux* models, in order to characterize the intrinsic optical properties of dental composite resins by means of affordable instrumentation and test their predictive performance for the spectral reflectance of samples with various thickness.

This thesis is divided into seven chapters. Chapter 1 reviews the state of the art in dental materials, their visual properties and their optical properties, explains fundamentals of colorimetry and color measurement, and presents the objectives of this thesis. Chapter 2 describes the measurement methods used to measure the reflectance and transmittance factors of dental materials. In Chapter 3 and Chapter 4, the *two-flux* models and *four-flux* models, from the simplest to the most advanced, are described and used to characterize the optical properties of dental

composite resin samples and predict their color. In Chapter 5, key parameters of these models and their influence on their accuracy are analyzed. The models are also tested on different composite resins, and their predictive performance is compared with the one of a state-of-the-art numerical method. Chapter 6 outlines ways in which the models can be extended to consider the phenomenon of fluorescence. The complete conclusion of this work is presented in Chapter 7. These chapters are followed by an appendix on the measurement of visual parameters in the dental field, an appendix on the matrix formalism, a list of the scientific contributions made, and a bibliography of the works cited in this manuscript.

Résumé

Les dents, bien que leur fonction principale soit la mastication, constituent un élément majeur dans l'esthétique de notre visage. Ainsi, les restaurations dentaires visent à rétablir cette fonctionnalité mécanique tout en préservant au mieux le caractère esthétique. Les recherches dans le domaine des matériaux dentaires sont de plus en plus poussées par cette nécessité d'esthétisme.

L'apparence des dents résulte des différentes propriétés optiques des tissus qui la composent, principalement l'émail et la dentine. Pour garantir le succès esthétique des restaurations dentaires, il est nécessaire de reproduire parfaitement l'apparence des dents naturelles avec des matériaux composites. Celle-ci varie fortement d'un individu à l'autre ; la couleur de la dent est comprise dans un gradient allant du blanc au jaune voire marron, le brillant est plus ou moins fort, la topologie est spécifique, la translucidité varie selon l'épaisseur de l'émail et l'âge du patient.

Ces dernières décennies, d'importants progrès dans la science des matériaux composites dentaires ont été réalisés, jusqu'au développement de matériaux composites aux propriétés mécaniques de résistance et de durabilité accrues, et imitant davantage les attributs visuels des dents naturelles. Pour les fabricants de matériaux dentaires, la caractérisation des propriétés optiques des matériaux permet de mieux maîtriser les attributs visuels des résines développées, en convergent plus rapidement vers un attribut ciblé. Pour les praticiens, le processus de sélection du ou des matériaux à utiliser dans une restauration représente une étape cruciale dans le succès esthétique d'une restauration dentaire. Ce processus est, pour la majorité des praticiens, réalisé à l'œil nu, et son succès dépend largement de leur entrainement, et de l'acuité de leur système visuel. Pour les fabricants de matériaux comme pour les praticiens, les modèles optiques décrivant les interactions entre la lumière et la matière sont prometteurs puisqu'ils permettent d'une part de caractériser les propriétés optiques intrinsèques aux matériaux, et d'autre part de prédire des grandeurs physiques comme le spectre de réflectance, -signal physique contribuant à la couleur-, en fonction de paramètres macroscopiques comme la forme ou l'épaisseur du matériau.

Dans le domaine dentaire, le modèle optique le plus utilisé à cette finalité est le modèle *Kubelka-Munk*, relativement simple à mettre en œuvre. Toutefois, ce modèle repose sur de fortes hypothèses simplificatrices, discutables lorsqu'il est appliqué aux matériaux très translucides comme les résines dentaires. Pourtant, des alternatives existent, et la littérature sur les modèles de diffusion de la lumière regorge de modèles plus rigoureux que le modèle *Kubelka-Munk*, comme le modèle à *quatre-flux*, ou l'*Equation des Transferts Radiatifs*.

L'objectif de cette thèse est d'améliorer des modèles de l'état de l'art, en particulier des modèles à *deux-flux,* extensions du modèle *Kubelka-Munk,* et des modèles à *quatre-flux,* pour caractériser les propriétés optiques intrinsèques de résines composites dentaires, et de tester leurs performances prédictives pour le spectre de réflectance de ces matériaux. L'étude sera simplifiée en considérant des échantillons plans, dont la seule variable macroscopique est l'épaisseur.

Cette thèse est constituée de sept chapitres. Dans le Chapitre 1, un état de l'art sur les matériaux dentaires, leurs propriétés visuelles et leurs propriétés optiques est proposé. Les principes fondamentaux sur la colorimétrie et la mesure de la couleur sont rappelés, et les objectifs de cette thèse sont présentés. Le Chapitre 2 décrit les méthodes de mesure mises en œuvre pour mesurer la reflectance et la transmittance des matériaux dentaires. Dans les Chapitres 3 et 4, les modèles à *deux-flux* et les modèles à *quatre-flux*, du plus simple au plus complexe, sont décrits et employés pour caractériser les propriétés optiques d'échantillons de résine composite dentaire et prédire leur couleur. Le Chapitre 5, présente l'analyse des paramètres de ces modèles et leur influence sur leur précision. Les modèles sont également testés sur différentes résines composites et leurs performances prédictives sont comparées avec celles d'une méthode numérique de l'état de l'art. Le Chapitre 6 présente des pistes d'extension des modèles afin de prendre en compte du phénomène de fluorescence. La conclusion complète de ces travaux est présentée au Chapitre 7. Ces chapitres sont suivis par une annexe sur la mesure des paramètres visuels dans le domaine dentaire, une annexe sur le formalisme matriciel pour les modèles à transfert de flux, une liste des contributions scientifiques réalisées, et une bibliographie des travaux cités dans ce manuscrit.

Content

Chapter 1. Introduction

The search for an aesthetic result is a growing demand in dentistry, driven by the desire of patients for their dental restorations to be indistinguishable, or to improve the appearance of their face. This trend is accompanied by a real boom in dental materials, which are more resistant, durable and have optical properties closer to human teeth. Practitioners must therefore take into account this increasingly important aesthetic constraint, in addition to medical constraints in their procedures.

However, to meet this high aesthetic expectation, practitioners mainly work with the naked eye, using a shade guide, which means that the aesthetic result depends on the practitioner's training in both shade matching and material handling, the precision of the practitioner’s visual system, and the resins itself used. In order to help material manufacturers and dentists in the aesthetic success of restorative procedures, a promising approach consists in using the knowledge acquired in the fields of optics and light scattering in order to determine the intrinsic optical properties of dental biomaterials (refractive index, light absorption and scattering properties) and predict their appearance versus the layer thickness, shape surroundings and illumination. The purpose of this thesis is to provide steps towards this goal in enhancing optical models from the state of the art in their capacity to describe optical properties of dental resin composites and testing their prediction accuracy for color prediction.

1.1 Composition of human teeth

The tooth is a rather complex organ due to the translucency or opacity of the different tissues that compose it. Its shape, its gloss, vary depending on whether we consider anterior teeth, *i.e.* maxillary (*upper*) and mandibular (*lower*) central and lateral incisors and canines, or posterior teeth, *i.e.* premolar and molar. Esthetic dentistry mainly concerns the crown, *i.e.* the part that emerges from the gingiva, which is composed of three layers of tissue from the outside to the inside: the enamel, the dentin and the pulp. A cross section of a tooth is visible in Figure 1.1. A schematic is shown in Figure 1.2.

Figure 1.1: Cross section of a natural tooth. Reprinted from [1].

Enamel, the outermost tissue of teeth, is composed of 92-96% of inorganic matter, mostly hydroxyapatite and 4% of organic material in weight [2]. Its microstructure consists of crystals arranged like rods perpendicular to the tooth surface [3,4]. Enamel has a high degree of translucency which varies depending on its mineralization and hydration [5]. Its thickness varies from thin near the gingiva to thick towards the tip, which causes a chroma gradient. Enamel is an opalescent tissue, meaning that blue light is backscattered more strongly than red lights according to Rayleigh scattering; it displays a blueish appearance in reflection and a red-yellowish in transmission.

Under the enamel is a layer of dentin, which is composed of approximately 70% of inorganic matter, 20% of organic matter and 10% of water in weight. These numbers are only average over the whole dentin of teeth, since the proportion of water on the outermost part of dentin is 20 times more than in deep dentin [6]. Dentin structure consists in tubules perpendicular to the enamel-dentin junction, which contain most of the water and which diameter increases towards the enamel. Dentin is the tissue which has the biggest influence on teeth chroma, and is also fluorescent [5].

The pulp is the innermost tissue of the tooth. It is composed of water at 75% and of organic matter at 25% in weight. This tissue contains nerves and vessels which vascularize the teeth [7]. Its contribution to the appearance of teeth is of marginal significance.

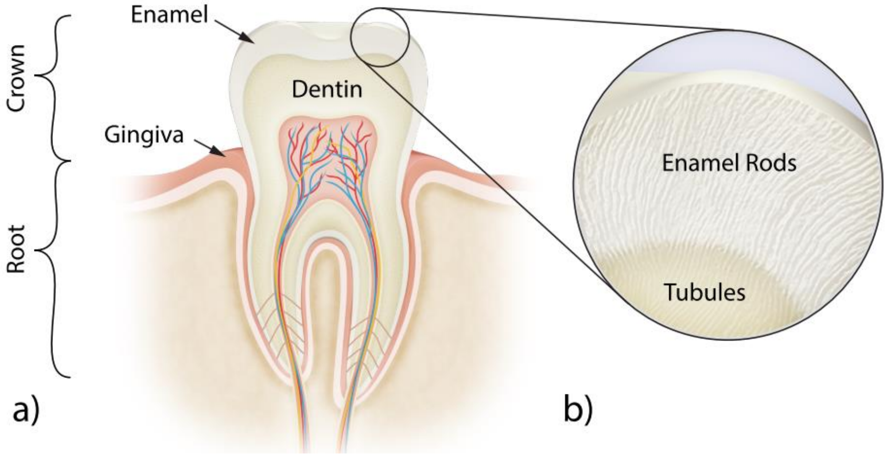

Figure 1.2: Schematic representation of a tooth. Reprinted from [5].

1.2 A Variety of Dental Materials

The primary purpose of dental restorations is to restore the chewing function of the mouth. Originally, unaesthetic metal amalgams, mostly silver-mercury, were mostly used despite several drawbacks: they often require the removal of healthy tissue for placement, and are toxic.

The 20th century saw great advancements in material sciences, with the development of metal-porcelain ceramics with better esthetic properties than amalgams. Progressively, ceramics containing less and less metals were developed, culminating to the development of *all-ceramic* materials, containing no metal, with very good strength, durability and esthetic properties. After taking the footprint of the patient’s mouth, restorations made of ceramics are created by dedicated companies and fitted to the patient in a subsequent appointment.

In the 1950s were developed the dental resin composites, enabling *direct* restorations, meaning that the restoration is made in the patient’s mouth and polymerized (self-cured before 1970s, then UV-cured and visible light cured after). Originally, these materials presented poor mechanical properties: the repair significantly shrank during the polymerization process, had high thermal expansion and poor adhesion to healthy tissues, but these issues were later partially resolved in newer materials.

Dental resin composite materials are composed of fillers, *i.e.* mineral compounds such as aluminum, titanium, zirconium, or zinc oxides, with interesting mechanical and optical properties, mixed in an organic or inorganic matrix that is easy to handle for the practitioner [8]. Developments improved mechanical properties of the materials like its viscosity, resistance to wear and stress, and adhesion to healthy tissue.

Material viscosity can be a selection criterion since fluid resins are recommended for certain clinical situations such as thin layers, anterior cavity, etc. High viscosity materials are also easier to handle, but it comes at the cost of poorer mechanical properties since the proportion of fillers in volume and weight is reduced.

Resistance is a key factor of dental composites since they are intended to last as long as possible. The lifespan of composite restorations is usually shorter than 10 years as they can fracture or must be replaced because of caries [9-13].

Adhesion to the cement, the latter being placed between healthy tissues and the dental composite, is important as a higher adhesion makes the process easier for the practitioner. It must be emphasized that the outcome, including the aesthetic result, largely depends on the ability of the practitioner. Thus, facilitating the process already means more durable and more aesthetic restorations and many developments are made towards this goal [14,15]. As such, self-adhering composites have been developed to eliminate the intermediate step required to facilitate the adhesion of the material to the tooth [16].

The more fillers there are in a resin, the more resistant and less fluid it is. There exist a number of different fillers bringing different mechanical, biological and optical properties to dental composites [17]. For example, zinc oxide inhibits bacterial growth [18] and is rather opaque. Al_2O_3 and TiO_2 and ZrO_2 can also be added to make the material opaquer [19]. On the other hand, opacity has a practical influence on the practitioner’s technique since high opacity reduces the depth of cure [17]. Furthermore, replacing fillers with smaller particles of spherical shape (100 nm in diameter) enables to control the level of opalescence of the material [20]. There also exist so-called self-healing fillers which release resin when a crack in the restoration appears, thus filling holes and preventing fracture [21]. The numerous fillers and their functionalities are reviewed in [22].

Fillers of different type and size can be used in a resin to achieve targeted mechanical and optical properties. Classification of dental resins according to filler size and distribution is presented in Table 1.1.

Table 1.1: Classification of dental composites according to their filler type in chronological order of development [14,23].

Type of composite	Average filler size	Distribution
Macrofill	10-50 μm	Evenly distributed large particles.
Microfill	40-50 nm	Evenly distributed small particles with clusters.
Hybrid	10-50 μm and 40 nm	Mix of large and small particles.
Midfill	1-10 μm and 40 nm	Mix of large and small particles.
Minifill / Microhybrid	0.6-1 μm and 40 nm	Mix of large and small particles.
Nanofill	5-100 nm	Small particles with high variability in size.
Nanohybrid	0.6-1 μm and 5-100 nm	Mix of large and small particles with high variability in size.

The organic resin matrix embedding fillers consists of viscous monomers forming the bulk of the resin composite. The main monomers used in dentistry are BisGMA, TEDGMA and UDMA [17]. BisGMA is used for its high resistance and low shrinkage, but has a high viscosity, which prevents the addition of too much fillers which would further increase the viscosity [24,25]. TEDGMA can be added as a diluent to BisGMA, although TEGDMA increases shrinkage [25-27]. UDMA possesses the advantages of BisGMA, but has a lower viscosity, which makes it an interesting monomer for dental resin composites [28-30]. Many derivatives of these base monomers, and new monomers have been developed to further enhanced properties of dental materials, and also remove bisphenol-A from BisGMA.

Overall, the creation of new dental composites requires careful balancing of monomers and fillers to achieve targeted mechanical and optical properties. Although aesthetics is considered by material manufacturers and practitioners, mechanical and biological properties remain central to the development of new dental composites and the clinical situation has a great influence on the practitioner’s choice of material.

1.3 Visual properties for dental materials

The appearance of teeth is quite peculiar in several aspects:

- Color varying from yellow to light depending on dentin color and enamel thickness and translucency,
- Opalescence aspect visible by blueish aspect of enamel under certain observation angles, especially visible in primary teeth,
- High translucency of enamel,
- Chroma and translucency gradient from the cervical to the incisal area caused by the change in thickness of the enamel and dentin layers,
- Glossy surface even when dry
- Opacity
- Texture

These appearance features are visual sensations resulting from the numerous light-matter interactions at the tooth level: specular reflection, direct transmission through enamel and dentin, scattering inside enamel and/or dentin, absorption by enamel and/or dentin, interreflections between enamel and dentin, interface reflection at air-enamel interface and enamel-dentin interface caused by the shift of refractive index between materials.

These features can be observed in Figure 1.3. In the cervical area, near the root of the teeth, a reddish tint is visible as light crosses the gingiva, taking a red coloration before passing through the teeth. In the incisal area, near the tip of the teeth, translucency is evident as the background is becoming visible. Because of translucency, the true color of the teeth is neither the color observed in the cervical area nor in the incisal area. Rather, our visual system understands “the” color based on the gradient of color from top to bottom. Gloss is visible from the specular highlights, the mostly vertical white bands in the image. Those specular highlights also provide cues to understanding the surface texture.

Colorimetry indices are used in dentistry to quantify some of the dental materials’ visual properties. Calculation of these indices is covered in Appendix A) Colorimetry indices in dentistry.

Several of these colorimetric indices, translucency indices, opalescence parameters and contrast ratio have been evaluated on dental materials, human dentin or enamel [31-46]. Their evolution after an aging process has been studied in [47-49], after a bleaching protocol in [50], after staining in [51], and their stability under different light sources has been evaluated in [52,53]. Different measuring methods for acquisition of visual parameters have been tested in [38,54,55]. In [56], visual parameters have been assessed with a cellphone. Also, the visual parameters displayed by shade guides, intended to help practitioners in the shade matching process, and their relevance with respect to natural teeth visual properties, have been evaluated in [32,57,58].

Figure 1.3: Central maxillary incisal restoration on the left and natural tooth on the right. The different visual attributes which make the restoration look natural are rather visible. Reprinted from [1].

1.3.1. Color: a complex sensation

Color is a sensation produced by our visual system, which comprises our eyes, optical nerves and the brain. The eye is composed of the cornea, lens, retina composed of layers of photosensitive cells terminating with rods and cones. Cones are photoreceptor cells which absorb photons according to their spectral sensitivity and convert it to an electric signal transmitted to a subsequent layer of photosensitive cells, and then to the brain through the optical nerve. There exist different types of cones sensitive to different wavelengths called L (*long* wavelengths, most sensitive at 569 nm), M (medium wavelengths, most sensitive at 541 nm), S (short wavelengths, most sensitive at 448 nm). Rods are highly sensitive photoreceptor cells allowing scotopic vision and are most sensitive at 507 nm. Cones are most concentrated at the fovea, while rods are most concentrated on the peripheral area of the retina. Color is associated with the electromagnetic field carried by the photons emitted by a given light source that have interacted with an object before reaching our retina. Photosensitive human cells are sensitive from 380 nm to 750 nm approximately. The sensitivity of photoreceptor cells, proportion of LMS cones and their distribution on the retina, varies from a person another one, and vary with age.

Color is a complex sensation; of which the sensitivity is developed during a long learning process during in first years of life. Color is highly dependent on the context in which an object is observed. The lighting, more precisely: its spectral power distribution, has an influence on the color of the illuminated object, but this can be partially compensated for by the chromatic adaptation mechanism. Thus, under many different illuminations, an object may be perceived as having the same color (color constancy). On the other hand, because of the simultaneous contrast effect, the color of an object can vary according to its immediate surroundings: it may appear paler if surrounded by a dark object, or brighter if surrounded by gray, or greener if surrounded by red. Color perception is not absolute: it is relative to what is known as a "white point", *i.e.* a light source or object in the visual field, often the most intense, that the brain defines as white at all times. These phenomena are all the more acute for a human facial organ, as humans are highly trained to analyze subtle color variations on faces. Measuring color quantitatively and objectively is therefore an arduous task for a set of teeth, present on the face and surrounded by highly colored surfaces such as the gums and lips and set against a black background (the oral cavity).

1.3.2. Complexity of visual attribute metrology

Colorimetry is a fantastic science that allows us to quantitatively measure sensations perceived by our visual system. Yet, it is based on mandatory simplifying assumptions that it is necessary to keep in mind [79]. Basically, colorimetry is only fully applicable for describing color in very limited theoretical cases, such as flat opaque objects. This is why researchers' study of the visual

Figure 1.4: Photos of the Aigues-Mortes salt marshes (South of France) taken with different cameras, white balance and settings. The picture on the left is taken 40 minutes before the one on the right, two hours before sunset. In the foreground, the town's salt marshes sometimes take on a remarkable rose/red hue, when algae rich in beta-carotene proliferate under high salinity levels.

properties of dental materials is carried out on flat samples. In the case of studying the colored appearance of a tooth or dental repair, a more global approach to appearance measurement would be required in order to control the various phenomena mentioned above. It is tempting to extrapolate results from color prediction methods to predict overall appearance. However, as we pointed out earlier, appearance, *i.e.* the perception we have of an object, often depends on much more than its color [80]. In the case of more complex objects, such as teeth [131], metallic surfaces [81], or skin [213], the appearance is the result of particularly complex brain mechanisms that are not fully understood to date. The study of color, according to the assumptions of colorimetry, is like looking at a flat colored object with only a white reference in the field of view, illuminated in the same way as the flat color, without any other element of context. Nevertheless, for all common objects or scenes, context helps our brain visualize appearance. For example, between the two photos of Aigues-Mortes in Figure 1.4, the color of the water is radically different due to the different camera conditions, yet the color I remember is very saturated, much closer to the color visible in the right image. On these photos, the pink/burgundy water appears more and more blue as the incidence of light rays from the sky becomes more and more grazing. These rays outweigh the light coming from the water and are reflected by the water-air interface and therefore do not leave the water body, creating a blue to rose gradient from the horizon to the foreground. This phenomenon was all the more striking when moving closer or away from the water. Motion can be essential to understand the different attributes of the appearance of objects [82-84]; for example, the oenologist always shakes his glass to observe the color of the wine. Thus, any attempt at predicting the appearance of teeth would require a global approach that includes the different components of appearance simultaneously. This work is therefore a step towards predicting the color of dental restorations but is by no means sufficient for a clinical approach to predict appearance.

1.3.3. Colorimetry

Although color has been studied long before [59], the Commission Internationale de l'Eclairage (CIE) provided the first standardization enabling to quantify this color stimuli in 1931 [60]. The so called 2° standard observer was described by a set of Color Matching Functions, which correspond to the colorimetric response of the average human visual system to a light stimulus on an area corresponding to 2° of his field of view on the retina, *i.e.* his fovea. In 1964, the 10° standard observer was described similarly [60]. The 2° standard observer's color matching functions correspond to the color stimuli felt from looking at a flat circular object of uniform color (meaning that irradiance on the object's surface is also uniform) of 1.7 cm in diameter at a 50 cm distance while the 10° refer to a circular object of 8.8 cm in diameter at a 50 cm distance. As color study in dentistry refers to rather small objects, the CIE 1931 color matching functions are commonly used. Age-related color matching functions were also established [61] and the choice of the color matching functions to be used depends on the field of study. Note that following developments on colorimetry rely on these assumptions: color stimulus is the sensation of looking at a flat object, 1.7 cm in diameter, uniformly illuminated and observed at a 50 cm distance. Noteworthy, notion of shape, shadows resulting from non-uniform illumination, are neglected.

Color stimulus is intrinsically related to illumination of an object. The CIE described several common sources of visible light, *i.e.*, standard illuminants by their Spectral Power Distribution. Illuminants A, B and C were first established and correspond to incandescent light, direct sunlight, and average daylight respectively. The D series illuminants were later introduced with D50, D55, D65 and D75, which correspond to daylight at different phases. The D65 illuminant corresponds to daylight and is defined as a reference illuminant for color measurement. In dental cabinets, scialytic lamps and ceiling light corresponding to ISO 9680:2021 mimic standard daylight. Illuminant E was introduced as an equal-energy radiator, mostly used as a theoretical reference. Then, illuminants F, from F1 to F12, were introduced and describe fluorescent lightings. Finally, 10 standard LED illuminants were proposed by the CIE to represent most of LED lightings [62].

Prior to CIE's standardization works, color was generally represented as a three-dimensional stimulus. The Munsell color space, proposed in 1905, describes color according to 3 properties: *hue* (base color), *chroma* (saturation), and *value* (lightness). The CIE defined several color spaces, one of the most used being the CIE XYZ color space proposed in 1931, in which a color stimulus, namely the color produced by the electromagnetic wave issued from a light source that interacts with an object and reaches the fovea, is represented by three coordinates, X Y and Z, which are called tristimulus values. Color coordinates in this color space are calculated as presented in formulae (1.1)-(1.4).

$$X = k\int S(\lambda)I(\lambda)\bar{x}(\lambda)d\lambda \tag{1.1}$$

$$Y = k\int S(\lambda)I(\lambda)\bar{y}(\lambda)d\lambda \tag{1.2}$$

$$Z = k\int S(\lambda)I(\lambda)\bar{z}(\lambda)d\lambda \tag{1.3}$$

$$k = \frac{100}{\int I(\lambda)\bar{y}(\lambda)d\lambda} \tag{1.4}$$

where $I(\lambda)$ is the spectral power distribution of the light source illuminating the object, $S(\lambda)$ is the spectral reflectance or transmittance of the object, and $\bar{x}$, $\bar{y}$ and $\bar{z}$ are the color matching functions.

Although this color space enables quantitative representation of color, it has the drawback that color differences in the CIE XYZ color space were not accurately correlated to perceived color difference [63-65]. The CIE L*a*b* color space was established to overcome this limitation while also enabling to account for chromatic adaptation, to a limited extent. The chromaticity coordinates L*, a* and b* are calculated from the XYZ tristimulus values according to formulae (1.5)-(1.8).

$$L^* = 116 f\left(\frac{Y}{Y_n}\right) - 16 \tag{1.5}$$

$$a^* = 500\left[f\left(\frac{X}{X_n}\right) - f\left(\frac{Y}{Y_n}\right)\right] \tag{1.6}$$

$$b^* = 200\left[f\left(\frac{Y}{Y_n}\right) - f\left(\frac{Z}{Z_n}\right)\right] \tag{1.7}$$

with

$$f(q) = \begin{cases} q^{1/3} & \text{if } q > 0.008856 \\ 7.787q + \frac{16}{116} & \text{if } q \le 0.008856 \end{cases} \tag{1.8}$$

and X_n, Y_n and Z_n correspond to the tristimulus values of the white reference (reflectance or transmittance equal to 100%) used for chromatic adaptation. L^* refers to the perceived lightness value while a^* and b^* refer to chromaticity coordinates along a green-red axis and a blue-yellow axis respectively. High absolute values of a^* and b^* corresponds to strongly saturated colors;

negative values of *a**, resp. *b** correspond to green, resp. blue, whereas positive values of *a**, resp. *b** correspond to red, resp. yellow, while values close to 0 correspond to achromatic colors: black for *L** close to 0 and white for *L** close to 100.

The L*a*b* color space is designed to be perceptually uniform, so that color differences in this space are correlated with perceived color differences. Thus, the color difference between two color stimuli, denoted ΔE^*_{ab}, can be calculated according to formula (1.9).

$$\Delta E^*_{ab} = \sqrt{(L^*_1 - L^*_2)^2 + (a^*_1 - a^*_2)^2 + (b^*_1 - b^*_2)^2} \tag{1.9}$$

Nevertheless, non-uniformities were found in the ΔE^*_{ab} formula, prompting the need for a more perceptually stable color difference metric. Several metrics were proposed [66-68]. The CIEDE2000 color difference metric, also denoted ΔE_{00}, was proposed in 2001 and became the CIE's recommendation for color difference calculation [69,70] since it provides much more perceptually stable color differences across the L*a*b* color space. The ΔE_{00} color difference is calculated according to formula (1.10).

$$\Delta E_{00} = \left[\left(\frac{\Delta L'}{K_L S_L}\right)^2 + \left(\frac{\Delta C'}{K_C S_C}\right)^2 + \left(\frac{\Delta H'}{K_H S_H}\right)^2 + R_T\left(\frac{\Delta C'}{K_C S_C}\right)\left(\frac{\Delta H'}{K_H S_H}\right)\right]^{1/2} \tag{1.10}$$

with $\Delta L'$, $\Delta C'$ and $\Delta H'$ the difference in luminance, chroma and hue respectively between the two objects. The chroma is calculated according to formula (1.11). The hue is calculated according to formula (1.12).

$$C^* = \sqrt{a^{*2} + b^{*2}} \tag{1.11}$$

$$h^\circ = \arctan\left(\frac{a^*}{b^*}\right) \tag{1.12}$$

K_L, K_C and K_H are correction terms accounting for experimental conditions of observation. S_L, S_C and S_H are weighting functions adjusting for the color variation in the location of $\Delta L'$, $\Delta a'$ and $\Delta b'$. R_T is the rotation function adjusting chromatic differences in the blue region. The CIEDE2000 color difference metric is the gold-standard color difference formula in most application domains, including dentistry.

1.3.4. Color difference thresholds in dentistry

An important concept related to the determination of the color difference between two stimuli is the threshold of noticeability, also called *Just Noticeable Distance, i.e.* the maximum color difference below which an observer is not be able to perceive a color difference between the two stimuli. This notion is important since the aesthetic challenge of dental restorations is often that the repair is indistinguishable from natural teeth. Thus, this concept must be incorporated into color measurement instruments, both in vivo and in vitro, in order to objectively measure the color accuracy of aesthetic procedures.

In the field of dental materials, several psycho-visual experiments have been conducted with lay-person observers or observers with background in the dental field, with the aim to relate the perception of color difference on dental materials to colorimetric measurements. In most cases, the experiment consists in placing the observer in a room with color-controlled illumination conditions and presenting them with pairs of dental material samples. The observer has to say whether he/she notices a difference in color between the two samples, while the colorimetric distance between the two samples has been measured with colorimetric instruments.

These studies have been conducted in the color space L*a*b*, with color difference formulas ΔE_{ab}, ΔE_{94} or ΔE_{00}. Two thresholds have been proposed: the 50:50% *Perceptibility Threshold* (PT) and the 50:50% *Acceptability Threshold* (AT). The 50:50% perceptibility threshold is the colorimetric distance below which the majority of observers do not perceive the color difference between the two samples. The 50:50% acceptability threshold is the colorimetric distance below which the majority of observers consider the color difference acceptable to produce a successful dental repair. This type of study was conducted on ceramic materials as well as on dental resin composites. Different values have been reported by several studies, with PT varying from 0.4 [71] to 1.9 [72] ΔE_{ab} units, AT varying from 1.7 [71] to 5.5 [73] ΔE_{ab} units. In [74], authors highlighted differences in PT values between different groups of observers, from average PT values at 0.62 ΔE_{00} units for dentists to 1.00 ΔE_{00} for laypersons. Furthermore, several studies highlighted [75,76] the relevance of using the ΔE_{00} formula instead of the ΔE_{ab} for measuring color differences in dentistry. Acceptability thresholds for lightness, chroma and hue differences were also investigated [77].

Nevertheless, the largest study [74] on this subject was conducted on 175 observers, which had dental or non-dental backgrounds, conducted at 7 different research centers in Europe and led to these thresholds being set at 0.8 ΔE_{00} unit for PT and 1.8 ΔE_{00} unit for AT. These values have since been incorporated into ISO/TR 28642:2016 [78] and are used as a reference for the evaluation of colorimetric differences in the dental environment. These thresholds will therefore be considered in this work.

1.3.5. CIE recommendations for color measurements

As we mentioned it previously, colorimetry relies on simplifying assumptions which are mandatory to link the measurement of the physical signal carrying color to the perceived color sensation. Indeed, colorimetric assessment is based on the reflectance denoted R and transmittance denoted

T, which are different from the reflectance and transmittance factors, denoted $\tilde{R}$ and $\tilde{T}$ respectively. The two latter quantities can be measured with spectrophotometer, but R and T cannot be measured directly. However, R and $\tilde{R}$, and respectively T and $\tilde{T}$, can be assumed to be equivalent for Lambertian or perfectly matte, non-luminescent samples, under precise measuring conditions (see details in [60]). These quantities are defined as:

$$R(\lambda) = \frac{\phi_R(\lambda)}{\phi_I(\lambda)} \tag{1.13}$$

$$T(\lambda) = \frac{\phi_T(\lambda)}{\phi_I(\lambda)} \tag{1.14}$$

$$\tilde{R}(\lambda) = \frac{\phi_R(\lambda)}{\phi_{REF}(\lambda)} \tag{1.15}$$

$$\tilde{T}(\lambda) = \frac{\phi_T(\lambda)}{\phi_{REF}(\lambda)} \tag{1.16}$$

where ϕ_R is the flux reflected by the sample, ϕ_T is the flux transmitted by the sample, ϕ_I is the flux incident on the sample, and ϕ_{REF} is either the flux reflected by a perfect white diffuser for the reflectance factor, or the flux measured in absence of the sample for the transmittance factor. λ denotes the wavelength of light. The reflectance ranges between 0 and 1, while the reflectance factor can be higher than 1, in the case where the sample reflects more light than a perfect white diffuser (for example, a white specular surface, or a mirror).

The CIE recommends [60] several measurement geometries: the 45°:0° geometry in which the sample or material is illuminated at 45° relatively to its surface normal and the reflected luminance is captured at an angle of 0° to the sample surface, and the d:8° geometry in which an integrating sphere is used to produce *diffuse* illumination on the sample and the luminance reflected at 8° is captured. This geometry is thus called hemispherical-directional in the Nicomedus classification [154]. The latter configuration is of interest because it also enables the characterization of glossy samples, with a flat, smooth surface, by including or excluding the component specularly reflected by the sample's air-material interface. These different measuring modes are called Specular Component Included (SCI), in which the measuring geometry is denoted di:8°, and Specular Component Excluded (SCE), in which the measuring geometry is denoted de:8°.

Some devices also allow transmittance factor measurements to be carried out on highly scattering but not totally opaque samples, such as sheets of paper, or to characterize the absorption of a liquid.

The d:8° geometry can also be used to measure the reflectance factor for samples of transparent materials, bearing in mind that the light reaching the detector only comes from one direction of the integrating sphere, namely from the 8° angle. The hemispherical-directional measurement geometry thus becomes a bi-directional 8°:8° geometry in this case [156]. From these measurements in reflectance mode, in transmittance mode, or both, we can derive the intrinsic properties of the material (refractive index, absorption coefficient, etc.) by means of equations based on simple optical laws [156]. In the case of transparent objects, as in the case of highly scattering ones, the lateral propagation of light is very weak. Thus, the area illuminated and that observed by the detector can be considered almost identical. In practice, the CIE recommends that the viewing area be slightly smaller than the illuminated area (details are given in [60]), which is generally considered in spectrophotometers available commercially.

1.4 Optical properties of dental materials

The optical properties of a material are the physical quantities that give rise to measurable macroscopic properties such as reflectance and transmittance, when light interacts with the material. These are mainly absorption and scattering coefficients, scattering phase function, asymmetry parameter, and refractive index. Let us also add fluorescence, because although this phenomenon is rarely taken into account in color prediction models, it plays a role in the final appearance of teeth. Furthermore, the reproduction of appearance must be optimal under different types of lighting, *e.g.*, natural or LED, whose spectral power distribution may generate more or less fluorescence emission by the dental tissue.

In the field of dental materials, absorption and scattering properties are almost exclusively studied using the Kubelka-Munk Reflectance Theory [85-87]. This model, which dates back to 1948, has a number of advantages: it is based on a few analytical formulas and requires only two reflectance factor measurements or one reflectance factor and one transmittance factor measurement of a sample to extract its optical properties, making it relatively simple to use. This model was first applied in dentistry in 1975 to characterize and compare human and bovine enamel, from 220 nm to 700 nm [88]. The authors show that the absorption and scattering coefficients are high in the short wavelengths (blue light), decreasing exponentially as the wavelength increases. Shortly later, the model was applied to materials used in dental restorations, in order to assess whether or not their optical properties are close to those of natural tissues [89]. Unfortunately, the authors did not report the values found across the whole visible spectrum. Subsequently, the *Kubelka-Munk Reflectance Theory* has been used in numerous studies to characterize human enamel and dentin [90-94] and also to study the influence of tooth decay [95]. At the same time, it has been applied to characterize dental materials, resin composites or ceramics, to assess their optical properties as a function of their composition, or in specific situations where the material is stained, undergoes an ageing or bleaching treatment, etc. [89,93,96-102].

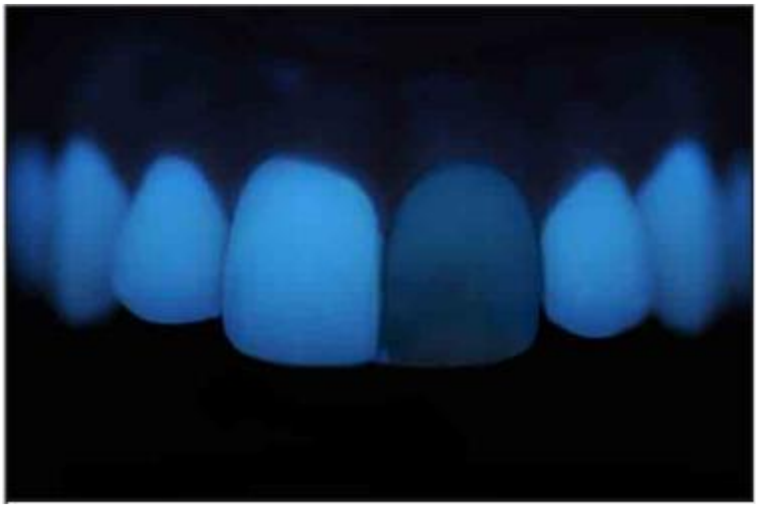

Figure 1.5: Ceramic restoration of anterior teeth observed under UV light. Natural teeth appear blue as UV radiation is absorbed and converted into blue light through fluorescence mechanism. Reprinted from [115].

The more complex *Radiative Transfer Equation* (RTE) has also been used to extract the absorption, scattering, refractive index and asymmetry parameter of the scattering phase function of dental materials [103-105]. The RTE provides a much more realistic optical description of light scattering in a material, enabling the extraction of more physically accurate optical properties. However, the complex instrumentation required to implement it probably explains why it is not widely used for characterizing dental materials.

Finally, the study of fluorescence requires specific instrumentation, since dental materials fluoresce even in the visible spectrum of light. Depending on the operating mode of the spectrophotometer used in each study on optical properties, it is possible that part of the signal measured results from the phenomenon of fluorescence and is misinterpreted. A non-fluorescent ceramic restoration is shown in Figure 1.5 under UV-light.

The fluorescence of enamel and dentin under UV light, and even under visible light, has first been described in the early 1920s [106]. Several studies have emphasized the importance of reproducing the fluorescence of natural teeth in the fabrication of dental restorations in order to improve the aesthetic quality of the filling [107]. Furthermore, it has been shown that fluorescence under daylight has an influence on color parameters of dental resin composites [108].

With the aim of improving esthetic quality of their biomaterials, dental resin composite manufacturers include fluorescent agents in the chemical composition with the aim to mimic the natural fluorescence of dental tissues. However, the fluorescence of natural human teeth is still not completely understood [109]. In particular, it seems that their fluorescence is caused by a combination of several fluorescence agents [110]. Because of this complexity, material manufacturers are still not able to fully reproduce the natural fluorescence of teeth [111].

In order to study the fluorescence of enamel, dentin, or dental biomaterials, several techniques have been proposed in the literature. The fluorescent spectrum of samples was observed with methods based on a photographic camera under UV light [112] or daylight [108], or with a spectrophotometer [113]. In other studies, a spectrofluorometer was used in order to measure the fluorescence emission spectrum for different excitation wavelengths, thus creating bi-spectral plots showing the fluorescence emission as a function of the excitation wavelength [114].

1.5 Objectives

A complete approach to appearance reproduction would include a measuring instrument capable of measuring the shape of the tooth, its various optical attributes: translucency, opalescence, color, gloss, etc. Associated with the instrument, an optical algorithm for appearance prediction would suggest one or more materials to be used in order to achieve the desired aesthetical goal.

Our work therefore focuses on the part of this method that would enable to identify the color of the material to be used so that the color of the repair matches the color of neighboring teeth perfectly. Ideally, we would like to be able to predict the appearance of a tooth repair based on the chemical composition of the dental composite. Besides, such a method would greatly benefit to dental material manufacturers in the development of new materials with a targeted appearance. However, our work was carried out on commercial materials whose precise composition is not known to us.

Thus, our aim is to identify optical methods combining a measuring instrument and an optical model of light propagation to characterize the optical properties of a dental material in a first step, without needing to know the composition of the material beforehand. Secondly, we will study the ability of these optical methods to extrapolate the color of a sample of a given material as a function of the thickness deposited, in the presence or absence of a background, and for given illumination conditions.

This work requires a perfect understanding of the measuring conditions and an awareness of the biases they may induce. As on the images of Aigues-Mortes in Figure 1.4, the conditions under which the optical measurements are carried out have an influence on the interpretation of the physical quantities that can be deduced, even with calibrated color measurement instruments. Furthermore, we keep in mind that these measuring instruments must be simple to use so that they can be used by specialists in the dental field who are not necessarily trained with optical measuring instruments. Thus, Chapter 2 of this thesis will present the different experiments implemented to measure the color of dental samples.

Then, we need to identify an algorithm that allows us to deduce the optical properties of the studied materials, then to extrapolate the color of a given sample. Our approach has been to study state-of-the-art optical models and propose new models describing the interactions between light and material to predict their color in reflection and transmission modes, *i.e.*, when the material is observed from the illumination side or held in front of the light source.

A classical approach to predict the color of a given material type consists in measuring a standard color chart and predict the color of similar materials via interpolation, or more advanced methods based on a principal component analysis (PCA) after studying the dimensionality of the representation space (colorimetric or spectral). This approach was applied to dental materials in recent studies [129-132]. However, it was demonstrated in several fields of application such as printed surfaces that an optical approach can be more efficient as it allows similar predictive performances while requiring less samples in the initial color chart (*e.g.* in four-color printing, about forty samples are enough for the optical approach while thousands are needed for the interpolation method [133], and predictions are then allowed with different ink thicknesses [134] or illumination or observation geometries [133], which is not possible with the interpolation method; or in camera color calibration; 6 samples instead of 24 are sufficient for an optical approach [135]).

The optical approach is based on macroscopic measurements, such as reflectance and transmittance measurements, enabling to access the intrinsic parameters of a material, *i.e.* its absorption and scattering parameters, refractive index. These parameters are intrinsic to the material and do not depend on the sample's shape or size. They can only be extracted from macroscopic measurements using optical models that physically describe the propagation of light within the material.

These models must be compatible with affordable and simple optical measuring instruments. As such, they are necessarily based on highly simplifying assumptions, *e.g.* that the material is perfectly homogeneous, that its interfaces with air are flat, which may not correspond to the reality of the dental samples we will be working with. For these reasons, our work involves first understanding precisely the interactions between light and matter, secondly identifying model parameters which may be problematic and finally suggesting improvements.

According to the literature in optics and light scattering, the best physical approach for an accurate prediction in reflectance and transmittance modes over the widest range of thicknesses would certainly be to perform an angular resolution of Radiative Transfer Equation [136,137]. Several methods for solving the RTE have been proposed, such as the discrete ordinate method [138], the spherical harmonic method [139], the adding-doubling method [140,141], or Monte-Carlo methods [142]. However, this approach is time consuming and needs sophisticated angular reflectance measurements for their calibration.

A well-known alternative in the field of optics consists in using the two-flux and four-flux models, which under some specific approximations, are angularly integrated solutions of the radiative transfer equation.

A review of the literature shows that the gold-standard method for obtaining the optical parameters of materials in the dental field is the Saunderson-corrected Kubelka-Munk reflectance model on black and white backgrounds, also called *Kubelka-Munk Reflectance Theory* [85-87]. This two-flux model has been used to characterize human and animal dentin and enamel [88,91,92,143], dental ceramics [93,96,98-100], commercial resin composites [89,101,102,144-152] or experimental dental composite resin materials [153] used to prepare direct and indirect dental restorations. It relies on simple analytical formulae and needs only two optical measurements: the reflectance factors of the layer in optical contact with a white background and with a black background with known spectral reflectance factors. The white background must be opaque and strongly scattering in order to ensure that light is perfectly diffuse, a ground assumption for the Kubelka-Munk Reflectance Theory. However, with these translucent biomaterials, even when illuminated with perfectly diffuse incident light, there is a risk that the light captured in one direction is not representative of the whole reflected light, especially in absence of highly scattering white background.

The four-flux model [161], although not new to the field of optical models, has never been used to characterize the optical properties of dental materials and its prediction accuracy has never been assessed. This model, while being more sophisticated than the two-flux model, remains compatible with measuring devices based on an integrating sphere, and, like the two-flux model, it is analytical.

Thus, our approach will be to extract the intrinsic parameters of a material via the macroscopic measurements made on a sample, and then to predict the measurements obtained for other samples of the same material when the thickness varies. Figure 1.6 shows a schematic representation of our workflow.

This thesis is divided into seven Chapters. In Chapter 2, the measurement strategies implemented to measure the reflectance and transmittance factors of dental material samples are presented and explained in detail. Chapter 3 covers the theory of the two-flux model, features the optical parameters extracted from a set of samples of a dental material, and the prediction accuracy of the several model variants for predicting the spectral reflectance and transmittance factors of samples with varying thickness. In Chapter 4, the four-flux model formalism is detailed, and we present the optical parameters and prediction accuracy of basic and enhanced four-flux models. In Chapter 5, several optical models' parameters are analyzed. The models are also applied to various sets of materials to investigate the variability of the prediction accuracy with respect to the sample composition. The optical models proposed in this thesis are also compared with an interpolation approach recently proposed in the field of dental materials [131]. In Chapter 6, we investigate an optical model which accounts for fluorescence, with the aim to integrate the fluorescence phenomenon in non-fluorescent optical models. Chapter 7 summarizes the conclusions of this thesis.

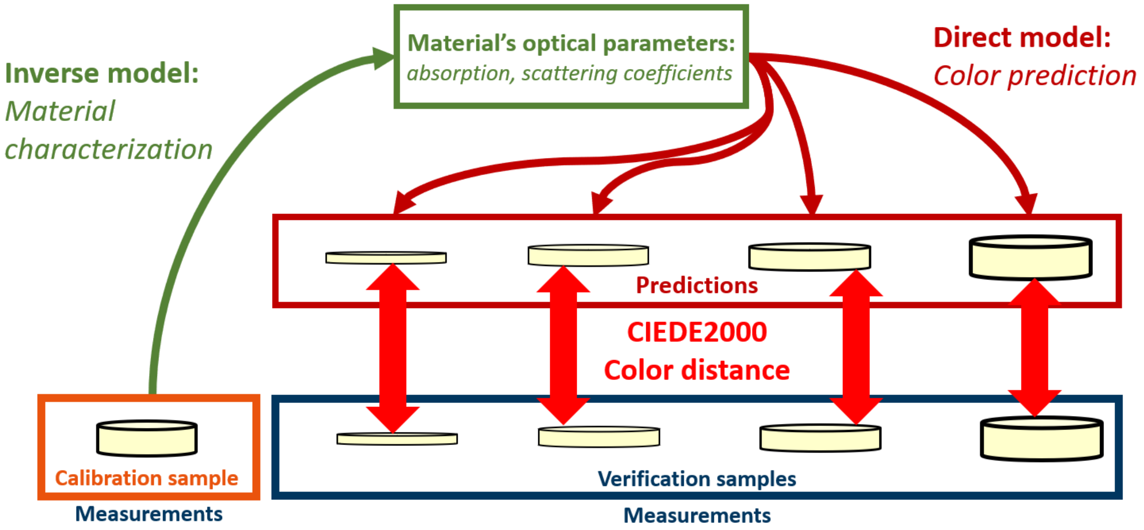

Figure 1.6: Workflow applied to assess the accuracy of optical model for characterization and color prediction of samples of dental resin composites.

Chapter 2.
Optical measurements of dental resin samples

Radiometric characterization of objects tends to become a usual practice, either to control directly the aspect of the objects in their final shape, or to determine the intrinsic optical properties of the materials from simply shaped samples in order to render the aspect of the object in the design process. Several companies now commercialize devices based on integrating sphere allowing affordable and ergonomic measurement of the spectral reflectance or transmittance factor of samples, from which colorimetric assessment can be carried out following recommendations formulated by the CIE [155]. These characterization protocols are rather well adapted to planar, uniform, opaque and matte samples in reflectance mode, because the spectral radiance reflected in every direction is the same, and therefore the color is independent of the viewing angle.

In the case of translucent materials, the measurement is much trickier to interpret, especially when it comes to deducing the material's intrinsic parameters. Firstly, the light reaching the detector does not necessarily come from the entire integrating sphere, even if the illumination is perfectly diffuse; nor does it come from precise, well-identified directions, as in the case of transparent objects. However, it is essential to know the light paths from the source to the detector in order to understand how they have been attenuated by scattering or absorption. The best option for this is to perform angular measurements for measuring the *Bidirectional Reflectance Distribution Function* BRDF, and *Bidirectional Transmittance Distribution Function* BTDF, but this type of measurement is costly and often restricted to laboratory studies. The second problem is that light can propagate laterally within the material and leave the detector's field of view. These lateral losses, a phenomenon commonly known as *edge-loss*, are essential to take into account, or to avoid, if possible, as they can lead to a misinterpretation of the optical properties of the material.

In the case of dental materials in particular, their fluorescence poses a problem, since they fluoresce even when excited by visible light. All these considerations have led us to dedicate an entire chapter to the measurement of samples, that we begin to introduce in the first section.

2.1 Samples studied

During our study, several measuring protocols were implemented on samples of dental resin composites of different brands and shades. These materials are given in Table 2.1, with details about their composition. These dental resin composites have been successfully used in aesthetic dentistry for many years [116-120].

Table 2.1: Names and manufacturers, classification, composition, shade and batch numbers of resin composites (information given by the manufacturers).

Names (Manufacturers)	**Classification**	**Composition**	**Shade (Batch numbers)**
Aura Easy Flow (SDI Ltd.)	Nano-hybrid resin composite	56% inorganic fillers (0.2-1 micron) multifunctional methacrylic esters (UDMA, TEGDMA, Bis-EMA), initiators, stabilizers, pigments.	Ae1 (1906100) Ae2 (190982) Ae3 (190964) Ae4 (190794)
Estelite Universal Flow SuperLow (Tokuyama)	Supra-nano filled resin composite	Spherical silica-zirconia filler (mean particle size: 200 nm), Composite filler Bis-GMA, Bis-MPEPP, TEGDMA, UDMA, Mequinol, Dibutyl hydroxyl toluene, UV absorber.	A1 (10621) A2 (01713) A3 (2178) A3.5 (4064) A4 (5042) A5 (60311)
Estelite Universal Flow Medium (Tokuyama)	Supra-nano filled resin composite	Spherical silica-zirconia filler (mean particle size: 200 nm), Composite filler Bis-GMA,Bis-MPEPP, TEGDMA, UDMA, Mequinol, Dibutyl hydroxyl toluene, UV absorber.	A2 (0717) A3 (2942) A4 (5104) OA2 (7122) OA3 (8096) OA4 (6562)

Samples were fabricated by Dr. Jean-Pierre Salomon at the Institut de Sciences des Matériaux de Mulhouse (IS2M). For each shade of the Aura Easy Flow and Estelite Universal Flow SuperLow materials, six samples of different thickness, 0.3 mm, 0.6 mm, 0.9 mm, 1.2 mm, 1.5 mm, and 1.8 mm, were fabricated. For each shade of the Estelite Universal Flow Medium material, eight samples with thickness 0.4 mm, 0.5 mm, 0.8 mm, 1.0 mm, 1.2 mm, 1.5 mm, 1.6 mm and 2.0 mm were fabricated. The flowable dental resin was injected between two glass-slides, whose spacing was controlled with high precision wedges (Mitutoyo company) defining the nominal thickness of the sample. The samples were light-cured with a LED light curing unit (Radii Xpert, SDI company operating at 1500 mW/cm2) according to the curing scheme I.S.O. 4049:2009 [122]: each sample was irradiated five times, 40 seconds each irradiation, at 12-3-6-9 o’clock positions and ending in the center of the sample. The sample diameter, determined by the volume of material deposited, was ranging from 20 mm to 22 mm. The thickness of each sample after curing was measured with a precision micrometer, since resin composites shrink during the curing process. Although the measured thicknesses were considered in the experiments, samples will be referred to by their nominal thickness hereinafter for clarity.

2.2 Hemispherical-directional reflectance and transmittance factors

A Color i7 (X-Rite, USA) spectrophotometer was used to measure the reflectance and transmittance factors of all samples in the different options allowed by the device. This spectrophotometer uses an integrating sphere for illumination and the radiance is captured at 8° from the surface normal in reflectance mode (d:8° geometry in the CIE nomenclature [60]) and at 0° in transmittance mode (d:0° geometry).

a) Total reflectance **b) Diffuse reflectance**

Measuring geometry: di:8° Measuring geometry: de:8°

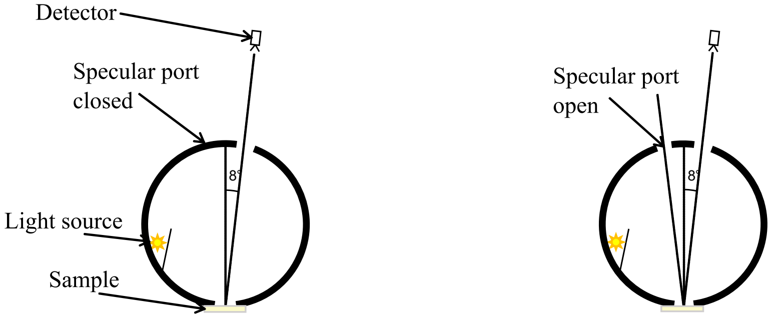

c) Total transmittance **d) Direct transmittance**

Measuring geometry: d:0° Measuring geometry: 0°:0°

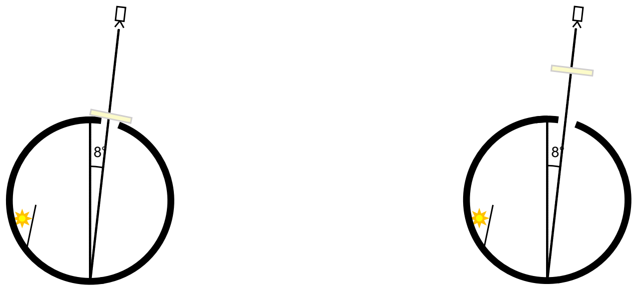

Figure 2.1: Measuring geometries allowed by the Color i7 spectrophotometer: (a) Reflectance factor with specular component included, (b) Reflectance factor with specular component excluded, (c) Transmittance factor with direct transmittance included, (d) Direct transmittance factor.

This device allows several measurement configurations. In reflectance mode, the specular component can either be included or excluded (SCI or SCE) in the measurements allowing to measure the *total reflectance factor* in the first mode or the *diffuse reflectance factor* in the second mode. In practice this spectrophotometer allows to measure the reflectance factor in SCI and SCE modes simultaneously. These two configurations are illustrated in Figure 2.1a) and Figure 2.1b).

In transmittance mode, the sample can be placed directly in front of the integrating sphere. In this case, the *total transmittance factor* of the sample is measured in the d:0° geometry. However, it can also be placed at a distance from the integrating sphere, and therefore receives a more collimated incident illumination. In this case, the *direct transmittance factor* is measured in a 0°:0° geometry. These two configurations are illustrated in Figure 2.1c) and Figure 2.1d).

2.2.1. Preventing Edge-Loss

The Color i7 allows to set the diameter of the area illuminated on the sample. This setting is called the *illumination aperture*, or *illumination area*. Several holders allow to choose between circular zones with diameters of 20 mm, 17 mm, 10 mm and 6 mm. The area over which the measurement is performed, called *measuring aperture*, can also be set. This area is necessarily equal or smaller than the illumination aperture and can be set to 20 mm, 17 mm, 10 mm or 6 mm in the software.

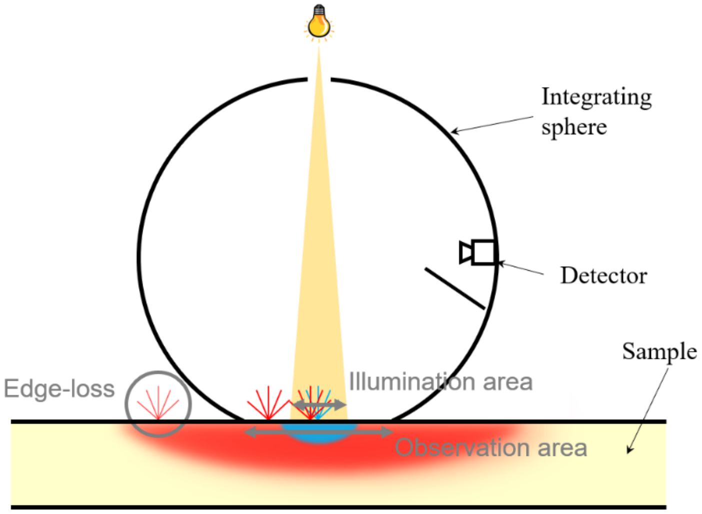

Figure 2.2: Schematic representation of the edge-loss phenomenon in a measurement occurring with a device based on the 8°:d geometry. Red light is typically more prone to edge-loss in skin and in dental materials.

These settings can significantly alter the measurement of translucent samples as they enable to limit or prevent the *edge-loss* phenomenon [123,124], namely, light which escapes detection by the sensor during measurement because of subsurface transport within the material layer. In translucent dental resin composites, light travels further than in the white spectralon used for calibration of the device. As a result, a fraction of light rays escapes the sensor's field of view (it escapes the integrating sphere in the case of 8°:d measuring instruments). This phenomenon is spectral, since red light travels further than blue light in dental materials, which is a significant issue when measuring the color of objects. A scheme of this phenomenon is represented in Figure 2.2.

Edge-loss occurring during the measurement of a translucent sample can be assessed with the material's Point Spread Function (PSF), which describes the probability of a photon exiting the material at a given location with respect to its entry point inside the material. For a given entry point (let us consider a collimated illumination perpendicular to the sample), the PSF can be assessed by the halo produced by the light around the point of impact; the larger the halo, the more translucent the sample is. Note however that the PSF is defined when an area infinitely small is illuminated on the sample. Figure 2.3 illustrates the translucency of a dental resin sample and shows a rough assessment of the sample's PSF. In Figure 2.3b), the halo is reinforced by the paper under the sample, which reflects light. Notice that there is almost no halo on the paper, since it is a highly scattering material with low subsurface scattering. Details on the PSF and edge-loss estimation for commercial spectrophotometers are given in [124].

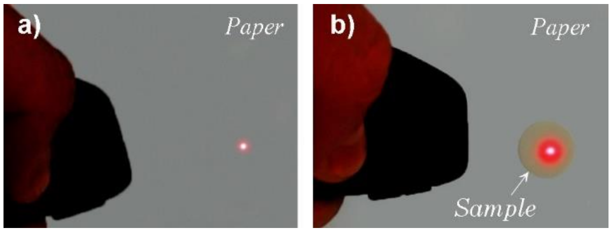

Figure 2.3 : Preview of the PSF, as revealed by a laser pointer beam, of a) paper, a strongly scattering medium, and b) a sample of dental material placed on top of the paper.

Figure 2.4: Samples of the Estelite Universal Flow SuperLow A3 material positioned on a drawdown card without optical contact, from the thinnest on the left-hand side to the thickest on the right-hand side.

Increasing the size of the sphere on the sample, *i.e.* the measuring aperture, can solve, this problem, at least partially. The influence of these aperture settings is illustrated in Figure 2.5, which shows the reflectance factor measured for several samples depending on the illumination and measuring aperture settings. The samples under study are samples of the EsteliteUniversalFlow SuperLow A3 material, shown in Figure 2.4.

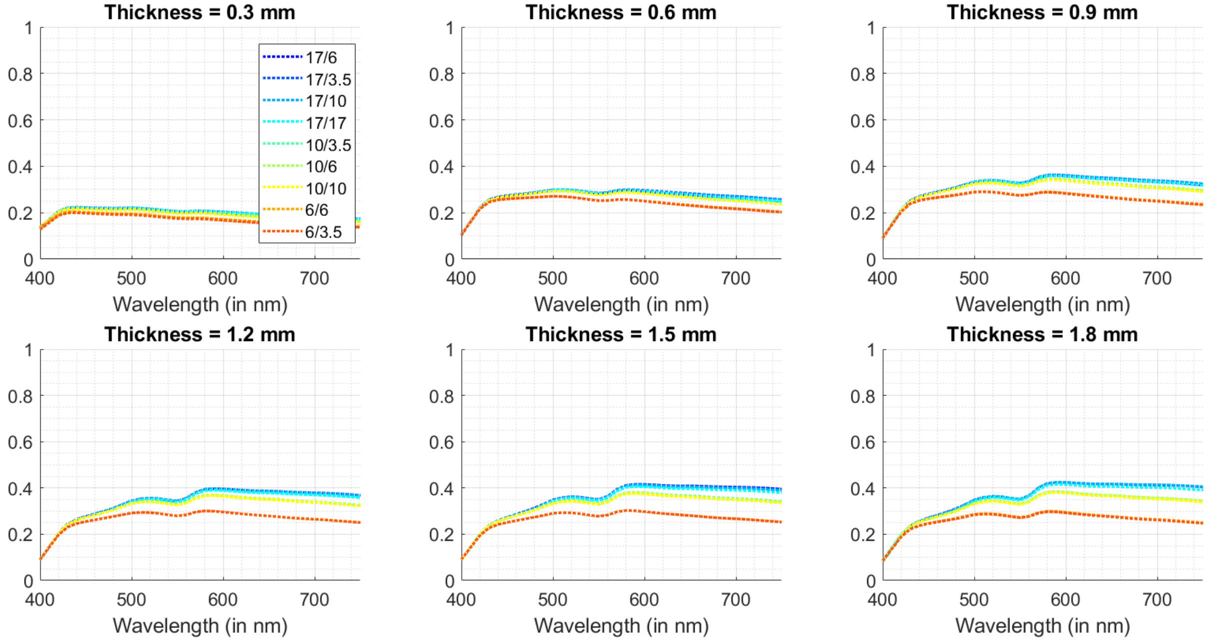

Figure 2.5: Reflectance factors of the samples Estelite Universal Flow SuperLow A3 of different thickness for different illumination/measurement aperture settings.

The edge-loss phenomenon is already noticeable for the thinnest sample, and it increases with respect to the thickness. The reflectance factor increases with respect to the illumination aperture/measuring aperture ratio as more light is captured by the detector with larger ratios; the reflectance factor is the highest for the 17/3.5 illumination/measuring aperture ratio and the lowest for the 6/3.5 illumination/measuring aperture ratio. Especially, it also increases with the wavelength. This confirms that light at longer wavelengths travels further inside the samples before being absorbed or reflected, and a fraction of it does not reach the sensor if the illumination/measuring aperture ratio is not large enough. It remains to be seen if 17 mm for the illumination aperture is large enough for these samples. For comparison, the same experiment is conducted on paper, which is known to be a highly scattering material. This is shown in Figure 2.6.

Almost no difference is found in the measurements with the different aperture ratios, except with the smallest settings, *i.e.* 6 mm in illumination aperture and 3.5 mm in measuring aperture.

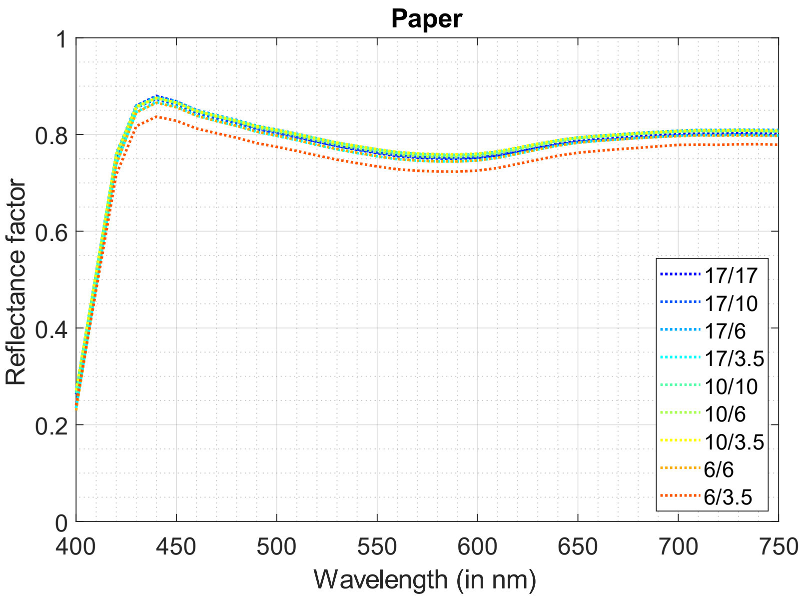

Figure 2.6: Reflectance factor of a sheet of paper for different illumination/measurement aperture settings.

In order to minimize edge-losses with a spectrophotometer of hemispherical directional geometry, such as d:8°, it is preferable to select the largest illumination aperture and the smallest measuring aperture. In the case of a spectrophotometer based on a directional-hemispherical geometry, such as a 8°:d geometry for example, edge-losses are minimized by selecting the smallest illumination aperture and the largest measuring aperture.

However, we are limited by the diameter of our samples, which is between 20 and 22 mm. The illumination aperture of 20 mm is slightly to narrow to allow comfortable measurements. Therefore, we selected the 17 mm illumination aperture and the 6 mm measuring aperture.

2.2.2. Controlling fluorescence

The Color i7 uses a Xenon pulsed light source for illumination, and the reflected or transmitted light is captured from 360 nm to 750 nm by steps of 10 nm. A UV filter can be placed in or removed to filter light below 400 nm, allowing for *UV-included* or *UV-excluded* measurements. The filter can also be placed in an intermediate position in order to reproduce the UV component within the standard D65 illuminant [60]. In this case, the spectrophotometer is calibrated with a specific fluorescent calibration standard in order to reproduce the L* value of the calibration standard under the D65 illuminant. This mode is denoted the *UV-calibrated* mode. Unless explicitly stated, all measurements are performed in UV-excluded mode to minimize the influence of fluorescence. Measurements including UV light are performed with the filter in the intermediate position reproducing daylight.

2.2.3. Example of reflectance and transmittance factors measured in the d:8° / d:0° geometry

Each measurement is repeated 7 times and averaged to limit uncertainties. The total reflectance and transmittance factors, diffuse reflectance and direct transmittance factors of samples of the EsteliteUniversalFlow SuperLow A3 material are presented in Figure 2.7, in UV-excluded mode.

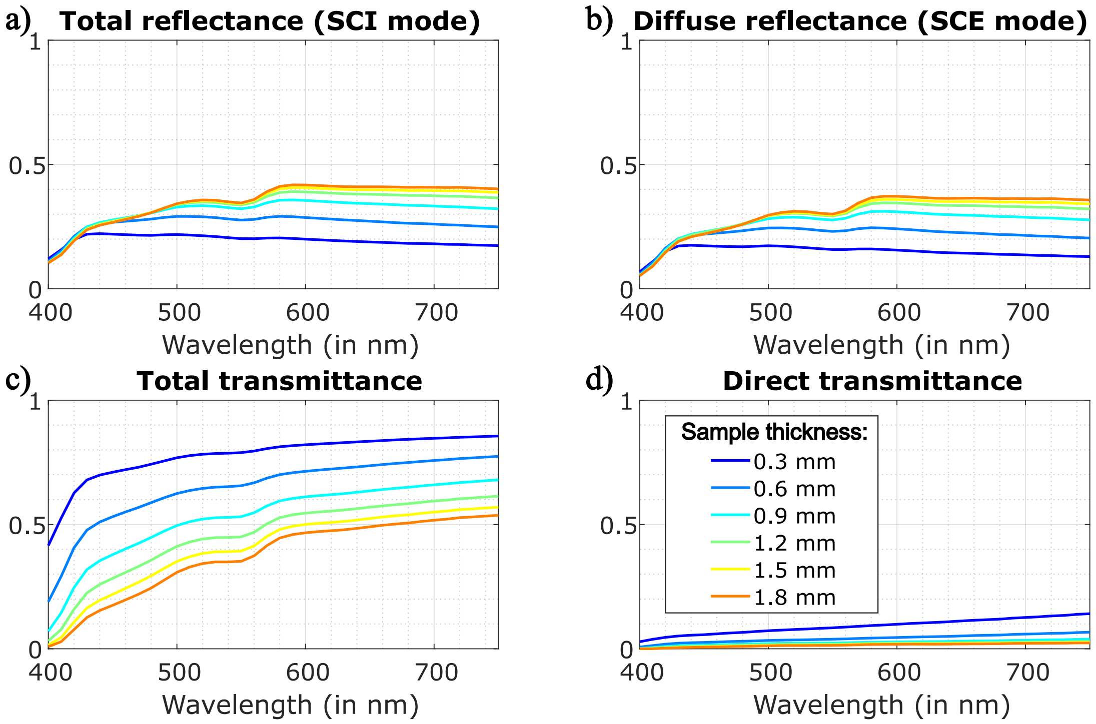

Figure 2.7: Measurements of the samples of the EsteliteUniversalFlow SuperLow A3 material performed with the color i7 spectrophotometer. a) Reflectance factor in SCI mode. b) Reflectance factor in SCE mode. c) Total transmittance factor. d) Direct transmittance factor.

The reflectance factors indicate that the thinnest sample has a rather white color, but the material takes on a reddish tint when thicker samples are considered. This is also visible in total transmittance. The direct transmittance factors show that only a small fraction of light remains specular, while the rest is scattered. However, it is probable that more light propagates along the specular direction than in any other fraction of geometrical extent in the hemisphere, especially for the thinnest sample for which the direct transmittance amounts for approximately 10% of the total transmittance factor. Finally, the transmittance factor is higher than the reflectance factor for thin samples for all wavelengths, which indicates that more light is transmitted through the sample. For the thickest samples, this is not true anymore, as shown in Figure 2.8. The transmittance factor is higher than the reflectance factor for short wavelengths (red light). Overall, samples of this dental material display a blueish tint in reflectance mode and a reddish tint in transmittance, which indicates that blue light is scattered as in Rayleigh scattering.

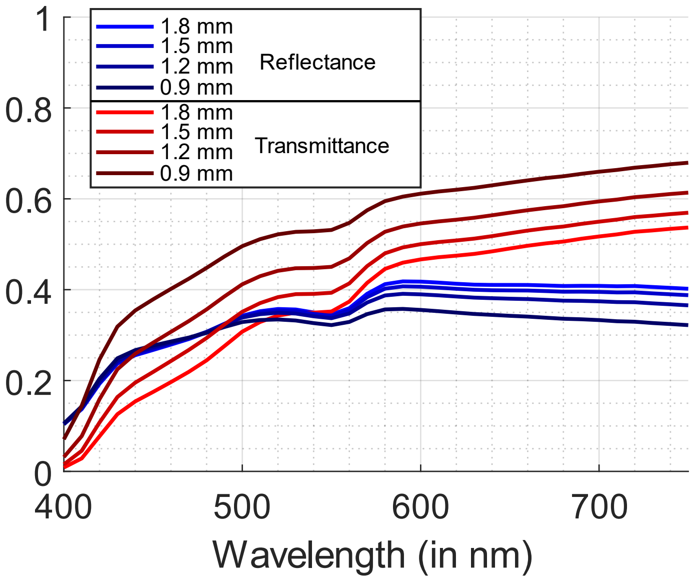

Figure 2.8: Reflectance and transmittance factors of the thickest samples of the EsteliteUniversalFlow SuperLow A3 material performed with the color i7 spectrophotometer.

These reflectance and transmittance factor measurements are rather easy to perform, and reproducible: the ΔE_{00} color difference between measurements performed after re-calibration of the device and re-placement of the sample is about 0.1 unit. It is however required that the room is completely dark to prevent perturbations by stray light.

2.3 Effective measuring geometry

The measurement geometry d:8° is recommended by the CIE for the measurement of the color of highly scattering objects. These objects, as opposed to non-scattering or low-scattering objects, pose fewer specific problems since it can be reasonably assumed that they reflect the same amount of light in all directions. This makes it possible to generalize the measurement made at one angle to all angles. However, this assumption must be questioned when the object under study is not strongly scattering.

Let us consider the case of a transparent glass plate. To a first approximation, this material can be considered as non-scattering and non-absorbing. The path of the light rays is only deviated by the change in refractive index at the air-glass interface, which is described by Snell's law. In the case of a measurement with an instrument based on the d:8° geometry, only light reaching the glass plate at an angle of -8° to the normal will be reflected back to the detector, at an 8° angle. All light falling on the sample from the rest of the hemisphere does not reach the detector. Thus, an instrument based on an 8°:8° geometry achieves the measurement as an instrument with a d:8° geometry. The effective geometry of the measurement is therefore said to be 8°:8°, and a distinction is made between the *effective* measuring geometry and the *instrument* geometry [156]. Let us stress that, in a transparent layer measured with a d:8° geometry instrument, there is diffuse light since illumination is diffuse, but the light that reaches the sensor has followed a directional path. This is the same when we see our reflection in a store window: the ambient lighting is diffuse, but our reflection is visible because the light rays reaching our eye have followed a directional path. Even if we used a device of d:8° geometry, it can be easier to think as if the device had a 8°:d geometry, which means exchanging the light source and the sensors.

This consideration allows a better understanding of the conditions under which a measurement is carried out. It is also important in the use of optical models, which will be discussed in detail in Chapter 3 and Chapter 4. Indeed, these models require the knowledge of the effective measuring geometry for their proper use. This notion becomes complex in the case of a material with intermediate scattering properties, *i.e.* in the case of a translucent material. This case corresponds to an intermediate situation in which the scattered light is likely to come from a more or less wide solid angle around the -8° direction. Even more complicated, given the opalescent properties conferred on dental materials by their composition, it is possible that the aperture of this solid angle depends on the wavelength.

For this reason, with translucent materials, it is preferable to use a spectrophotometer with an integrating sphere rather than one with a bidirectional geometry, such as an instrument with a 45°:0° geometry, because the integrating sphere of an 8°:d instrument makes it possible to capture all of the light scattered by the sample. Furthermore, the diffuse-directional geometry is consistent with the situation that is most representative of daily life: the objects we observe are illuminated by diffuse light, such as the sun, and we look at them at a specific angle with respect to their normal. With an instrument of 45°:0° geometry, it is possible that a fraction of light, which contributes to the final appearance of the object is lost when viewed in a diffuse-directional configuration. This is illustrated in Figure 2.9. It shows that depending on the Point Spread Function of the sample, the area of illumination on the sample and the area of observation of the detector have an influence on the measurement, and, as the Point Spread Function is spectral, this influence can be stronger at certain wavelengths than others. Depending on the spectral scattering phase function of the sample, some of the light contributing to the samples color might not be recorded in the 0°:45° geometry. Note that the Point Spread Function considerations are also true for devices with d:8° and 8°:d geometries.

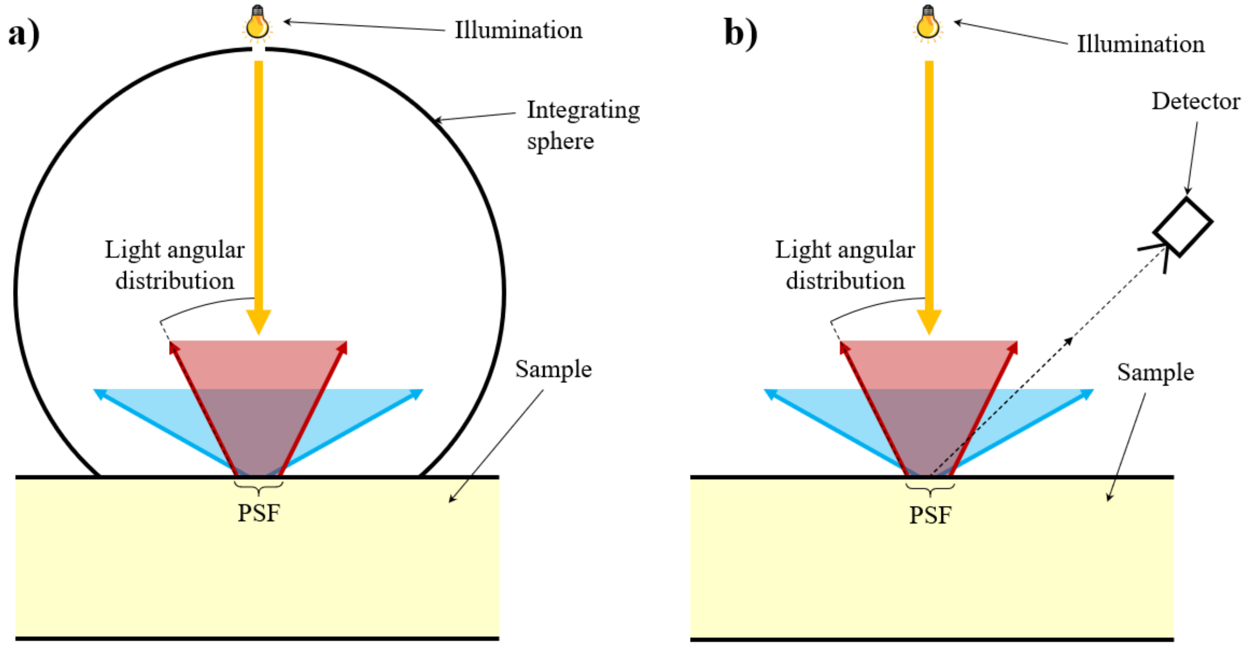

Figure 2.9 : Schematic representation of potential measurement biases with devices based on a) the 8°:d geometry, and b) the 0°:45° geometry.

2.4 Reflectance factor of samples on backgrounds

Some visual properties, such as the translucency parameter or contrast ratio (see 0) require the measurement of the material when it is on top of black and white backgrounds. These measurements are also necessary to implement a version of the two-flux model, described in Chapter 3. In most studies on the optical properties of dental materials, authors perform reflectance measurements against a black and white background rather than without a background since the translucency parameters and the aforementioned two-flux model formalism are the preferred approaches in this field.

In this case, it is required that the sample is in optical contact with the background, as would be dental restorations on their substrate. Optical contact means that there is no air between the sample and the background. It is performed by binding the sample to the background with a liquid of same refractive index which is approximately 1.5, such as a saturated sucrose solution (index 1.5 for an 85% solution) [92,125,148], glycerin [126,127], or dedicated index matching liquids. The measurement setup is presented in Figure 2.10.

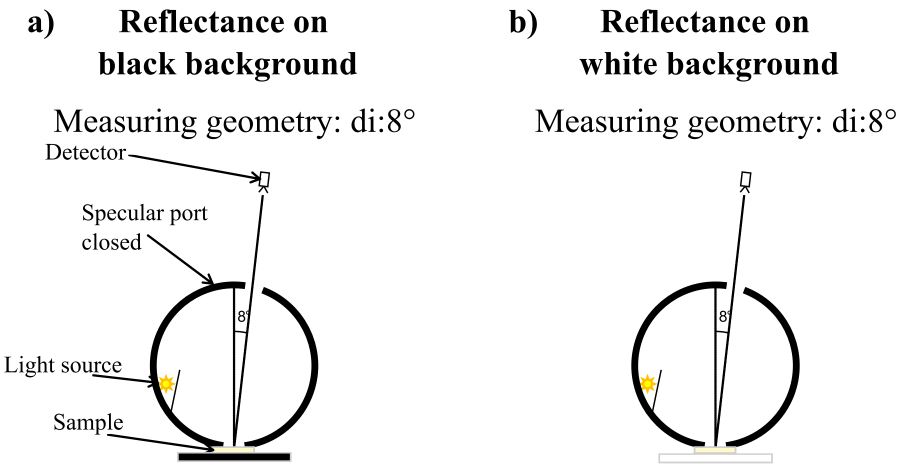

Figure 2.10: Configuration allowing reflectance measurements of a sample in optical contact (a) with a black background and (b) with a white background.

The index matching liquid is deposited on the background and the sample is placed on the liquid until all air is removed from behind the sample. As a result, no light reflection occurs at the sample-liquid interface nor at the liquid-background interface. In absence of liquid, these interfaces have a significant influence on the color of the material, which is lighter as the interfaces back-reflect significant amount of light [128]. This is illustrated by the pictures in Figure 2.11.

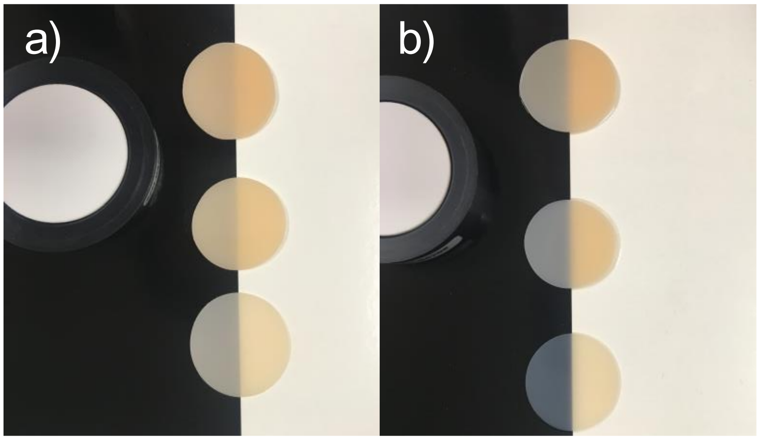

Figure 2.11: Samples of the EsteliteUniversalFlow SuperLow A3 material with thickness, from top to bottom, 1.8 mm, 1.2 mm, and 0.6 mm, placed on a black and on a white background. a) No optical contact is performed. b) Optical contact is performed.

We have measured the reflectance factors of samples in optical contact with a black and a white background. The reflectance factors of the samples of the EsteliteUniversalFlow SuperLow A3 material are presented in Figure 2.12. The drawdown cards used for these measurements are the Byko-charts with L* = 8.20, a* = -0.07, b* = 0.28 for the black side and L* = 91.5, a* = -0.46 and b* = 4.65 for the white side. The reflectance factor on a white background decreases with respect to the sample thickness, as samples absorb light reflected by the background, but the reflectance factor on a black background increases with respect to the sample thickness as the light crossing the sample is absorb by the background. Notice that the background color has almost no influence on the reflectance factor of the thickest sample; curves are almost equal. This shows that the sample is almost opaque for blue light.

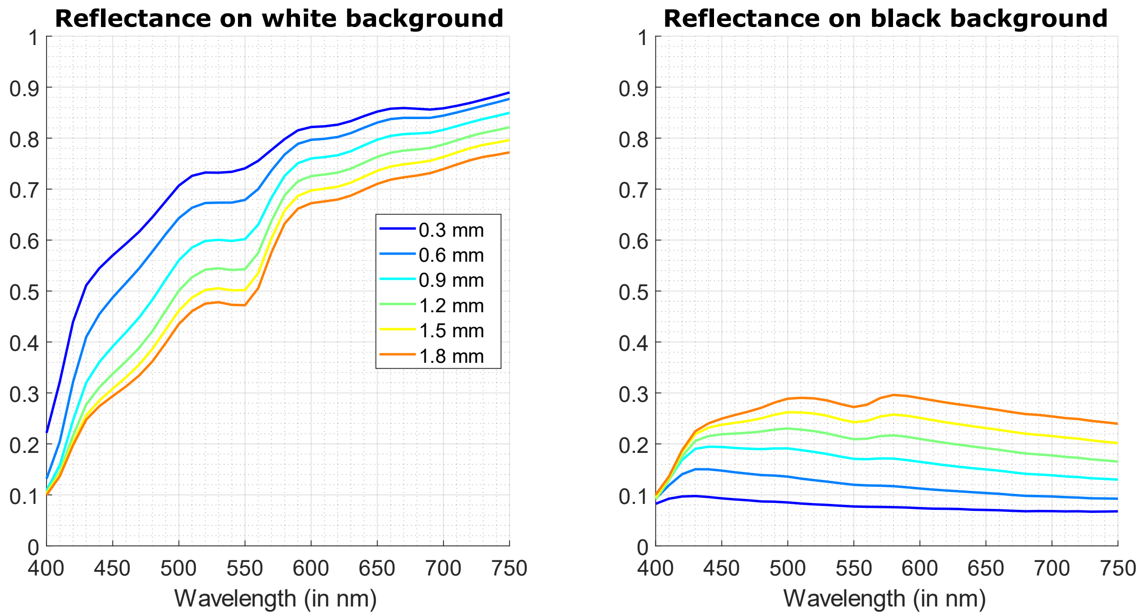

Figure 2.12: Reflectance factors of samples of the EsteliteUniversalFlow SuperLow A3 material (a) on a white background, (b) on a black background.

Measurement of the reflectance factor of samples on a background are slightly more tedious because they require optical contact between the background and the sample. Especially with our device, the sample must be held vertically. This makes it hard to keep the sample still for the measurement because liquids used to make the optical contact are usually very slippery. The Immersion Oil Type B from Cargille has the nice property of being viscous, which facilitates it a bit. Nevertheless, standard deviation over repeated measurements is slightly higher than for reflectance and transmittance factor measurement, with about 0.15 ΔE_{00} between two reflectance factor measurements of the same sample in optical contact on a black background after re-calibration of the device and re-placement of the sample, versus <0.10 ΔE_{00} for reflectance and transmittance factor measurements. Also note that measuring the reflectance factor in optical contact on a black background is not equivalent to measuring the reflectance factor without optical contact, and also not equivalent to measuring the reflectance factor without background. In all these situations, the path of light is different because of the successive changes of refractive index, from the medium to air and from air to the background.

Chapter 3.
Performance of two-flux models

The Saunderson corrected Kubelka-Munk model [85-87] is a reference model for the optical characterization of materials. It has been applied in dentistry for many purposes, such as deriving absorption and scattering coefficients of enamel, dentine, new materials, materials after different aging, staining, or bleaching protocols [88-102,126,143-153,158-160]. Its validity domain and applicability conditions were checked in several studies [152,188-193], which emphasized its inaccuracy for thin materials or materials which are weakly scattering. It was also applied in many other fields to study the influence of pigments, as in paints or colorants [194-198], fabrics [199-201] or detect pigments used in cultural heritage works of art [202-208]. It was also applied on skin to derive its optical properties [209-214] or study the influence of makeup or foundation on skin's appearance [215,216].

3.1 The Kubelka-Munk theory

The Kubelka-Munk model describes light propagation in a layer of homogeneous scattering medium considered without any interface at its boundaries, as if the medium was surrounded by a clear medium with same optical index. The medium-air interfaces, where light is reflected or refracted due to the change in refractive index between the material and air, are accounted for by the Saunderson correction later described. A system of two differential equations represents the attenuation due to absorption, and mutual exchanges due to backscattering, of two fluxes assumed perfectly diffused going into opposite directions. It is given in equation (3.1).

$$\begin{cases} \dfrac{dI}{dz} = -(K+S)I(z) + SJ(z) \\ \dfrac{dJ}{dz} = (K+S)J(z) - SI(z) \end{cases} \tag{3.1}$$

where $I(z)$ represent the Lambertian flux travelling in the direction of the incident illumination, along the depth z, and J(z) the Lambertian flux travelling in the opposite direction. Both fluxes are attenuated by absorption, described by the spectral absorption coefficient $K(\lambda)$, and scattering, described by the scattering coefficient $S(\lambda)$, and strengthened by backscattering from the opposite flux. This model is non-spectral, meaning that its assumptions and formalism does not depend upon the wavelength of light. The model's schematization is presented in Figure 3.1.

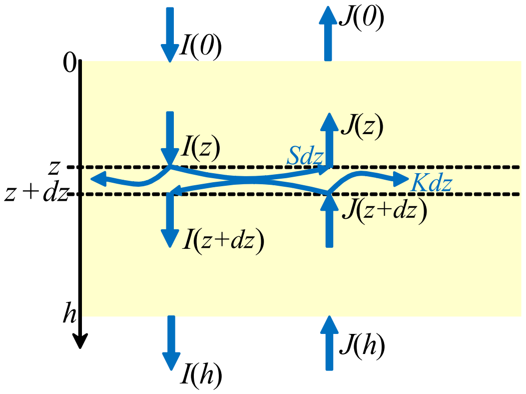

Figure 3.1: Schematic representation of fluxes accounted for in the differential equation system of the Kubelka-Munk model. Fluxes are assumed to be isotropic.

The Kubelka-Munk model assumes that the incident flux, as well as the two fluxes $I(z)$ and $J(z)$ which propagate downwards and upwards respectively at any depth in the material, are perfectly diffuse (Lambertian). As measuring devices are often based on a *bi-directional*, *directional-hemispherical*, or *hemispherical-directional* geometry, the latter assumption is equivalent to assuming that the material under study is highly scattering, so that it can be assumed that a collimated pencil of light is scattered isotropically inside the layer of material at any depth. The emerging flux is also assumed to be perfectly diffuse, and the radiance captured in one direction is proportional to the whole exitance. According to the Kubelka-Munk model, the intrinsic reflectance and intrinsic transmittance of the layer can be deduced according to equation (3.2).

$$\begin{aligned} \rho &= J(0)/I(0) \\ \tau &= I(h)/I(0) \end{aligned} \tag{3.2}$$

where h is the layer thickness.

By integration of the differential equation system, the intrinsic reflectance $\rho(\lambda)$ and intrinsic transmittance $\tau(\lambda)$, intrinsic reminding that the medium is considered without interfaces at its boundaries, can be derived. They are given by close form formulae (3.3) and (3.4).

$$\rho = \frac{\sinh(bSh)}{b\cosh(bSh) + a\sinh(bSh)} \tag{3.3}$$

$$\tau = \frac{b}{b\cosh(bSh) + a\sinh(bSh)} \tag{3.4}$$

with

$$a = \frac{1-\rho^2-\tau^2}{2\rho} = 1 + K/S$$

$$b = \sqrt{a^2-1}.$$

Considering opaque layers, Saunderson proposed a correction to account for the shift of refractive index and subsequent light reflections and refractions [87], given in equation (3.5).

$$R = r_e + \frac{T_{in}T_{out}\rho}{1-r_i\rho} \tag{3.5}$$

All flux transfers accounted for in the Saunderson-corrected two-flux model are accounted for are presented in Figure 3.2.

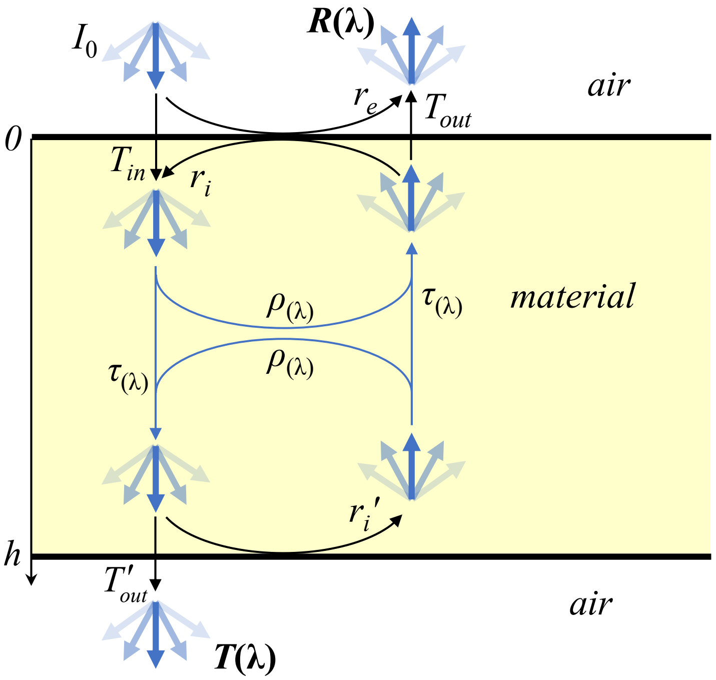

Figure 3.2: Schematic representation accounted for in the two-flux model.

In the case of non-opaque layers, the reflectance and transmittance factors, $R(\lambda)$ and $T(\lambda)$ respectively, which can be measured with a spectrophotometer based on a *directional-hemispherical* or *hemispherical-directional measuring geometry*, are derived from the intrinsic reflectance and transmittance factors, $\rho(\lambda)$ and $\tau(\lambda)$, using an extended Saunderson correction given in equations (3.6) and (3.7) [156]. The Saunderson correction assumes a flat interface (no surface scattering), and also assumes that flux transfers at the lower interface and upper interface are the same, therefore, $r_i' = r_i$ and $T_{out} = T_{out}'$ in Figure 3.2.

$$R = r_e + T_{in} T_{out} \frac{\rho - r_i(\rho^2 - \tau^2)}{(1 - r_i\rho)^2 - r_i^2\tau^2} \tag{3.6}$$

$$T = \frac{T_{in} T_{out} \tau}{(1 - r_i\rho)^2 - r_i^2\tau^2} \tag{3.7}$$

This formalism is called the **2F-RT**model hereinafter. Note that equation (3.6) reduces to equation (3.5) when $\tau = 0$, as in an opaque layer considered in the original Saunderson correction.

r_e denotes the fraction of flux externally reflected by the air-material interface at the air side and is calculated using Fresnel's formula given in equation (3.8) and is equal to 0.04 for $n = 1.5$ if the specular component is included in the measurement, or 0 if it is excluded. Note that in the general case, $n = n_1/n_2$, n_2 being the index of the material and n_2 the index of the surrounding medium, which is most cases is air, and we approximate $n_1 = 1$.

$$r_e = \frac{(n-1)^2}{(n+1)^2} \tag{3.8}$$

r_i represents the fraction of diffuse light that is internally reflected by the interface at the medium side. Its expression, when isotropic scattering is considered, is given in equation (3.9)[182]:

$$r_i = \int_{\theta=0}^{\pi/2} R_{21}(\theta)\sin(2\theta)d\theta \tag{3.9}$$

where $R_{21}(\theta)$ is given by Fresnel's laws [183]:

$$R_{21}(\theta) = \frac{1}{2}\left(R_{p21}(\theta) + R_{s21}(\theta)\right) \tag{3.10}$$

with

$$R_{p12}(\theta) = \left|\frac{n^2\cos\theta - \sqrt{n^2 - \sin^2\theta}}{n^2\cos\theta + \sqrt{n^2 - \sin^2\theta}}\right|^2 \tag{3.11}$$

$$R_{s12}(\theta) = \left|\frac{\sqrt{n^2 - \sin^2\theta} - \cos\theta}{\sqrt{n^2 - \sin^2\theta} + \cos\theta}\right|^2 \tag{3.12}$$

where subscript p (resp. s) referring to light with a p (resp. s) polarization. T_{in} represents the fraction of diffuse incident light crossing the interface from air to medium, according to the measuring geometry. T_{out} represents the fraction of radiance issued from the medium that crosses the interface in the direction of the detector. For a spectrophotometer with a d:8° measuring geometry and n = 1.5, we have:

$$\begin{aligned} r_i &= 0.5963 \\ T_{in} &= n^2(1-r_i) = 0.9083 \\ T_{out} &= (1-r_e)/n^2 = 0.4267 \end{aligned}$$

The two-flux model can also be used to predict the spectral reflectance factor of a layer in optical contact with a background of reflectance $R_g(\lambda)$ and intrinsic reflectance $\rho_g(\lambda)$. The Kubelka-Munk model enables to predict the intrinsic reflectance $\rho_{hg}(\lambda)$ of a layer of thickness h in optical contact against a background, according to:

$$\rho_{hg} = \frac{1-\rho_g(a-b\coth(bSh))}{a-\rho_g+b\coth(bSh)} \tag{3.13}$$

with $a = 1 + K/S$ and $b = \sqrt{a^2-1}$.

Then, the reflectance factor of the layer in optical contact with the background, denoted $R_{hg}(\lambda)$, is derived by applying the Saunderson correction [87] given in equation (3.5).

Thus, the two-flux model relies on four parameters for predicting the spectral reflectance and transmittance factors, denoted $R(\lambda)$ and $T(\lambda)$ respectively: the spectral absorption coefficient $K(\lambda)$, the spectral scattering coefficient $S(\lambda)$, the refractive index $n(\lambda)$ of the material, and thickness h of the sample. Note that all parameters except the thickness h may depend upon the wavelength of light. The refractive index is often assumed to be 1.5 over the visible spectral domain for dental materials. Unless stated otherwise, we will also assume that n = 1.5 in this thesis.

The two-flux model can be inverted to allow the determination of a material's absorption and scattering coefficients $K(\lambda)$ and $S(\lambda)$ respectively from reflectance and transmittance factor measurements, $R(\lambda)$ and $T(\lambda)$ respectively, or from reflectance factor measurements of the sample in optical contact on a black and on a white background, $R_b(\lambda)$ and $R_w(\lambda)$ respectively. The different calibration methods and their predictive performance are described in the following sections.

3.2 Two-flux model on drawdown cards

The two-flux model calibrated from reflectance factor measurements on black and white backgrounds [85-87] is the gold-standard method for optical characterization in dentistry because the white background, being Lambertian, makes translucent dental biomaterials appear like highly scattering materials, which is more consistent with the assumptions of the two-flux model. It is however slightly more tedious to put into practice than the two-flux model based on reflectance and transmittance factor measurements as performing the optical contact between the sample and the background is sometimes delicate.

The optical contact is mandatory to prevent reflections and refractions at the background-layer interface, which could have a significant impact on the global reflectance of the sample whereas they are not accounted for in the model. The optical contact is performed by binding the sample to the background with a liquid of same refractive index, such as a saturated sucrose solution, glycerin or dedicated index matching liquids [92,125,126,148].

Close-form formulae give the material's spectral absorption coefficient $K(\lambda)$ and scattering coefficient $S(\lambda)$ as functions of the measured spectral reflectance factor measurements of the sample placed in optical contact against a black background and a white background. This formalism relies on the assumptions that collimated light is scattered isotropically inside the material. Therefore, the value of the internal reflectance of the upper interface r_i is 0.5963 for n = 1.5.

The spectral reflectance factor of a material layer is successively measured on a white background, denoted $R_w(\lambda)$ and on a black background, denoted $R_k(\lambda)$. The reflectance factor of the black background, denoted $R_{kb}(\lambda)$, and the reflectance factor of the white background, denoted $R_{wb}(\lambda)$, are also measured. The measurements of the sample in optical contact with the background are illustrated in Figure 2.10.

The inverse Saunderson correction is applied to derive, from the measured reflectance factors, the intrinsic reflectance of the layer on a black background $\rho_k(\lambda)$, the intrinsic reflectance of the layer on a white background $\rho_w(\lambda)$, the intrinsic reflectance of the black background $\rho_{kb}(\lambda)$ and the intrinsic reflectance of the white background $\rho_{wb}(\lambda)$ according to the inverse Saunderson correction given in equation (3.14).

$$\rho_i = \frac{R_i - r_e}{T_{in}T_{out} + r_i(R_i - r_e)} \tag{3.14}$$

where subscript i stands either for w, k, wb or kb. For a d:8° or 8°:d geometry and a material with a refractive index n = 1.5, we have $r_e = 0.04$, $r_i = 0.5963$, $T_{in} = 0.908$, and $T_{out} = 0.4267$.

This enables to derived the scattering and absorption coefficients, respectively S and K, according to equations (3.15):

$$\begin{aligned} S &= \frac{1}{h \cdot \sqrt{u^2 - 1}} \operatorname{arccoth}\left(\frac{v}{\sqrt{u^2-1}}\right) \\ K &= S \cdot (u - 1) \end{aligned} \tag{3.15}$$

where h is the thickness of the layer and

$$u = \frac{(\rho_{wb} - \rho_{kb})(1 + \rho_k \rho_w) + (\rho_k - \rho_w)(1 + \rho_{kb}\rho_{wb})}{2(\rho_k \rho_{wb} - \rho_w \rho_{kb})}$$
$$v = \frac{(\rho_{wb} - \rho_{kb})(1 - \rho_k \rho_w) - (\rho_k - \rho_w)(1 - \rho_{kb}\rho_{wb})}{2(\rho_k \rho_{wb} - \rho_w \rho_{kb})} \quad (3.16)$$

When the thickness of the layer is unknown, the dimensionless quantities *Sh* and *Kh* can be derived instead of *S*(λ) and *K*(λ). This calibration formalism of the two-flux model is hereafter denoted the **2F-Rbw** model.

The absorption and scattering coefficients extracted from the samples of the A3 material with this method are presented in Figure 3.3. Those show that the material is strongly absorbing in short wavelengths, as was suspected from measurements on a background presented in Figure 2.12. Values vary depending on the sample thickness, which is not theoretically expected by the model; *K*(λ) and *S*(λ) are expected to be invariant with respect to the sample thickness *h*. Absorption coefficients and scattering coefficients decrease rapidly towards very small values, close to 0 m^{-1} for the absorption coefficient. Some negatives values are reached for the absorption coefficient of the thinnest sample, which is not plausible. This shows that the assumptions of the model are not fully applicable if the sample is too thin. The problem probably comes from measurements of the reflectance factor on a black background; the model assumes a Lambertian light distribution, but light is only weakly scattered by the thin layer of material and thus fails to meet this assumption.

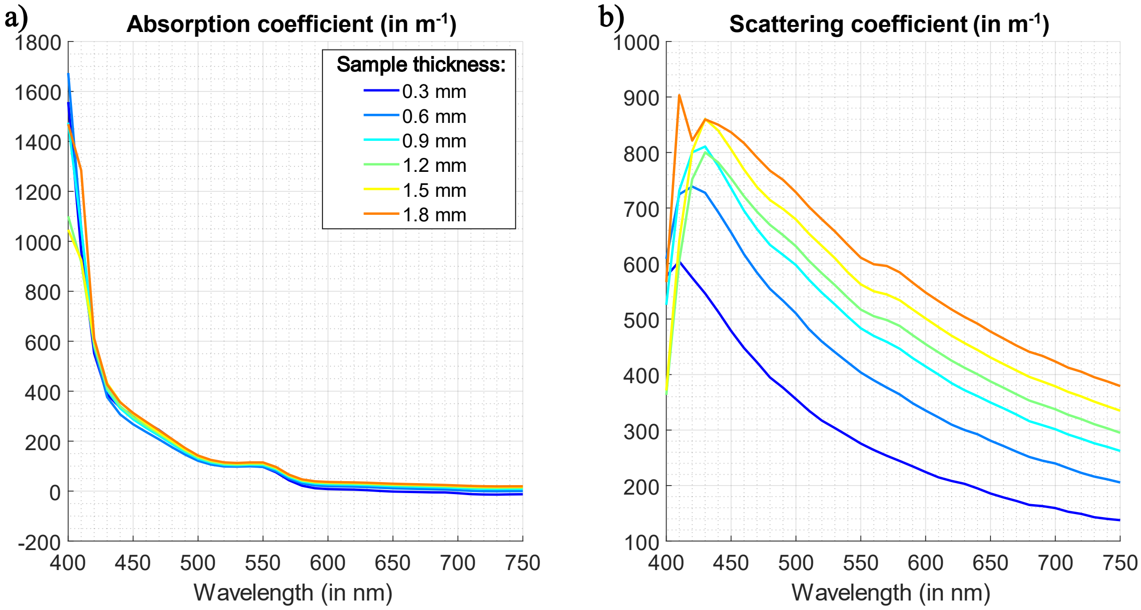

Figure 3.3: a) Absorption coefficients *K*(λ) and b) scattering coefficients *S*(λ) extracted from reflectance factor measurements on black and white backgrounds $R_b(\lambda)$ and $R_w(\lambda)$ respectively of the EsteliteUniversalFlow SuperLow A3 samples of different thicknesses using the **2F-Rbw** model.

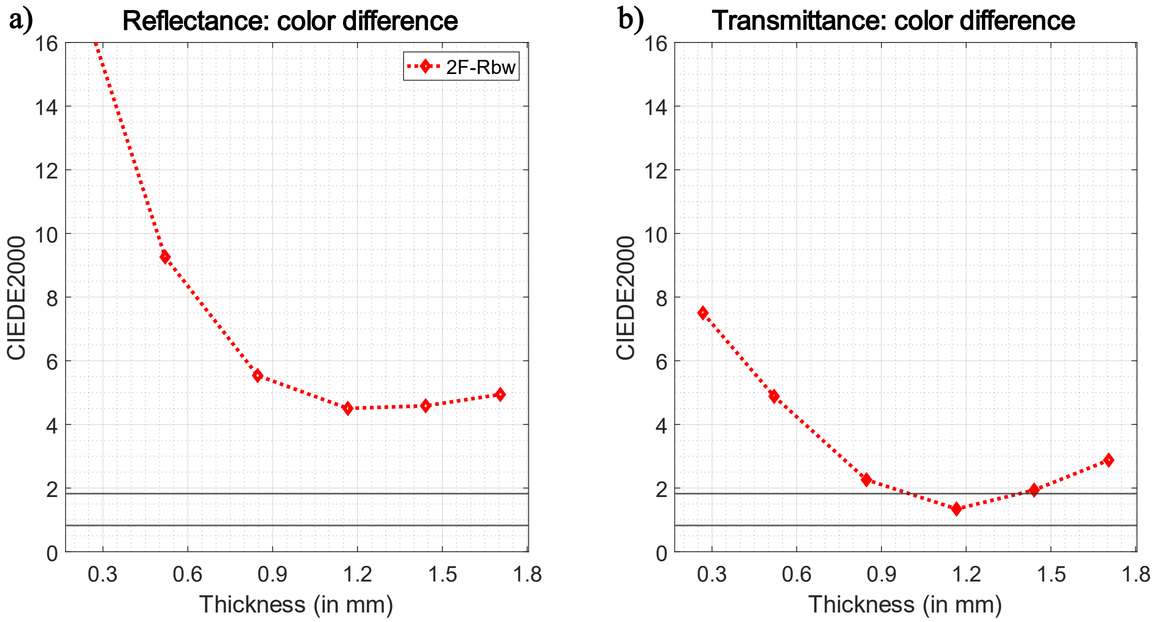

Figure 3.4: Equivalent color difference metric expressing the deviation between a) the measured spectral reflectance factors and b) transmittance factors of samples with various thickness made of the EsteliteUniversalFlow composite shade A3 and the corresponding predictions given by the **2F-RT (calib. 2F-Rbw)** model. The sample with thickness 1.2 mm is used as calibration sample.

The reflectance and transmittance factors prediction accuracy of this method for the A3 material samples is evaluated by taking the coefficients extracted from the calibration samples, with thickness 1.2 mm, and predicting the reflectance and transmittance factors of the other samples. Coefficients are extracted from reflectance factors of the calibration sample on black and white backgrounds using equations (3.14)-(3.16), corresponding to the **2F-Rbw** model. The reflectance and transmittance factors are predicted using equations (3.3), (3.4), (3.6), and (3.7), which correspond to the **2F-RT** formalism. Therefore, the reflectance and transmittance predictions are obtained with the **2F-RT** model calibrated using the **2F-Rbw** model, which is denoted **2F-RT (calib. 2F-Rbw)** model but is labeled **2F-Rbw** in the figures for simplification.

The prediction accuracy of this model is presented in Figure 3.4, with color differences between the reflectance and transmittance factor prediction and the corresponding measurements are plotted as functions of the sample thickness. Each point of the curve corresponds to the color difference between the predicted and the measured spectra, which will be presented in Figure 3.9. The acceptability threshold at 1.8 ΔE_{00} unit is represented by the upper gray strip and the perceptibility threshold 0.8 ΔE_{00} unit is represented by the lower gray strip. A color difference is acceptable when the ΔE_{00} color difference is below the acceptability threshold and is accurate when the ΔE_{00} color difference is below the perceptibility threshold.

The prediction accuracy of this model is very poor, especially for thin samples; most color differences are above the acceptability threshold. However, the prediction accuracy improves with respect to the thickness. Since light is more and more scattered within thick layers of dental materials, these are more in line with the model's assumption of isotropic light, which improves the prediction accuracy. The poor prediction accuracy of this method for the reflectance and transmittance factors makes questionable the validity of the model's assumptions, and thus the physical accuracy of the *K* and *S* values extracted.

3.3 Diffuse reflectance-transmittance two-flux model

The diffuse reflectance-transmittance two-flux model is calibrated using reflectance and transmittance factors, $R(\lambda)$ and $T(\lambda)$ respectively, measured with a spectrophotometer based on a *directional-hemispherical* or *hemispherical-directional* geometry. The intrinsic reflectance and transmittance, $\rho(\lambda)$ and $\tau(\lambda)$, can be derived from the reflectance and transmittance factors using the inverse Saunderson correction extended to non-opaque layers given in equations (3.17) and (3.18). Note that equation (3.17) reduces to equation (3.14) when $T = 0$, in the case where an opaque background is placed in optical contact behind the sample.

$$\rho = \frac{(R-r_e)T_{in}T_{out} + r_i((R-r_e)^2 - T^2)}{\left[r_i((R-r_e)-T)+T_{in}T_{out}\right]\left[r_i((R-r_e)+T)+T_{in}T_{out}\right]} \tag{3.17}$$

$$\tau = \frac{T_{in}T_{out}\tau}{\left[r_i((R-r_e)-T)+T_{in}T_{out}\right]\left[r_i((R-r_e)+T)+T_{in}T_{out}\right]} \tag{3.18}$$

$\rho(\lambda)$ and $\tau(\lambda)$ are used to calculate the absorption and scattering coefficients, $K(\lambda)$ and $S(\lambda)$ respectively, according to equations (3.19) and (3.20).

$$S = \frac{1}{bh}\operatorname{arcsinh}\left(\frac{b\rho}{\tau}\right) \tag{3.19}$$

$$K = S(a-1) \tag{3.20}$$

with

$$a = \frac{1-\rho^2-\tau^2}{2\rho}$$

$$b = \sqrt{a^2-1}$$

Since this model, as the **2F-Rbw** model, assumes that the light reaching the sensor has been scattered isotropically, we can use the same terms for r_e, r_i, T_{in} and T_{out} as for backgrounds, *i.e.*, r_e

= 0.04, r_i = 0.5963, T_{in} = 0.908, and T_{out} = 0.4267 for n = 1.5 in the Saunderson correction. This model is denoted the **2F-RT** model.

The absorption and scattering coefficients extracted using the **2F-Rbw** model and the **2F-RT** model would be the same if the material and measurement conditions satisfied the assumptions of the model, but this is not the case in reality and the $K(\lambda)$ and $S(\lambda)$ values given by the two methods are most often different, with sometimes significant deviations from each other, especially with translucent materials.

The absorption and scattering coefficients, $K(\lambda)$ and $S(\lambda)$ respectively, extracted from samples of the EsteliteUniversalFlow SuperLow A3 material using the **2F-RT** model are presented in Figure 3.5. Although the shape of curves is similar, the spectral curves extracted with respect to the material layer are significantly different. Also, negative scattering coefficients are extracted for samples from 0.3 to 1.2 mm in thickness and negative absorption coefficients are extracted from samples with 0.3 and 0.6 mm in thickness, which is not physically plausible. Such irrelevant values indicate that the model is not valid for the samples under study due to its simplifying assumptions.

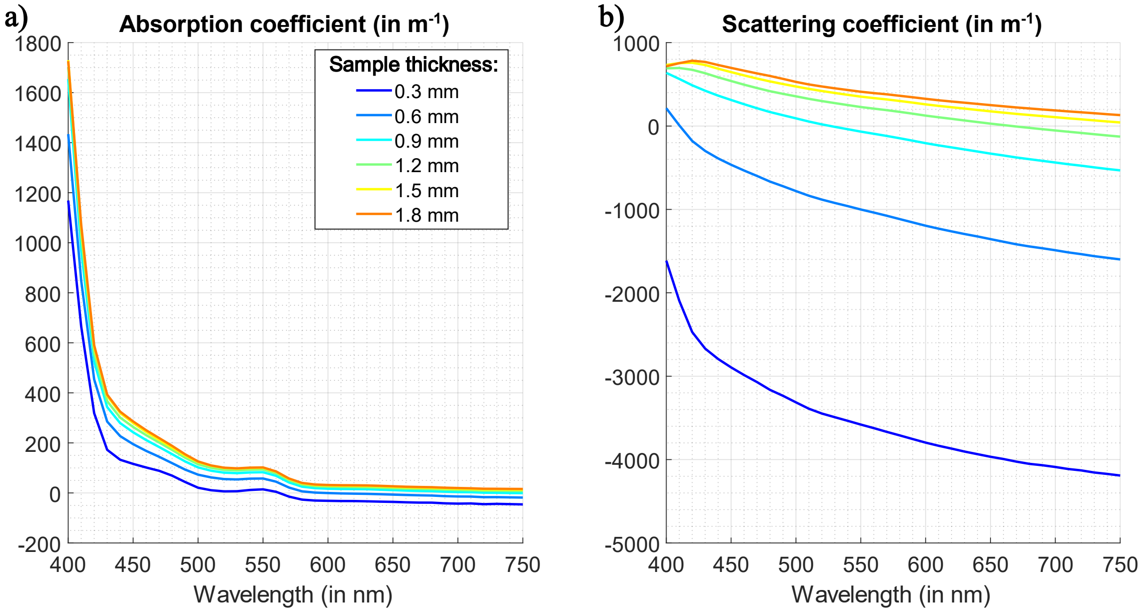

Figure 3.5: a) Absorption coefficients $K(\lambda)$ and b) scattering coefficients $S(\lambda)$ extracted from reflectance and transmittance factor measurements $R(\lambda)$ and $T(\lambda)$ respectively of the EsteliteUniversalFlow SuperLow A3 samples of different thicknesses using the **2F-RT** model.

The predictive performance of this model for predicting the reflectance and transmittance factors of samples is presented in Figure 3.6. Absorption and scattering coefficients were extracted from the reflectance and transmittance factors of the calibration sample, with thickness 1.2 mm, using equations (3.17), (3.18), (3.19), and (3.20). The reflectance and transmittance factors of all samples are then predicted using equations (3.3), (3.4), (3.6), and (3.7), which correspond to the **2F-RT** formalism. Therefore, the reflectance and transmittance predictions are obtained with the **2F-RT** model calibrated using the **2F-RT** model; this is simply denoted as **2F-RT**.

Notice that the color difference between the prediction and the measurement of the calibration sample, with thickness 1.2 mm, is 0 in both reflectance and transmittance modes. This is expected since equations (3.3), (3.4), (3.6), and (3.7) are analytical inversions of equations (3.17), (3.18), (3.19), and (3.20).

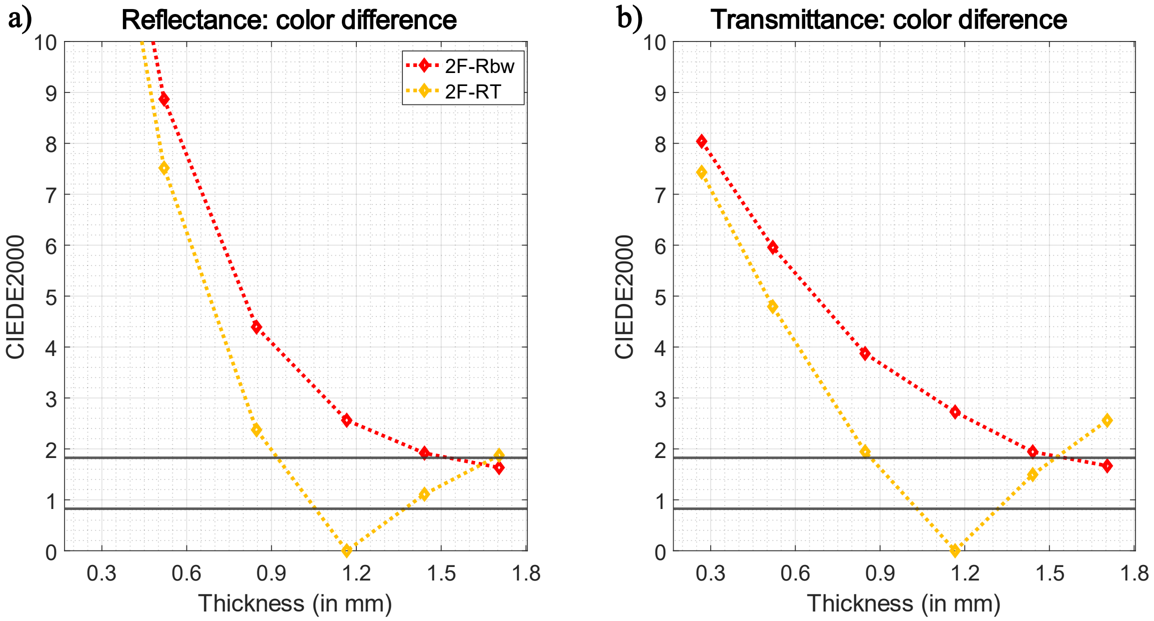

Figure 3.6: Equivalent color difference metric expressing the deviation between a) the measured spectral reflectance factors and b) transmittance factors of samples with various thickness made of the EsteliteUniversalFlow composite shade A3 and the corresponding predictions given by the **2F-RT (calib. 2F-Rbw)** and the **2F-RT** models. The sample with thickness 1.2 mm is used as calibration sample.

Although the **2F-RT** model provides more accurate predictions in both reflectance and transmittance modes than the **2F-Rbw** model, several color differences are highly above the acceptability threshold of 1.8 ΔE_{00} unit, which indicates that the model is not suitable to predict the reflectance and transmittance factors of the material samples. The color difference for the calibration sample is 0 as the model is analytically inversible. This does not mean, however, that the model is more relevant. Notice that the color differences increase rapidly for thicknesses lower than the calibration thickness and increase less rapidly for thicknesses higher than the calibration thickness, in both reflectance and transmittance modes. Both models are more accurate for thick samples than for thin samples. This can be explained because the model's assumptions, namely diffuse flux, is more valid for thick samples. As the thickness increases, light is more scattered throughout the layer, and the light angular distribution is more Lambertian, getting closer to the model's assumptions. On the contrary, for thin samples, only a small fraction of the incident light is scattered by the material, which thus appear more transparent, comparable to glass windows. Thus, we need to improve the two-flux model's prediction accuracy, by accounting for this observation.

3.4 Directional reflectance-transmittance two-flux model

The two-flux model relies on the main assumption that the material is highly scattering, and therefore that the angular distribution of light within the layer and at its interfaces is Lambertian. Based on the results obtained in the previous section, this assumption is likely wrong. Therefore, we tried to apply the two-flux model by considering that the material as a non-scattering material.

In the directional two-flux model we assume that the light rays reaching the sensor mainly follow a directional path, in front of the sensor's field of view, and therefore that the effective measuring geometry is 8°:8° despite the instrument geometry being d:8° (remind Section 2.3 Effective measuring geometry). We argue that for a translucent layer through which transmitted light remains mainly directional, the values of the Saunderson correction parameters are far away from the ones used in the **2F-RT** model for strongly scattering layers. Here we assume that this material's scattering properties are closer to optical properties of a non-scattering material than a highly scattering material. For a non-scattering sample, light remains collimated throughout the layer. When measuring the reflectance factor of such a material with a device of d:8° geometry, the radiance captured by the detector at 8° for the sample's normal only comes from the opposite direction at -8° degree because light is only reflected specularly by the interfaces. Thus, the effective measuring geometry is 8°:8°. This changes the value of r_i from 0.5963 to 0.04 for $n = 1.5$, and therefore $T_{in} = T_{out} = 0.96$ in the calibration step and in the prediction step. Other than the value of r_i, T_{in} and T_{out}, this model is used exactly like the **2F-RT** model, meaning that $K(\lambda)$ and $S(\lambda)$ are extracted using equations (3.17), (3.18), (3.19), and (3.20), but with new values for r_e, r_i, T_{in}, and T_{out}. This model is denoted the **dir2F-RT** model hereinafter.

The absorption and scattering coefficients of same samples as previously, extracted with this model, are presented in Figure 3.7. The absorption coefficients are similar to those extracted with the **2F-Rbw** and **2F-RT** models (see Figure 3.3 and Figure 3.5), with negative values for samples with thickness 0.3 mm and 0.6 mm. Absorption is very high in the short wavelengths and almost zero in longer wavelengths. Scattering coefficients are all positive which is more relevant than with the **2F-RT** model. They show stronger scattering in the short wavelengths (blue light) than in the longer ones (red light), with a trend similar to the scattering spectral values extracted with the **2F-**

Rbw model. The **dir2F-RT** and **2F-Rbw** models provide absorption and scattering spectral curves with similar trends although the values are different. However, there is a noticeable difference: according to coefficients extracted with the **2F-Rbw** model, thick samples are the most scattering, while thin samples are the most scattering according to the **dir2F-RT** model. This is because of the models' assumptions: we assume that layers are strongly scattering in the **2F-Rbw** model while we assume that they are no-scattering in the **dir2F-RT** model. Thus, scattering coefficients extracted from the different samples compensate for these simplifying assumptions, which are both extreme cases, inaccurate for translucent materials.

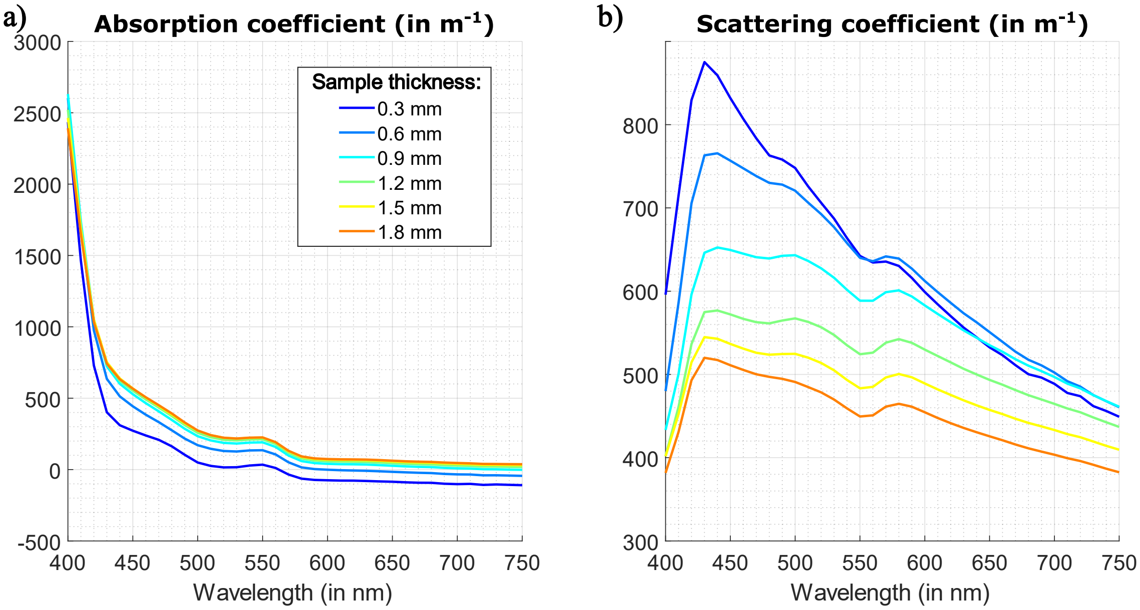

Figure 3.7: a) Absorption coefficients $K(\lambda)$ and b) scattering coefficients $S(\lambda)$ extracted from reflectance and transmittance factor measurements $R(\lambda)$ and $T(\lambda)$ respectively of the EsteliteUniversalFlow SuperLow A3 samples of different thicknesses using the **dir2F-RT** model.

Figure 3.8 shows the predictive performance of the **dir2F-RT** model for predicting the reflectance and transmittance factors of samples. To achieve these predictions, the **dir2F-RT** model is used exactly as the **2F-RT** model with equations (3.3), (3.4), (3.6), and (3.7), except that values of r_e, r_i, T_{in}, and T_{out} are replaced with $r_e = r_i = 0.04$ and $T_{in} = T_{out} = 0.96$. The sample with thickness 1.2 mm is used as calibration sample. The deviation between measured and predicted reflectance factors is lower with the **dir2F-RT** model than with the **2F-RT** and **2F-Rbw** models, with a significant difference especially for thin samples of thickness 0.3 mm and 0.6 mm. The prediction accuracy of the reflectance factor is slightly worse for samples of thickness 1.5 mm and 1.8 mm, but for the transmittance factor, the **dir2F-RT** brings a clear improvement compared to the **2F-RT** and **2F-Rbw** models, as the ΔE_{00} is below the perceptibility threshold for all samples, except for the 1.8 mm thick sample. Although the **dir2F-RT** model is much more accurate than the **2F-RT** model, the color difference for the reflectance factor remains higher than the acceptability threshold for some samples.

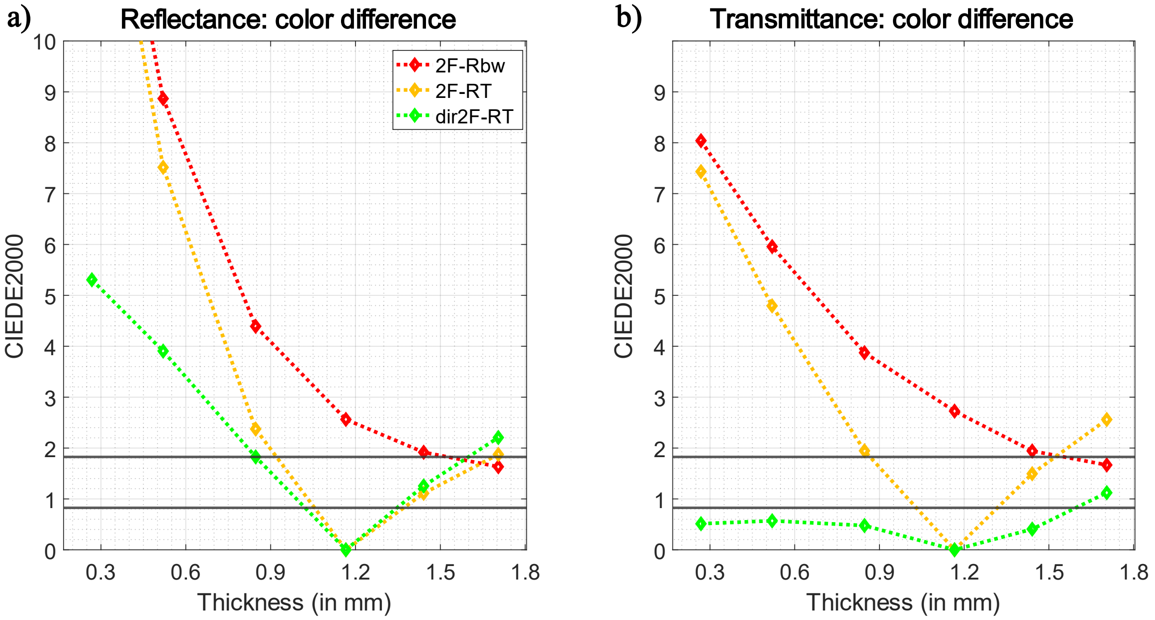

Figure 3.8: Equivalent color difference metric expressing the deviation between a) the measured spectral reflectance factors and b) transmittance factors of samples with various thickness made of the EsteliteUniversalFlow composite shade A3 and the corresponding predictions given by the **dir2F-RT**, **2F-RT (calib. 2F-Rbw)** and the **2F-RT** models. The sample with thickness 1.2 mm is used as calibration sample.

The spectral factors measured and predicted for each sample and model are presented in Figure 3.9. The reflectance spectra predicted by the **2F-RT** and **2F-RT (calib. 2F-Rbw)** models are quite far removed from measurements. The differences are greater at longer wavelengths, while they are smaller at shorter wavelengths. Remember that these models assume that all light is scattered isotropically inside the sample and at its interfaces. Furthermore, we noticed that the scattering coefficients extracted with these models higher at short wavelengths (blue light) and lower at longer wavelengths (red light), indicating that the material is more scattering for blue light than for red light. Models' assumptions are therefore better verified at shorter wavelengths, which probably explains why the discrepancies are less pronounced at shorter wavelengths. Conversely, reflectance spectra predicted by the **dir2F-RT** model, which is based on the specular flux assumption, deviate more at short wavelengths than at long wavelengths, where the scattering coefficient is close to zero, which is thus in line with this model assumption of directional light. Furthermore, the transmittance spectra predicted by the **dir2F-RT** model are very accurate. Light passing through the sample is either directly transmitted, diffuse in the forward direction, or results from multiple

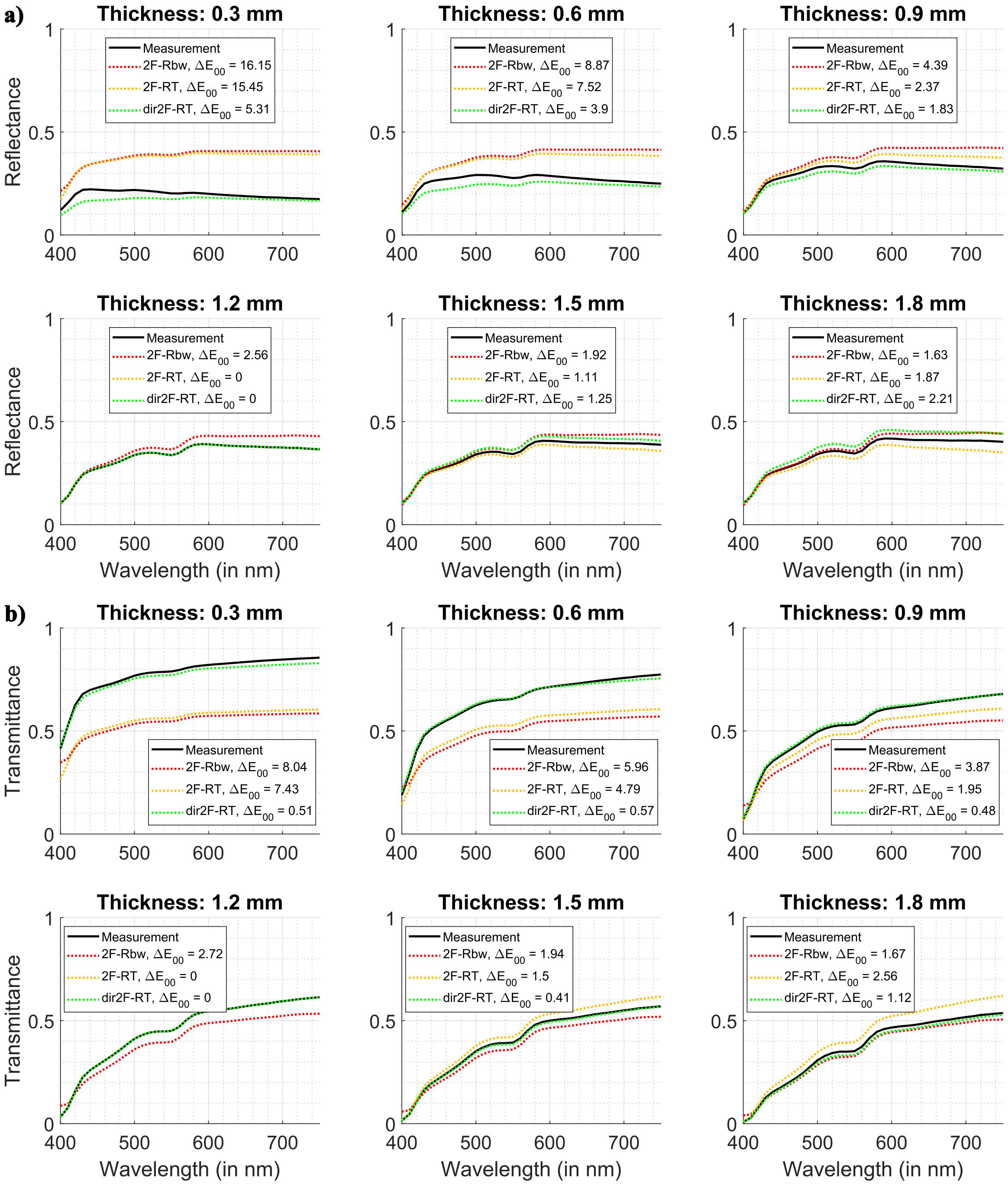

Figure 3.9: a) Reflectance factors and b) transmittance factors measured for each sample of the EsteliteUniversalFlow SuperLow A3 material compared to the reflectance and transmittance factors predicted by the **2F-RT (calib. 2F-Rbw)**, **2F-RT**, and **dir2F-RT** models.

backscattering or interreflection at the interface. It is rather safe to assume that most of the light transmitted has followed one of the first two possibilities. Thus, light passing through the sample is much less scattered, and thus, the directional angular distribution of light at the interfaces is more relevant in transmittance mode than in reflectance mode.

This first development of the two-flux model highlights the importance of rigorously taking into account the angular distribution of light at the interfaces. This distribution represents the predominant light trajectories reaching the detector, and its inclusion can considerably improve the models' accuracy at predicting the reflectance and transmittance factors of samples. The Lambertian distribution assumption, as used in the classical two-flux models of the state of the art, *i.e.* the **2F-RT** and **2F-Rbw** models, proves unsatisfactory. On the other hand, the directional distribution assumption offers better results, although this assumption is probably exaggerated and partly unrealistic. The physical reality lies somewhere between these two extremes and also depends on sample thickness. For thinner samples, a more directional distribution seems appropriate, while for thicker samples, a wider angular distribution is required to account for greater luminance scattering. These considerations led us to evaluate the four-flux model, which distinguishes between the propagation of specular and diffuse fluxes. This is covered in Chapter 4. However, we first evaluate the two-flux model's ability to predict the reflectance factor of layered sample.

3.5 Layered samples

In dentistry, most restorations involve layering resin composite materials, with one more opaque material replacing dentin and another material, more translucent, replacing enamel. In our study, the case that comes closest to this procedure is the stacking of two samples on top of each other, constituting a layered sample. Optical contact must be made between the two samples to prevent reflections and transmissions at the material-air interfaces between the two material layers. In practice, the dentist applies the fluid resin onto the first solidified layer before photopolymerizing it, thus ensuring optical continuity between the two layers. In our case, optical contact was performed using the clear *Immersion Oil Type B* from Cargille.

The ability of the Kubelka-Munk Reflectance Theory to predict the color of layered samples has already been assessed in several studies [90,91,125], in particular with respect to resin composition in [126,159]. In [129,130], the prediction accuracy of interpolation methods has also been assessed. Here, we evaluate the **2F-Rbw** model's ability to predict the reflectance of a sample on a black and white background, when it is calibrated with either the absorption and scattering coefficients extracted using the **2F-Rbw** model (measurements on backgrounds), the **2F-RT** model (**2F-Rbw calib. 2F-RT**) (reflectance and transmittance measurements), and or the **dir2F-RT** model (**2F-Rbw calib. dir2F-RT**) (reflectance and transmittance measurements). Secondly, we test the models' ability to predict the reflectance of dentin+enamel layered samples, like illustrated in Figure 3.10. This work has been published in [226].

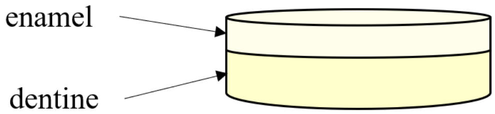

Figure 3.10: Schematic representation of layered samples studied in this section.

3.5.1. Prediction accuracy on black and white backgrounds

The two-flux model's formalism provides formula (3.21) to calculate the intrinsic reflectance factor $\rho_{h,g}$ of a sample on a background of specified reflectance factor, denoted R_g, as a function of the background's intrinsic reflectance denoted ρ_g, which is calculated by applying the inverse Saunderson correction to R_g as in formula (3.14), the absorption coefficient K, scattering coefficient S of the material, and h the thickness of the material layer:

$$\rho_{h,g} = \frac{1-\rho_g(a-b\coth(bSh))}{a-\rho_g+b\coth(bSh)} \tag{3.21}$$

with

$$a = 1+K/S$$
$$b=\sqrt{a^2-1}$$

The reflectance factor of the layer in optical contact with a background, denoted $R_{h,g}$ is then derived by applying the Saunderson correction formula (3.5) and recalled here:

$$R = r_e + \frac{T_{in}T_{out}\rho}{1-r_i\rho} \tag{3.22}$$

Therefore, this formalism can be used to predict the reflectance of samples of dental material on black and white backgrounds or of any other color using absorption K and scattering S coefficients extracted from the **2F-RT** (formulae (3.17)-(3.20)), **dir2F-RT** (formulae (3.17)-(3.20) with $r_e = r_i = 0.04$, $T_{in} = T_{out} = 0.96$), and **2F-Rbw** (formulae (3.14)-(3.16)) models. Thus, we investigate the **2F-Rbw (calib. 2F-RT)** model, the **2F-Rbw (calib. dir2F-RT)** model, and the **2F-Rbw** model. For clarity, these models will only be referred to by the name of the model used to derive the absorption and scattering coefficients, since the model used to predict the reflectance factor of the layer on a background is always the **2F-Rbw** model (formulae (3.21) and (3.22)). Regardless of the method used to extract the absorption and scattering coefficients, either **2F-RT**, **dir2F-RT**, or **2F-Rbw**, the Saunderson correction applied to derive $R_{h,g}$ is done considering isotropic angular distribution of light at the upper interface, thus $r_i = 0.5963$, $T_{in} = 0.9083$ and $T_{out} = 0.4267$. This assumption is relevant as backgrounds used in this experiment are Lambertian. There interface is glossy, but its influence is cancelled because of the optical contact between the material and the background. The prediction accuracy of the different models is shown in Figure 3.11.

For predicting the reflectance factor of the dental samples in optical contact with a white background, the **2F-RT** and especially the **2F-Rbw** models are rather accurate, and all color differences are below the acceptability threshold. The **2F-Rbw** is the most accurate model and all predictions are below the perceptibility threshold. As expected, the **dir2F-RT** model, however, is totally inaccurate, which shows that the assumption of collimated flux at interfaces is not valid in the case where a highly reflecting diffusing background is placed behind the sample.

With a black background, the **2F-RT** and **dir2F-RT** models are inaccurate. The **2F-Rbw** model only provides acceptable predictions for samples with thickness close to the one of the calibration sample, 1.2 mm. Obviously, the black background is almost totally absorbing. The light that crosses the layer is therefore absorbed by the background, and only the light backscattered within the material can exit towards the sensor. For sure, this backscattered light is not directional. The **2F-RT** is not accurate either, because the *K* and *S* determined during the calibration process on a sample without background come from reflectance and transmittance factor measurements in which the light paths are mainly directional, therefore very different from those mainly involved in the reflection of light by the sample on a white background.

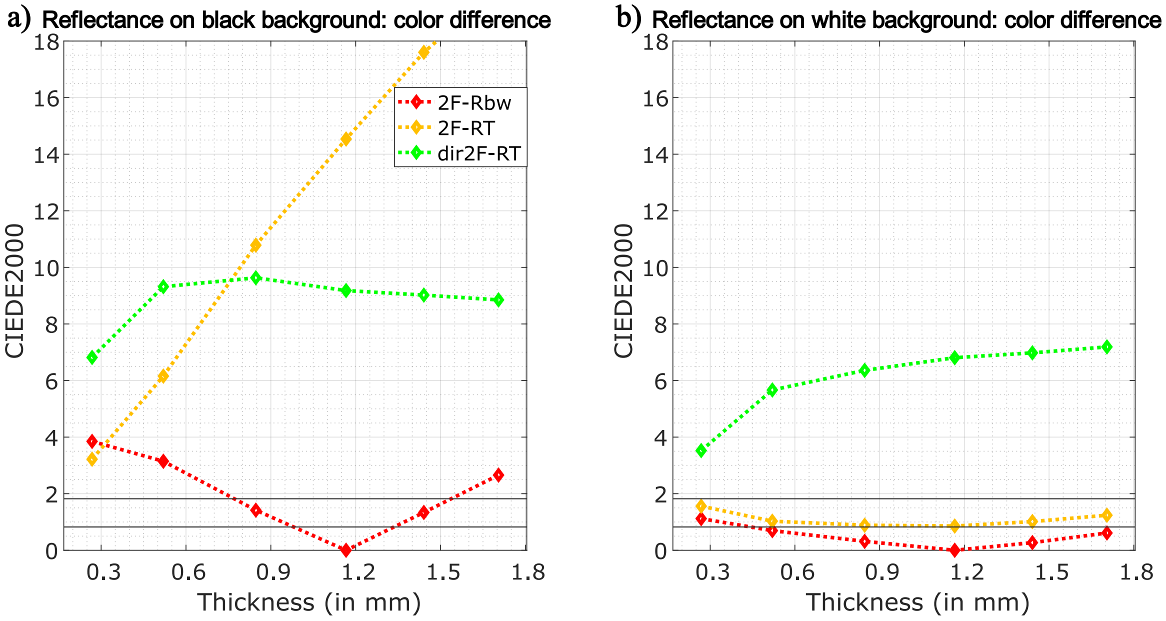

Figure 3.11: Equivalent color difference metric expressing the deviation between a) the measured spectral reflectance factors on black background and b) reflectance factors on white background of samples with various thickness made of the EsteliteUniversalFlow composite shade A3 and the corresponding predictions given by the **2F-Rbw** model, the **2F-RT** model and the **dir2F-RT** model. The sample with thickness 1.2 mm is used as calibration sample.

3.5.2. Prediction accuracy for layered samples

In this section, we considered samples of the EsteliteUniversalFlow Medium A2 enamel-like material and the EsteliteUniversalFlow Medium OA2 dentin-like material. Therefore, the prediction accuracy of two-flux models for monolithic layers of these two materials on black and white backgrounds is shown in Figure 3.12 and Figure 3.13.

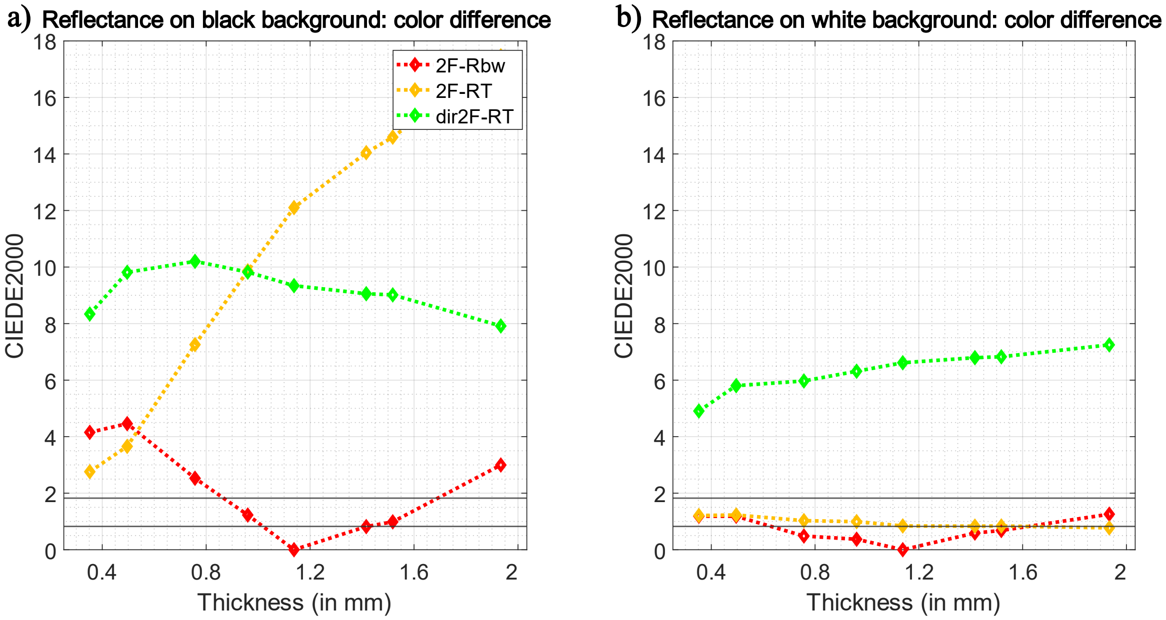

Figure 3.12: Equivalent color difference metric expressing the deviation between a) the measured spectral reflectance factors on black background and b) reflectance factors on white background of samples with various thickness made of the EsteliteUniversalFlow Medium composite shade A2 and the corresponding predictions given by the **2F-Rbw** model, the **2F-RT** model and the dir2F-**RT** model. The sample with thickness 1.2 mm is used as calibration sample.

The **2F-Rbw** model could be used to predict the reflectance of a layered sample, however, this formalism assumes that the background (here the dentin-like sample) is opaque, which is not necessarily the case. Thus, we use the formalism proposed by Kubelka [157] which considers the case of a non-symmetric diffusing layer composed by a layer of enamel and a layer of dentin. The two layers are characterized by their respective intrinsic reflectance and transmittance factors, denoted ρ_e and τ_e, ρ_d and τ_d. ρ_e, τ_e, ρ_d and τ_d are derived with the Kubelka-Munk model given in formulae (3.3) and (3.4), with the absorption and scattering coefficients of each material, K_e, S_e, K_d and S_d being derived for each material separately using either the **2F-Rbw** (formulae (3.14)-(3.16)), the **2F-RT** (formulae (3.17)-(3.20)) or the **dir2F-RT** (formulae (3.17)-(3.20) with $r_i = 0.04$, $T_{in} = T_{out} = 0.96$) model on the calibration sample.

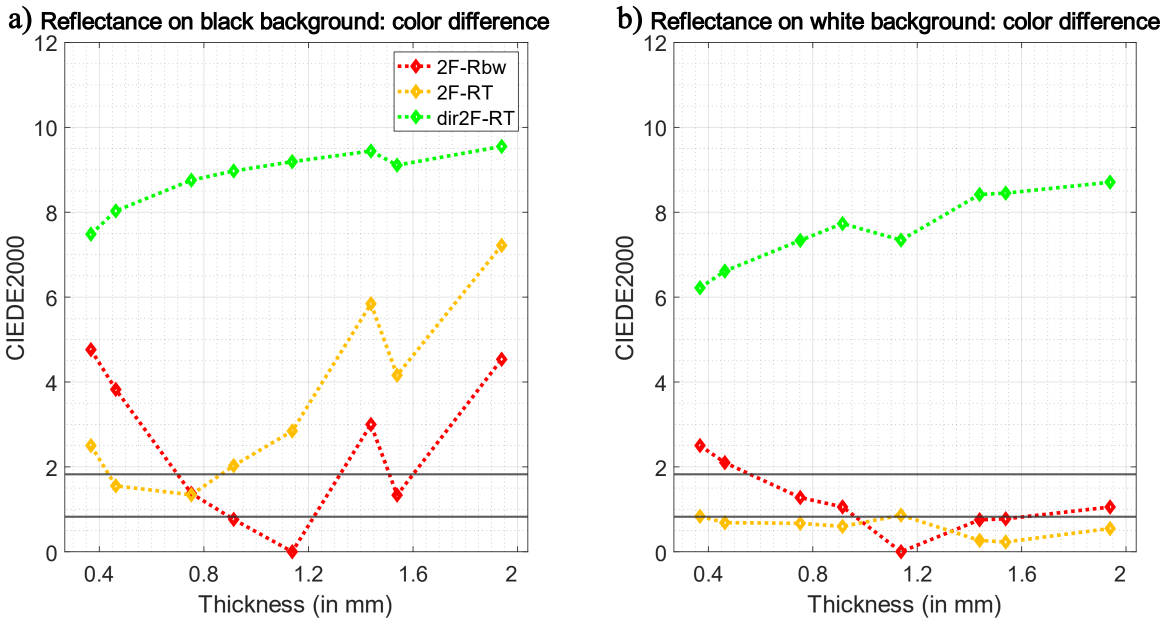

Figure 3.13: Equivalent color difference metric expressing the deviation between a) the measured spectral reflectance factors on black background and b) reflectance factors on white background of samples with various thickness made of the EsteliteUniversalFlow Medium composite shade OA2 and the corresponding predictions given by the **2F-RT** model, the **dir2F-RT** model and the **2F-Rbw** model. The sample with thickness 1.2 mm is used as calibration sample.

The intrinsic reflectance and transmittance factors are given by formulae (3.23) and (3.24), assuming that each separate layer is homogeneous:

$$\rho_{e+d} = \rho_e + \frac{\tau_e^2 \rho_d}{1-\rho_e \rho_d} \tag{3.23}$$

$$\tau_{e+d} = \frac{\tau_e \tau_d}{1-\rho_e \rho_d} \tag{3.24}$$

Note that these formulae are valid for a layered sample of enamel on a dentine sample (the enamel sample is facing the sensor during reflectance measurements); the reflectance of a layered sample being different on the enamel side and on the dentine side. The reflectance and transmittance factors of the layered sample is then derived by applying the extended Saunderson correction given in formula (3.6) and (3.7), and recalled here:

$$R = r_e + T_{in} T_{out} \frac{\rho - r_i(\rho^2 - \tau^2)}{(1-r_i\rho)^2 - r_i^2 \tau^2} \tag{3.25}$$

$$T = \frac{T_{in} T_{out} \tau}{(1-r_i\rho)^2 - r_i^2 \tau^2} \tag{3.26}$$

with $r_e = r_i = 0.04$ and $T_{in} = T_{out} = 0.96$ for the **dir2F-RT** model, $r_e = 0.04$, $r_i = 0.5963$, $T_{in} = 0.908$ and $T_{out} = 0.5963$ for the **2F-RT** and **2F-Rbw** models. Note that a flux transfer matrix formalism extensively described in [156] can also be used and can easily be adapted for N layers of diffusing layers. Details are given in 0.

Several stacks of dentin+enamel (resp. OA2+A2 materials) samples were formed, and their reflectance factor was measured. The A2 enamel-like material was always placed on the illumination side for the measurement, as this material is always supposed to face outward the mouth in a clinical situation. The pairs formed are presented in Table 3.1. The **2F-Rbw**, **2F-RT**, and **dir2F-RT** models were calibrated independently. The A2 and OA2 samples with thickness 1.0 mm were used for the calibration of the **2F-Rbw** model while A2 and OA2 samples with thickness 2.0 mm were used for the calibration of the **2F-RT** and **dir2F-RT** models. This was found to enable the best prediction accuracy for each model.

Table 3.1: Pairs of A2/OA2 samples evaluated for the prediction of their reflectance factor, and color differences expressed as CIEDE2000 units between the measurements and the predictions of each model. Thicknesses are given in mm.

A2 sample nominal thickness	OA2 sample nominal thickness	Total thickness	Color difference in reflectance		
			2F-Rbw	2F-RT	dir2F-RT
0.5	0.5	0.96	1.47	1.65	3.26
0.5	1.0	1.41	0.38	0.79	1.42
1.0	0.5	1.42	0.65	0.80	1.47
1.0	1.0	1.87	0.25	0.57	0.62
1.5	0.5	1.88	0.26	0.48	0.55
0.5	1.5	1.93	0.40	0.64	0.58
0.4	2.0	2.29	0.45	0.60	0.70
1.5	1.0	2.33	0.45	0.62	0.84
1.0	1.5	2.40	0.46	0.60	0.85
0.5	2.0	2.43	0.58	0.56	0.67
0.8	2.0	2.70	0.74	0.54	0.71
1.5	1.5	2.85	0.62	0.68	1.23
1.0	2.0	2.90	0.55	0.56	1.10
1.2	2.0	3.08	0.84	0.71	1.01
1.5	2.0	3.35	0.77	0.66	1.41
1.6	2.0	3.46	0.64	0.68	1.51
2.0	2.0	3.87	1.01	0.92	1.61

The prediction accuracy of each model is displayed in Figure 3.14.

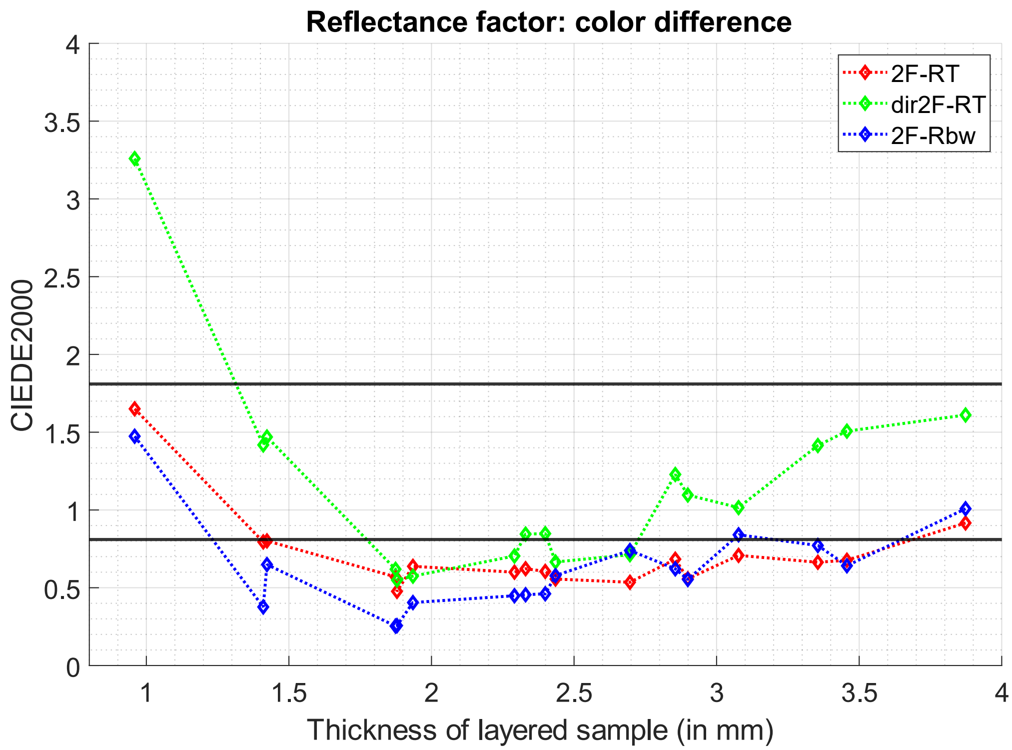

Figure 3.14: Deviation between measured and predicted reflectance factors expressed in CIEDE2000 color difference units, for A2/OA2 layered samples of the Estelite Universal Flow Medium material. The A2 and OA2 samples with thickness 1.0 mm are used for the calibration of the **2F-Rbw** model while A2 and OA2 samples with thickness 2.0 mm are used for the calibration of the **2F-RT** and **dir2F-RT** models.

For all three models, almost all color differences are below the acceptability threshold, and even below the perceptibility threshold with the **2F-RT** and **2F-Rbw** models. In contrast with the previous observations on monolithic samples, the **2F-Rbw** is the most accurate model. In this situation, the A2 samples are placed in optical contact against the OA2 sample, a more opaque (although still translucent) white background. Thus, optical parameters of the A2 and OA2 samples extracted with the **2F-Rbw** model are necessarily closer to this case than the optical parameters extracted from reflectance and transmittance factor measurements, which partly explains the good predictive performance of this model. The fact that the **2F-RT** model is almost as accurate as the **2F-Rbw** model, and the **dir2F-RT** is the least accurate, indicates that the assumption of a Lambertian angular light distribution at both interfaces of the stack generally applies in these thick, multilayer samples. This assumption is made more valid thanks to the higher thickness of the multilayer sample, and that the dentin-like sample is more opaque and more highly scattering. Remind that the **dir2F-RT** model provided very inaccurate predictions of the reflectance factor on both black and white background. In the case of layered materials, the **dir2F-RT** model being rather accurate as well, enabling acceptable predictions for almost every stack, shows that the assumption of the angular distribution of light at interfaces is less important for thick layered materials than it is for thin monolithic samples.

Thus, we can conclude that the **2F-Rbw** model is accurate for color prediction of the tested layered samples, which is consistent with results already published in [125,159] which focused on similar types of translucent dental materials for thicknesses greater than 4.0 mm. We also find that the **2F-RT** model is almost as accurate as the **2F-Rbw** model. However, our study on multilayer samples is limited to only one material type, and should therefore be confirmed with different dental materials, and with layering of different shades.

3.6 Conclusion on two-flux models

The investigations obtained in this chapter are summarized in Table 3.2.

Table 3.2: Comparison of the models' assumptions, measurements required for their calibration, and their prediction accuracy.

Model	Main assumption within the bulk	Main assumption at interfaces	Measurements required	Accuracy for single layer samples	Accuracy for bilayer samples
2F-Rbw	Lambertian light	Lambertian light, same r_i at both interfaces	R_b and R_w	inaccurate for R and T, almost acceptable for R_b and accurate for R_w	accurate
2F-RT	Lambertian light	Lambertian light, same r_i at both interfaces	R and T	inaccurate for R, T and R_b, acceptable for R_w	accurate
dir2F-RT	Collimated light	Collimated light, same r_i at both interfaces	R and T	inaccurate for R, R_b, R_w, accurate for T	acceptable

All three models, the **2F-Rbw**, **2F-RT**, and **dir2F-RT** models are inaccurate to predict the reflectance factor of the samples investigated, even though the **dir2F-RT** achieves more accurate predictions than the other models, especially for thin samples. For the prediction of the transmittance factor, only the **dir2F-RT** enables accurate predictions. However, this model is inaccurate to predict the reflectance factor of samples on a black or white background, whereas the **2F-RT** model allows for acceptable predictions of the reflectance factor of samples on a white background (but inaccurate on a black background), and the **2F-Rbw** models achieves accurate predictions of the reflectance factor of samples on a white background and acceptable predictions for the reflectance factor of samples on a black background.

Chapter 4.
Performance of four-flux models

The four-flux model was originally proposed by Maheu *et al.* [161]. Despite offering a refined description of light propagation in comparison to the Kubelka-Munk model, the four-flux model is less used because of its slightly higher complexity. The model requires four measurements for its calibration instead of two for the two-flux model. Moreover, it is not inversible analytically, and relies on two additional optical parameters, namely the average path length parameter and the forward scattering ratio, which cannot be measured directly. To this aim, several modifications have been proposed over time [162-166], and inversion strategies have been proposed [167,168].

Four-flux models were used in various fields for applications where the Kubelka-Munk model was not satisfying in terms of accuracy. Thus, it has been used to derive the optical index of pigments [169,170], characterize coatings [171-173], paints [174], ceramics [175,176] or solar cells [177], or predict the appearance of 3D prints [178-181]. In this thesis, we investigated the four-flux model originally proposed by Maheu *et al.* [161], a similar model proposed by Rozé *et al.* [165], a variant recently published by Eymard *et al.* [177], and we propose a new method based on the previous models. Each of the following sections presents separately Maheu's four-flux model, Rozé's four-flux model, Eymard's four-flux model, and our four-flux model, along with the optical parameters derived from samples of the EsteliteUniversalFlow SuperLow A3 material, and the models' prediction accuracy for predicting the reflectance and transmittance factors of the samples.

4.1 Maheu's four-flux model

According to the four-flux model by Maheu *et al.*, denoted **Maheu4F-RT** hereinafter, the macroscopic properties of a material layer of thickness h result from the propagation of diffuse and collimated light fluxes. The optical properties of the material, according to the four-flux model, are described by four parameters: the absorption coefficient denoted $k(\lambda)$, the scattering coefficient denoted $s(\lambda)$, the forward scattering ratio denoted $\zeta(\lambda)$, and the average path length parameter denoted $\varepsilon(\lambda)$. Coefficients $k(\lambda)$ and $s(\lambda)$ are different from the coefficients $K(\lambda)$ and $S(\lambda)$ considered in the two-flux model. The relationship between them is discussed in [188,217]. A system of four differential equations describes the mutual exchanges between collimated and diffuse fluxes, which are also illustrated in Figure 4.1. It is given in equations (4.1).

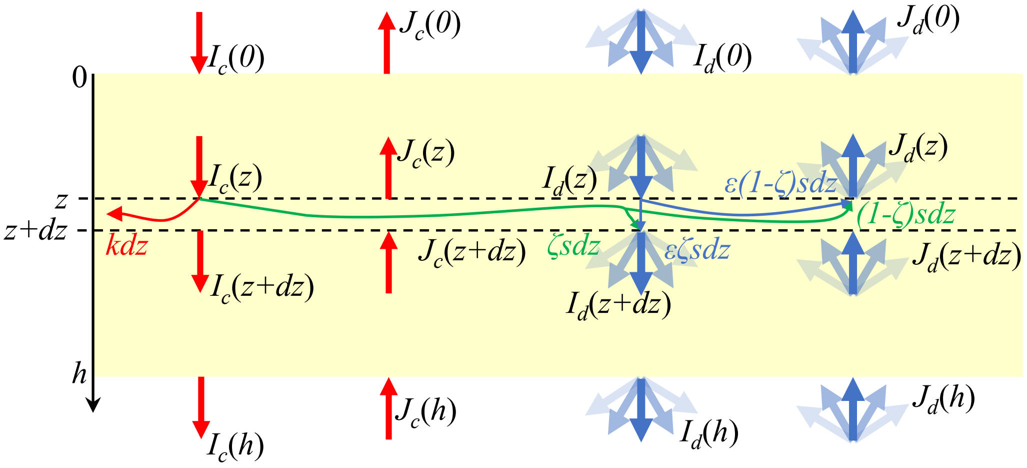

Figure 4.1: Mutual exchanges between collimated and diffuse fluxes considered in the four-flux model. Only flux transfers from incident fluxes flowing downwards are represented for clarity.

$$\begin{cases} \dfrac{dI_c}{dz} = -(k+s)I_c \\ \dfrac{dJ_c}{dz} = +(k+s)J_c \\ \dfrac{dI_d}{dz} = -\varepsilon k I_d - \varepsilon(1-\zeta)sI_d + \varepsilon(1-\zeta)sJ_d + \zeta sI_c + (1-\zeta)sJ_c \\ \dfrac{dJ_d}{dz} = +\varepsilon k J_d + \varepsilon(1-\zeta)sJ_d - \varepsilon(1-\zeta)sI_d - (1-\zeta)sI_c - \zeta sJ_c \end{cases} \tag{4.1}$$

The collimated fluxes are attenuated by absorption and by forward and backward scattering. The diffuse fluxes are augmented by scattering from collimated fluxes and backscattering from the diffuse flux flowing in opposite direction. The propagation of diffuse fluxes is described by two parameters: the forward scattering ratio $\zeta(\lambda)$ which describes the proportion of the flux scattered in the forward hemisphere, and the average path-length parameter $\varepsilon(\lambda)$ which accounts for the longer distance travelled by light rays of the diffuse flux travelling sideways into the material respectively to light rays travelling along the incident direction normal to the sample's interfaces. The forward scattering ratio is necessary between 0 and 1. The average path length parameter corresponding to collimated propagation is 1 while the value corresponding to isotropic scattering is 2.

The fluxes considered in the four-flux model are presented in Figure 4.2. The layer is assumed to be infinitely large so that side effects are neglected. The layer can be illuminated with collimated and/or diffuse light from upper side. The four-flux model accounts for the propagation of collimated flux inside the layer, its attenuation due to absorption and scattering, and its reflection at the lower and upper bordering interfaces in case the surrounding medium (in practice: air) has a different refractive index than the material. The *collimated-to-collimated* reflectance $R_{cc}(\lambda)$ and *diffuse* reflectance $R_{diffuse}(\lambda)$ are collected at the upper side (illumination side). The *diffuse* reflectance is the sum of the *collimated-to-diffuse* reflectance $R_{cd}(\lambda)$, *i.e.* the diffuse flux resulting from the scattering of collimated light, represented in green in Figure 4.2, and the *diffuse-to-diffuse* reflectance $R_{dd}(\lambda)$, *i.e.* the diffuse flux resulting for the reflection of the incident diffuse flux into the material. Similarly, the *collimated-to-collimated* transmittance $T_{cc}(\lambda)$ and the *diffuse* transmittance $T_{diffuse}(\lambda)$ are collected at the lower side of the layer. The *diffuse* transmittance is the sum of the *collimated-to-diffuse* transmittance, represented in green in Figure 4.2, and the *diffuse-to-diffuse* transmittance.

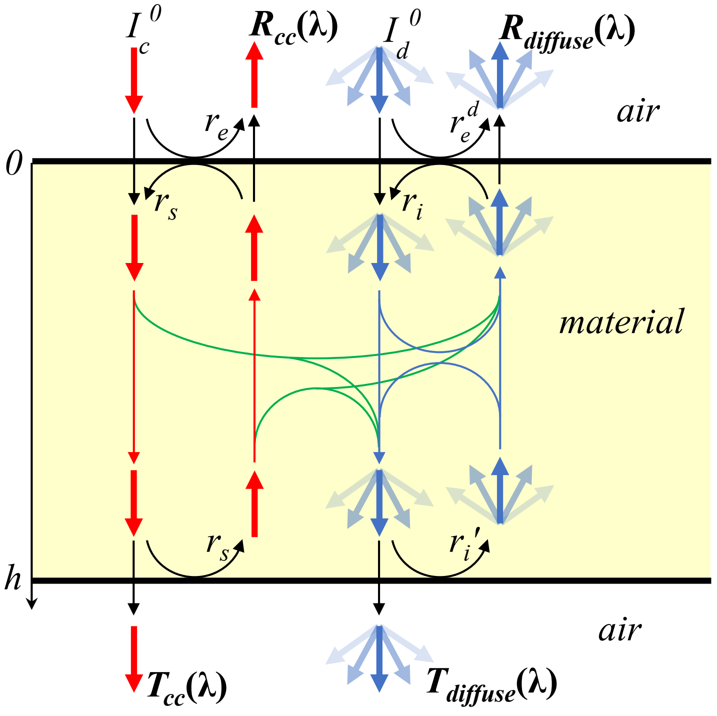

Figure 4.2: Flux transfers accounted for in the four-flux model.

According to the four-flux model, the *total* reflectance factor $R(\lambda)$ and *total* transmittance factor $T(\lambda)$ are given by:

$$R(\lambda) = R_{cc}(\lambda) + R_{cd}(\lambda) + R_{dd}(\lambda) \tag{4.2}$$

and

$$T(\lambda) = T_{cc}(\lambda) + T_{cd}(\lambda) + T_{dd}(\lambda) \tag{4.3}$$

In practice, the total reflectance and transmittance factors are measured with a device based on a *hemispherical-directional* or *directional-hemispherical* geometry, which corresponds to the case where the layer is illuminated with collimated light and no diffuse light, while all the flux is collected at the upper side (reflectance factor) and lower side (transmittance factor). In the absence of diffuse illumination, as with measuring devices based on *hemispherical-directional* geometry, the *diffuse-to-diffuse* components $R_{dd}(\lambda)$ and $T_{dd}(\lambda)$ are zero. With the Color i7 spectrophotometer, the *total* reflectance factor $R(\lambda)$ is measured in SCI mode as illustrated in Figure 2.1a), the *collimated to diffuse* reflectance factor $R_{cd}(\lambda)$ is measured in SCE mode as illustrated in Figure 2.1b). The *collimated-to-collimated* reflectance factor $R_{cc}(\lambda)$ is deducted by subtracting $R_{cd}(\lambda)$ to $R(\lambda)$. The total transmittance factor is measured in total transmittance mode as illustrated in Figure 2.1c), and the collimated to collimated transmittance factor is measured in direct transmittance mode as illustrated in Figure 2.1d). Likewise, the *collimated to diffuse* transmittance factor is deduced by subtracting the *collimated-to-collimated* transmittance factor to the *total* transmittance factor.

At both upper and lower interfaces of the material, which are assumed to be flat, the model considers that a fraction r_i of the diffuse light is reflected internally. r_i is calculated by taking into account the angular radiance distribution $L(\theta)$ if the light falling on the interface:

$$r_i = \int_{\theta=0}^{\pi/2} R_{21}(\theta) L(\theta) \sin(2\theta) d\theta \Big/ \int_{\theta=0}^{\pi/2} L(\theta) \sin(2\theta) d\theta \tag{4.4}$$

where $R_{21}(\theta)$ still denotes the Fresnel angular reflectance of the interface at the side of the medium with highest optical index [182]. When the flux is isotropic at the interface, $L(\theta)$ is a constant and thus r_i simplifies into equation (4.4):

$$r_i = \int_{\theta=0}^{\pi/2} R_{21}(\theta) \sin(2\theta) d\theta \tag{4.5}$$

as in equation (3.9). For a material with refractive index $n = 1.5$, we still have $r_i = 0.5963$.

The model also considers the fractions r_e and r_s of the collimated light that are reflected externally and internally. Both fractions are equal. At normal incidence, r_e and r_s are calculated according to:

$$r_e = \frac{(n-1)^2}{(n+1)^2} \tag{4.6}$$

Then, for a material layer of thickness h, the four-flux model enables to calculate the collimated-to-collimated reflectance $R_{cc}(\lambda)$, collimated-to-collimated transmittance $T_{cc}(\lambda)$, collimated-to-diffuse reflectance $R_{cd}(\lambda)$, collimated-to-diffuse transmittance $T_{cd}(\lambda)$, according to

$$R_{cc} = r_e + \frac{(1-r_e)^2 r_e \exp[-2(k+s)h]}{1-r_e^{\,2} \exp[-2(k+s)h]} \tag{4.7}$$

$$\begin{aligned}R_{cd} &= \frac{(1-r_i)(1-r_e)\exp[-(k+s)h]}{[A_1-(k+s)^2]\{1-r_e^2\exp[-2(k+s)h]\}}\\ &\cdot\frac{1}{\sqrt{A_1}(r_i^2-1)\cosh(\sqrt{A_1}h)+[A_5(2r_i)-A_4(1+r_i^2)]\sinh(\sqrt{A_1}h)}\\ &\cdot(\sqrt{A_1}[A_3+A_2r_e-r_i(A_2+A_3r_e)]\\ &+\{\sqrt{A_1}(A_2r_i-A_3)\cosh(\sqrt{A_1}h)+[A_2(A_5-A_4r_i)+A_3(A_5r_i-A_4)]\sinh(\sqrt{A_1}h)\}\exp[(k+s)h]\\ &+r_e\{\sqrt{A_1}(A_3r_i-A_2)\cosh(\sqrt{A_1}h)+[A_3(A_5-A_4r_i)+A_2(A_5r_i-A_4)]\sinh(\sqrt{A_1}h)\}\exp[-(k+s)h])\end{aligned} \tag{4.8}$$

$$T_{cc} = \frac{(1-r_e)^2\exp[-(k+s)h]}{1-r_e^2\exp[-2(k+s)h]} \tag{4.9}$$

$$T_{cd} = \frac{(1-r_i)(1-r_e)\exp[-(k+s)h]}{[A_1-(k+s)^2][1-r_e^2\exp[-2(k+s)h]]}\cdot\frac{N}{D} \tag{4.10}$$

with

$$\begin{aligned}N = &\sqrt{A_1}[r_iA_3-A_2+r_e(r_iA_2-A_3)]\cosh(\sqrt{A_1}h)\\ &+[(A_5-r_iA_4)(A_3+A_2r_e)-(A_4-r_iA_5)(A_2+A_3r_e)]\sinh(\sqrt{A_1}h)\\ &+\sqrt{A_1}\{(A_2-r_iA_3)\exp[(k+s)h]+r_e(A_3-r_iA_2)\cdot\exp[-(k+s)h]\}\end{aligned} \tag{4.11}$$

$$D = \sqrt{A_1}(r_i^2-1)\cosh(\sqrt{A_1}h)+[r_i(2A_5-r_iA_4)-A_4]\sinh(\sqrt{A_1}h) \tag{4.12}$$

$$\begin{aligned}A_1 &= \varepsilon^2k(k+2(1-\zeta)s)\\ A_2 &= s[\varepsilon k\zeta+\varepsilon s(1-\zeta)+\zeta(k+s)]\\ A_3 &= s(1-\zeta)(k+s)(\varepsilon-1)\\ A_4 &= \varepsilon[k+(1-\zeta)s]\\ A_5 &= \varepsilon(1-\zeta)s\end{aligned} \tag{4.13}$$

The four-flux model is not easily invertible, which means there are no formula enabling to retrieve $k(\lambda)$, $s(\lambda)$, $\zeta(\lambda)$, $\varepsilon(\lambda)$ and $n(\lambda)$ as functions of reflectance and transmittance factors. Although they can sometimes be deduced from information about the material pigments' shape, size, concentration and refractive index using the Lorenz-Mie theory [161,181], or calculated analytically [164,167,168], we will use them as free parameters to be determined numerically by means of an optimization algorithm. However, the four-flux model relies on four measurements, namely $R_{cc}(\lambda)$, $R_{cd}(\lambda)$, $T_{cc}(\lambda)$ and $T_{cd}(\lambda)$, which means that no more than four parameters can be fitted without risk of overfitting. Therefore, the refractive index $n(\lambda)$ will be approximated at 1.5.

We implemented a local optimization algorithm which finds the combination of the model's four optical parameters that predicts directional and diffuse reflectance (resp. direction and diffuse transmittance) factors minimizing the root mean square deviation from the measured spectra. The optimization workflow is illustrated in Figure 4.3.

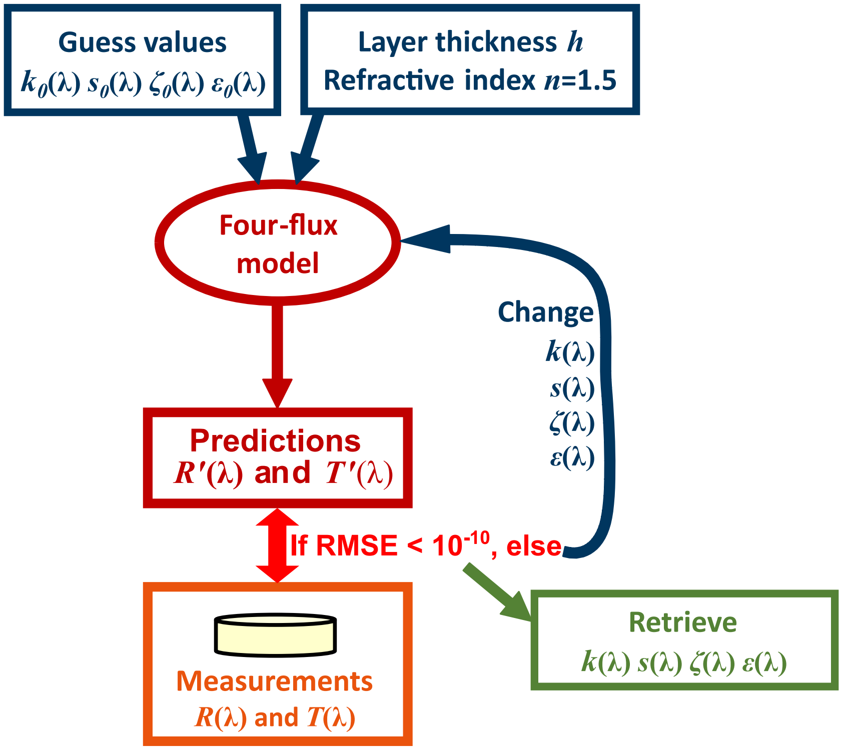

Figure 4.3: Optimization workflow allowing to derive a sample's optical parameters according to the **Maheu4F-RT** model.

The algorithm utilizes the *fmincon* function from Matlab® with a sequential quadratic programming "sqp" algorithm in order to minimize the root mean square difference between the prediction and the measurement of the directional and diffuse reflectance (resp. transmittance) factors for each wavelength. The boundaries for the optimization were 0 and 10000 m^{-1} for the absorption and scattering coefficients, the forward scattering ratio was constrained between 0 and 1 and the average path length parameter was constrained between 1 and 3. First guesses are fed as starting points to the algorithm:

$$k_0 = \frac{1}{h}\left|-\ln\left(\frac{T}{(1-r_e)^2}\right)\right|,$$

$$s_0 = \frac{1}{h}\left|-\ln\left(\frac{T_{cc}}{(1-r_e)^2}\right)\right|,$$

$\zeta_0 = 0.5$ and $\varepsilon_0 = 1.5$.

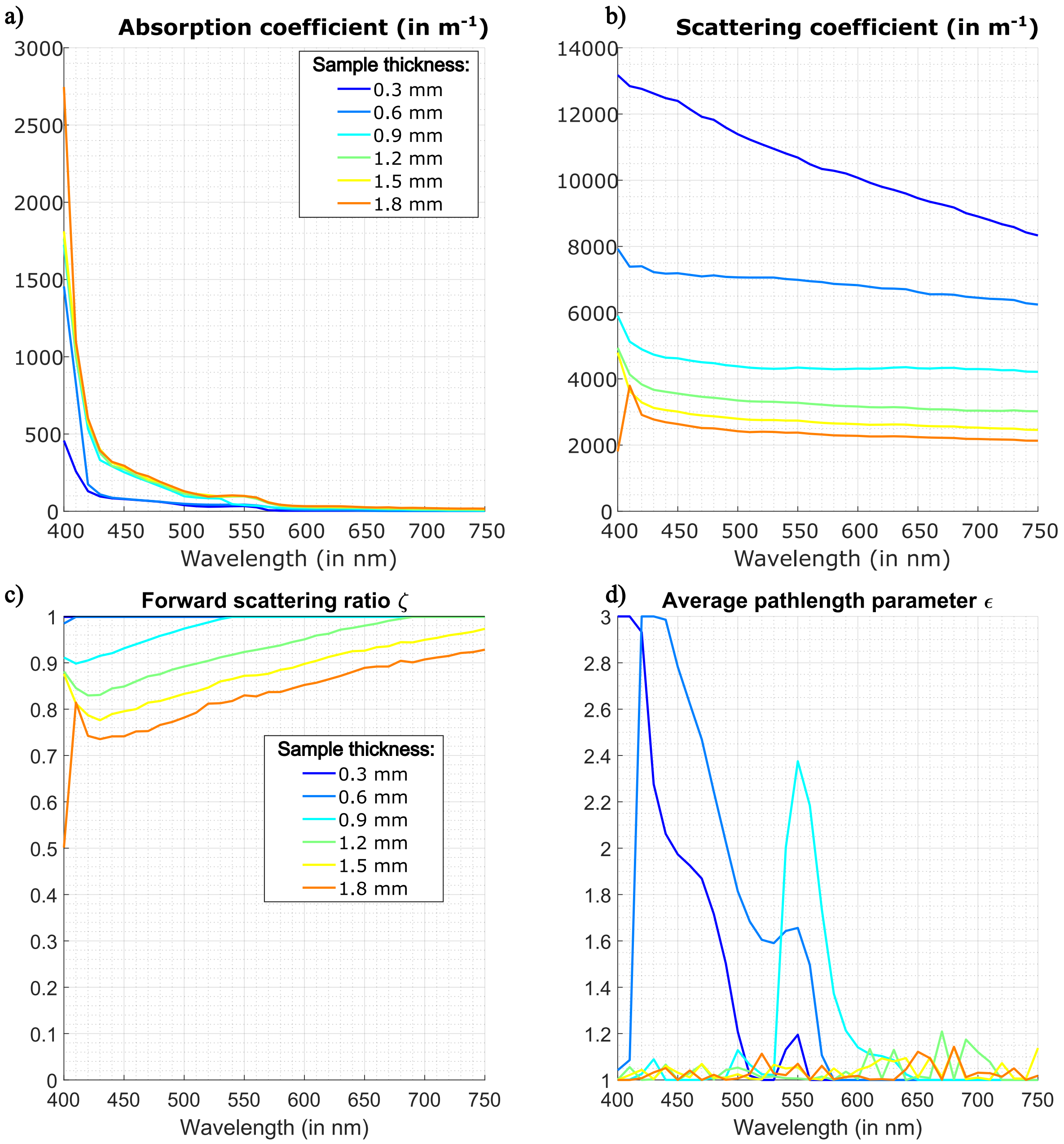

Figure 4.4: a) Absorption coefficients $k(\lambda)$, b) scattering coefficient $s(\lambda)$, c) forward scattering ratio $\zeta(\lambda)$, and d) average path length parameter $\varepsilon(\lambda)$ extracted from reflectance and transmittance factor measurements $R(\lambda)$ and $T(\lambda)$ respectively of the EsteliteUniversalFlow SuperLow A3 samples with different thickness using the **Maheu4F-RT** model.

The algorithm is fast and stable regardless of the initial parameters. However, to ensure that the local optimization algorithm converges towards the best solution possible, a global optimization algorithm was also implemented, using the *GlobalSearch* Matlab® function. This algorithm is more robust in finding the best solution but is very time-consuming (up to 10 seconds for the extraction at each wavelength, versus 0.1 second for the local algorithm). In every test carried out, the global optimization and local optimization algorithms were found to converge towards the same solutions (deviation below 10^{-4}%), which confirms that the local optimization algorithm can be safely used.

This optimization algorithm enables to extract the optical parameters $k(\lambda)$, $s(\lambda)$, $\zeta(\lambda)$ and $\varepsilon(\lambda)$ of a material, which is referred to as the calibration process. For each sample of the Estelite Universal Flow SuperLow A3 material, the parameters extracted are presented in Figure 4.4. The absorption coefficients extracted show stronger absorption in short wavelengths than in longer wavelengths, which is consistent with extractions made with the two-flux models in Chapter 3. Scattering also appears stronger in short wavelengths than in longer wavelengths. The forward scattering ratio indicates that scattering is almost always forward, and average path length parameter close to 1 is consistent with forward and specular propagation of light. However, the high variability of the coefficients with respect to the sample thickness indicates that the model does not accurately represent light propagation inside the investigated material. Furthermore, for the forward scattering ratio and average path length parameter, boundary values are reached by the algorithm for several samples, mainly $\zeta(\lambda) = 1$ and $\varepsilon(\lambda) = 1$ at certain wavelengths. These values indicate that the scattering occurs along the collimated axis, which recalls the assumption of the **dir2F-RT** model, but it is probably not physically accurate. Alleviating these boundaries would improve the extraction algorithm, however, $\zeta(\lambda) > 1$ and $\varepsilon(\lambda) < 1$ are not physically plausible. We therefore choose to not allow them in the extraction algorithm.

Figure 4.5 shows the prediction accuracy of the **Maheu4F-RT** model, the sample with thickness 1.2 mm serving as calibration sample. Parameters $k(\lambda)$, $s(\lambda)$, $\zeta(\lambda)$ and $\varepsilon(\lambda)$ extracted from this sample were used to predict the reflectance and transmittance factors of the slices with varying thickness according to equations (4.7)-(4.13). Notice that the color difference for reflectance prediction of the calibration sample (thickness 1.2 mm) is not 0, which means that the optimization algorithm could not find parameters enabling to predict a reflectance factor equal to the one measured. In transmittance mode, the algorithm was able to find such parameters, and the prediction accuracy of the model is overall better. In reflectance mode, predictions with thickness higher than 0.9 mm are acceptable, which is an improvement compared to the two-flux models. However, the color difference increases rapidly for samples thinner than 0.9 mm. In transmittance mode, the color differences are acceptable for samples with thickness 0.9 to 1.5 mm and increase moderately below and above this interval. The **Maheu4F-RT** model is less accurate than the **dir2F-RT** model in transmittance mode. Overall, its prediction accuracy is not sufficient since only the predictions for the calibration sample fall below the perceptibility threshold. All spectra, predicted and measured, will be presented at the end of this Chapter, in section 4.4 Figure 4.20 and compared with those of the other four-flux models.

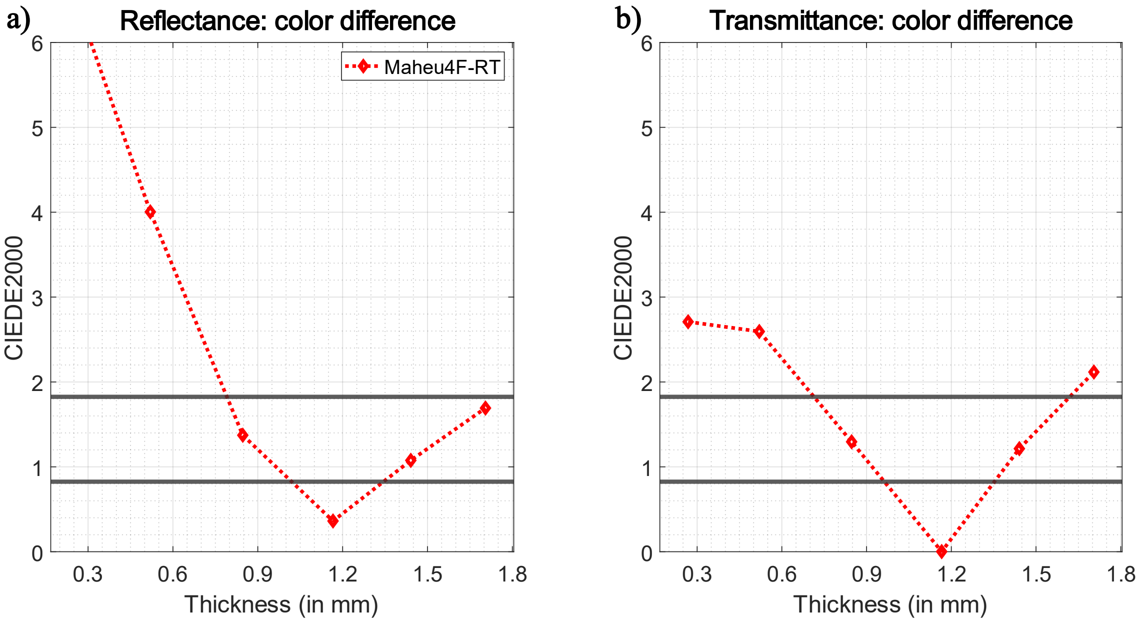

Figure 4.5: Equivalent color distance metric expressing the deviation between a) the measured spectral reflectance factors and b) transmittance factors of samples with various thickness made of the EsteliteUniversalFlow composite shade A3 and the corresponding predictions given by the **Maheu4F-RT** model. The sample with thickness 1.2 mm is used as calibration sample.

4.2 Rozé's four-flux model

As the forward scattering ratio and the average path length parameter, $\zeta(\lambda)$ and $\varepsilon(\lambda)$ respectively, are not easily known for a material, Rozé *et al.* [165] proposed look-up tables enabling to interpolate these parameters as functions of the absorption coefficient $k(\lambda)$, scattering coefficient $s(\lambda)$, the thickness of the material h, and the asymmetry parameter of the Henyey-Greenstein phase function $g(\lambda)$ [184]. The look-up tables were established by comparing the four-flux model with Monte Carlo simulations with an asymmetry parameter $g(\lambda)$ value lying between -0.25 and +0.99. This enables to reduce the number of free parameters available for optimization from 4, *e.g.*, $k(\lambda)$, $s(\lambda)$, $\zeta(\lambda)$ and $\varepsilon(\lambda)$, to 3, *e.g.*, $k(\lambda)$, $s(\lambda)$, $g(\lambda)$. Thus, the refractive index $n(\lambda)$ can be used as an additional fitting parameter instead of using a guess value, which is involved in the calculation of the internal reflectance of the air-material interfaces of the layer. Thus, Rozé's four-flux model [165,166] allows to extract the refractive index $n(\lambda)$, absorption and scattering coefficients $k(\lambda)$ and $s(\lambda)$, and asymmetry parameter $g(\lambda)$ of dental resin composites. The forward scattering ratio and average path length parameter of the four-flux model can then be deduced via interpolation with Rozé's look-up tables. The boundaries considered for extraction of the asymmetry parameter g are -0.25 and +0.99, accordingly to boundaries of Rozé's look-up tables, and the boundaries considered for the refractive index are 1.01 and 2.00. The model is denoted **Rozé4F-RT** hereinafter. The protocol is detailed in Figure 4.6.

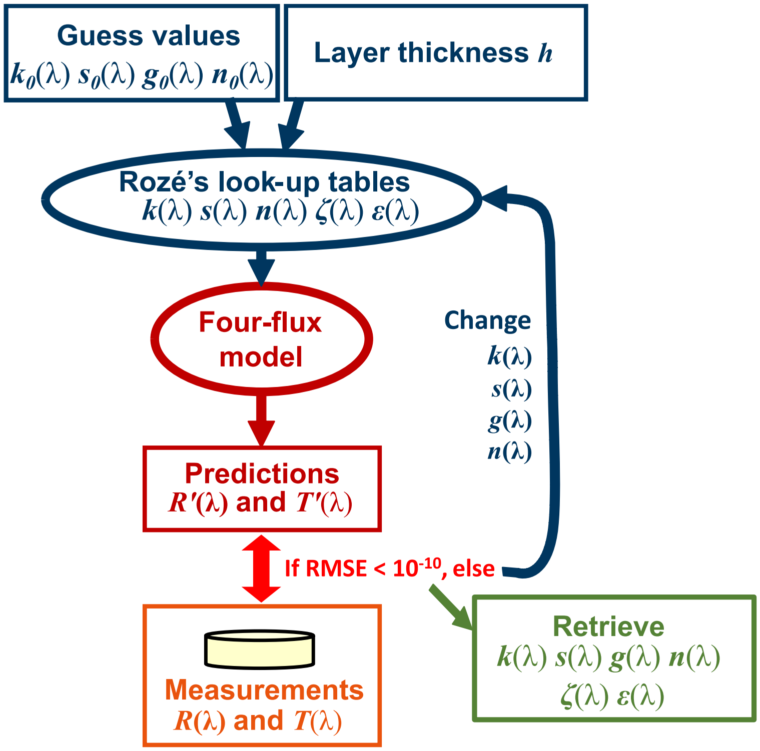

Figure 4.6: Optimization workflow allowing to derive a sample's optical parameters according to the **Rozé4F-RT** model.

The parameters extracted with the **Rozé4F-RT** model from samples of the EsteliteUniversalFlow SuperLow A3 material with different thickness are presented in Figure 4.7. The spectral curves of the absorption coefficient, scattering coefficient and forward scattering ratio extracted with this model are similar to those extracted with the **Maheu4F-RT** model, with boundary values being extracted for the forward scattering ratio again. For thin samples, the asymmetry parameter extracted reaches the boundary value 0.99 which indicates anisotropic forward scattering. The refractive index extracted from thin samples is abnormally low, which is caused by boundary on the g parameter. This indicates that the model is not really accurate for extracting the parameters on thin samples. It is expected that parameters extracted with the **Maheu4F-RT** and the **Rozé4F-RT** models are similar, since the **Rozé4F-RT** model, by construction, is identical to the **Maheu4F-RT** model, except that it involves the asymmetry parameter of the Henyey-Greenstein phase function.

Figure 4.8 shows prediction accuracy of the **Rozé4F-RT** model calibrated using the sample with thickness 1.2 mm. Each predicted spectrum corresponding to a point in these figures will be presented in section 4.4, Figure 4.20. The prediction accuracy of this model is very close to the prediction accuracy of the **Maheu4F-RT** model in both reflectance and transmittance modes. Once again, this is expected since the two models are very similar in the way that light propagation is

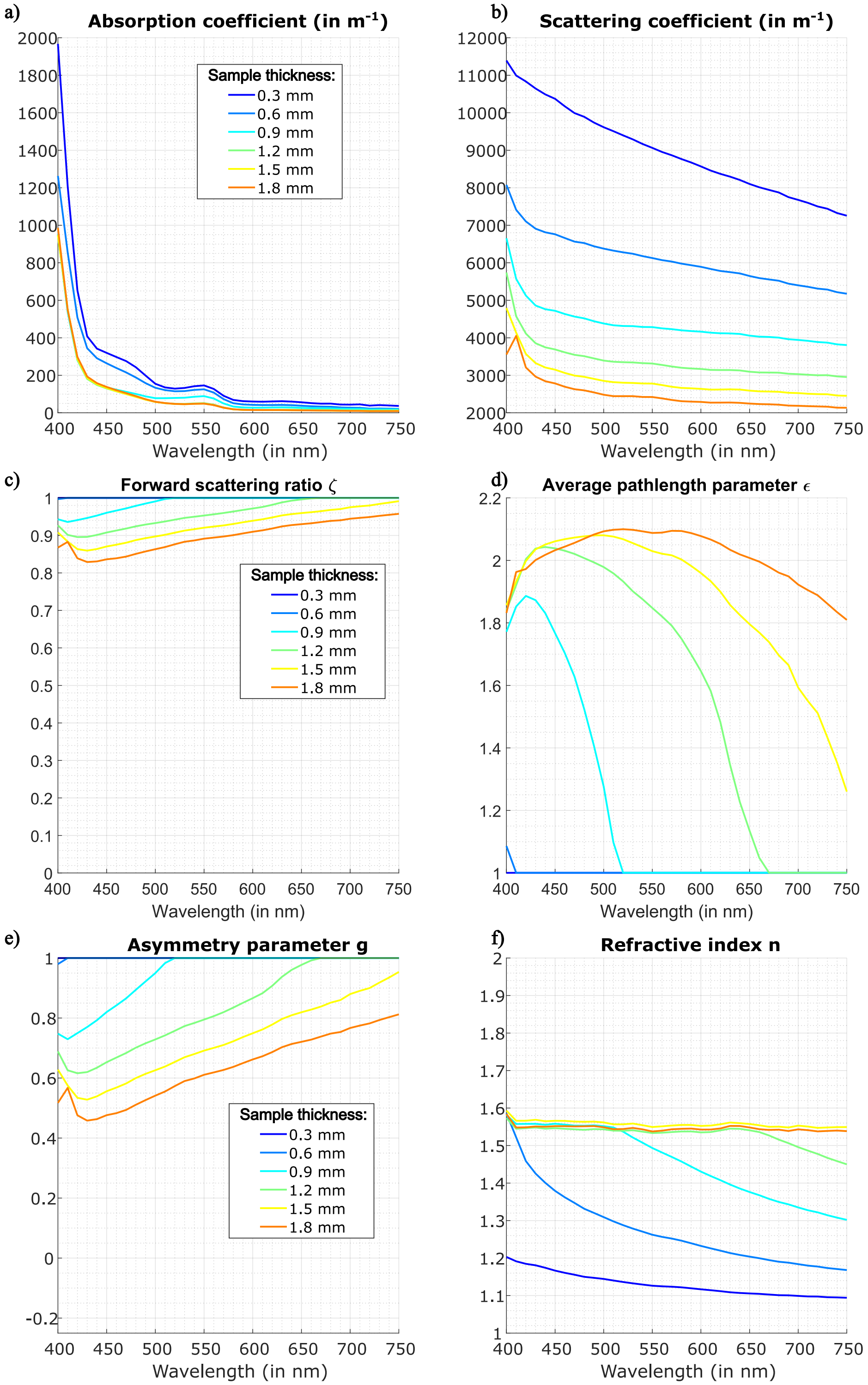

Figure 4.7: a) Absorption coefficients $k(\lambda)$, b) scattering coefficient $s(\lambda)$, c) forward scattering ratio $\zeta(\lambda)$, d) average path length parameter $\varepsilon(\lambda)$, e) asymmetry parameter $g(\lambda)$, and f) refractive index $n(\lambda)$ extracted from samples with different thickness of the EsteliteUniversalFlow SuperLow A3 with the **Rozé4F-RT** model.

described within the bulk of the material. Notice however that for the **Rozé4F-RT** model, the optimization algorithm is able to find parameters so that the prediction of the calibration sample's reflectance factor equals the measurement. The **Maheu4F-RT** and **Rozé4F-RT** models consider collimated light and perfectly diffuse light at the material's interfaces. However, it is probable that the diffuse light which travelling inside the layer which is detected by the sensor does not follow a Lambertian distribution. Thus, we need to revise the assumption of isotropic light even for the diffuse fraction of the flux considered in the four-flux model.

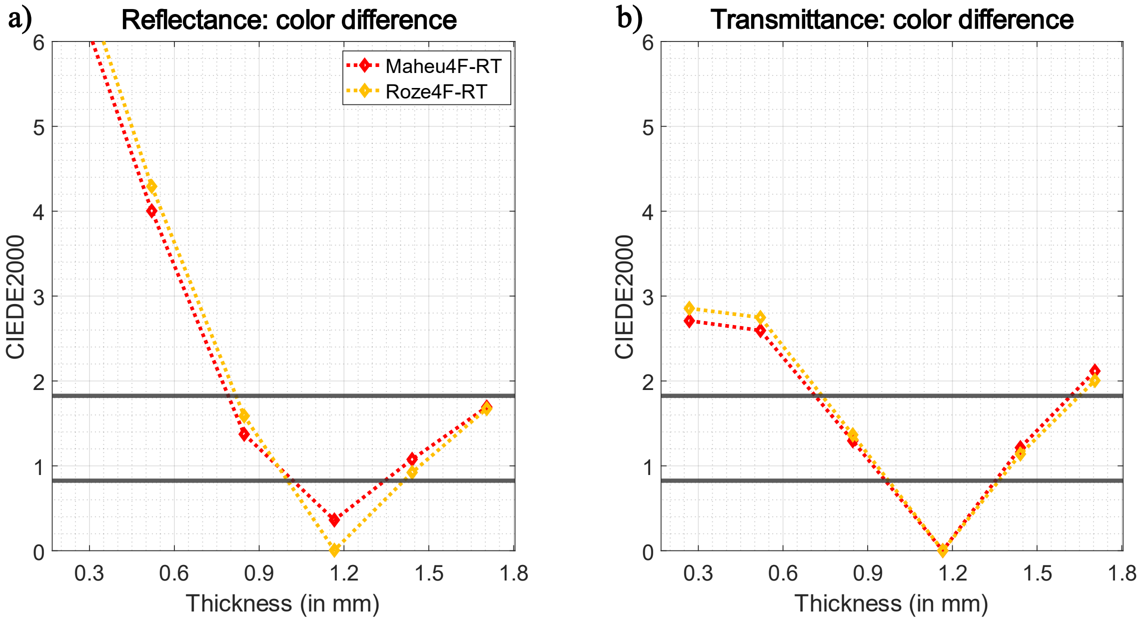

Figure 4.8: Equivalent color difference metric expressing the deviation between a) the measured spectral reflectance factors and b) transmittance factors of samples with various thickness made of the EsteliteUniversalFlow composite shade A3 and the corresponding predictions given by the **Rozé4F-RT** model and the **Maheu4F-RT** model. The sample with thickness 1.2 mm is used as calibration sample.

4.3 Eymard's four-flux model

Eymard's four-flux model [177] was originally proposed to characterized backscattering in photovoltaic cell encapsulants. Its implementation is very similar to the **Rozé4F-RT** model. The only difference is in the calculation of the internal interface reflectance r_i, which is calculated according to formula (4.14) instead of formula (4.5). Eymard *et al.* proposed to account for the anisotropic angular light distribution by using the Henyey-Greenstein phase function, which was already used by Rozé *et al.* to produce look-up tables interpolating $\zeta(\lambda)$ and $\varepsilon(\lambda)$ as function of $k(\lambda)$, $s(\lambda)$, and $g(\lambda)$.

$$r_i(g,n) = \frac{\int_{\theta=0}^{\pi/2} R_{21}(\theta) P_{HG}(\theta,g)\sin(2\theta)d\theta}{\int_{\theta=0}^{\pi/2} P_{HG}(\theta,g)\sin(2\theta)d\theta} \tag{4.14}$$

The parameters extracted by this model from the samples of the EsteliteUniversalFlow SuperLow A3 with different thicknesses are presented in Figure 4.9. The absorption parameters extracted indicated that the material is strongly absorbing in short wavelengths and very weakly absorbing in longer wavelengths, similarly to two-flux models. Also, the scattering coefficients indicate stronger scattering in short wavelengths than in longer wavelengths, but the variability of these parameter with respect to the sample thickness is important. Notably, scattering coefficients extracted from thin samples are much higher than scattering coefficients extracted from thicker samples. This must be analyzed together with extracted forward scattering ratios, which are higher for thin samples than for thicker samples. It is possible that these parameters somehow compensate in a way that increasing the scattering coefficient while decreasing the forward scattering ratio value might lead to similar reflectance and transmittance factors. The forward scattering ratios' spectral curves $\zeta(\lambda)$ show that most light is scattered in the forward hemisphere, *i.e.* in the same direction as the illumination, with values around 0.9. The spectral curves of the average path length parameter are close to 2 for thick samples, which corresponds to isotropic light, and close to 1.5 for thin samples, which indicate a slightly more directional light propagation. The values extracted of asymmetry parameter $g(\lambda)$ of the Henyey-Greenstein phase function indicate a rather anisotropic angular light distribution for all samples as values extracted are mostly between 0.6 and 0.8. The spectral values of the refractive index extracted are close to 1.55 for most samples over the whole visible spectrum of light and decrease for thin samples.

Figure 4.10 shows the r_i parameters derived from these asymmetry parameters according to formula (4.14). Values calculated are much lower than 0.5963, which corresponds to the Lambertian assumption for $n = 1.5$. Spectral values of the internal reflectance of interfaces are higher for thick samples than for thin samples, for which the value is closer to 0.04, which corresponds to the directional assumption for $n = 1.5$. Note that by calculating the angular distribution according to a phase function rather than integrating the phase function using a radiative transfer model means that we consider that scattering occurs according to single scattering regime, *i.e.*, light is scattered only once along its path in the material, whereas multiple scattering is neglected. This assumption might be valid for very thin slabs, but it is rather unlikely as thickness increases.

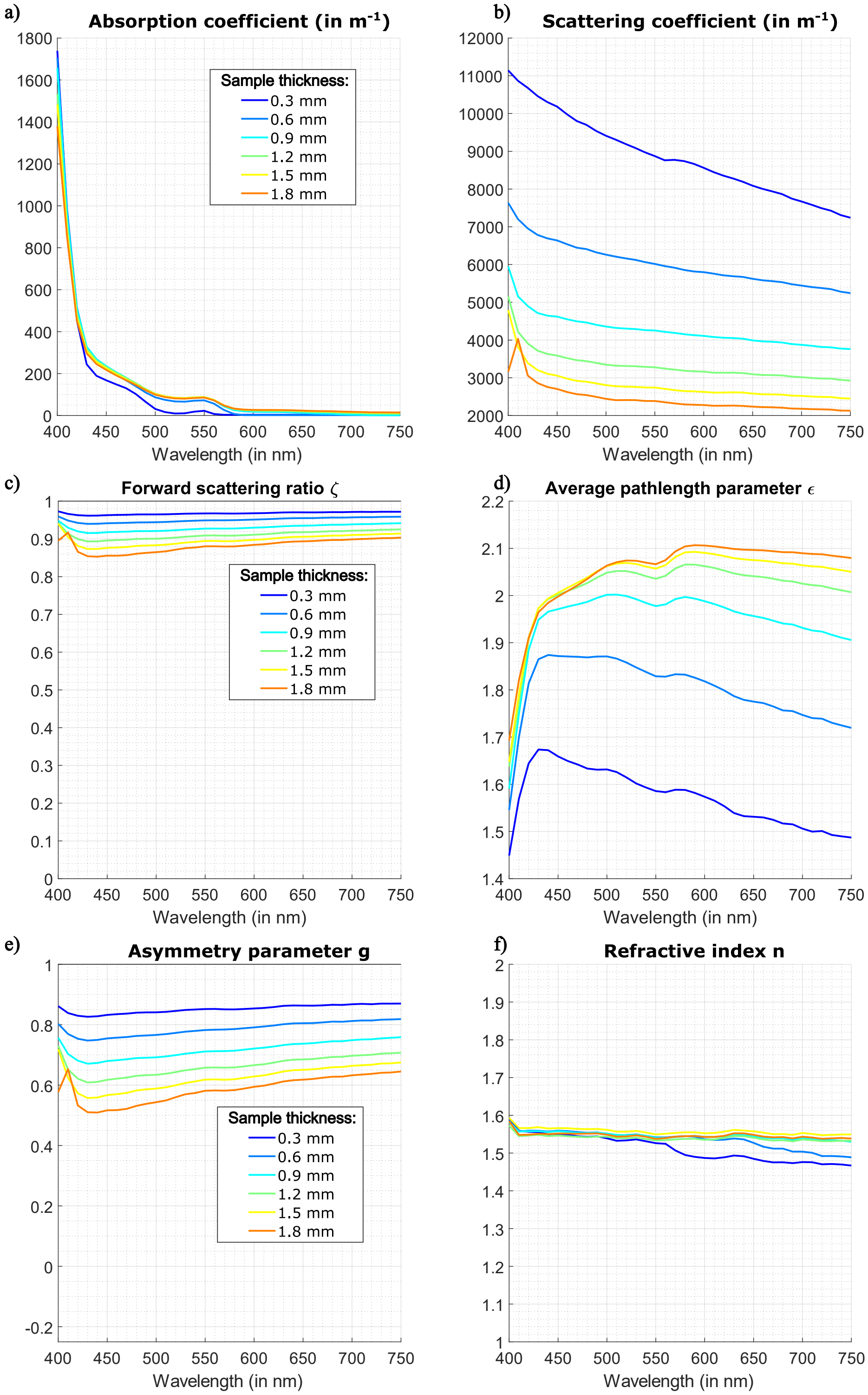

Figure 4.9: a) Absorption coefficients $k(\lambda)$, b) scattering coefficient $s(\lambda)$, c) forward scattering ratio $\zeta(\lambda)$, d) average path length parameter $\varepsilon(\lambda)$, e) asymmetry parameter $g(\lambda)$, and f) refractive index $n(\lambda)$ extracted from samples with different thickness of the EsteliteUniversalFlow SuperLow A3 with the **Eymard4F-RT** model.

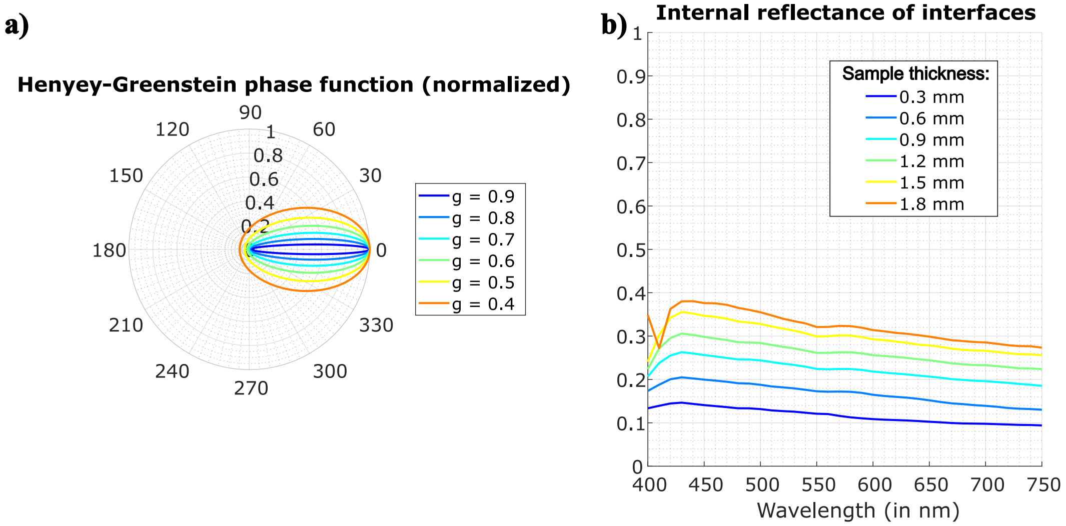

Figure 4.10: a) Normalized representation of the Henyey-Greenstein phase function for various values of *g*. b) Internal reflectance parameters calculated with formula (4.14)

Figure 4.11 shows the prediction accuracy of the **Eymard4F-RT** model for predicting the reflectance and transmittance factors of samples of the EsteliteUniversalFlow SuperLow A3 material with the sample with thickness 1.2 mm as calibration sample. It is more accurate than **Rozé4F-RT** and **Maheu4F-RT** models for all samples evaluated in both reflectance and transmittance modes. In reflectance mode, the improvement in prediction accuracy is more important for thin samples of thickness between 0.3 and 0.9 mm, inferior to the thickness of the calibration sample, for which it is the most important to account for a non-isotropic angular distribution of light at interfaces, in the calculation of the r_i parameter. The improvement is not that significant for thicker samples of thickness 1.5 and 1.8 mm. This might be because the simple scattering assumption that we do implicitly in the calculation of r_i is not verified for thick samples. The reflectance and transmittance factors of all samples are predicted within acceptable color difference, *e.g.*, $\Delta E_{00} < 1.8$, except for the reflectance factor of the thinnest sample. The predictions accuracy for samples of thickness 0.9 and 1.5 mm, close to the calibration sample, are below or very close to the perceptibility threshold, *e.g.*, $\Delta E_{00} < 0.8$, which is a significant improvement compared to the previous models.

Between the **Rozé4F-RT** and **Eymard4F-RT** models, the only difference is in the calculation of the internal reflectance of the interfaces for diffuse flux, denoted r_i. However, we have already observed in section 3.4 the dramatic importance of this parameter for accurate spectral prediction of dental material samples' reflectance and transmittance factors. Let us display the values that were fitted for each model in Figure 4.12. Remind that in order to predict the reflectance and transmittance factor of other samples, only the r_i parameter extracted from the calibration sample with thickness 1.2 mm is used.

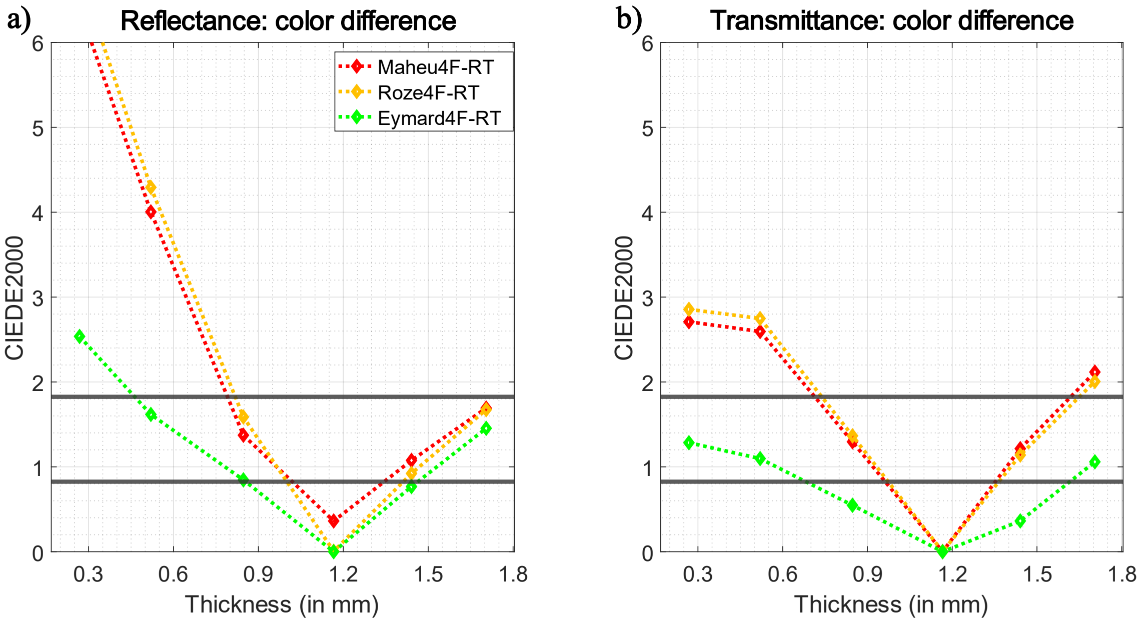

Figure 4.11: Equivalent color difference metric expressing the deviation between a) the measured spectral reflectance factors and b) transmittance factors (on the right) of samples with various thickness made of the EsteliteUniversalFlow composite shade A3 and the corresponding predictions given by the **Eymard4F-RT** model, the **Rozé4F-RT** model and the **Maheu4F-RT** model. The sample with thickness 1.2 mm is used as calibration sample.

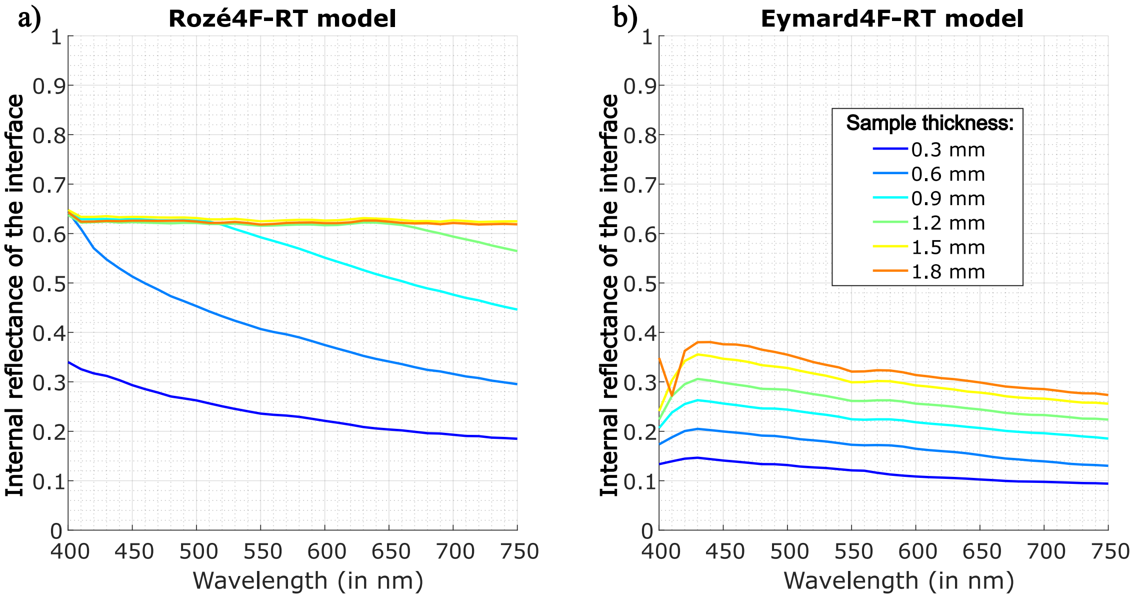

Figure 4.12: Internal reflectance of the internal reflectance parameter r_i fitted for each sample in a) the **Rozé4F-RT** model and b) the **Eymard4F-RT** model. The value used in the **Maheu4F-RT** model is 0.5963 as it is assumed that n = 1.5 in this model.

For the **Rozé4F-RT** model, the decrease of the internal reflectance parameter at longer wavelengths for samples with thickness 1.2 mm and thinner ones is due to boundary constraints of the optimization algorithm, preventing the model from using non-physical values of the asymmetry parameter of the Henyey-Greenstein phase function. This shows that a value of the r_i parameter lower than 0.5963, the assumption for isotropic angular light distribution, increases the prediction accuracy of the four-flux model. In the case of this material, the value considered by the **Eymard4F-RT** is between 0.2 and 0.3; the angular distribution of light is far from being isotropic, but rather close to a cone centered on the normal direction of propagation. This makes us want to calculate this parameter r_i more rigorously in terms of intrinsic material properties, which we attempt in the next section.

4.4 Four-flux model enhanced with RTE

The **RTE-4F-RT** model is an attempt to bring the more complex light propagation modelled by the Radiative Transfer Equation into the simpler formalism of the four-flux model. Using the RTE implementation by Gautheron *et al.* [185], the luminance exiting a translucent layer of given thickness was calculated and used to calculate the internal reflectance at both upper and lower interfaces according to the general Fresnel formula given in equation (4.4). In the **RTE-4F-RT** model, we no longer assumed that the internal reflectance of the interface is equal at both upper and lower interfaces. Therefore, $r_i(\lambda)$ denotes the internal reflectance at the upper interface (illumination side) while $r_i'(\lambda)$ denotes the internal reflectance of the lower interface.

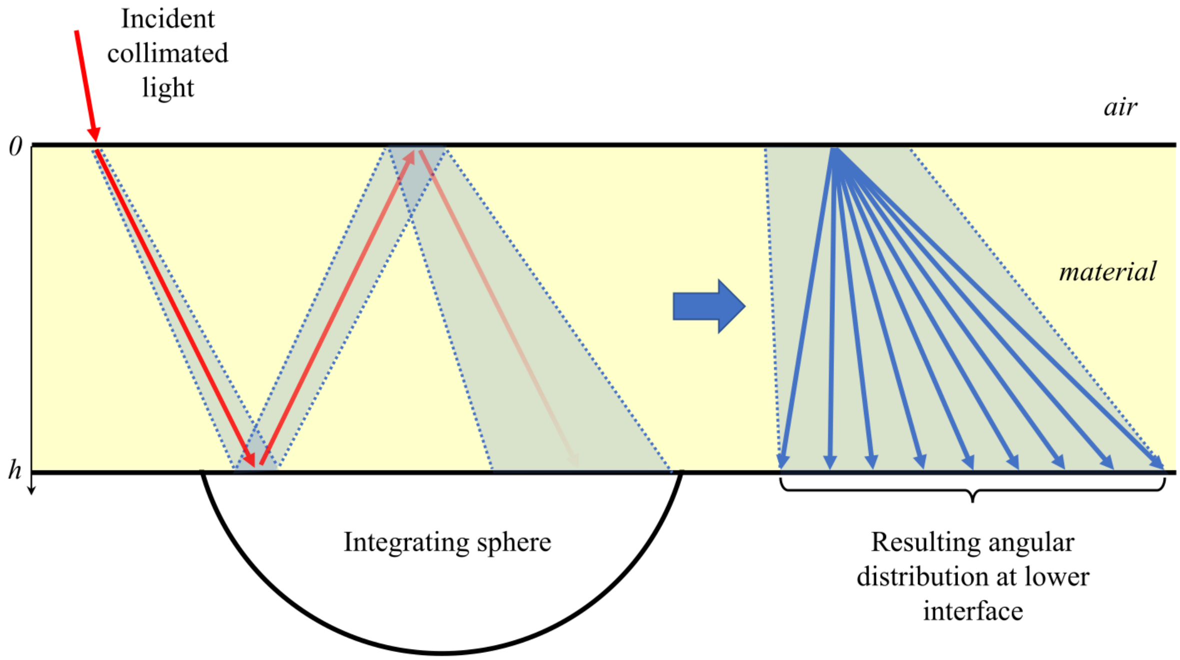

Figure 4.13: Schematic representation of the scattering of incident collimated light inside a layer of weakly scattering material and the final angular distribution.

Figure 4.13 shows a schematic representation of light propagation in a weakly scattering material, which we try to implement into the **RTE-4F-RT** model. The more $g(\lambda)$ is close to 0, the more scattering is isotropic. Thus, collimated light will be attenuated more rapidly, and the resulting angular distribution of light will be close to a hemisphere. For a given value of $g(\lambda)$, the resulting angular distribution will be wider in a thicker layer since the luminance will be more scattering inside the material. Note that this drawing corresponds to a measurement with a 8°:d instrument, and the reasoning remains valid for a device of d:8° geometry. In the latter case, light propagation must be considered in the opposite direction, from the sphere to the collimated beam going to the detector.

The propagation of diffuse light, light resulting from the scattering of incident collimated light, across a scattering layer of given absorption coefficient μ_a, scattering coefficient μ_s, asymmetry parameter g, refractive index n, and thickness h was modelled using the Radiative Transfer Equation, given in formula (4.15), with the discrete ordinate method [136,137].

$$\mathbf{s}.\mathbf{grad}(I) = -(\mu_a + \mu_s) I(\mathbf{r}, \mathbf{s}) + \frac{\mu_a + \mu_s}{4\pi} \int_{4\pi} p(\mathbf{s}, \mathbf{s}') I(\mathbf{r}, \mathbf{s}') d\mathbf{s}' \tag{4.15}$$

with I the radiance (also called specific intensity), r the coordinate in space, s the vector subtending the direction of incident light, s' the direction of the exiting light, and p the scattering phase function.

The resulting luminance at the upper and lower interfaces was analyzed for many combinations of these parameters, representatives of weakly scattering and highly scattering materials. To simplify the study, the materials were studied with respect to their albedo denoted ω_0 and their optical thickness τ_d, with

$$\omega_0 = \frac{\mu_s}{\mu_a + \mu_s} \tag{4.16}$$

and

$$\tau_d = h(\mu_a + \mu_s) \tag{4.17}$$

Luminances calculated for a material albedo of 0.7 with varying optical thickness are shown in Figure 4.14. The internal reflectance at the interface is then calculating according to equation (4.18) and values corresponding to each luminance are also presented in Figure 4.14 .

$$r_i = \int_{\theta=0}^{\pi/2} R_{21}(\theta) L(\theta) \sin(2\theta) d\theta \Bigg/ \int_{\theta=0}^{\pi/2} L(\theta) \sin(2\theta) d\theta \tag{4.18}$$

a) Top interface

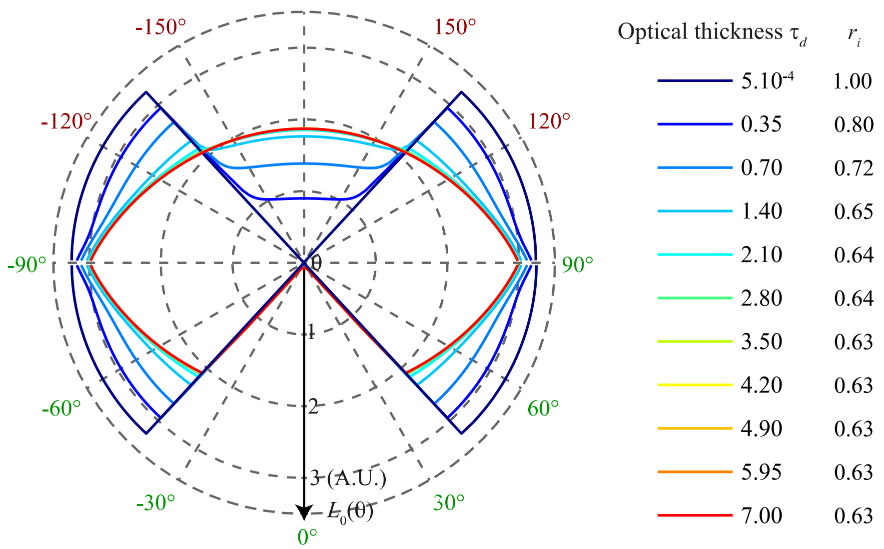

b) Bottom interface

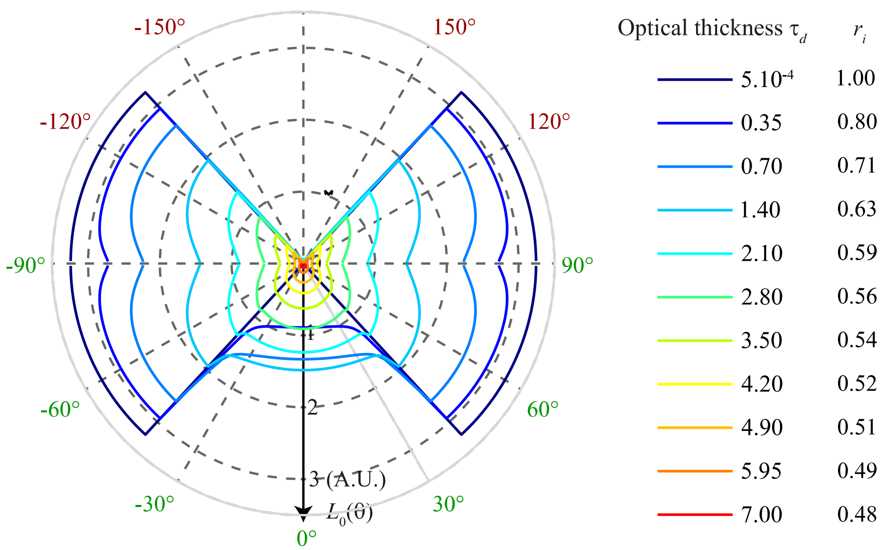

Figure 4.14: Polar plot of the radiance at a) the top $L_0(\theta)$ and b) the bottom $L_d(\theta)$ for layers of different optical thicknesses in presence of absorption (refractive index n = 1.5, albedo ω_0 = 0.7). Optical thickness is given in meters.

At the upper interface (Figure 4.14a)), for a layer of thin optical thickness (blue curve), which either means a very thin layer of scattering material or a layer of a very weakly scattering material, the angular distribution of luminance resembles a butterfly shape: luminance in the collimated direction is zero while luminance at high angles of incident is maximum. Remind that we only view the diffusion luminance, which explains the absence of a specular peak at normal incidence. The sharp decrease of luminance corresponds to the critical angle above which all light is reflected internally. In fact, this shows that for a weakly scattering layer, most of the diffuse light inside the material is reflected internally, and thus r_i = 1. This is because light propagating at lower angles relative to the layer's surface exit the layer quickly, since the latter is thin. The more optical thickness increases, the more the luminance resembles an eye (red curve). In thicker layer, more light is scattered within the layer, creating a more isotropic luminance distribution at the interface. In this case, r_i is 0.63, a value closer to the value assumed by Judd, r_i = 0.5963 for n = 1.5 [182]. Similar reasoning also applies at the lower interface (Figure 4.14b)) for thin layer. However, for thick layers, the luminance at the lower interface becomes negligible; the layer becomes opaque. These luminance distributions are analyzed in detail in [185].

This modelling enables us to derive the value of the internal reflectance parameter for diffuse flux at the upper (resp. lower) interface, denoted r_i (resp. denoted r_i'). The evolution of these two parameters with respect to the optical thickness, and for different albedo, is presented in Figure 4.15.

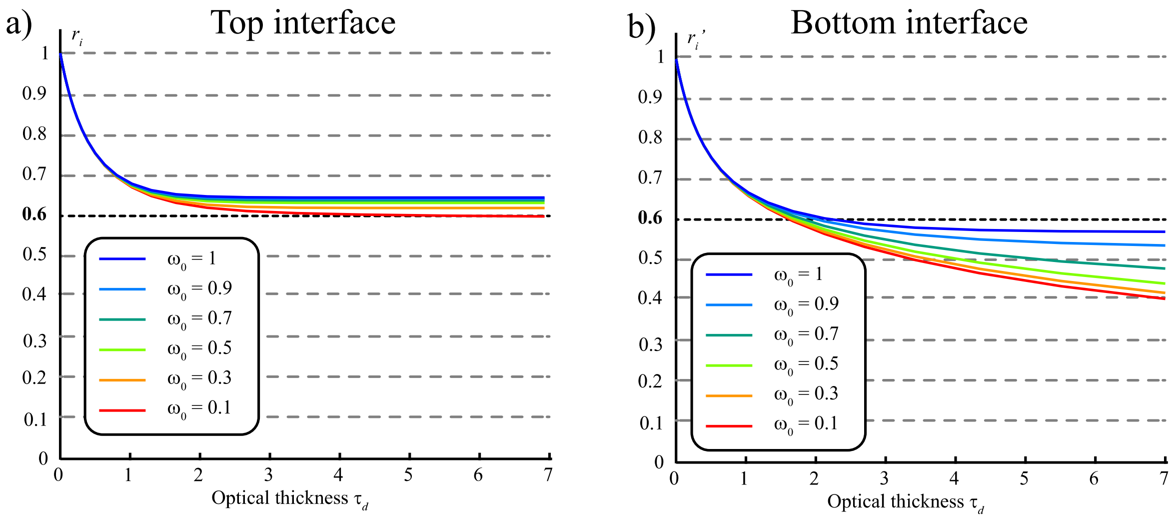

Figure 4.15: a) Internal reflectance r_i of the top interface and b) internal reflectance r_i' of the bottom interface with respect to optical thickness for several albedo ω_0, with $\mu_a+\mu_s = 5$ cm^{-1}. The bold dashed line at 0.6 corresponds to the value usually found by [182] and considered in most applications of the Saunderson correction.

Based on these results, look-up tables giving r_i and r_i' as functions of the μ_a and μ_s coefficients, asymmetry parameter g of the Henyey-Greenstein phase function, refractive index n and thickness of the layer h were established. The look up tables rely on scattering and absorption coefficients of the RTE, namely μ_a and μ_s respectively, which are by definition different from absorption coefficients k and s considered in the four-flux model. Several authors have proposed relationships between absorption and scattering parameters of the four-flux model and the RTE [186,187], however, we found that using these relationships decrease the prediction accuracy of the **RTE-4F-RT** in all cases. Therefore, look-up tables were used as if $k = \mu_a$ and $s = \mu_s$. The **RTE-4F-RT** model is implemented exactly like the **Rozé4F-RT** model (shown in Figure 4.6), but the r_i and r_i' parameters are given by the look-up tables with respect to *k*, *s*, *g*, *n* and *h*.

Figure 4.16 shows the parameters extracted by this model. Note that this model takes much more computation time than the previous four-flux models: it can take 1 to 5 seconds to extract the optical parameters at one wavelength, compared to about 0.1 seconds for the previous models. Once again, parameters extracted with the **RTE-4F-RT** model vary depending on the thickness of the sample evaluated, especially for the scattering parameter $s(\lambda)$, forward scattering ratio $\zeta(\lambda)$, average path length parameter $\varepsilon(\lambda)$, and asymmetry parameter $g(\lambda)$. For each sample of the EsteliteUniversalFlow SuperLow A3 material, the parameters extracted using the **RTE-4F-RT** model are very close to the parameters extracted using the **Eymard4F-RT** model. Most differences are visible for the forward scattering ratio and average path length parameter, but they remain slim. The forward scattering ratios extracted from all samples with the **RTE-4F-RT** model are closer to each other than the curves extracted with the **Eymard4F-RT** model.

The spectral curves of the internal reflectance parameter at the upper interface and the lower interface are shown in Figure 4.17a) and b), with the curves used in the **Eymard4F-RT** model shown as a reminder in c) and d). Note that the curves in Figure 4.17c) and d) are identical since no difference is made between the upper and lower interface in the **Eymard4F-RT** model. The internal reflectance of the upper interface used in the **RTE-4F-RT** model is higher than the one for the lower interface, and slightly above 0.5963, the value corresponding to Lambertian angular distribution. It increases for thin samples, for which diffuse light is mostly trapped since it hits the interface with an angle higher than the critical angle. The internal reflectance of the lower interface is lower for thin samples and tends towards 0.6 for thick samples. The internal reflectance of the interface used in the **RTE-4F-RT** model, regardless of the interface and sample thickness, is much higher than the value used in the **Eymard4F-RT** model.

Figure 4.18 shows the prediction accuracy of the **RTE-4F-RT** model. In reflectance mode, it is significantly more accurate than the **Eymard4F-RT** model, especially for thin samples. Almost all color differences between predictions and measurements are below the perceptibility threshold, and the average color difference is at 0.4 unit, far below the perceptibility threshold. In transmittance mode, the improvement in accuracy is not that significant compared to the **Eymard4F-RT** model. The **RTE-4F-RT** model is able to predict the color of slices of this dental material color differences below the perceptibility threshold. Therefore, this model is a good candidate to characterize the optical properties of dental materials and predict their color in reflectance and transmittance mode.

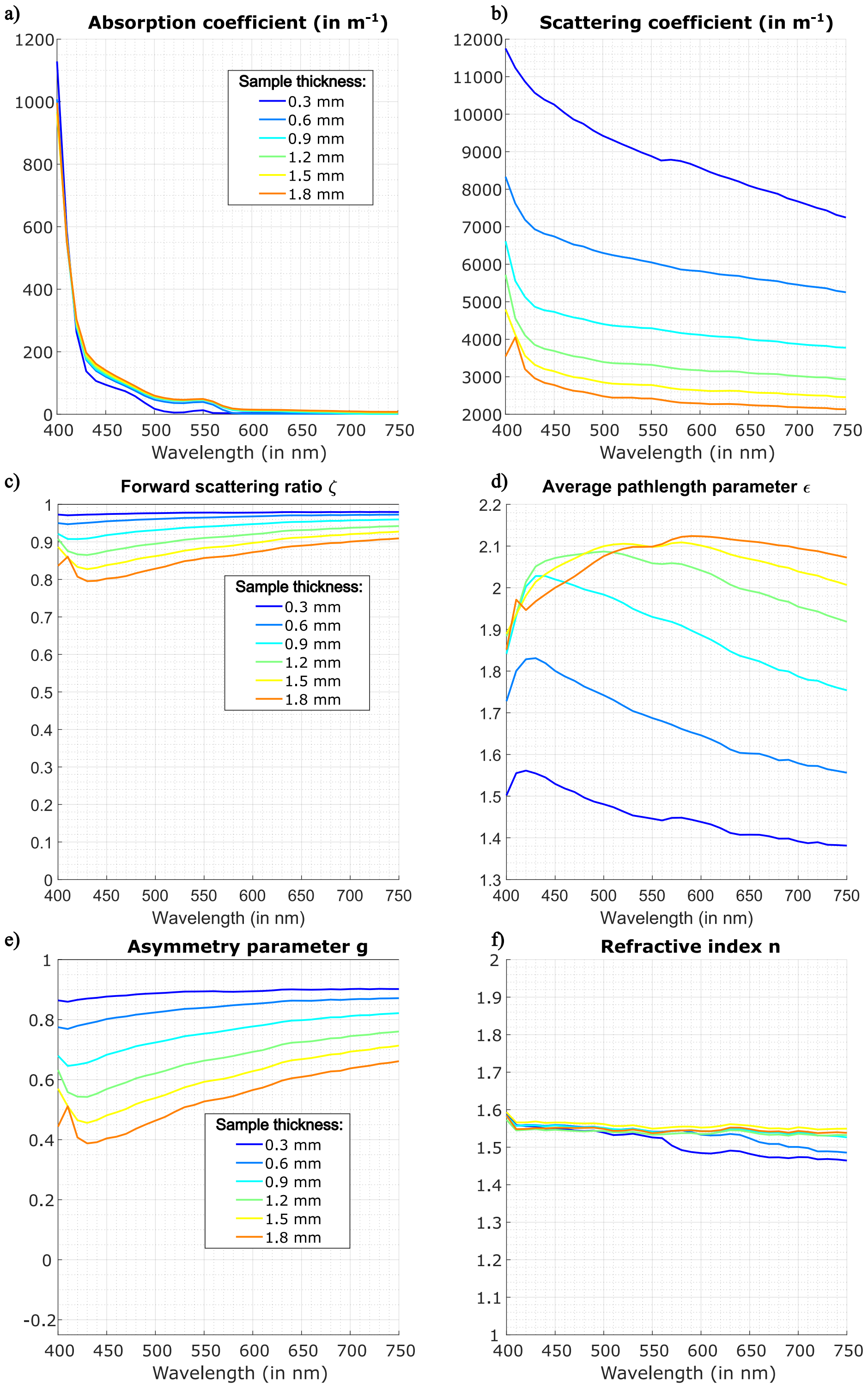

Figure 4.16: a) Absorption coefficients $k(\lambda)$, b) scattering coefficient $s(\lambda)$, c) forward scattering ratio $\zeta(\lambda)$, d) average path length parameter $\varepsilon(\lambda)$, e) asymmetry parameter $g(\lambda)$, and f) refractive index $n(\lambda)$ extracted from samples with different thickness of the EsteliteUniversalFlow SuperLow A3 with the **RTE-4F-RT** model.

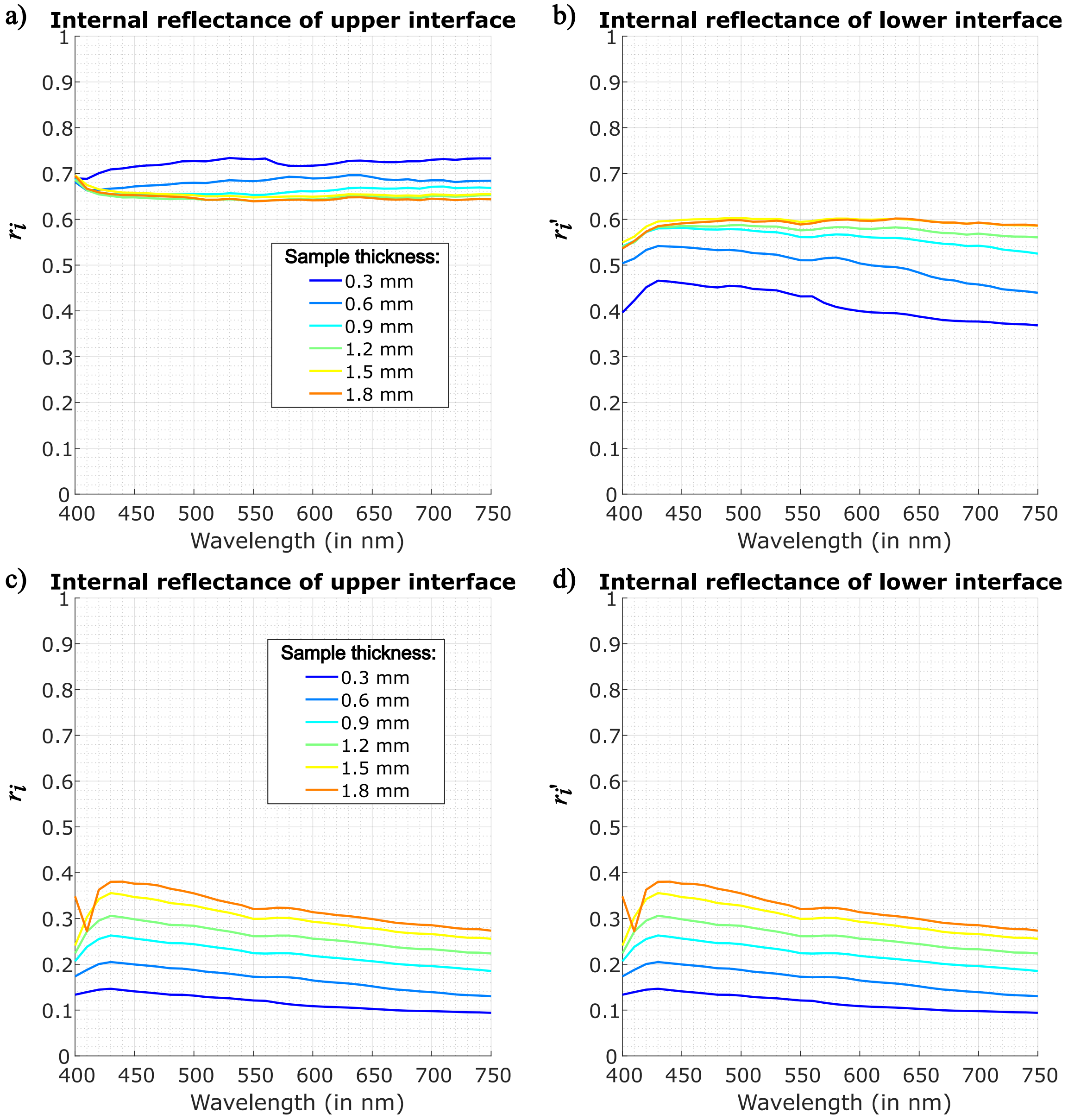

Figure 4.17: Internal reflectance parameters used to extract the optical parameters of all six samples of the EsteliteUnivseralFlow SuperLow A3 material with different thickness for a) the upper interface in the **RTE-4F-RT** model, b) the lower interface in the **RTE-4F-RT** model, c) the upper interface in the **Eymard4F-RT** model, d) the lower interface in the **Eymard4F-RT** model.

This improvement in prediction accuracy is due to internal reflectance of the interface being different at both interfaces, namely $r_i(\lambda)$ and $r_i'(\lambda)$, and values simulated by taking more rigorously the angular distribution of light at the interfaces thanks to an angular model, based on the radiative transfer equation. Also, these look-up tables account for all parameters of the four-flux model: the absorption coefficient $k(\lambda)$, the scattering coefficient $s(\lambda)$, the asymmetry parameter $g(\lambda)$ of the Henyey-Greenstein phase function, the refractive index $n(\lambda)$ of the material, and the thickness of

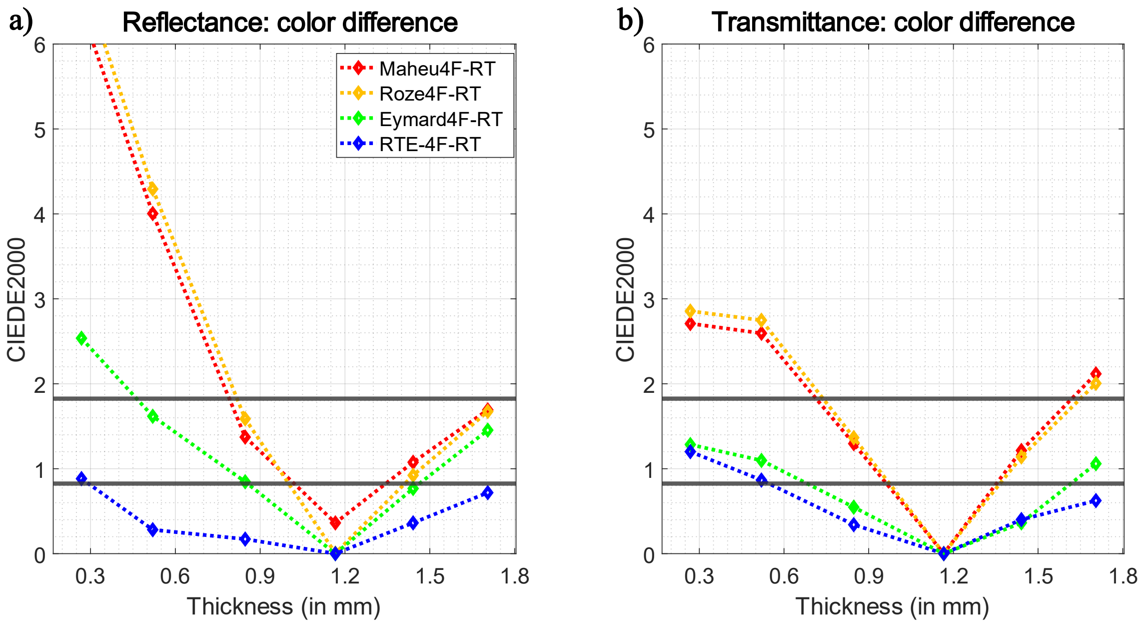

Figure 4.18: Equivalent color difference metric expressing the deviation between a) the measured spectral reflectance factors and b) transmittance factors of samples with various thickness made of the EsteliteUniversalFlow SuperLow composite shade A3 and the corresponding predictions given by the **RTE-4F-RT** model, the **Eymard4F-RT** model, the **Rozé4F-RT** model and the **Maheu4F-RT** model. The sample with thickness 1.2 mm is used as calibration sample.

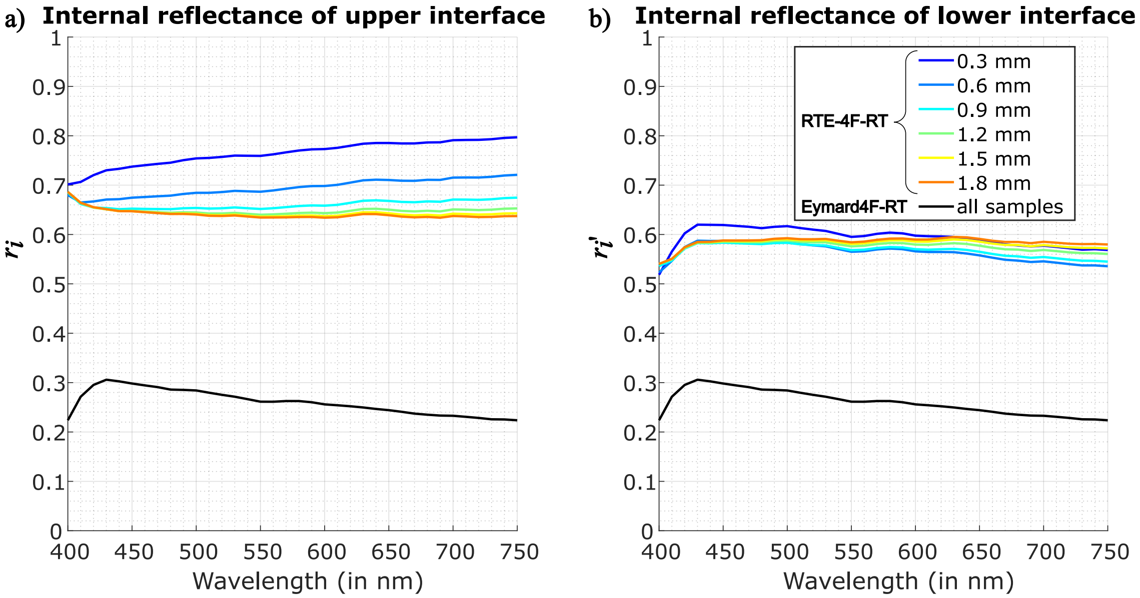

Figure 4.19: Internal reflectance of the a) upper interface and b) lower interface used in the prediction of the reflectance and transmittance factors by the **RTE-4F-RT** and **Eymard4F-RT** models.

each layer *h*. This means that the values for $r_i(\lambda)$ and $r_i'(\lambda)$ change depending on the thickness of the layer even in prediction mode. The values used to predict the reflectance and transmittance factors of each sample are shown in Figure 4.19. Note that they are necessarily different from values presented in Figure 4.17a) and b), since they consider the optical parameters $k(\lambda)$, $s(\lambda)$, $g(\lambda)$ and $n(\lambda)$ extracted from the calibration sample with thickness 1.2 mm.

Remind that the value usually considered for perfectly diffuse light is 0.5963 and the value considered for collimated light is 0.04, for n = 1.5. In the case of the **Eymard4F-RT** model, the value used for predictions is around 0.25, thus closer to 0.04 than 0.5963. In the **RTE-4F-RT** model, values for r_i and r_i' are quite different between the upper and lower interface, especially for thin samples. In thin samples, the diffuse part of the flux is probably less important than the collimated part, as light is less scattered within thin samples. The majority of diffuse light remaining within the layer travels at an angle higher than the critical angle for total reflection. For thicker samples, light is more scattered across the layer and therefore, the angular distribution of light is more isotropic. As a result, the internal reflectance of the interface is closer to 0.6 for both interfaces. The internal reflectance of the upper interface is closer to 0.6, the value for isotropic scattering assumption, because light flowing upwards mostly results from backscattering which is rather isotropic, even for high values of the asymmetry parameter. On the contrary, scattering in the forward hemisphere occurs within a narrower cone for high values of the asymmetry parameter. Thus, light transmitted is mostly the result of forward scattering and collimated light. These phenomena are discussed and explained in [185].

Figure 4.20 shows the predicted reflectance and transmittance factors predicted by the four-flux models investigated in this thesis. The **Maheu4F-RT** and **Rozé4F-RT** predict almost the same spectra for each sample in both reflectance and transmittance modes. Therefore, the two models are rather equivalent for predicting the color of dental materials in reflectance and transmittance modes, although the **Rozé4F-RT** model links the asymmetry parameter of the Henyey-Greenstein phase function to the forward scattering ratio $\zeta(\lambda)$ and average path length parameter $\varepsilon(\lambda)$, allowing to fit the refractive index $n(\lambda)$. On the other hand, the spectra predicted by the **Eymard4F-RT** and **RTE-4F-RT** models are closer to the measured spectra.

In reflectance mode, the greatest deviations occur at long wavelengths. Reflectance factors predicted by the **Maheu4F-RT** and the **Rozé4F-RT** models are greatly overestimated when the sample thickness is inferior to thickness of the calibration sample, and underestimated when the sample thickness is superior to the calibration thickness. Deviations are much slimmer for the reflectance factors predicted by the **Eymard4F-RT** and **RTE-4F-RT** models.

It is this opposite in transmittance mode: the transmittance factors are overestimated by optical models for sample with thickness lower than the thickness of the calibration sample, and overestimated for other samples.

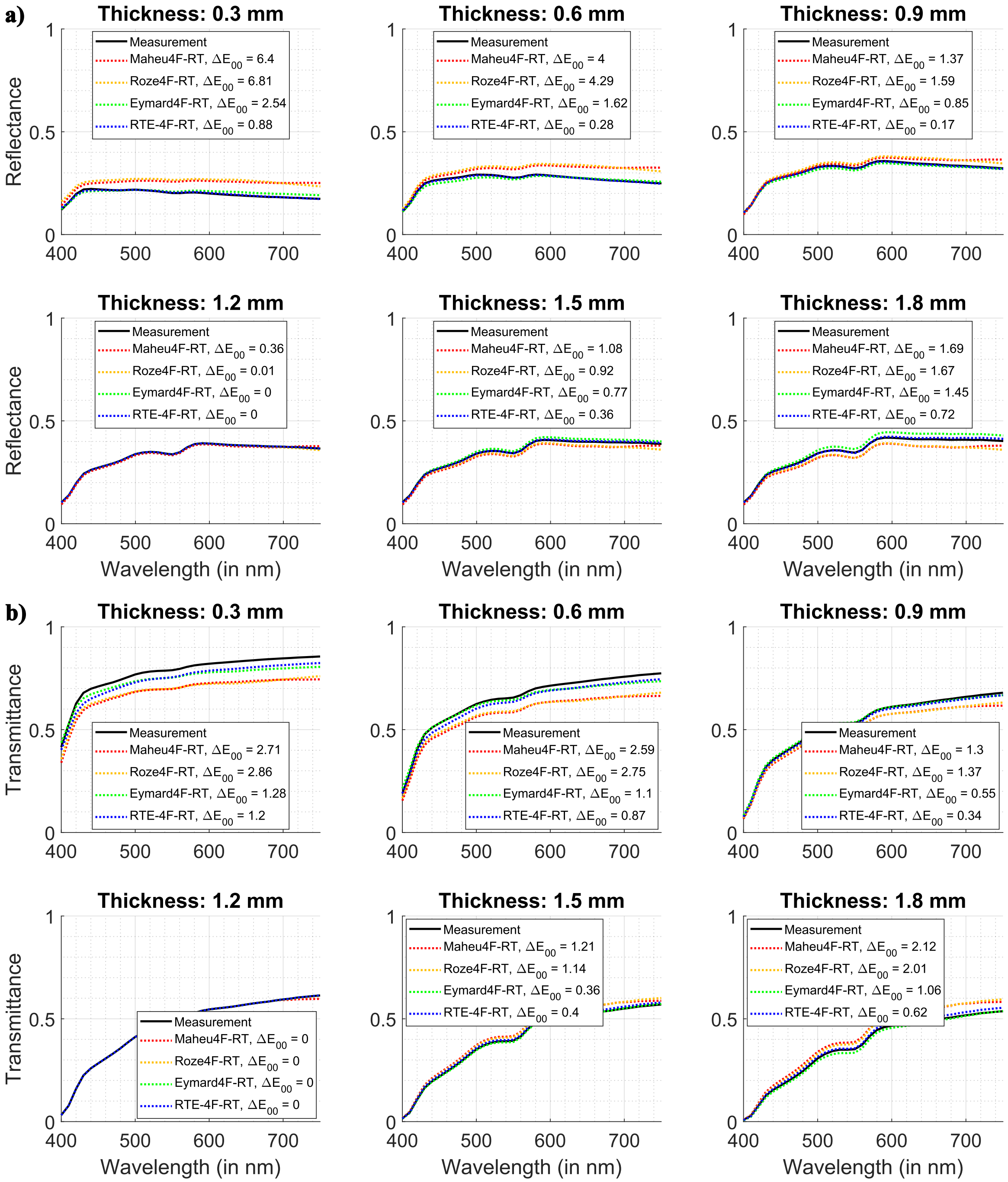

Figure 4.20: a) Reflectance factors and b) transmittance factors measured for each sample of the EsteliteUniversalFlow SuperLow A3 material compared to the reflectance and transmittance factors predicted by the **Maheu4F-RT**, **Rozé4F-RT**, **Eymard4F-RT**, and **RTE-4F-RT** models. The sample with thickness 1.2 mm is used as calibration sample.

Considering the **Eymard4F-RT** and the **RTE-4F-RT** models in reflectance mode, for samples with thickness 0.3 and 0.6 mm, the predicted and measured curves cross around 550 nm, the reflectance being underestimated at lower wavelengths and overestimated at higher wavelengths. For the other samples, the curves of the spectra predicted and measured do not cross, and the reflectance factor is underestimated for the sample with thickness 0.9 mm and overestimated for samples with thickness 1.5 and 1.8 mm. The fact that curves cross for thin samples and not for thicker samples might be due to edge-loss occurring in the measurements of the calibration with thickness 1.2 mm, which is passed into the optical parameters extracted during the calibration process. As observed in Figure 2.5, edge-loss is a spectral phenomenon, affecting red light more strongly than blue light. Therefore, preventing edge-loss more accurately in measurements would probably slightly increase accuracy of optical models, but it was not possible with our spectrophotometer.

4.4.1. Comparison with the Radiative Transfer Equation

The Radiative Transfer Equation was directly applied to predict the reflectance and transmittance factors of the samples of the EsteliteUniversalFlow SuperLow A3 material, using the reflectance and transmittance factor measurements of the calibration sample with thickness 1.2 mm. An optimization algorithm similar to the previous one was implemented and used for the model calibration.

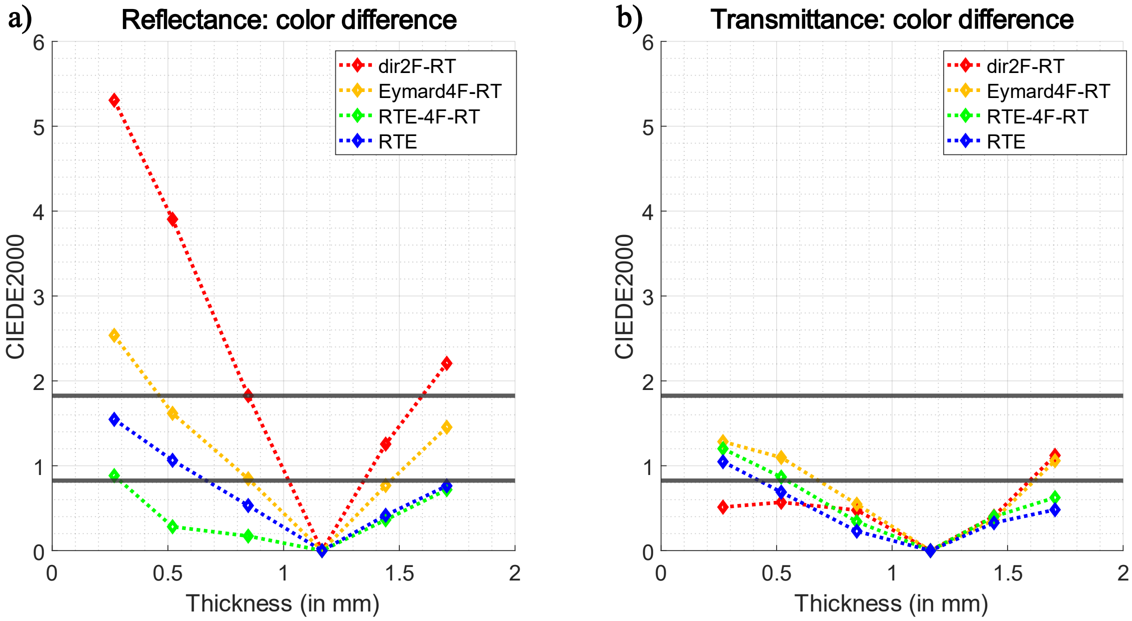

Figure 4.21: Equivalent color difference metric expressing the deviation between a) the measured spectral reflectance factors and b) transmittance factors of samples with various thickness made of the EsteliteUniversalFlow SuperLow composite shade A3 and the corresponding predictions given by the Radiative Transfer Equation (RTE), the **RTE-4F-RT** model, the **Eymard4F-RT** model and the **dir2F-RT**. The sample with thickness 1.2 mm is used as calibration sample.

Figure 4.21 shows the prediction accuracy of this model compared to the previous four-flux models. It shows that the prediction accuracy given by the RTE is slightly worse than that of the **RTE-4F-RT** model in reflectance mode, which can be surprising at first sight. However, remind that the Radiative Transfer Equation, being an angular model, should preferably be calibrated using angular measurements for more accurate description of the light paths inside the medium. The RTE is slightly more accurate than the **RTE-4F-RT** model in transmittance mode, but the **dir2F-RT** model is more accurate for the two thinnest samples.

The prediction accuracy of the RTE varies slightly depending on the solving parameters, namely, the order of the Legendre polynomial considered in the resolution of the RTE. Figure 4.22 shows the color difference as function of the Legendre polynomial order. It shows that the ΔE_{00} values vary of about 0.2, but the optimal polynomial value is not the same for every sample. Also, the Radiative Transfer Equation code was sometimes subject to numerical errors with the thickest samples, which occurred when the optical opacity is reached, because the resolution of the RTE assumed a slab of finite thickness. This is visible by the interrupted orange lines on Figure 4.22. Further investigations would be required to optimize this model. However, it shows the relevance of the **RTE-4F-RT** model, which is more accurate than the RTE, while being also simpler to

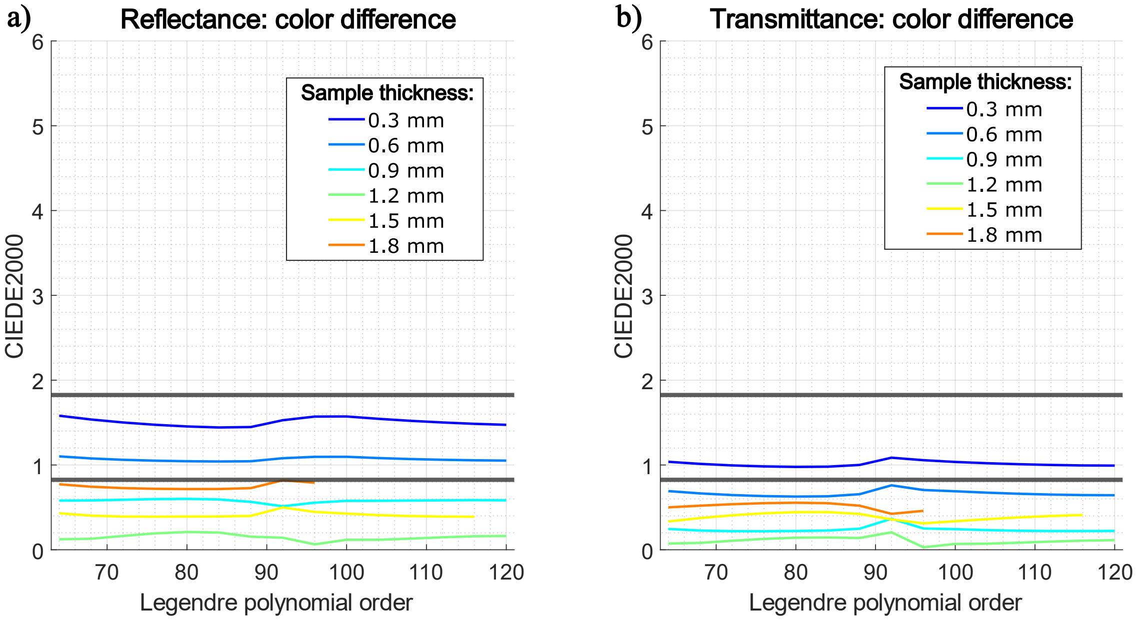

Figure 4.22: Equivalent color difference metric expressing the deviation between a) the measured spectral reflectance factors and b) transmittance factors of samples with various thickness made of the EsteliteUniversalFlow SuperLow composite shade A3 and the corresponding predictions given by the Radiative Transfer Equation (RTE) as function of the order of the Legendre polynomial used in the extraction of optical parameters and the prediction of reflectance and transmittance factors.

implement and a lot quicker to solve (computation time around 1 min for the **RTE-4F-RT** model whereas several hours are necessary for the Radiative Transfer Equation).

4.5 Conclusion on optical models

In previous chapters, we proposed improved two-flux and four-flux models for characterizing the optical properties of dental resin samples and assessing their ability to predict their spectral reflectance and spectral transmittance factors and compared them with state-of-the-art two-flux and four-flux models. Here, we propose a comparison of the prediction accuracy of the models and recall their capabilities while taking into account their simplicity of implementation. Figure 4.23 shows the prediction accuracy of the different models investigated in this thesis.

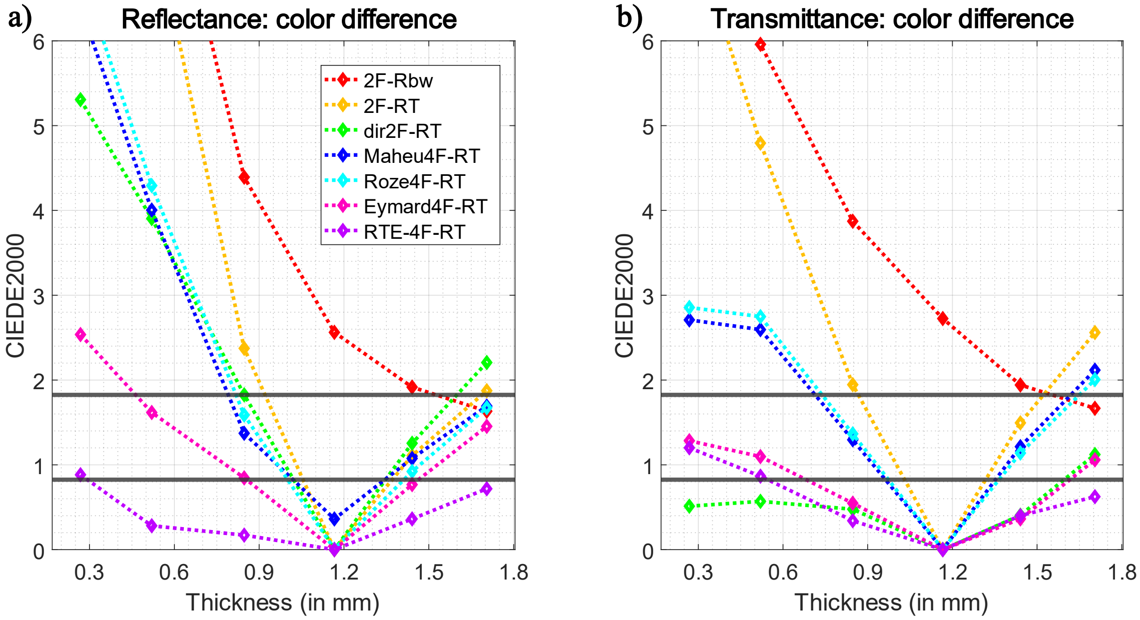

Figure 4.23: Equivalent color difference metric expressing the deviation between a) the measured spectral reflectance factors and b) transmittance factors of samples with various thickness made of the EsteliteUniversalFlow SuperLow composite shade A3 and the corresponding predictions given by the **2F-RT (calib. 2F-Rbw)**, **2F-RT**, **dir2F-RT**, **Maheu4F-RT**, **Rozé4F-RT**, **Eymard4F-RT**, and **RTE-4F-RT** models. The sample with thickness 1.2 mm is used as calibration sample.

The **RTE-4F-RT** model is by far the most accurate for predicting the reflectance factor of dental resin samples. The oldest models, **2F-RT** and **2F-Rbw**, are highly inaccurate, especially for the thinnest samples. The older four-flux models, namely the **Maheu-4F-RT** and **Rozé4F-RT**, are more accurate, although their precision is severely degraded for thin samples. The **dir2F-RT** model, a simple adaptation of the **2F-RT** model, yields predictive performances similar to that of

Table 4.1: Computation cost of models, the optical properties that can be extracted, and their prediction accuracy in reflectance and transmittance modes for the EsteliteUniversalFlow SuperLow A3 material.

Model	**2F-Rbw**	**2F-RT**	**dir2F-RT**	**Maheu4F-RT**	**Rozé4F-RT**	**Eymard4F-RT**	**RTE-4F-RT**
Main assumption within the layer	Lambertian light	Lambertian light	Collimated light	Collimated and partially diffuse light	Collimated and partially diffuse light	Collimated and partially diffuse light	Collimated and partially diffuse light
Main assumption at both layer interfaces	Lambertian light, same r_i	Lambertian light, same r_i	Collimated light, same r_i	Lambertian light, same r_i	Lambertian light, same r_i	Partially diffuse light, same r_i	Partially diffuse light, different r_i
Measurements required	R_b and R_w	R and T	R and T	R, R_c, T, T_c	R, R_c, T, T_c	R, R_c, T, T_c	R, R_c, T, T_c
Calculation time per wavelength	~10^{-4} second	~10^{-4} second	~10^{-4} second	~10^{-2} second	~10^{-1} second	~10^{-1} second	~10^{0} second
Optical parameters extracted	Absorption, Scattering	Absorption, Scattering	Absorption, Scattering	Absorption, Scattering, Forward scattering ratio, Average path length	Absorption, Scattering, Forward scattering ratio, Average path length, Asymmetry parameter, Refractive index	Absorption, Scattering, Forward scattering ratio, Average path length, Asymmetry parameter, Refractive index	Absorption, Scattering, Forward scattering ratio, Average path length, Asymmetry parameter, Refractive index
Average reflectance color difference	> AT	> AT	> AT	> AT	> AT	< AT	< PT
Average transmittance color difference	> AT	> AT	< PT	< AT	< AT	< AT	< PT

the **Maheu4F-RT** and **Rozé4F-RT** models, but is much simpler to implement. The **dir2F-RT** is even more accurate for thin samples. However, the **Eymard4F-RT** and, above all, the **RTE-4F-RT** models are far more accurate and offer satisfactory predictive performance with regard to acceptability and perceptibility thresholds over the thickness range tested.

In transmittance, the **dir2F-RT** model is extremely accurate. It is even more accurate than the **RTE-4F-RT** model on average, despite its simplifying assumptions. This shows that, in this case, there's no need for a complex model to predict the transmittance factor of dental resin samples. Table 4.1 compares the capabilities of optical models, the measurements required for their calibration and their prediction accuracy.

This table clearly shows the improvement in predictive performance that can be achieved with more complex optical models, and the optical properties they can access. However, this improved performance comes at a cost. Computation time is longer for four-flux models, particularly for the **RTE-4F-RT** model. These models also rely on more measurements for their calibration which might not be compatible with certain measuring devices even though none of these methods requires angular measurements.

Chapter 5.
Model analysis: critical parameters and comparison with an interpolation approach

The accuracy of the two-flux and four-flux models described in depth in Chapter 3 and Chapter 4 may vary according to different criteria. We will not mention here the measurement conditions that could degrade model accuracy, especially if the adequacy between measurements and models is not carefully analyzed. This has already been discussed in Chapter 2.

We have seen the importance of the r_i parameter in the four-flux model and developed a method to estimate it precisely with respect to the layer's optical parameters, thickness, and top or bottom interface. In this chapter's first section, we extend this method to the two-flux model, for which the prediction accuracy remains to be improved. Then, we evaluate the influence of the calibration sample thickness on the prediction accuracy of all the models for the reflectance and transmittance spectra. Indeed, one of the strengths of the approach we proposed is that it requires only one sample to extrapolate the color of samples of different thicknesses. Yet, a legitimate question remains: could these models be more accurate if several samples were used to calibrate the models? This question is tackled in section 0.

Another parameter that can influence model accuracy is the matrix composition of the dental material. Obviously, the size, shape and concentration of pigments in the materials have an influence on the optical properties of the materials, and therefore on the ability of the models to characterize them. To evaluate this parameter, we will test the models described above on different dental materials at our disposal following the same protocol as in Chapter 3 and Chapter 4. The results are presented in section 5.3.

Finally, the accuracy of the models developed in this thesis will be compared with an interpolation approach for color prediction recently applied in the dental field, in section 5.4.

5.1 Significance of the interface's internal reflectance

The internal reflectance of the interface, a parameter denoted r_i which is involved in the two-flux and four-flux models, is crucial in the prediction accuracy of the reflectance and transmittance factors for translucent materials, as highlighted in the previous chapters. In the literature, this parameter has been investigated to determine its optimal value in the case of a highly scattering material [182,218]. In [182], r_i is calculated for different refractive index values and the theoretical value of $r_i = 0.596$ for $n = 1.5$ is proposed. In [218], the value of r_i for two-flux, four-flux and N-flux models is simulated and deviations have been found between experimental verifications and simulations by the two-flux and four-flux models. Whenever the two-flux model was applied to dental materials, the value of this parameter was set to values for proposed for glossy or matt surfaces, 0.5963 [88,90], regardless of intrinsic scattering properties of the material. Values of this parameter were also studied in [219] for translucent materials. However, the values reported are very close to the values for highly scattering materials. Their validity was assessed in [125] for dental materials, considering samples measured in optical contact with a scattering background. Thus, our study seems to be the first investigation of this parameter in the dental field when the sample has no background. The look-up table produced by simulating light propagation within translucent layers with the Radiative Transfer Equation allows to estimate the value of r_i to be used according to the absorption and scattering properties of the material, its refractive index and the sample thickness. We showed in Chapter 4 that it is highly effective for the four-flux model, and we now extend it to the two-flux model.

5.1.1. Two-flux model enhanced with RTE

The angular distribution of light at the interfaces cannot be known via measurements based on an integrating sphere. It can only be estimated using an angular model, such as the Radiative Transfer Equation. In the same way as the methodology presented in section 4.4, we used the Radiative Transfer Equation to simulate the angular distribution of light at the interfaces. Since the two-flux model does not distinguish collimated light from diffuse light, look-up tables consider both collimated and diffuse light in the calculation of the internal reflectance of the upper and lower interfaces, and the average between values for collimated and diffuse flux is calculated while accounting for the proportion of collimated and diffuse light at the interfaces. This means that the internal reflectance parameter to be used in two-flux models is calculated according to the following formula:

$$r_i = \frac{r_{ic} I_c + r_{id} I_d}{I_c + I_d} \tag{5.1}$$

where r_i denotes the internal reflectance of the upper interface, to be used in the two-flux model, r_{ic} denotes the internal reflectance of the upper interface for collimated light (0.04 for $n = 1.5$), I_c denotes the proportion of collimated flux at the upper interface, r_{id} denotes the internal reflectance of the upper interface for diffuse light (0.5963 for $n = 1.5$ if the angular distribution of light is isotropic), and I_d is the proportion of diffuse flux at the upper interface. A symmetrical formula is used for calculating the global internal reflectance of the lower interface:

$$r_i' = \frac{r_{ic}' I_c' + r_{id}' I_d'}{I_c' + I_d'} \tag{5.2}$$

In this two-flux model, hereinafter denoted **RTE-2F-RT**, $r_i(\lambda)$ denotes the internal reflectance at the upper interface (illumination side) while $r_i'(\lambda)$ denotes the internal reflectance of the lower interface. The look-up tables give r_i and r_i' as functions of the absorption coefficient $K(\lambda)$, scattering parameter $S(\lambda)$, the asymmetry parameter of the scattering phase function denoted $g(\lambda)$, the refractive index $n(\lambda)$ and the layer thickness h. As the two-flux model assumes isotropic scattering, the asymmetry parameter g is assumed equal to 0. Furthermore, since the absorption and scattering coefficients depend upon the wavelength, so do $r_i(\lambda)$ and $r_i'(\lambda)$, in contrast with the constant value 0.5963 or 0.04 considered in the **2F-RT** and **dir2F-RT** models respectively. The values of r_i and r_i' simulated by the Radiative Transfer Equation are shown in Figure 5.1. It shows that r_i and r_i' should be almost 0.04 for thin and transparent layers, but the values of r_i and r_i' tend towards 0.6 for more highly scattering layers.

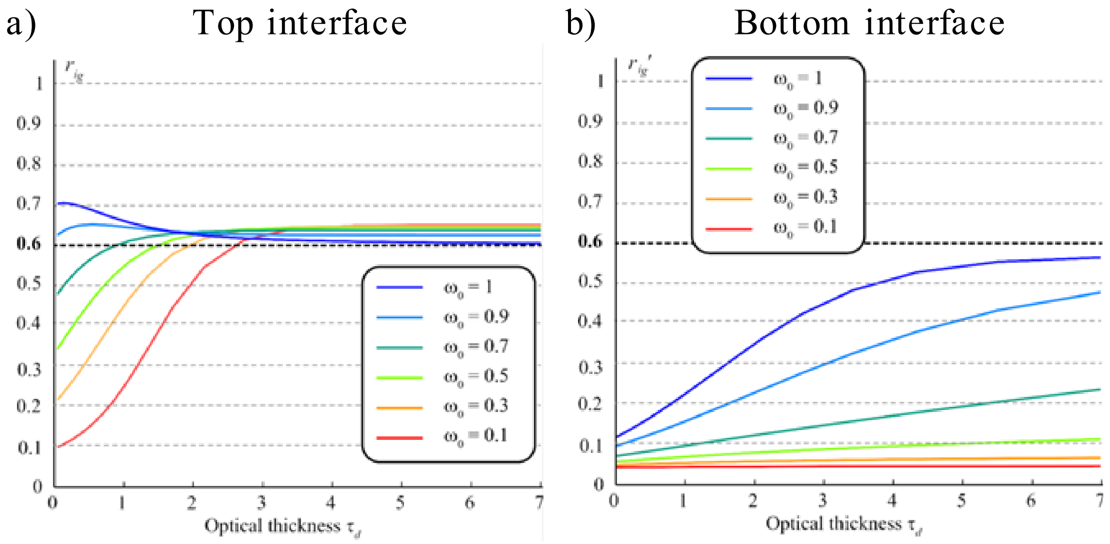

Figure 5.1: a) Total internal reflectance r_i of the top interface and b) total internal reflectance r_i’ of the bottom interface with respect to optical thickness for several albedo ω_0, with $\mu_a+\mu_s = 5$ cm^{-1}. The bold dashed line at 0.6 corresponds to the value usually found by [182] and considered in most applications of the Saunderson correction.

The calibration of this model, *i.e.*, the extraction of absorption and scattering coefficients from measurements of the calibration sample, relies on the values of r_i and r_i’, which depend on the absorption and scattering coefficients of the layer. Thus, this model cannot be analytically inversed like the **2F-RT** and **dir2F-RT** models, and the calibration approach presented through equations (3.17), (3.18), (3.19) and (3.20) is not used. Rather, the Kubelka-Munk model, equations (3.3) and (3.4), are used to calculate the intrinsic reflectance and transmittance $\rho(\lambda)$ and $\tau(\lambda)$ respectively. Then, the flux transfer matrix formalism [156] (see 0) is used to apply the Saunderson correction and derive the reflectance and transmittance factors $R(\lambda)$ and $T(\lambda)$ respectively.

$$\begin{pmatrix} M_{11} & M_{12} \\ M_{21} & M_{22} \end{pmatrix} = \begin{pmatrix} 1/T_{in} & -r_i/T_{in} \\ r_e/T_{in} & \dfrac{T_{in}T_{out}-r_e r_i}{T_{in}} \end{pmatrix} \begin{pmatrix} 1/\tau & -\rho/\tau \\ \rho/\tau & \dfrac{\tau^2-\rho^2}{\tau} \end{pmatrix} \begin{pmatrix} 1/T'_{out} & -r'_e/T'_{out} \\ r'_i/T'_{out} & \dfrac{T'_{in}T'_{out}-r'_e r'_i}{T'_{out}} \end{pmatrix} \tag{5.3}$$

with ρ and τ being calculated with the Kubelka-Munk model, formulae (3.3) and (3.4), and:

$$R(\lambda) = M_{21} / M_{11} \tag{5.4}$$

$$T(\lambda) = 1 / M_{11} \tag{5.5}$$

Then, an optimization algorithm, similar to the one used in Chapter 4 with four-flux models is implemented to extract $K(\lambda)$ and $S(\lambda)$. The optimization algorithm predicts the reflectance and transmittance factors $R(\lambda)$ and $T(\lambda)$ respectively as functions of $K(\lambda)$, $S(\lambda)$, the thickness of the sample h and $r_i(\lambda)$ and r_i’(λ) (the two latter depend upon $K(\lambda)$ and $S(\lambda)$, the asymmetry parameter g assumed to be 0, the refractive index n assumed to be 1.5 and the thickness of the layer h) and minimizes the deviation between the measured and predicted reflectance and transmittance factors for each wavelength as presented in equation (5.6):

$$\text{deviation}(\lambda) = \frac{\left|R_{mes}(\lambda) - R_{pred}(\lambda)\right| + \left|T_{mes}(\lambda) - T_{pred}(\lambda)\right|}{2} \tag{5.6}$$

with $R_{mes}(\lambda)$ (resp. $T_{mes}(\lambda)$) the measured reflectance (resp. transmittance) factor and $R_{pred}(\lambda)$ (resp. $T_{pred}(\lambda)$) the predicted reflectance (resp. transmittance) factor. We used the *fmincon* local optimization function from Matlab® with a sequential quadratic programming “sqp” algorithm in order to minimize the deviation. This optimization process, as the optimization process for the **RTE-4F-RT** model, is longer than other methods as it requires about 2 to 3 seconds with a standard computer to extract $K(\lambda)$ and $S(\lambda)$ for each wavelength. The boundaries for the optimization were 10^{-2} m^{-1} and 10^{4} m^{-1} for the absorption and scattering coefficients, and the first guess value was set to 1000 m^{-1} for both coefficients. We observed that the choice of the first guess value did not influence the optimization process; the extracted parameters were the same in all cases.

Spectral curves obtained for $K(\lambda)$ and $S(\lambda)$ extracted from the samples of the EsteliteUniversalFlow SuperLow A3 material (same material as in Chapter 3 and Chapter 4) are shown in Figure 5.2. The internal reflectance of the top and bottom interfaces, $r_i(\lambda)$ and $r_i'(\lambda)$ respectively, are shown in Figure 5.3 as a function of the sample thickness.

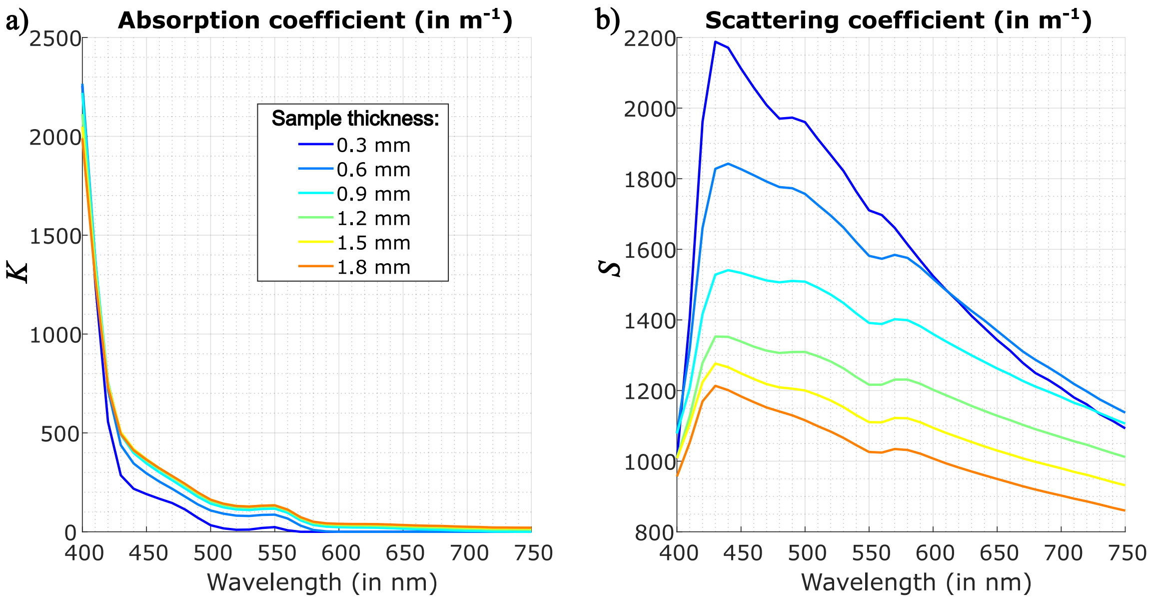

Figure 5.2: a) Absorption $K(\lambda)$ and b) scattering coefficients $S(\lambda)$ extracted from the measured reflectance and transmittance factors $R(\lambda)$ and $T(\lambda)$ of the EsteliteUniversalFlow SuperLow A3 samples using the **RTE-2F-RT** model.

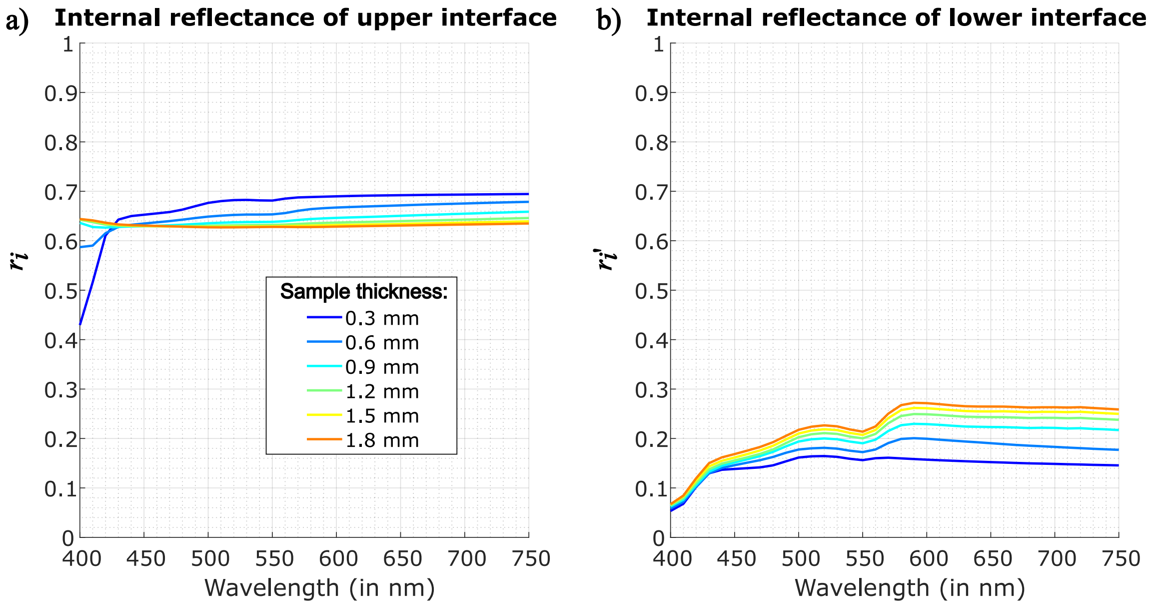

Figure 5.3: Internal reflectance of the a) top interface $r_i(\lambda)$ and b) bottom interface $r_i'(\lambda)$ coefficients from RTE look-up tables in order to extract absorption and scattering coefficients for samples of the EsteliteUniversalFlow SuperLow A3 material using the **RTE-2F-RT** model.

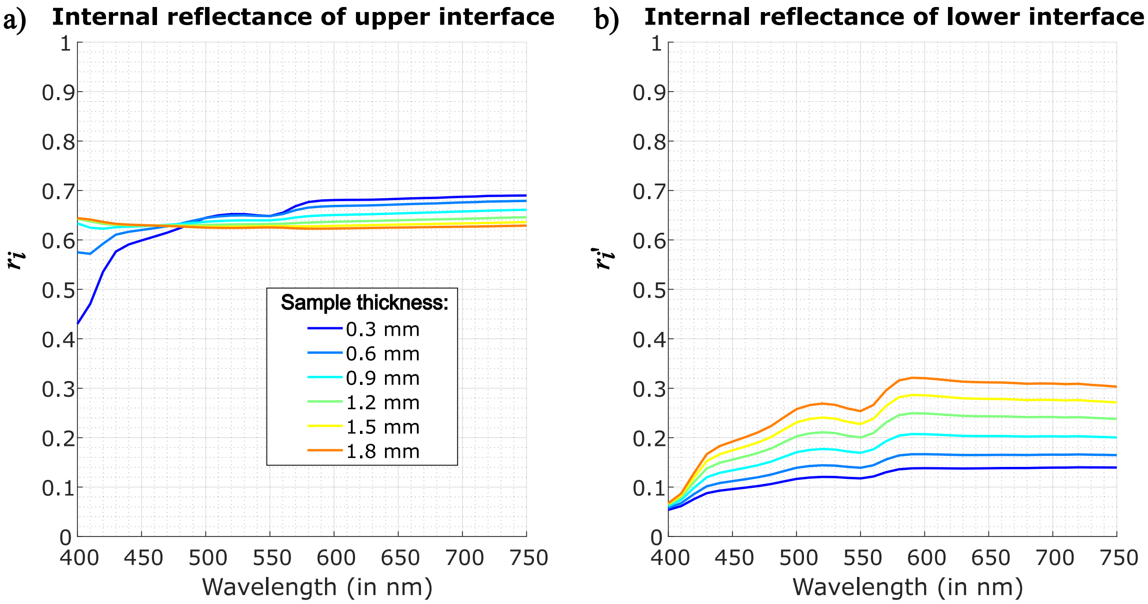

Figure 5.4: Internal reflectance of the a) upper interface and b) lower interface used in the prediction of the reflectance and transmittance factors by the **RTE-2F-RT** model.

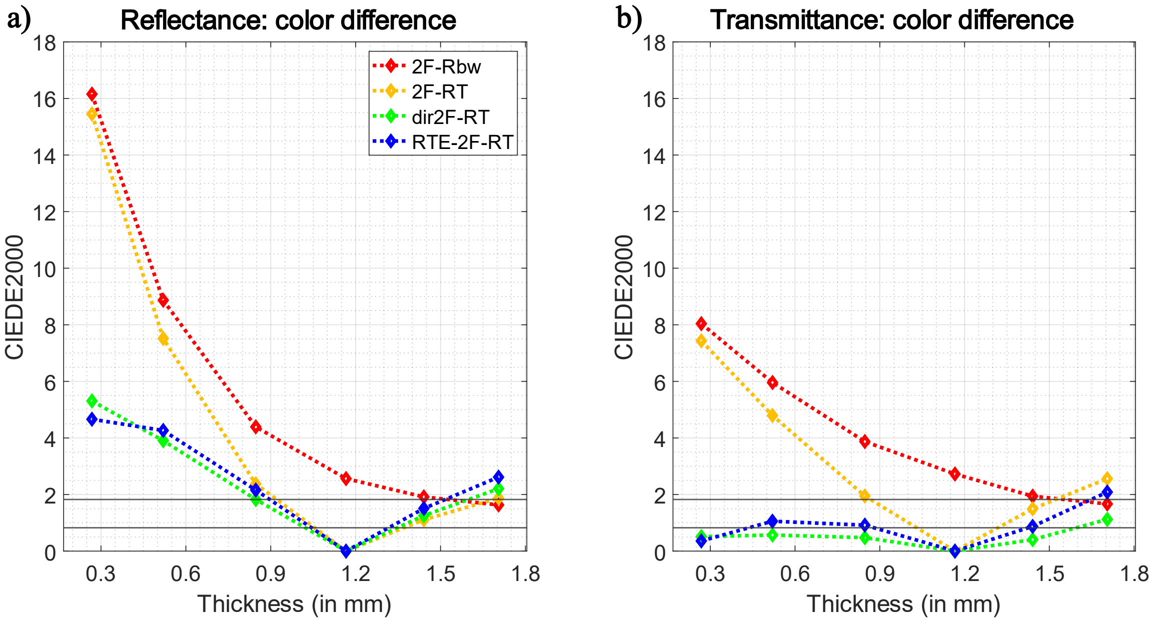

Figure 5.5: Equivalent color difference metric expressing the deviation between a) the measured spectral reflectance factors and b) transmittance factors of samples with various thickness made of the EsteliteUniversalFlow composite shade A3 and the corresponding predictions given by the **2F-RT (calib. 2F-Rbw)** model, the **2F-RT** model, the **dir2F-**

RT model, and the **RTE-2F-RT (assuming $g = 0$)** model. The sample with thickness 1.2 mm is used as calibration sample.

The $r_i(\lambda)$ and $r_i'(\lambda)$ values used for predicting the spectral reflectance and transmittance factors are shown in Figure 5.4. The predictive performance of the **RTE-2F-RT** model is presented in Figure 5.5. It is less accurate than the **dir2F-RT** model for all samples except the thinnest one. Overall, this model does not provide any gain in accuracy compared to the simpler and faster **dir2F-RT** model. This might be because of the assumption made on the asymmetry parameter of the Henyey-Greenstein phase function, assumed to be $g = 0$. However, the extraction of parameter was repeated for different values of g and no significant improvement was found. The poor performance of this complex model is probably due to inadequacy of look-up table generated with the RTE for the two-flux model, as both models are exceedingly different in the way they describe light propagation. We can conclude that the **dir2F-RT** model is the most accurate two-flux model for color prediction in both reflectance and transmittance modes for the investigated dental resin composite.

5.1.2. Fitted r_i two-flux model

Using the r_i and r_i' values from the RTE look-up tables did not provide any gain in the prediction accuracy of the two-flux model. We will therefore try to fit these parameters according to the thickness of the material considered. To do this, we will use the absorption K and scattering S parameters extracted using the **2F-Rbw** model for reflectance factor measurements on black and white backgrounds of the 1.2 mm calibration sample. To extract these parameters the assumption of Lambertian light distribution is more justified than for the other models since the sample is placed on a highly scattering white background. This idea is supported by several studies in the dental field [125,159] in which good prediction accuracy is found with the **2F-Rbw** model for predicting the reflectance factor of samples in optical contact on an opaque white background. Secondly, the K and S coefficients are used to predict the reflectance and transmittance factors of other samples, as it was done in Chapter 3 (**2F-RT calib. 2F-Rbw** model). However, we implement an optimization algorithm that seeks to minimize the deviation between the predicted and measured reflectance and transmittance spectra by using the internal reflectance at top and bottom interfaces, r_i and r_i' respectively, as fitting parameters for each thickness. This protocol was repeated for different materials at our disposal, and the fitted values are presented in Figure 5.6.

Unsurprisingly, values of r_i and r_i' show a strong dependence to the thickness of the sample, especially for thin samples. For thick samples, the assumption of Lambertian light distribution seems verified at the top interface, but values for the bottom interface are lower, indicating a non-isotropic light distribution. This is expected since the collimated light crossing the layer and hitting the lower interface is less scattered than light reaching the upper interface, which has been backscattered. Then, a fraction is reflected by the interface towards the upper interface and is more scattered along its path. Thus, as the sample thickness decreases, values tend towards 0.04, the value associated with purely directional light. This is also consistent with the modelling presented by Gautheron *et al.* [185] and reported in Figure 5.1. However, it is not consistent with values used in the prediction with the **RTE-2F-RT** model, see Figure 5.3, for the EsteliteUniversalFlow SuperLow A3 material. For this material, spectral values of r_i were around 0.6, even for the thinnest sample, while values of r_i' were around 0.2 for all samples. Therefore, further investigation is needed to improve the accuracy of the two-flux model applied to dental materials.

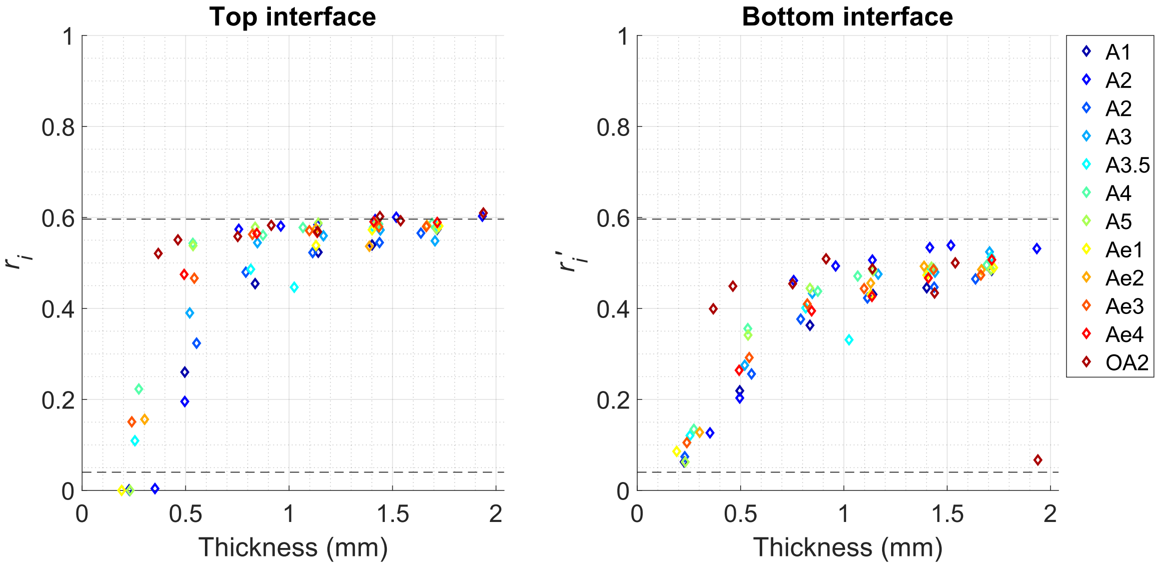

Figure 5.6 : r_i and r_i' parameters fitted from numerous translucent dental resin composites.

5.2 Influence of the calibration sample(s)

In order to evaluate the influence of the thickness of the calibration sample, we repeated the prediction process by considering different calibration samples. Specifically, the thickest sample, being more scattering than thinner samples, is more in line with the assumption of diffuse light on which the tested models rely and is therefore relevant to test. This comparison is tested between the models specifically adapted to translucent materials, *e.g.* the **dir2F-RT**, **RTE-2F-RT**, **Eymard4F-RT**, and **RTE-4F-RT** models. The results are shown in Figure 5.7.

It appears that all models lose in accuracy on average when using the sample with thickness 0.6 or 1.8 mm as calibration sample. As the thickness deviates from the calibration thickness, the ΔE_{00} values increase. However, we retrieve the general trend observed in previous chapters: in reflectance mode, the **RTE-4F-RT** model is the most accurate model, followed by the **Eymard4F-RT** model, and the **RTE-2F-RT** and **dir2F-RT** have a similar accuracy, except for the thinnest sample for which the **RTE-2F-RT** is more accurate. In transmittance mode, the prediction accuracy of models depends on the sample thickness, but overall, most color differences are acceptable. It is

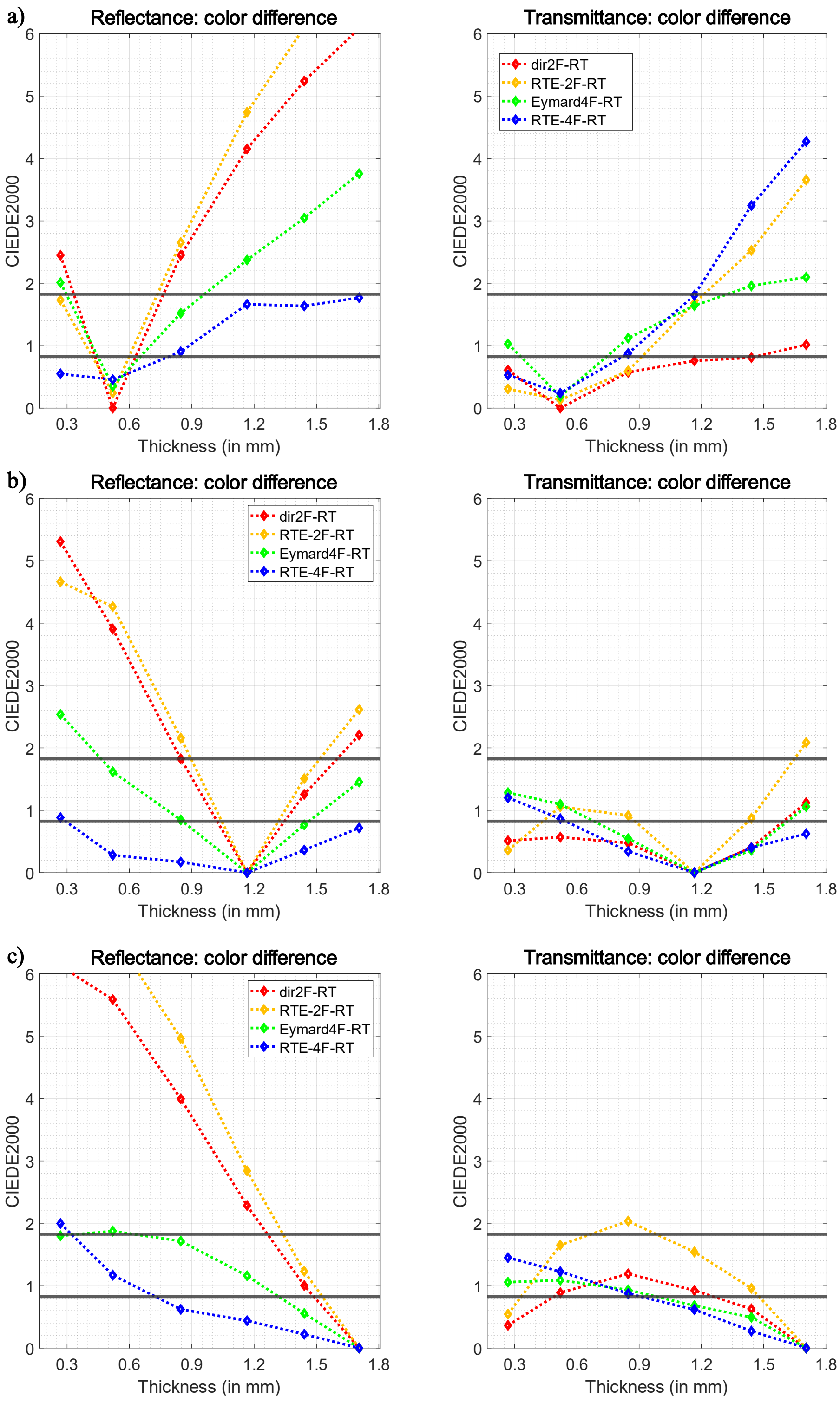

Figure 5.7: Equivalent color difference metric expressing the deviation between the measured spectral reflectance factors (left graphs) and transmittance factors (right graphs) of samples with various thickness made of the EsteliteUniversalFlow composite shade A3 and the corresponding predictions given by the **dir2F-RT** model, the **RTE-2F-RT (assuming *g* = 0)** model, the **Eymard4F-RT** and the **RTE-4F-RT** model. a) The sample with thickness 0.6 mm is used as calibration sample. b) The sample with thickness 1.2 mm is used as calibration sample. c) The sample with thickness 1.8 mm is used as calibration sample.

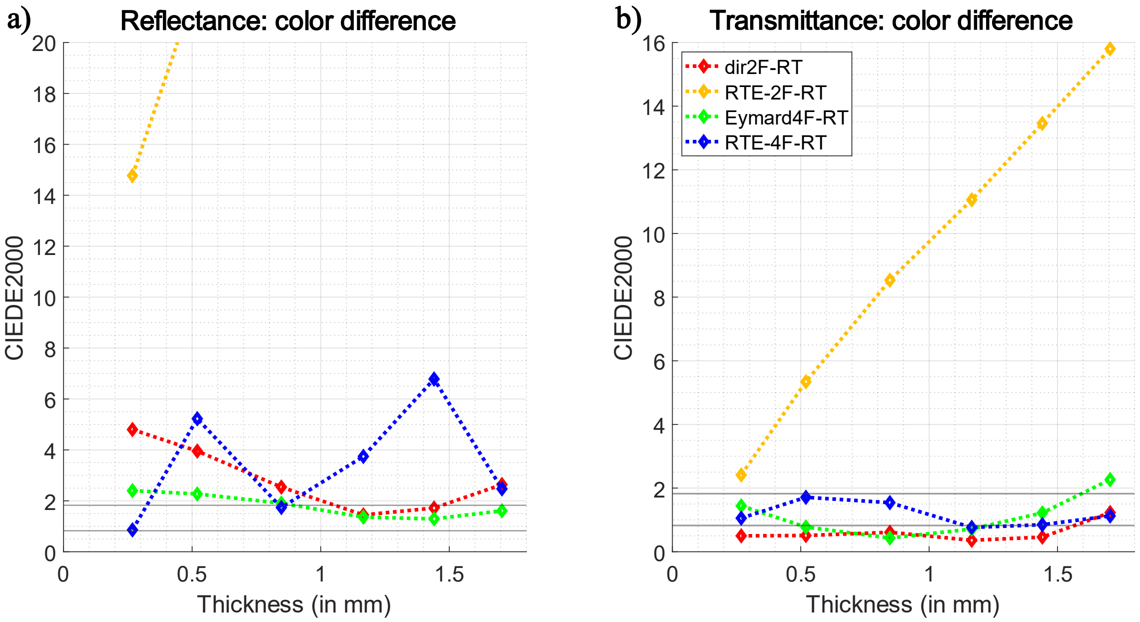

Figure 5.8: Equivalent color difference metric expressing the deviation between a) the measured spectral reflectance factor and b) transmittance factors of samples with various thickness made of the EsteliteUniversalFlow composite shade A3 and the corresponding predictions given by the **dir2F-RT** model, the **RTE-2F-RT (assuming $g = 0$)** model, the **Eymard4F-RT** and the **RTE-4F-RT** model. All samples are used for calibration of each model.

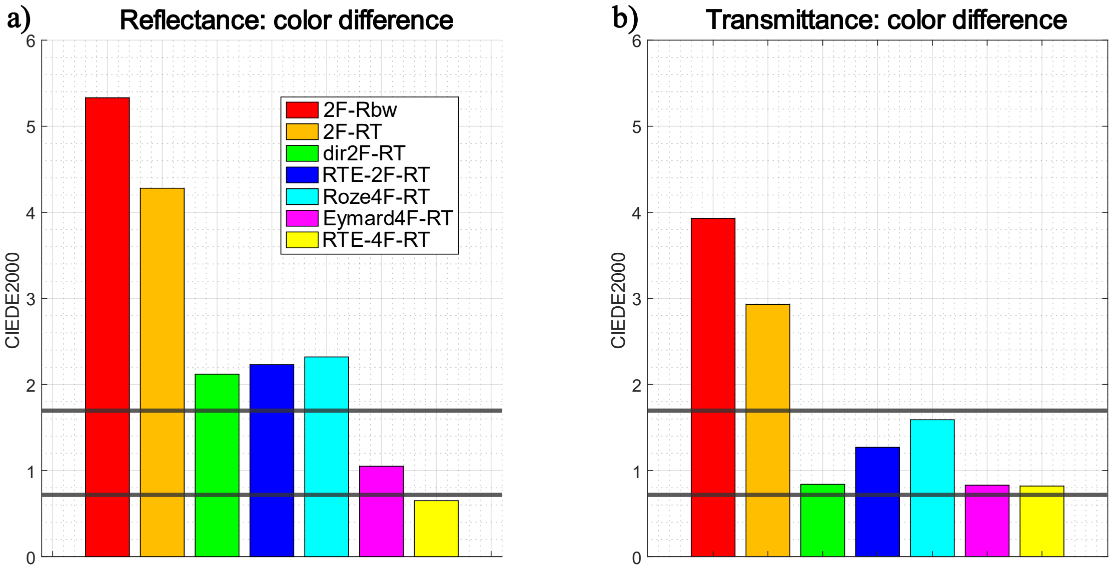

Figure 5.9: Equivalent color difference metric averaged on all samples expressing the deviation between a) the measured spectral reflectance factors and b) transmittance factors of all samples with various thickness and the corresponding predictions given by the **2F-Rbw**, **2F-RT**, **dir2F-RT**, the **RTE-2F-RT (assuming $g = 0$)**, **Roze4F-RT**, **Eymard4F-RT** and the **RTE-4F-RT** model. For each material type, the sample with thickness 1.2 mm is used as calibration sample.

obvious that the prediction accuracy of the investigated models depends on the thickness of the calibration sample. The calibration sample with a middle range thickness provides the most accurate predictions.

However, the question that arises is whether the prediction accuracy of optical models of these models is improved when calibrating them from all the sample thicknesses, as it is done in studies based on interpolation methods [129,130]. Therefore, for each sample (test sample), we calibrated the models from measurements of the other five samples (training samples) in order to predict the reflectance and transmittance factor of the test sample. The resulting prediction accuracy of the models is shown in Figure 5.8. Interestingly, it appears that all models lose in accuracy. In reflectance mode, most color differences are above the acceptability threshold, for all models. Most notably, the **RTE-2F-RT** and **RTE-4F-RT** models are totally unreliable. In transmittance mode, the prediction accuracy is similar as to where models are calibrated with the 1.2 mm thickness sample, except for the **RTE-2F-RT** model for which the prediction accuracy is unsatisfactory. The decrease in prediction accuracy might be due to difficulties found by the optimization algorithm coupled to the model to find solution for many calibration samples.

This is probably because light-matter interaction phenomena are rather different from the thinnest to the thickest sample. Although this might not be an issue when using angular models, it is for the two-flux and four-flux models which rely on several simplifying assumptions, which cannot encompass samples with high thickness difference. In this case, the models are simply not able to find optical parameters to describe the reflectance and transmittance factor of samples of different thicknesses during the calibration process. Thus, inaccurate parameters are extracted, leading to imprecise reflectance and transmittance factor predictions. This confirms that optical models are the most accurate when calibrated with one sample with intermediary thickness.

5.3 Prediction accuracy of optical models on several sets of dental materials

All models described in the previous chapters and this one, have been applied to all dental materials at our disposal. Each model was calibrated using the sample with thickness 1.2 mm. The prediction accuracy obtained with all models and averaged for all samples at our disposal is shown in Figure 5.9. The gain in prediction accuracy for both the reflectance factor and the transmittance factor is clearly visible, from the rather inaccurate state of the art models, namely the **2F-Rbw** and **2F-RT** models, to the most advanced **RTE-4F-RT** model developed in this thesis.

5.3.1. Comparison table

The color difference between predicted and measured reflectance and transmittance factors are given in Table 5.1. Only predictions given by the most accurate optical models, namely the **dir2F-RT**, **RTE-2F-RT**, **Eymard4F-RT**, and **RTE-4F-RT** models are displayed in this table.

Table 5.1: CIEDE2000 equivalent color difference metric expressing the deviation between the measured spectral reflectance factors and transmittance factors of samples the corresponding predictions given by the dir2F-RT model, the RTE-2F-RT model, the Eymard4F-RT model and the RTE-4F-RT model. Color differences below PT are highlighted in green while color differences below AT are highlighted in yellow. The sample with thickness 1.2 mm is used as calibration sample.

Sample	**Color difference in reflectance**				**Color difference in transmittance**			
AuraEasyFlowAe1	**dir2F**	**RTE-2F**	**Eymard4F**	**RTE-4F**	**dir2F**	**RTE-2F**	**Eymard4F**	**RTE-4F**
0.3	3.73	3.96	1.77	0.91	0.62	0.69	0.56	1.29
0.6	3.34	3.89	1.50	0.95	0.28	0.92	0.57	1.13
0.9	1.64	2.19	0.74	0.50	1.08	1.57	0.87	0.36
1.2	0.00	0.00	0.00	0.00	0.00	0.00	0.00	0.00
1.5	1.10	1.18	0.68	0.62	0.54	0.51	0.58	1.10
1.8	1.92	2.16	1.00	0.74	0.86	1.38	0.75	1.80
AuraEasyFlowAe2								
0.3	3.86	2.69	2.85	1.85	0.81	0.75	0.83	1.73
0.6	4.22	3.80	2.08	1.20	0.66	0.78	0.75	1.65
0.9	1.53	1.83	0.53	0.75	0.40	0.88	0.36	0.74
1.2	0.00	0.00	0.00	0.00	0.00	0.00	0.00	0.00
1.5	1.01	1.17	0.43	0.18	0.08	0.53	0.22	0.62
1.8	2.05	2.33	1.05	0.25	0.33	1.30	0.34	1.23
AuraEasyFlowAe3								
0.3	3.81	2.70	2.50	1.52	1.02	0.91	1.02	1.88
0.6	2.79	3.14	0.78	0.88	0.25	0.74	0.62	1.01
0.9	1.34	1.68	0.37	0.50	0.56	0.94	0.62	0.10
1.2	0.00	0.00	0.00	0.00	0.00	0.00	0.00	0.00
1.5	1.32	1.42	0.58	0.39	0.35	0.47	0.45	1.14
1.8	2.10	2.34	0.96	0.47	0.33	1.28	0.39	1.39
AuraEasyFlowAe4								
0.3	3.41	2.59	1.40	1.42	0.86	0.85	0.63	1.44
0.6	2.89	2.76	1.08	1.03	0.27	0.53	0.64	0.97
0.9	1.07	1.53	0.26	0.95	0.86	1.16	1.02	0.46

1.2	0.00	0.00	0.00	0.00	0.00	0.00	0.00	0.00
1.5	1.60	1.50	1.07	0.61	1.21	0.91	1.14	1.68
1.8	2.62	2.63	1.47	0.50	1.16	0.76	1.08	2.26
EsteliteUniversalFlowMediumA2								
0.4	4.87	4.48	2.92	1.93	0.68	0.79	1.37	1.23
0.5	3.81	3.63	2.40	1.78	0.59	0.90	1.08	1.22
0.8	2.05	2.33	0.99	0.51	0.80	1.29	0.84	0.49
1.0	0.88	0.91	0.50	0.45	0.57	0.83	0.53	0.36
1.2	0.00	0.00	0.00	0.00	0.00	0.00	0.00	0.00
1.5	1.33	1.57	0.86	0.36	0.51	0.99	0.37	0.26
1.6	1.78	2.08	1.16	0.45	0.76	1.42	0.55	0.30
2.0	2.72	3.14	1.71	0.37	1.96	3.42	1.63	0.39
EsteliteUniversalFlowMediumA3								
0.4	4.58	3.78	3.28	2.62	0.92	0.57	1.68	1.75
0.5	3.69	3.31	2.58	2.20	0.76	0.82	1.46	1.45
0.8	1.92	1.92	1.24	1.16	0.49	0.69	0.88	1.02
1.0	0.81	0.86	0.47	0.43	0.39	0.63	0.42	0.26
1.2	0.00	0.00	0.00	0.00	0.00	0.00	0.00	0.00
1.5	1.40	1.51	0.66	0.36	0.97	1.66	0.81	0.32
1.6	1.60	1.77	0.73	0.36	1.37	2.22	1.16	0.45
2.0	2.50	2.62	1.11	0.64	2.34	4.18	2.06	0.58
EsteliteUniversalFlowMediumA4								
0.4	4.26	3.39	2.60	1.96	0.70	0.56	1.39	1.57
0.5	4.61	4.99	1.36	0.32	1.50	1.96	2.00	0.92
0.8	2.29	2.33	0.98	0.63	0.47	0.99	0.73	0.60
1.0	1.48	1.45	1.49	1.50	2.58	2.56	2.58	2.61
1.2	0.00	0.00	0.00	0.00	0.00	0.00	0.00	0.00
1.5	1.26	1.30	0.52	0.32	0.67	1.28	0.67	0.27
1.6	1.64	1.71	0.69	0.33	1.03	1.88	1.00	0.37
2.0	2.57	2.61	1.13	0.66	2.13	3.88	2.10	0.55
EsteliteUniversalFlowMediumOA2								
0.4	4.37	6.25	1.20	1.53	1.60	2.54	1.01	1.64
0.5	3.56	5.11	0.97	1.17	1.57	2.53	1.03	1.56
0.8	1.57	2.18	0.39	0.48	0.46	0.93	1.03	1.58
1.0	0.72	0.98	0.15	0.33	0.39	0.69	0.59	0.88

1.2	0.00	0.00	0.00	0.00	0.00	0.00	0.00	0.00
1.5	0.87	1.06	0.38	0.16	1.09	1.72	0.37	0.31
1.6	1.01	1.22	0.41	0.19	1.44	2.28	0.47	0.31
2.0	1.40	1.67	0.69	0.16	2.53	4.13	0.89	0.75
EsteliteUniversalFlowMediumOA3								
0.4	4.91	6.33	1.42	1.58	1.61	2.65	1.03	1.21
0.5	4.03	5.16	1.16	1.30	1.66	2.74	0.98	1.12
0.8	1.80	2.20	0.50	0.45	1.19	1.95	0.56	0.65
1.0	0.71	0.85	0.19	0.19	0.87	1.19	0.69	0.77
1.2	0.00	0.00	0.00	0.00	0.00	0.00	0.00	0.00
1.5	0.69	0.74	0.18	0.23	0.67	1.30	0.26	0.71
1.6	0.89	0.94	0.26	0.24	1.05	1.94	0.29	0.69
2.0	1.33	1.28	0.40	0.35	2.23	3.97	0.94	0.74
EsteliteUniversalFlowMediumOA4								
0.4	7.15	9.24	3.69	2.75	4.59	5.62	3.97	2.61
0.5	2.97	2.68	2.83	3.77	3.41	3.11	3.84	4.99
0.8	2.00	2.47	0.58	0.35	1.79	2.62	0.99	0.37
1.0	0.89	1.05	0.24	0.17	0.70	1.17	0.23	0.35
1.2	0.00	0.00	0.00	0.00	0.00	0.00	0.00	0.00
1.5	0.76	0.80	0.27	0.19	1.01	1.66	0.43	0.33
1.6	0.81	0.86	0.18	0.21	1.29	2.20	0.46	0.53
2.0	1.29	1.23	0.41	0.37	2.54	4.22	1.28	0.53
EsteliteUniversalFlowSuperLowA1								
0.3	4.53	5.00	2.59	1.36	1.13	0.64	1.74	2.15
0.6	4.11	4.90	2.03	0.94	0.75	1.30	1.02	1.00
0.9	1.70	2.14	0.89	0.26	0.39	0.79	0.39	0.52
1.2	0.00	0.00	0.00	0.00	0.00	0.00	0.02	0.00
1.5	1.11	1.41	0.71	0.26	0.63	1.02	0.48	0.42
1.8	2.39	3.00	1.96	1.10	1.21	2.18	0.96	0.70
EsteliteUniversalFlowSuperLowA2								
0.3	4.72	4.16	2.91	1.17	1.06	0.62	1.55	1.94
0.6	3.64	4.24	1.70	0.53	0.65	1.16	1.00	0.73
0.9	1.93	2.33	1.00	0.26	0.36	0.77	0.52	0.51
1.2	0.00	0.00	0.00	0.00	0.00	0.00	0.00	0.00
1.5	1.44	1.81	0.93	0.45	0.60	1.10	0.53	0.56

1.8	2.08	2.62	1.42	0.65	1.00	1.88	0.89	0.74
EsteliteUniversalFlowSuperLowA3								
0.3	5.31	4.66	2.54	0.88	0.51	0.36	1.28	1.20
0.6	3.90	4.26	1.62	0.28	0.57	1.06	1.10	0.87
0.9	1.83	2.16	0.85	0.17	0.48	0.92	0.55	0.34
1.2	0.00	0.00	0.00	0.00	0.00	0.00	0.00	0.00
1.5	1.25	1.51	0.77	0.36	0.41	0.87	0.36	0.40
1.8	2.21	2.62	1.45	0.72	1.12	2.09	1.06	0.62
EsteliteUniversalFlowSuperLowA3.5								
0.3	4.72	3.78	2.49	0.56	0.94	0.57	1.49	1.67
0.6	3.51	3.86	1.31	0.52	0.50	0.91	1.09	0.61
0.9	1.35	1.63	0.61	0.45	0.32	0.65	0.43	0.21
1.2	0.00	0.00	0.00	0.00	0.00	0.00	0.00	0.00
1.5	1.88	2.17	1.07	0.60	0.84	1.60	0.88	0.46
1.8	2.89	3.29	1.77	0.99	1.30	2.73	1.36	1.00
EsteliteUniversalFlowSuperLowA4								
0.3	4.83	3.43	2.54	0.51	1.26	1.02	1.59	1.81
0.6	3.61	3.63	1.33	0.31	0.29	0.55	1.07	0.74
0.9	1.21	1.35	0.49	0.26	0.07	0.36	0.28	0.32
1.2	0.00	0.00	0.00	0.00	0.00	0.00	0.00	0.00
1.5	1.80	2.04	0.98	0.63	0.84	1.54	1.02	0.40
1.8	2.76	3.08	1.65	1.06	1.45	2.70	1.78	0.76
EsteliteUniversalFlowSuperLowA5								
0.3	4.78	2.55	2.97	0.84	1.61	1.48	1.71	2.11
0.6	4.01	3.82	1.34	0.42	0.37	0.51	1.18	0.82
0.9	2.02	2.17	0.77	0.52	0.50	0.89	0.64	0.29
1.2	0.00	0.00	0.00	0.00	0.00	0.00	0.00	0.00
1.5	1.38	1.45	0.63	0.39	0.37	0.87	0.53	0.31
1.8	2.48	2.61	1.30	0.82	0.85	1.95	1.15	0.69
	Reflectance factor				**Transmittance factor**			
	dir2F	**RTE-2F**	**Eymard4F**	**RTE-4F**	**dir2F**	**RTE-2F**	**Eymard4F**	**RTE-4F**
Mean CIEDE2000	2.12	2.23	1.05	0.65	0.84	1.27	0.83	0.82
95th percentile	4.79	5.01	2.86	1.93	2.36	3.89	2.01	2.11
% under AT	50.00	43.52	83.33	93.52	91.67	75.00	94.44	91.67
% under PT	18.52	15.74	47.22	71.30	56.48	37.96	51.85	62.04

On average, the **RTE-4F-RT** is the most accurate at predicting the reflectance and transmittance factor of the dental resin composites under study. In reflectance mode, the average ΔE_{00} is 0.65, and 93% of all color differences are below the acceptability threshold. 71% are even below the perceptibility threshold. In transmittance mode, the average color difference is 0.82. 91% of color differences are below the acceptability threshold and 62% are below the perceptibility threshold. The model is slightly less accurate in transmittance mode than in reflectance mode. Most predictions above the perceptibility threshold occur for the thinnest samples of each material, with thickness 0.3 or 0.4 mm. Despite major improvement in the prediction accuracy of two-flux and four-flux models, the prediction of the reflectance factor of these samples remains the hardest.

Previous observations made on a single material in the previous sections remain valid on all materials, which validates our assumptions and physical understanding of the models. The **RTE-2F-RT** is the least accurate of the developed models; the **dir2F-RT** model is more accurate in both reflectance and transmittance modes. The **Eymard4F-RT** model is more accurate than the **dir2F-RT** model, although the accuracy difference in transmittance mode is slim.

The prediction accuracy varies slightly depending on the material. Reflectance factor predictions are on average more accurate for samples of the EsteliteUniversalFlow SuperLow material (all shades) than for samples of the Aura EasyFlow material (all shades). The Aura EasyFlow material has fillers of a higher diameter (0.2 to 1.0 micron) compared to the EsteliteUniversalFlow material (mean filler size of 0.2 micron). The difference between these 2 models in accuracy of average color differences in reflectance mode is about 0.2 ΔE_{00} unit, which remains small.

Despite its slightly higher complexity, and the two additional measurements required to implement the **RTE-4F-RT** model, the improvement in prediction accuracy compared to the **dir2F-RT** model is significant. Therefore, we would recommend using the **RTE-4F-RT** model for the optical characterization of dental resin composites and for prediction of their appearance in reflectance mode.

5.3.2. To go further

This experiment was conducted on two different flowable dental resin composites concerning mainly the fillers' size and shape for clinically relevant thicknesses. However, samples with thicknesses greater than 2.0 mm should also be investigated for completion. Also, other types of dental resins should be investigated as it was demonstrated that fillers size and shape [220], metallic colored pigments [221], white pigments and opacifiers [42,121], resin matrix composition [222] and viscosity [223] influence the propagation of light inside the material and thus its appearance. Furthermore, human enamel being opalescent [46], so-called opalescent resin composites were specifically developed to reproduce this behavior [46,224,225]. Therefore, the prediction accuracy of optical models may vary depending on the composition of resin composites.

5.4 Optical methods and interpolation approach compared

In a recent thesis [131], an interpolation approach based on a principal component analysis (PCA) of spectral curves has been developed in order to predict the reflectance factor of samples of dental materials [129]. Using a set of samples of a given dental material, this approach consists in measuring the reflectance factor of all samples (training set), performing a principal component analysis to reduce the dimensionality of measurements, and then use a 2nd order polynomial to interpolate the reflectance of other samples (testing set) using eigen vectors of the reflectance factor measurements on the training set. The prediction accuracy of the models and this approach for the EsteliteUniversalFlow SuperLow A3 material is presented on Figure 5.10. The average prediction accuracy of this method, compared to two-flux and four-flux models is presented in Table 5.2. For the PCA model, when the color difference between the measurement of a sample and the prediction of the model is assessed, the evaluated sample is the *testing* sample and all other samples of the same material are the *training* set, from which the model is constructed.

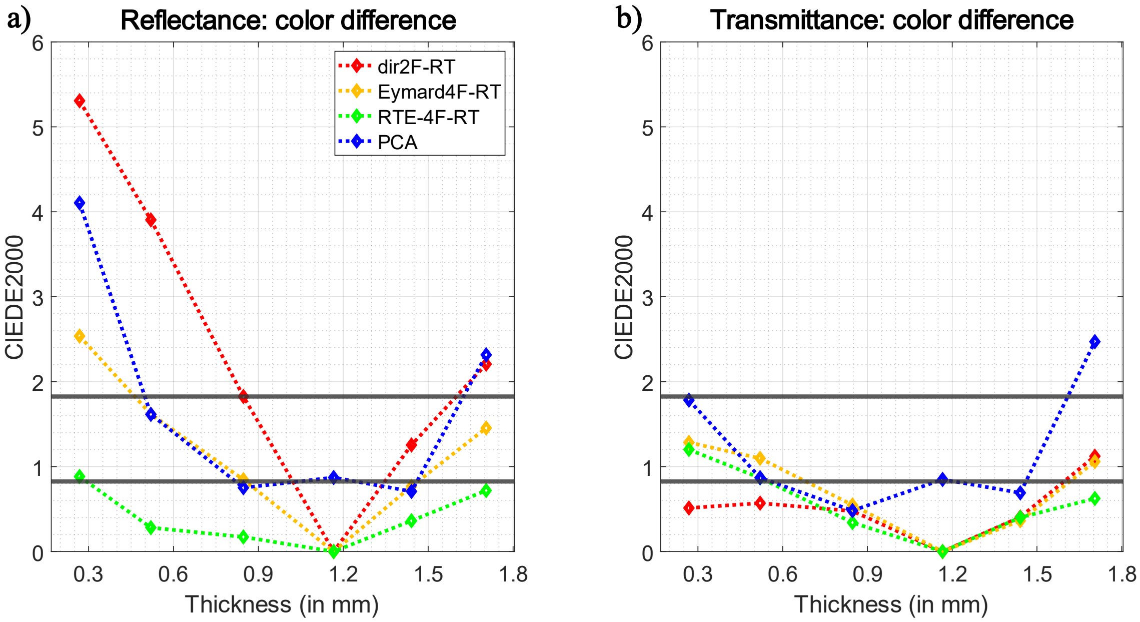

Figure 5.10: Equivalent color difference metric expressing the deviation between a) the measured spectral reflectance factors and b) transmittance factors of samples with various thickness made of the EsteliteUniversalFlow SuperLow composite shade A3 and the corresponding predictions given by the **dir2F-RT** model, the **Eymard4F-RT** model, the

RTE-4F-RT model and the **Maheu4F-RT** model. The sample with thickness 1.2 mm is used as calibration sample for optical models.

Table 5.2: CIEDE2000 equivalent color difference metric expressing the deviation between the measured spectral reflectance factors and transmittance factors of samples the corresponding predictions given by the dir2F-RT model, the Eymard4F-RT model, the RTE-4F-RT model and the PCA model. The sample with thickness 1.2 mm is used as calibration sample for the optical models.

	Reflectance factor				**Transmittance factor**			
	dir2F	Eymard4F	RTE-4F	PCA	dir2F	Eymard4F	RTE-4F	PCA
Mean CIEDE2000	2.12	1.05	0.65	1.26	0.84	0.83	0.82	1.94
95th percentile	4.79	2.86	1.93	4.49	2.36	2.01	2.11	6.46
% under AT	50.00	83.33	93.52	78.70	91.67	94.44	91.67	75.00
% under PT	18.52	47.22	71.30	54.63	56.48	51.85	62.04	57.41

In reflectance mode, the **PCA** model is more accurate than the **dir2F-RT** model but less accurate than the **Eymard4F-RT** and **RTE-4F-RT** models. However, the comparison is not completely fair, because in order to predict the reflectance and transmittance factors of the thinnest and thickest samples, the **PCA** algorithm has to extrapolate from the other samples whereas it is intended to work in interpolation mode. Therefore, Table 5.3 presents the same results but excluding extreme thicknesses for all models.

Table 5.3: CIEDE2000 equivalent color difference metric expressing the deviation between the measured spectral reflectance factors and transmittance factors of samples the corresponding predictions given by the dir2F-RT model, the Eymard4F-RT model, the RTE-4F-RT model and the PCA model. The sample with thickness 1.2 mm is used as calibration sample for the optical models. Samples with extreme thicknesses are excluded from the comparison.

	Reflectance factor				**Transmittance factor**			
	dir2F	Eymard4F	RTE-4F	PCA	dir2F	Eymard4F	RTE-4F	PCA
Mean CIEDE2000	1.57	0.72	0.48	0.61	0.63	0.63	0.61	0.79
95th percentile	4.01	2.04	1.35	1.46	1.59	1.25	1.60	2.09
% under AT	67.11	93.42	97.37	97.37	97.37	96.05	97.37	90.79
% under PT	26.32	63.16	82.89	73.68	72.37	67.11	73.68	72.37

The average prediction accuracy of the **PCA** model is significantly increased in both reflectance and transmittance modes, and it becomes more accurate than the **Eymard4F-RT** model. Nonetheless, the prediction accuracy of the **PCA** model remains slightly below that of the **RTE-**

4F-RT model. Further work is underway in the team in Granada (Spain) to improve the prediction accuracy of the **PCA** model.

This numerical approach has several advantages and disadvantages compared to our optical approach. The main advantage is the computation time, which is almost instantaneous, while several minutes are required for the **RTE-4F-RT** model. The implementation is also a lot easier. Finally, it only requires reflectance factor measurements whereas four-flux models require 4 measurement configurations, some of which might be impossible to some spectrophotometers. However, it requires the fabrication of several samples to train the model, while optical models require only a single sample. Also, optical models' utility is two-fold since they enable to extract optical properties for a material, and also to predict the reflectance and transmittance factors. Overall, both approaches show rather good predictive accuracy and could be used for different purposed depending on the user's goal and measuring instruments.

Chapter 6.
Extending the models to fluorescence

Despite a good prediction performance, the accuracy of optical models is undermined by fluorescence since dental materials are fluorescent even in the visible spectrum of light and the light emitted by fluorescence is mixed with the reflection and transmission of light. In this case, fluorescence effects are incorporated into the spectral values of optical parameters of the models even though they are not taken into account explicitly: they are falsely interpreted as absorption or scattering. Thus, it would be possible to improve the accuracy of spectral reflectance/transmittance prediction models for slices of dental biomaterials by accounting for the fluorescence phenomenon. Such a method would also enable to predict the color of samples of dental resin composites observed under illuminants with more of less UV light.

Therefore, the aim of this study is to predict the spectral fluorescence emission of slices of a flowable resin composite with respect to their thickness. Our research hypotheses are that the spectral exitance of a slice of material, different at the two sides of the slice ("reflection" and "transmission" modes), that it varies according to the excitation wavelength and that its amplitude varies with respect to the thickness of the sample. To verify these hypotheses, we use a set of samples of varying thickness of one dental resin composite and measure the spectral fluorescence exitance of each sample under a near UV light source in reflectance mode and in transmittance mode. A two-flux model extended to fluorescence [228] is used to predict the amplitude of the peak of fluorescence for each measurement. This model requires coefficients describing the absorption and scattering of light for both the excitation wavelengths (near-UV) and emission wavelengths, which will be determined be means of the **dir2F-RT** model calibrated from reflectance and transmittance factor measurements performed with the Color i7 spectrophotometer under white light.

6.1 Fluorescence measurements

The influence of fluorescence under a broadband light source can be assessed with the Color i7 spectrophotometer, by comparing measurements performed in UV-calibrated and UV-excluded modes. Figure 6.1a) shows the reflectance factor of samples of the Estelite Universal Flow Medium A2 material measured in both modes as well as their transmittance factor. The difference between UV-calibrated and UV-excluded measurements is shown in Figure 6.1b) for each sample and provides a rough idea of the fluorescence contribution to reflectance and transmittance factors under a broadband illuminant. The L*a*b* color coordinates for each measurement are calculated by using the color matching functions established with a 2° standard observer, the D65 power spectral distribution as illuminant [60] and a perfectly white diffuser (reflectance factor equal to 1) as reference for the chromatic adaptation. The L*a*b* color coordinates and CIEDE2000 color difference between UV-calibrated and UV-excluded measurements are given in Table 6.1.

Unfortunately, these measurements alone do not enable us to model fluorescence since we cannot know if the signal measured at one wavelength results from fluorescence emitted with an excitation wavelength λ_1 or λ_2, or results from reflection.

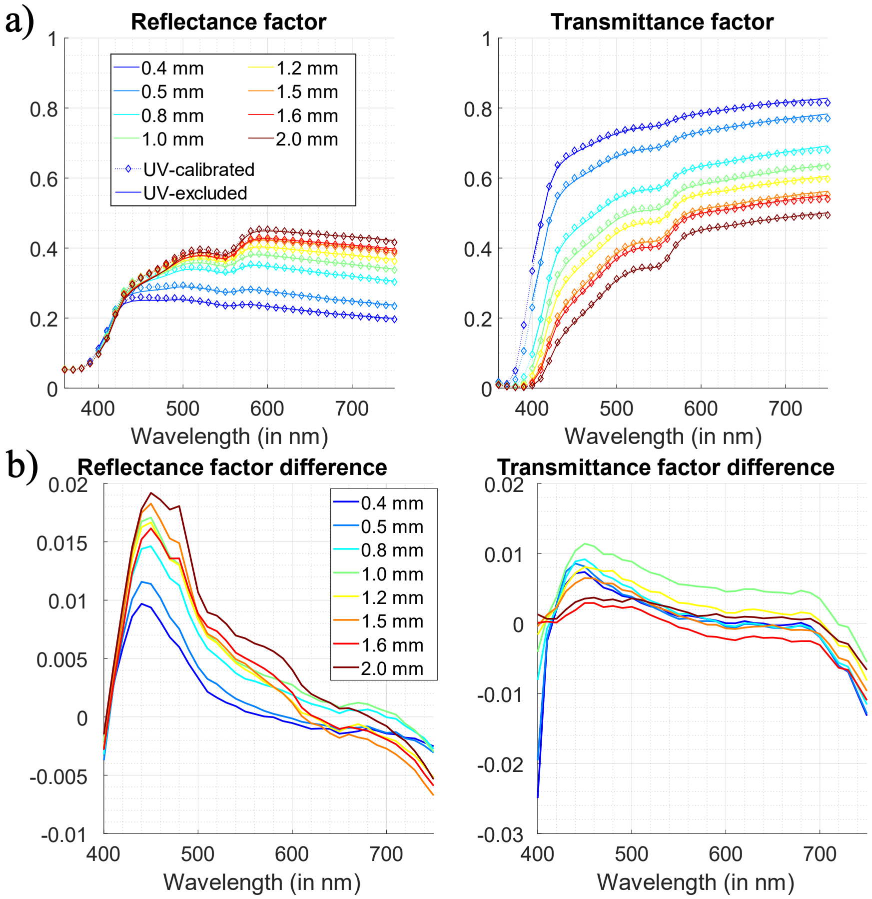

Figure 6.1: a) Spectral reflectance and transmittance factor of Estelite Universal Flow Medium A2 samples with specified thickness. b) Difference between measurements in the UV-calibrated and UV-excluded mode.

Table 6.1: L*a*b* color coordinates of samples measured with the Color i7 spectrophotometer in UV-included and UV-excluded modes and CIEDE2000 color difference between measurements in both modes.

Nominal thickness	UV-calibrated L*	a*	b*	UV-excluded L*	a*	b*	ΔE_{00}
0.4 mm	56.05	-1.57	-2.20	55.97	-1.74	-1.10	1.06
0.5 mm	59.89	-2.00	0.18	59.76	-2.15	1.36	1.13
0.8 mm	65.11	-2.14	5.15	64.81	-2.23	6.39	1.02
1.0 mm	66.94	-1.72	7.30	66.58	-1.81	8.72	1.08
1.2 mm	68.09	-1.55	9.46	67.78	-1.51	10.91	1.04
1.5 mm	69.00	-0.90	10.68	68.69	-0.83	12.30	1.11
1.6 mm	69.20	-0.83	11.40	68.84	-0.66	12.72	0.94
2.0 mm	70.28	-0.20	13.01	69.80	-0.10	14.57	1.04

In order to measure the spectral exitance of samples of the Estelite Universal Flow Medium A2 material caused by fluorescence alone, an optical bench was designed to measure it both on the illuminated side ("reflectance mode") and on the opposite side ("transmittance mode"), with monochromatic light sources (lasers at 380 nm and 405 nm). These measurement setups are presented in detail below, as well as the analysis of the measurements obtained.

The optical bench uses a 380 nm fiber injected laser diode source (LBX-375-200-HPE-PPA from Oxxius) with a diaphragm enabling to tune the size of the incident (excitation signal at 380 nm). The tunable output power of the laser was set very low to minimize non-linear effects. Samples were placed on a sample holder at approximately 15 cm from the laser. A fiber spectrophotometer (QEPro from OceanInsight with a round-to-linear fiber bundle PL200-2-UV-VIS from OceanInsight) was placed behind the sample at an approximately 15 cm distance in a 0°:0° geometry in transmittance mode and in a 0°:20° geometry in reflectance mode. A lens was used to control the measuring aperture of the spectrophotometer on the sample. The diaphragm on the laser source was set so that only a small spot hits the center of the sample, while the lens on the spectrophotometer was set so that it collects light emerging from the whole area of the sample. The experimental setup is similar to the setup presented in Figure 6.3 for measurements with a 405 nm light source. The integration time of the sensor was set to 60 seconds (the emittance of the samples being low with the selected irradiance of the samples). Each acquisition was performed 5 times and the average was calculated. Because of the high spectral resolution of the spectrophotometer (0.4 nm), a rolling average was then calculated for each measurement, which are shown in Figure 6.2a) while the peak of fluorescence with respect to the sample thickness is shown in Figure 6.2b).

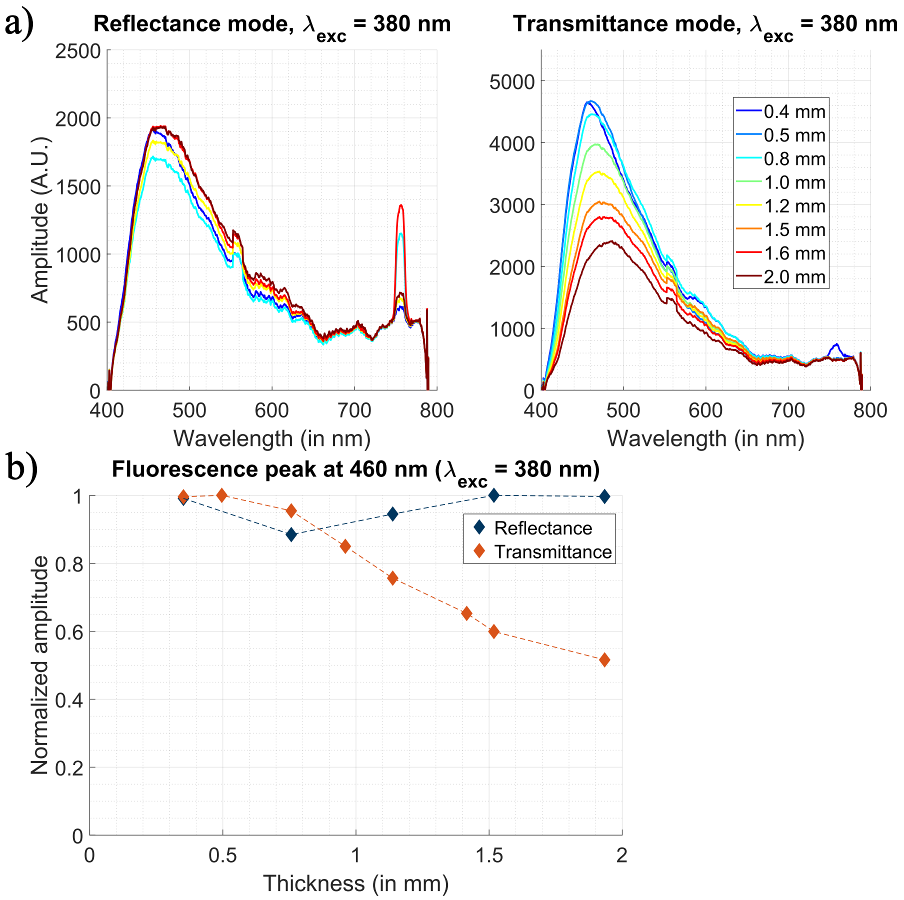

Figure 6.2: a) Fluorescence emission spectrum in reflectance and transmittance modes of the samples with different thicknesses under a 380 nm light source. A peak visible at 760 nm is the 2nd order emission of the laser and does not result from samples' fluorescence. b) Fluorescence peak in reflectance mode and transmittance mode with respect to sample thickness.

The fluorescence signal measured in reflectance mode is almost the same for all samples: the spectral shape is similar. We also observe that the amplitude is nearly constant for samples with thickness above 1.5 mm. It is probable that the excitation beam at 380 nm is totally attenuated across the thinnest sample (0.4 mm). Consequently, no more flux is emitted within thicker samples and the exitance at the side of the incident beam (reflectance mode) remains the same for all the samples. The evolution of the maximum of amplitude measured in reflectance mode is asymptotic. At the other side ("transmittance mode"), the exitance decreases if the sample thickness increases because the light emitted in the first 0.4 mm of the sample must cross the rest of the sample's volume where it is attenuated by absorption and backscattering.

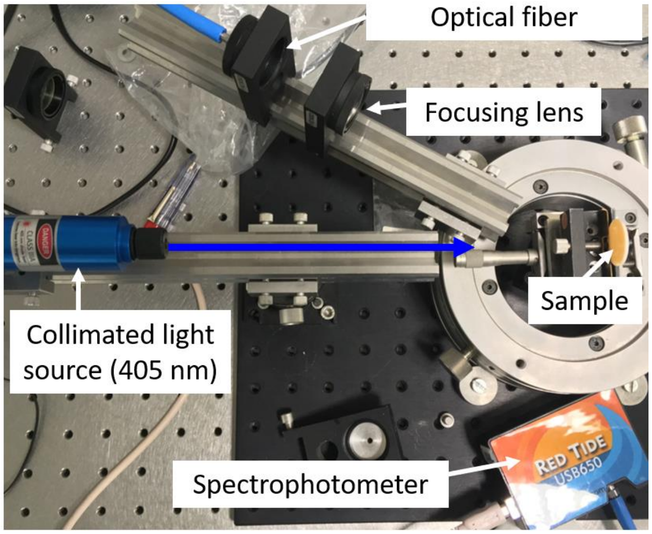

Figure 6.3: Optical setup used to measure the fluorescence spectrum in reflectance and transmittance modes. The optical fiber collects light exiting from the samples and directs it to the spectrophotometer. A rotatable arm enables to easily switch between the reflectance and transmittance configurations.

An optical setup similar to the one used for illuminating the samples at 380 nm was made to illuminate them at 405 nm and record the resulted fluorescence signal. The setup is presented in Figure 6.3. The light source used for excitation is a laser diode emitting light at 405 nm commercialized by DidaConcept with a focusing lens enabling to focus the laser spot on the center of the sample. The fiber spectrophotometer used is a Red Tide USB650 commercialized by OceanOptics. A focusing lens ensures that the spectrophotometer captures light emerging from the whole surface of the sample. The measuring geometry was 0°:25° in reflectance mode and 0°:0° in transmittance mode.

The integration time for measurements was ranging from 400 ms to 500 ms depending on the thickness of the sample, and each measurement was the average of 10 acquisitions. Measurements are presented in Figure 6.4a). This measuring process was repeated 5 times in order to evaluate the repeatability of measurements and the average of the fluorescence peak with respect to the sample thickness is presented in Figure 6.4b).

The amplitude of the fluorescence signal in reflectance mode varies with the sample thickness; it increases before reaching a plateau for samples thicker than 1.0 mm. This hints that the absorptance of the material at 405 nm might be lower than at 380 nm, and light travels deeper within the layer, until about 1 mm. Therefore, the fluorescence signal measured in reflectance and transmittance modes increases from 0.4 to 1.0 mm as more fluorophores are excited and emit fluorescence. Beyond 1.0 mm, the excitation signal is totally absorbed and the signal in reflectance mode reaches a plateau while the signal in transmittance mode is attenuated by absorption and backscattering (as with an excitation signal at 380 nm).

For a given light source and an observation mode (reflectance or transmittance mode), the shape of the fluorescence signal is very similar with respect to the sample thickness. Small variations can be observed and are probably due to absorption and scattering of the fluorescence signal by the resin composite, which increases with the sample thickness. It is reasonable to assume that the shape of the curve is constant with respect to the sample thickness, at least in the range of thicknesses tested, and that it is therefore sufficient to predict the exitance at the wavelength where the spectrum is maximal (amplitude of the peak of fluorescence) to predict the whole spectral exitance in each mode. The peak of fluorescence is at 460 nm for an excitation light source at 380 nm, and at 495 nm for an excitation light source at 405 nm.

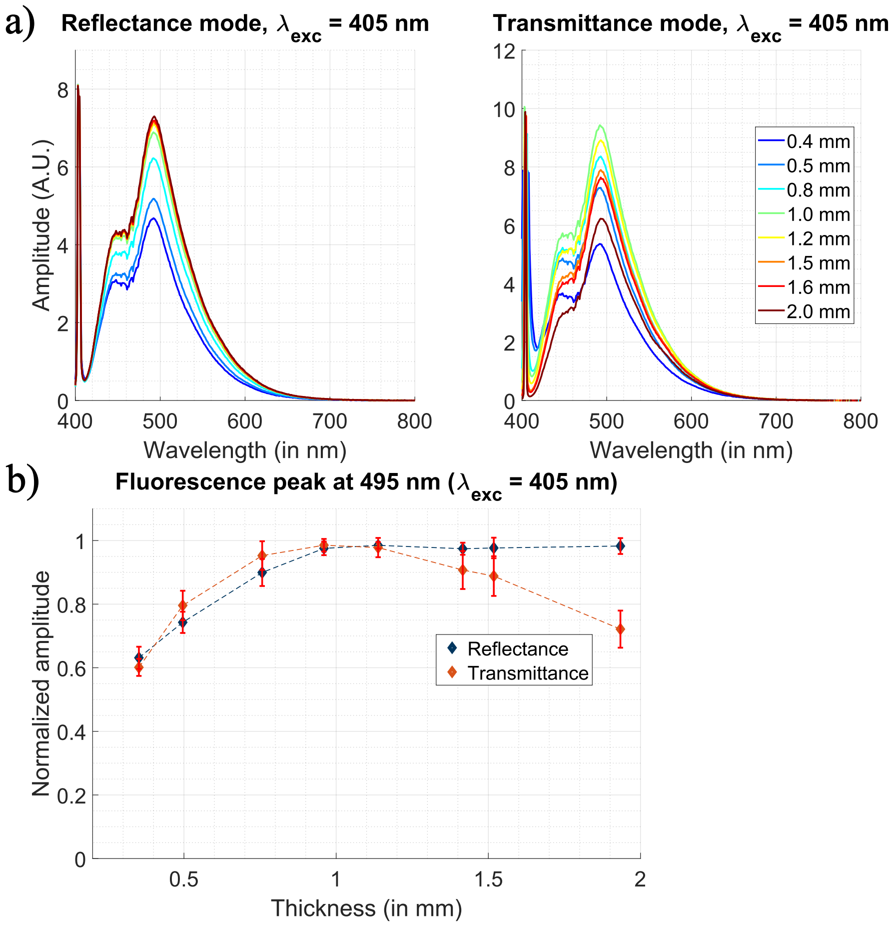

Figure 6.4: a) Fluorescence emission spectrum in reflectance and transmittance modes of samples under a 405 nm light source. b) Fluorescence peak in reflectance mode and transmittance mode with respect to sample thickness.

6.2 Two-flux model extended to fluorescence

In order to predict the spectral exitance of the samples for a given excitation wavelength, we implemented a two-flux model accounting for fluorescence proposed by Simonot *et al.* [228]. This model described the propagation of incident light at wavelength λ_A inside the diffusing layer according to the Kubelka-Munk model:

$$\begin{cases} \dfrac{dI_A}{dz} = -(K_A + S_A)I_A(z) + S_A J_A(z) \\ \dfrac{dJ_A}{dz} = (K_A + S_A)J_A(z) - S_A I_A(z) \end{cases} \tag{6.1}$$

where K_A refers to the absorption coefficient at the absorption (= excitation) wavelength, S_A the scattering coefficient at the absorption wavelength (= excitation), and subscript A refers to the excitation wavelength λ_A of the incident light.

Then, the model describes the propagation of the light emitted by fluorescence at wavelength λ_E at each depth z according to a second Kubelka-Munk model:

$$\begin{cases} \dfrac{dI_E}{dz} = -(K_E + S_E)I_E(z) + S_E J_E(z) + P(z) \\ \dfrac{dJ_E}{dz} = (K_E + S_E)J_E(z) - S_E I_E(z) - P(z) \end{cases} \tag{6.2}$$

where K_E refers to the absorption coefficient at the emission wavelength, S_E the scattering coefficient at the emission wavelength, subscript E refers to the emission wavelength λ_E, and $P(z)$ the contribution of luminescence at depth z. Therefore, the total flux absorbed by the material at depth z within an infinitesimal sublayer of thickness dz is $K_A(I_A+J_A)dz$. The luminescence emission in this sublayer is $\phi F K_A(I_A+J_A)dz$, with ϕ the luminescent quantum efficiency and F the intrinsic normalized spectral emission distribution. Since fluorescence emission is an isotropic phenomenon, the fluorescence emission is equally distributed in both forward and backward hemisphere. Thus, we have:

$$P(z) = \frac{1}{2}\phi F K_A[I_A(z) + J_A(z)] \tag{6.3}$$

In their article, Simonot *et al.* propose an analytical resolution of both systems of differential equations (6.1) and (6.2), enabling to derive the flux exiting the layer of thickness h at the illumination side ("reflectance mode"), denoted $J_E(z=0)$ and at the opposite side ("transmittance mode") denoted $I_E(z=h)$ at wavelength λ_E.

$$J_E(z=0) = \frac{C_1}{\alpha_A^2 - \alpha_E^2} + \frac{C_2}{\alpha_A^2 - \alpha_E^2} + C_3(1+\beta_E) + C_4(1-\beta_E) \tag{6.4}$$

$$I_E(z=h)=\frac{D_1}{\alpha_A^2-\alpha_E^2}e^{\alpha_A h}+\frac{D_2}{\alpha_A^2-\alpha_E^2}e^{-\alpha_A h}+C_3(1-\beta_E)e^{\alpha_A h}+C_4(1+\beta_E)e^{-\alpha_A h} \tag{6.5}$$

with

$$\begin{cases}\alpha_i=\sqrt{K_i(K_i+2S_i)}\\ \beta_i=\sqrt{K_i/(K_i+2S_i)}\end{cases} \tag{6.6}$$

$$\begin{cases}B_{1i}=1+\beta_i-R_g(1-\beta_i)\\ B_{2i}=1-\beta_i-R_g(1+\beta_i)\end{cases} \tag{6.7}$$

$$\begin{cases}A_1=\dfrac{-B_{2A}e^{-\alpha_A h}}{(1+\beta_A)B_{1A}e^{\alpha_A h}-(1-\beta_A)B_{2A}e^{-\alpha_A h}}I_0\\ A_2=\dfrac{B_{1A}e^{\alpha_A h}}{(1+\beta_A)B_{1A}e^{\alpha_A h}-(1-\beta_A)B_{2A}e^{-\alpha_A h}}I_0\end{cases} \tag{6.8}$$

$$\begin{cases}C_1=-\phi F K_A A_1(\alpha_E/\beta_E+\alpha_A)\\ C_2=-\phi F K_A A_2(\alpha_E/\beta_E-\alpha_A)\end{cases} \tag{6.9}$$

$$\begin{cases}D_1=-\phi F K_A A_1(\alpha_E/\beta_E-\alpha_A)\\ D_2=-\phi F K_A A_2(\alpha_E/\beta_E+\alpha_A)\end{cases} \tag{6.10}$$

$$\begin{cases}C_3=\dfrac{1}{\alpha_A^2-\alpha_E^2}\dfrac{B_{2E}(D_1+D_2)e^{-\alpha_E h}-(1+\beta_E)[(C_1-R_{gE}D_1)e^{\alpha_A h}+(C_2-R_{gE}D_2)e^{-\alpha_A h}]}{(1+\beta_E)B_{1E}e^{\alpha_E h}-(1-\beta_E)B_{2E}e^{-\alpha_E h}}\\ C_4=-\dfrac{1}{1+\beta_E}\left(\dfrac{D_1+D_2}{\alpha_A^2-\alpha_E^2}+C_3(1-\beta_E)\right)\end{cases} \tag{6.11}$$

where subscript *i* refers to either *A* or *E*, R_g the reflectance of the background, which is set to 0 in our case since samples are measured without a background.

In practice, reflections and transmissions occur at the interfaces of the layer and must be accounted for by applying the extended Saunderson correction given in formulae (3.6) and (3.7), and recalled here:

$$R=r_e+T_{in}T_{out}\frac{\rho-r_i(\rho^2-\tau^2)}{(1-r_i\rho)^2-r_i^2\tau^2} \tag{6.12}$$

$$T=\frac{T_{in}T_{out}\tau}{(1-r_i\rho)^2-r_i^2\tau^2} \tag{6.13}$$

where ρ is replaced with $J_E(z=h)$ and τ is replaced with $I_E(z=0)$. We assume that n = 1.5 in this chapter.

The flux propagation considered by this model are represented in Figure 6.5.

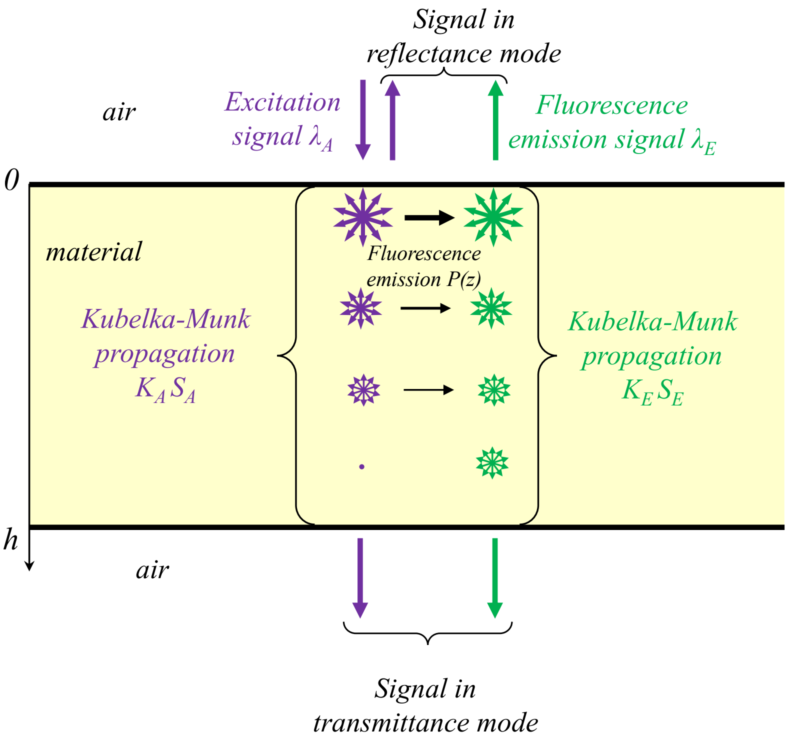

Figure 6.5: Flux transfers accounted for in the fluorescence two-flux model by Simonot *et al.* [228].

The model depends on the parameters K_A, S_A, K_E, S_E, as well as F, the intrinsic normalized fluorescence spectral distribution, and ϕ, the luminescent quantum efficiency of the medium.

The six parameters listed above of the two-flux model extended to fluorescence are unknown. In the general case, the reflectance and transmittance factors are measured using a spectral broadband illumination, as it is the case with the Color i7 spectrophotometer, preventing to distinguish excitation signals from fluorescence emission signals. Therefore, the two-flux model extended to fluorescence can only be used when the wavelength of the excitation signal does not overlap with wavelengths of the emission signal, as is the case for our optical benches used for measuring the fluorescence emission with an incident signal at 380 nm or 405 nm.

In the latter case, the absorption (K_A) and scattering (S_A) parameters for the excitation signal can be extracted from reflectance and transmittance factor measurements performed with a spectrophotometer using the **dir2F-RT** model, as described in section 3.4. As we have seen thin samples of dental materials are weakly scattering and thus the angular distribution of light cannot be assumed to be isotropic. We considered this value of 0.04 for the extraction of K_A, S_A, K_E and S_E parameters, assuming that the incident light is almost not scattered. However, fluorescence emission being isotropic, it is relevant to consider r_i = 60% in the two-flux model extended for fluorescence in order to predict the amplitude of the fluorescence peak.

In the case where the wavelength of the excitation signal is 380 nm, UV-included measurements must be used to extract the K_A and S_A parameters, as the UV filter blocks light below 400 nm. However, for the excitation signal of 405 nm, UV-excluded measurements must be used to extract the K_A and S_A parameters. Indeed, the fluorescence emission signal resulting from an excitation signal at 380 nm is not negligible at 405 nm. Therefore, using UV-included measurements would cause K_A and S_A parameters extracted at 405 nm to incorporate some fluorescence signal resulting from excitation at lower wavelengths. Furthermore, it is highly likely that the samples investigated are fluorescent at 360 nm, which means that a fraction of K_A(380 nm) and S_A(380 nm) incorporates fluorescence, which is a limitation of our approach.

The absorption and scattering parameters for the fluorescence signal, namely K_E and S_E, can be derived from measurements performed with a spectrophotometer with a UV-excluded mode. Ideally, these parameters should be extracted from measurements in which the fluorescence phenomenon is absent, but this could not be done with the dental resin composite under study as it is fluorescent even at wavelengths longer than 420 nm. This approximation is mitigated by the fact that intensity of the fluorescence signal is much lower than the intensity of the reflected or transmitted signal. Alternatively, a spectrophotometer with dual monochromators should be used instead of the Color i7, but none was available to us.

The normalized fluorescence spectral distribution F and the luminescent quantum efficiency ϕ of the medium are unknown in the general case. However, when the fluorescence peak signal is considered, F is equal to 1, which leaves only ϕ to be fitted numerically.

6.3 Prediction of the amplitude of the fluorescence spectrum

Let us compare the exitances measured with our setup and the ones predicted by the two-flux model extended to fluorescence at the wavelength corresponding to the peak of fluorescence: 460 nm for an excitation at 380 nm and 495 nm for an excitation at 405 nm.

For the propagation of the excitation light beam, the coefficients K_A(380 nm) and S_A(380 nm) are extracted from UV-included reflectance and transmittance factor measurements of the sample with thickness 1.2 mm (calibration sample) made with the Color i7, by means of an inverse two-flux model considering r_i = 4% in the Saunderson correction (**dir2F-RT** model). K_A(405 nm), S_A(405 nm), K_E(460 nm), S_E(460 nm), K_E(495 nm) and S_E(495 nm) are extracted similarly, but from UV-excluded measurements. The normalized fluorescence emission spectrum F reaches its highest value for the fluorescence peak (460 nm under an incident light at 380 nm and 495 nm under an incident light at 405 nm). At this wavelength, we therefore assume that its value is 1. The luminescent quantum efficiency ϕ(460 nm) [resp. ϕ(495 nm)] is unknown and is therefore fitted to the fluorescence peak of measurements of other samples in reflectance mode and in transmittance mode with an excitation signal at 380 nm (resp. 405 nm).

The two-flux model extended to fluorescence is used to predict the fluorescence emission in reflectance and transmittance modes for thicknesses between 0.2 mm and 2.0 mm. According to the method described above, we find K_A(380 nm) = 4.6 mm^{-1}, S_A(380 nm) = 0.2 mm^{-1}, K_E(460 nm) = 0.4 mm^{-1}, S_E(460 nm) = 0.6 mm^{-1} and ϕ(460 nm) = 0.8. Because of geometric and radiometric uncertainties in the measurements, the amplitude of the signals measured in reflectance mode are not comparable to the ones measured in transmittance mode. We therefore decided to represent them on a normalized scale, by setting the highest amplitude to 1 in each mode. The same normalization is applied to the predictions. The comparison between the measured and predicted amplitudes is shown in Figure 6.6.

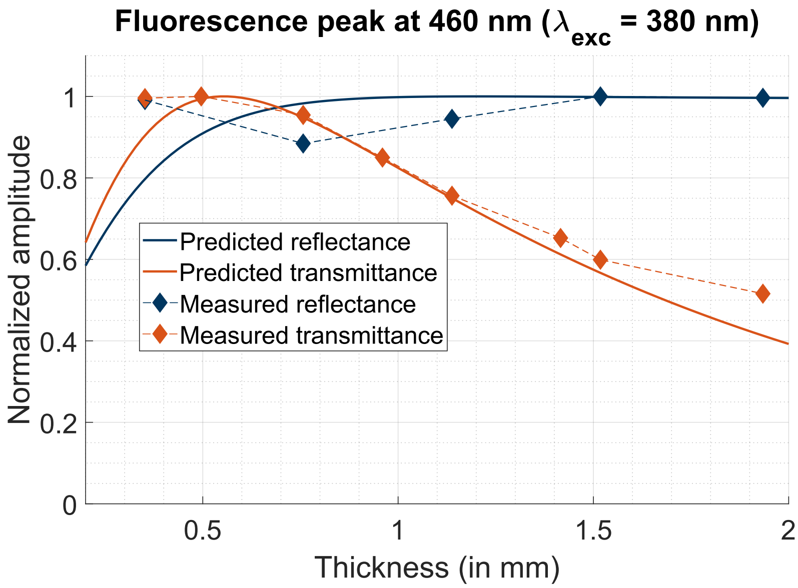

Figure 6.6: Maximum of fluorescence in reflectance and transmittance modes predicted by the two-flux extended model (solid lines) and measured (dashed lines). The excitation signal is at 380 nm and the peak of the emission signal is at 460 nm.

Within the limits of the measurement accuracy, the two-flux model extended to fluorescence seems fairly accurate in both reflectance and transmittance modes for predicting the fluorescence peak at 460 nm under a 380 nm excitation signal.

The two-flux model extended to fluorescence is used to predict the fluorescence emission in reflectance and in transmittance mode for thicknesses between 0.2 mm and 2.0 mm. According to the method described above, we find K_A(405 nm) = 2.0 mm^{-1}, S_A(405 nm) = 0.4 mm^{-1}, K_E(495 nm)

= 0.2 mm^{-1}, S_E(495 nm) = 0.6 mm^{-1} and ϕ(495 nm) = 0.5. The same normalized scaling is used as for the excitation at 380 nm, for both the measured and predicted amplitudes shown in Figure 6.7.

As for an excitation at 380 nm, the model predicts well the general evolution of the normalized amplitude as a function of the sample thickness with an excitation at 405 nm. This result is rather satisfying given the difficult experimental conditions (low irradiances, fluctuations in time of laser sources, position of the samples, etc.) The slight difference of slope may be due to a small estimation error of the absorption and scattering coefficients, since they are computed from a simple two-flux model that does not take into account fluorescence and has limitations (see Chapter 3).

There is thus floor for improvement, for example by improving the coefficient estimation method, or by using a monochromator for the illumination of the sample: for each incident wavelength λ_A, the component emitted by fluorescence (at wavelengths larger than λ_A) could be distinguished from the reflected/transmitted component at λ_A. Furthermore, the use of a spectrofluorometer would enable to extend this study to other wavelengths.

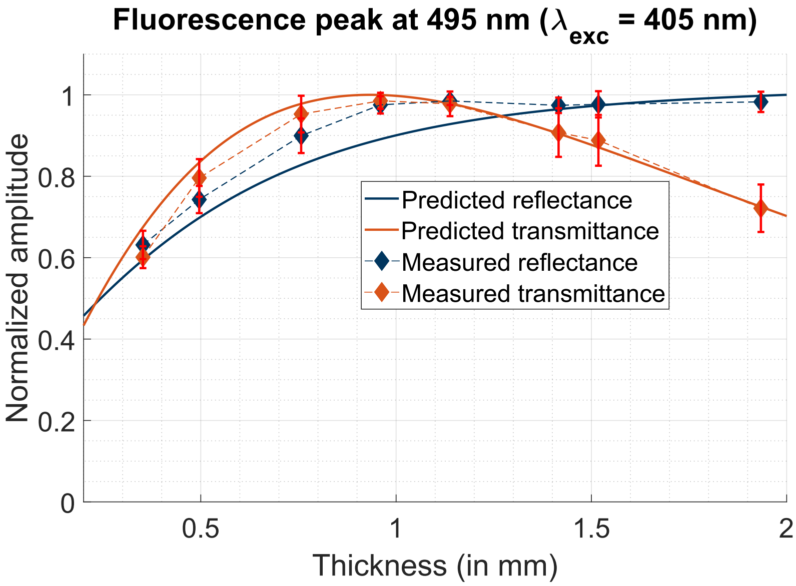

Figure 6.7: Maximum of fluorescence in reflectance (blue) and transmittance (orange) modes predicted by the two-flux extended model (solid lines) and measured (dashed lines). The excitation signal is at 405 nm and the peak of the emission signal is at 495 nm.

Despite measurements uncertainty and despite the known limitations of the two-flux model to capture light scattering in translucent, partially diffusing materials, this work shows that the two-flux model extended to fluorescence enables to predict quite well the amplitude of the fluorescence peak in reflectance and transmittance modes with respect to the thickness of the sample evaluated, for a given excitation wavelength.

As we observed that the shape of the fluorescence spectrum is mostly independent on the sample thickness, this simple and efficient method also enables to predict for a given excitation wavelength the whole fluorescence spectrum in reflectance and transmittance modes.

To the best of our knowledge, this work is the first attempt at predicting the fluorescence signal of dental materials. However, further work is needed to merge fluorescence prediction within more advanced reflectance and transmittance prediction models. This could be done by estimating the fluorescence contribution in the measurements of the calibration sample and subtracting it, applying the optical model without fluorescence for predicting the reflectance and transmittance spectra of other samples, then adding the estimated fluorescence contribution for each sample of different thickness.

Chapter 7.
Conclusions

In the course of this thesis, phenomena affecting light propagation within translucent dental composite resin samples were highlighted. The effect of edge-loss and geometrical considerations on the measurement of the spectral reflectance and transmittance factors have been identified, helping to explain certain spectral deviations with respect to sample thickness. This has led to the development of a methodology to minimize their influence when measuring translucent samples. These crucial considerations must be kept in mind in order to correctly interpret the measurements made and might be the source of inaccuracies in handheld devices intended to measure the color of teeth.

Numerous samples made from different dental resins were fabricated and measured using different measurement devices. Firstly, a spectrophotometer was used to measure the reflectance and transmittance factors of the samples, and their reflectance factors on black and on white background. These measurements enable to study the visual properties of the samples and use optical models for color prediction. Measurements were performed with a commercially available instrument, meeting the highest standards of color measurement laid down by the CIE, and easily usable by specialists and non-specialists alike. In addition, fluorescence measurements were performed on specific samples to further analyze light-matter interactions in dental resin composites.

State-of-the-art two-flux and four-flux models, describing light propagation in a flat layer of scattering material using simplifying assumptions compatible with the chosen measuring devices, were implemented and their ability to predict the spectral reflectance and transmittance factors of dental resin samples was investigated. Accurate prediction of these spectra enables, thank to colorimetry, to extrapolate the color of the sample as perceived by an observer. In addition to the state-of-the-art models, improvements dedicated to translucent materials have been proposed, based on a critical analysis of the angular distribution of light at the interfaces of the material's upper and lower interfaces with air. Among these models, the **RTE-4F-RT** model enables accurate prediction of the reflectance spectrum of the samples evaluated, with color differences below the acceptability threshold in almost all cases, and even below the perceptibility threshold in most cases. These optical models have also been compared with a numerical approach recently published in the state of the art and show interesting performances.

The two-flux models were tested in a configuration where two samples are superimposed, thus creating layered samples, which reproduces a clinical situation very common in dental practice. The satisfying prediction accuracy of all two-flux models tested alike confirmed observations already made in several studies in the dental field and showed that the considerations of optical models mentioned above are less important in the case of thick layered samples. Further work is needed to extend all models to the prediction of spectral reflectance and transmittance factors of layered samples of two or more materials. In addition, a two-flux model was tested to predict the amplitude of the fluorescence spectrum with respect to sample thickness, paving the way for a full integration of fluorescence in spectral reflectance prediction models.

The four-flux and two-flux models developed where applied on a wide array of dental materials of different shade and their predictive performances were assessed. However, it remains necessary to study the performance of these models on different types of dental materials, as the wide variability in their composition can impact the predictive performance of the models. This is particularly apparent between the different resins we tested in this work. In addition, it will be necessary to study the accuracy of models for geometric shapes more complex than flat layers, by studying samples of a shape closer than that of a tooth. This could be done using a visual rendering software and would enable to better control the color of dental restoration, even under various illuminants such as LED or other artificial lightings, possibly including UV light.

Moreover, the optical models developed in this thesis could readily be used by material manufacturers in order to control the optical properties of their material. The next step would be to identify the optical properties of single fillers and pigments of the dental resin and identify mixing laws to predict the optical properties of a dental resin composite with respect to its composition. This would enable material manufacturers to achieve more easily specific visual properties with new materials.

Appendix A.
Colorimetric indices in dentistry

Translucency, whiteness and gloss are important aesthetic characteristics of the appearance of teeth; they contribute to the attractiveness of the smile and a poor reproduction may easily give the impression of a false tooth or result in discomfort for the patient.

Gloss is usually measured with a glossmeter [229,230], which sends a light beam at three different angles: 20°, 60° and 85° from the sample surface and measures the reflected intensity at 20°, 60° and 85° respectively. The value at each angle is compared to a reference gloss sample and a gloss-value is determined.

Translucency is assessed by measuring the reflectance factor of a material on a black and on a white background, denoted R_B and R_W respectively [231]. The sample must be in optical contact with the background. Then, translucency indices have been introduced to assess this optical property [232], firstly the TP_{ab} parameter, and then the TP_{00} parameter has been developed to better describe translucency.

$$TP_{ab} = [(L_B^* - L_W^*)^2 + (a_B^* - a_W^*)^2 + (b_B^* - b_W^*)^2]^{1/2} \tag{A.1}$$

$$TP_{00} = \left[\left(\frac{L'_B - L'_W}{K_L S_L}\right)^2 + \left(\frac{C'_B - C'_W}{K_C S_C}\right)^2 + \left(\frac{H'_B - H'_W}{K_H S_H}\right)^2 + R_T\left(\frac{C'_B - C'_W}{K_C S_C}\right)\left(\frac{H'_B - H'_W}{K_H S_H}\right)\right]^{1/2} \tag{A.2}$$

Whiteness is evaluated with a whiteness index. Several indices were developed [233-235]. The *WIC* index is recommended by the CIE and used in textile, paint and plastic, but is not efficient for dental materials. The *WIO*, the *W* and later the WI_D indices were specifically developed for teeth.

$$WIC = Y + 800(x_n - x) + 1700(y_n - y) \tag{A.3}$$

$$WIO = Y + 1075.0.12(x_n - x) + 145.516(y_n - y) \tag{A.4}$$

$$W = \sqrt{(100 - L^*)^2 + a^{*2} + b^{*2}} \tag{A.5}$$

$$WI_D = 0.511L^* - 2.24a^* - 1.100b^* \tag{A.6}$$

where x and y are the chromaticity coordinates of the sample and x_n and y_n the chromaticity coordinates of the white reference, Y the tristimulus value of the sample, and L^*, a^* and b^* the color coordinates of the sample.

The yellowness of teeth is also characterized by a dedicated yellowness index [236].

$$YIO = -Y - 851.716(x_n - x) - 436.962(y_n - y) \tag{A.7}$$

Opalescence is the property of a dental material to display blueish reflection at certain viewing angles. It is assessed by an opalescence parameter [46,237], calculated from L*a*b* color coordinates of a material obtained in reflectance mode (index $_R$) and transmittance mode (index $_T$).

$$OP = \left[(a_T^* - a_R^*)^2 + (b_T^* - b_R^*)^2 \right]^{1/2} \tag{A.8}$$

Another opalescence parameter based on reflectance factor of the material measured on a black and on a white background has also been used in [151].

$$OP = \left[(a_B^* - a_W^*)^2 + (b_B^* - b_W^*)^2 \right]^{1/2} \tag{A.9}$$

An interesting property of dental materials is their ability to mask the background on which they are applied. This is important for covering black or yellow stains, for example. This property is evaluated with the contrast ratio CR [238,239] with Y_B (resp. Y_W) the Y tristimulus value of the material measured on black background (resp. white background). $CR = 1$ corresponds to an opaque sample.

$$CR = \frac{Y_B}{Y_W} \tag{A.10}$$

Appendix B.

Flux Transfer matrix formalism for multilayers of diffusing materials

The flux transfer matrix formalism is a convenient method allowing to describe the light propagation through successive layers, for which each reflectance and transmittance are known. Combined with the Kubelka-Munk model or any other flux transfer model giving the reflectance and transmittance factors of a slice, it allows to predict the reflectance factor of any stack of layers of known thickness, absorption and scattering coefficients and refractive index. It is presented in detail in [156], and the main results are reported here.

Let us consider a non-symmetric layer for which the reflectance at the upper side is ρ_1, the reflectance at the lower side is ρ_1', the transmittance from upper side to lower side is τ_1, and the transmittance from lower side to upper side is τ_1', as described in Figure B.1.

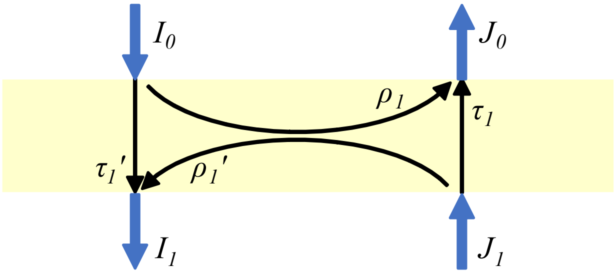

Figure B.1: Fluxes going towards or outwards a non-symmetric layer of scattering material.

The layer is illuminated from the top interface by the flux I_0 and from the bottom interface by the flux J_1. At first, we neglect the refraction occurring at the interface due to the shift of refractive index between the material and air. The flux outgoing from the upper interface is denoted J_0 while the flux outgoing from the lower interface is denoted I_1. Flux transfers can be described by the following equations:

$$\begin{cases} J_0 = \rho_1 I_0 + \tau_1' J_1 \\ I_1 = \rho_1' J_1 + \tau_1 I_0 \end{cases} \tag{B.1}$$

which can also be written:

$$\begin{cases} \rho_1 I_0 - J_0 = -\tau_1' J_1 \\ \tau_1 I_0 = I_1 + \rho_1' J_1 \end{cases} \tag{B.2}$$

which can be written as a vector equation:

$$\begin{pmatrix} \rho_1 & -1 \\ \tau_1 & 0 \end{pmatrix} \begin{pmatrix} I_0 \\ J_0 \end{pmatrix} = \begin{pmatrix} 0 & -\tau_1' \\ 1 & -\rho_1 \end{pmatrix} \begin{pmatrix} I_1 \\ J_1 \end{pmatrix} \tag{B.3}$$

Provided that the transmittance τ_1 of the layer is not zero, we can write:

$$\begin{pmatrix} I_0 \\ J_0 \end{pmatrix} = M_1 \begin{pmatrix} I_1 \\ J_1 \end{pmatrix} \tag{B.4}$$

with:

$$M_1 = \frac{1}{\tau_1} \begin{pmatrix} 1 & -\rho_1' \\ \rho_1 & \tau_1 \tau_1' - \rho_1' \rho_1 \end{pmatrix} \tag{B.5}$$

where M_1 is the flux transfer matrix of the layer of scattering material 1.

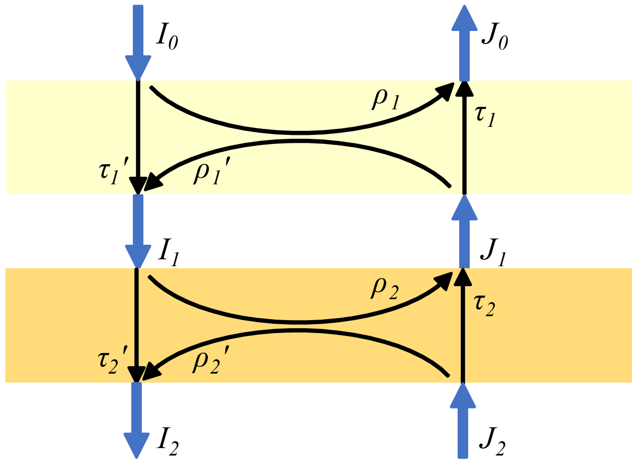

Figure B.2: Fluxes going towards or outwards a stack of two non-symmetric layers of scattering materials.

In the case of multilayers, as described in Figure B.2, the propagation of light can be described by formula (B.6).

$$\begin{pmatrix} I_0 \\ J_0 \end{pmatrix} = M_1 M_2 \begin{pmatrix} I_2 \\ J_2 \end{pmatrix} \tag{B.6}$$

with $M_1 = \frac{1}{\tau_1}\begin{pmatrix} 1 & -\rho_1' \\ \rho_1 & \tau_1\tau_1' - \rho_1'\rho_1 \end{pmatrix}$ and $M_2 = \frac{1}{\tau_2}\begin{pmatrix} 1 & -\rho_2' \\ \rho_2 & \tau_2\tau_2' - \rho_2'\rho_2 \end{pmatrix}$, where *M1* (resp. *M2*) is the flux transfer matrix of the layer of scattering material 1 (resp. 2).

Similarly, flux transfers at interfaces can be described by transfer matrices, such that the case presented in Figure B.3 is described by formula (B.7).

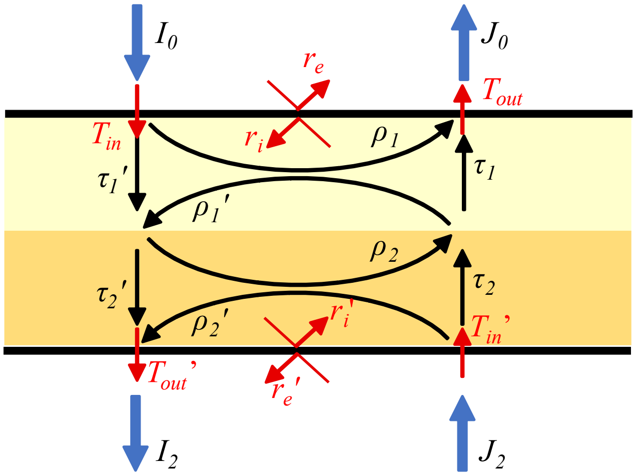

Figure B.3: Fluxes going towards or outwards a stack of two non-symmetric layers of scattering materials, accounting for air-material interfaces.

$$\begin{pmatrix} I_0 \\ J_0 \end{pmatrix} = M_{i-top} M_1 M_2 M_{i\_bottom} \begin{pmatrix} I_2 \\ J_2 \end{pmatrix} \tag{B.7}$$

with $M_{i-top} = \frac{1}{T_{in}}\begin{pmatrix} 1 & -r_i \\ r_e & T_{in}T_{out} - r_i r_e \end{pmatrix}$ and $M_{i-bottom} = \frac{1}{T_{in}'}\begin{pmatrix} 1 & -r_i' \\ r_e' & T_{in}'T_{out}' - r_i' r_e' \end{pmatrix}$,

where $M_{i\text{-}top}$ (resp. $M_{i\text{-}bottom}$) is the flux transfer matrix of the top (resp. bottom) interface.

The flux transfer matrix representing the whole pile can be written as M_{tot}, with:

$$M_{tot} = \begin{pmatrix} m_{11} & m_{12} \\ m_{21} & m_{22} \end{pmatrix} = M_{i-top} M_1 M_2 M_{i\_bottom} \tag{B.8}$$

Thus, it comes that:

$$\begin{cases} R = m_{21}/m_{11} \\ R' = -m_{12}/m_{11} \\ T = 1/m_{11} \\ T' = \det\left(M_{tot}\right)/m_{11} \end{cases} \tag{B.9}$$

Scientific contributions

International peer-reviewed journals

V. Duveiller, R. Clerc, J. Eymard, J.-P. Salomon, M. Hébert. "Performance of two-flux and four-flux models for predicting the spectral reflectance and transmittance factors of flowable dental resin composites", Dental Materials (2023).

A. Gautheron, R. Clerc, **V. Duveiller**, L. Simonot, B. Montcel, M. Hébert. "On the validity of two-flux and four-flux models for light scattering in translucent layers: angular distribution of internally reflected light at the interfaces", Optics Express (submitted).

J. Eymard, R. Clerc, **V. Duveiller**, B. Commault, M. Hébert. "Solar Energy Materials and Solar Cells Characterization of UV – Vis – NIR optical constants of encapsulant for accurate determination of absorption and backscattering losses in photovoltaics modules". Sol Energy Mater Sol Cells 2022, vol. 240.

International peer-reviewed conferences with proceedings

V. Duveiller, A. Gautheron, A. Cazier, L. Simonot, R. Clerc, J.-P. Salomon, M. Hébert. *"Estimation of the fluorescence emission spectrum of dental composite resin samples of varying thickness"*. Electronic Imaging 2023, Society for Imaging Science and Technology IS&T, San Francisco, United States, 2023.

F. Dailliez, M. Hébert, L. Simonot, L. Chagas, T. Fournel, **V. Duveiller**, A. Blayo. *"Impact of a coating layer on the appearance of various halftone patterns"*. Electronic Imaging 2023, Society for Imaging Science and Technology IS&T, San Francisco, United States, 2023.

V. Duveiller, E. Kim, M. Locquet, A. Gautheron, R. Clerc, J.P. Salomon, M. Hébert. *"Two-flux transfer model predicting the reflectance factor of translucent layered dental resin composites"*. Colour and Visual Computing Symposium, Gjøvik, Norway, 2022.

A. Gautheron, R. Clerc, **V. Duveiller**, L. Simonot, B. Montcel, M. Hébert. *"Light scattering in translucent layers: angular distribution and internal reflections at flat interfaces"*, Electronic Imaging 2022, Society for Imaging Science and Technology IS&T, online, 2022.

V. Duveiller, L. Gevaux, R. Clerc, J.-P. Salomon, M. Hébert. *"Reflectance and transmittance of flowable dental resin composite predicted by the two-flux model: on the importance of analyzing the effective measurement geometry"*. Color Imaging Conference CIC28, Society for Imaging Science and Technology IS&T, online, 2020.

National conferences, invited seminar and poster

V. Duveiller, J.-P. Salomon, R. Clerc, M. Hébert. *"Predicting the color of dental repairs"*. Poster presented at Manutech Sleight Science Event #7, Saint-Etienne, France, 2022.

V. Duveiller, L. Gevaux, J.-P. Salomon, R. Clerc, M. Hébert. *"Predicting the Reflectance and Transmittance of translucent dental resins"*. Invited Seminar at IS&T, online, 2021.

V. Duveiller, R. Clerc, J.-P. Salomon, M. Hébert, *"Predicting the appearance of flowable dental resin composites. How to predict their spectral reflectance and transmittance ?"*. Oral presentation at GDR APPAMAT, online, 2021.

V. Duveiller, L. Gevaux, R. Clerc, J.-P. Salomon, M. Hébert. *"Reflectance and transmittance of flowable dental resin composite predicted by the two-flux model: on the importance of analyzing the effective measurement geometry".* Oral presentation at Manutech Sleight Graduate Interdisciplinary Session #5, online, 2021.

References

[1] Raptis NV, Michalakis KX, Hirayama H. Optical behavior of current ceramic systems. Int J Periodontics Restorative Dent 2006;26:31–41. https://doi.org/10.11607/prd.00.0671.

[2] Hueb L, Oliveira DEM, Torres CP, Gomes-silva JM, Chinelatti MA, Carlos F, et al. Microstructure and Mineral Composition of Dental Enamel of Permanent and Deciduous Teeth. Microsc Res Tech 2010;73:572–7. https://doi.org/10.1002/jemt.20796.

[3] Fava M, Myaki SI, Ramos CJ, *et al.* Scanning electron microscopy observations of the prismless layer in fissures of erupted primary molars. *Pós Grad Rev Fac Odontol Sao José dos Campos*, 1999, vol. 2, p. 1-7.

[4] Ten Cate, Arnold Richard. *Oral histology: development, structure, and function*. St. Louis; Toronto: Mosby, 1998.

[5] Velinov Z, Papas M, Bradley D, Gotardo P, Mirdehghan P, Marschner S, et al. Appearance capture and modeling of human teeth. SIGGRAPH Asia 2018 Tech Pap SIGGRAPH Asia 2018 2018;37. https://doi.org/10.1145/3272127.3275098.

[6] Tjäderhane LEO, Carrilho MR, Breschi L, Tay FR, Pashley DH. Dentin basic structure and composition — an overview. Endod Top 2012;20:3–29.

[7] Bernick S, Nedelman C. Effect of aging on the human pulp. J Endod 1975;1:88–94.

[8] Bowen RL. Properties of a silica-reinforced polymer for dental restorations. The Journal of the American Dental Association 1963;*66*(1), 57-64.

[9] Downer MC, Azli NA, Bedi R, et al. How long do routine dental restorations last? A systematic review. Br Dental J 1999;187:432–9.

[10] Casagrande L, Seminario AT, Correa MB, et al. Longevity and associated risk factors in adhesive restorations of young permanent teeth after complete and selective caries removal: a retrospective study. Clin Oral Investig 2017;21(3): 847–55.

[11] da Veiga AM, Cunha AC, Ferreira DM, et al. Longevity of direct and indirect resin composite restorations in permanent posterior teeth: a systematic review and meta-analysis. J Dent 2016;54:1–12.

[12] Laske M, Opdam NJM, Bronkhorst EM, Braspenning JCC, Huysmans MC. Longevity of direct restorations in Dutch dental practices. Descriptive study out of a practice based research network. J Dent 2016;46:12–7.

[13] Beck F, Lettner S, Graf A, Bitriol B, Dumitrescu N, Bauer P, Moritz A, Schedle A. Survival of direct resin restorations in posterior teeth within a 19-year period (1996-2015): a meta-analysis of prospective studies. Dent Mater 2015;31:958–85.

[14] Pfeifer CS. Polymer-Based Direct Filling Materials. Dent Clin North Am 2017;61:733–50. https://doi.org/10.1016/j.cden.2017.06.002.

[15] Vaderhobli RM. Advances in dental materials. Dent Clin North Am 2011;55:619–25. https://doi.org/10.1016/j.cden.2011.02.015.

[16] Shaalan OO, Abou-Auf E, El Zoghby AF. Clinical evaluation of self-adhering flowable composite versus conventional flowable composite in conservative Class I cavities: Randomized controlled trial. J Cons Dent 2018;21:485.

[17] Elfakhri F, Alkahtani R, Li C, Khaliq J. Influence of filler characteristics on the performance of dental composites : A comprehensive review. Ceram Int 2022. https://doi.org/10.1016/j.ceramint.2022.06.314.

[18] Aydin Sevinç B, Hanley L. Antibacterial activity of dental composites containing zinc oxide nanoparticles, J. Biomed. Mater. Res. B Appl. Biomater 2010;94(1):22–31.

[19] Montoya C, Jain A, Mondono JJ, Correa S, Lelkes PI, Melo MA, Orego S. Multifunctional dental composite with piezoelectric nanofillers for combined antibacterial and mineralization effects. ACS Appl. Mater. Interfaces 2021;13(37):43868–43879.

[20] Tabatabaei MH, Nahavandi AM, Khorshidi S, Hashemikamangar SS. Fluorescence and opalescence of two dental composite resins. Eur. J. Dermatol 2019;13:527-534.

[21] Lahari K, Jaidka S, Somani R, Revelli A, Kumar D, Jaidka R. Recent advances in composite restorations. Int J Adv Res 2019;7:761-79.

[22] Wang Y, Zhu M, Zhu XX. Functional fillers for dental resin composites. Acta Biomater 2021;122:50–65. https://doi.org/10.1016/j.actbio.2020.12.001.

[23] Ferracane JL. Resin composite — State of the art. Dent Mater 2011;27:29–38. https://doi.org/10.1016/j.dental.2010.10.020.

[24] Floyd CJE, Dickens SH. Network structure of Bis-GMA- and UDMA-based resin systems. Dent Mater 2006;22(12):1143–1149.

[25] Gonçalves F, et al. Influence of BisGMA, TEGDMA, and BisEMA contents on viscosity, conversion, and flexural strength of experimental resins and composites. Eur J Oral Sci 2009;117(4):442–446

[26] Feilzer AJ, Dauvillier BS. Effect of TEGDMA/BisGMA ratio on stress development and viscoelastic properties of experimental Two-paste composites, J. Dent. Res. 2003;82(10):824–828.

[27] Gonçalves F, Pfeifer CCS, Stansbury JW, Newman SM, Braga RR. Influence of matrix composition on polymerization stress development of experimental composites, Dent. Mater. 2010;26(7):697–703.

[28] Amirouche-Korichi A, Mouzali F, Watts DC. Effects of monomer ratios and highly radiopaque fillers on degree of conversion and shrinkage-strain of dental resin composites, Dent. Mater. 2009;25(11):1411–1418.

[29] Peutzfeldt A. Resin composites in dentistry: the monomer systems, Eur. J. Oral Sci. 1997;105(2):97–116.

[30] Aguiar FHB, Braveiro ATB, Glaucia MBA, Lovadino JR. Hardness and diametral tensile strength of a hybrid composite resin polymerized with different modes and immersed in ethanol or distilled water media, Dent. Mater. 2005;21(12):1098–1103.

[31] Pecho OE, Ghinea R, Ionescu AM, De La Cruz Cardona J, Paravina RD, Del Mar Pérez M. Color and translucency of zirconia ceramics, human dentine and bovine dentine. J Dent 2012;40:34–40. https://doi.org/10.1016/j.jdent.2012.08.018.

[32] Ahn JS, Lee YK. Color distribution of a shade guide in the value, chroma, and hue scale. J Prosthet Dent 2008;100:18–28. https://doi.org/10.1016/S0022-3913(08)60129-8.

[33] Joiner A, Hopkinson I, Deng Y, Westland S. A review of tooth colour and whiteness. J Dent 2008;36:2–7. https://doi.org/10.1016/j.jdent.2008.02.001.

[34] Pop-Ciutrila IS, Dudea D, Eugenia Badea M, Moldovan M, Cîmpean SI, Ghinea R. Shade correspondence, color, and translucency differences between human dentine and a CAD/CAM hybrid ceramic system. J Esthet Restor Dent 2016;28:S46–55. https://doi.org/10.1111/jerd.12195.

[35] Kobayashi S, Nakajima M, Furusawa K, Tichy A, Hosaka K, Tagami J. Color adjustment potential of single-shade resin composite to various-shade human teeth: Effect of structural color phenomenon. Dent Mater J 2021;40:1033–40. https://doi.org/10.4012/dmj.2020-364.

[36] Durand LB, Ruiz-López J, Perez BG, Ionescu AM, Carrillo-Pérez F, Ghinea R, et al. Color, lightness, chroma, hue, and translucency adjustment potential of resin composites using CIEDE2000 color difference formula. J Esthet Restor Dent 2021;33:836–43. https://doi.org/10.1111/jerd.12689.

[37] Afrashtehfar KI, Assery MKA, Bryant SR. Aesthetic Parameters and Patient-Perspective Assessment Tools for Maxillary Anterior Single Implants. Int J Dent 2021. https://doi.org/10.1155/2021/6684028.

[38] Soldo M, Illeš D, Ćelić R, Zlatarić DK. Assessment of Color Parameters on Maxillary Right Central Incisors Using Spectrophotometer and RAW Mobile Photos in Different Light Conditions. Acta Stomatol Croat 2021;54:353–62. https://doi.org/10.15644/ASC54/4/2.

[39] Luo W, Westland S, Li Y, Joiner A. Investigation of hue effects in tooth whiteness perception. J Esthet Restor Dent 2021;33:1045–50. https://doi.org/10.1111/jerd.12801.

[40] Zhang X, Ma X, Liao M, Liu F, Wei Q, Shi Z, et al. Properties of Bis-Gma Free Bulk-Filled Resin Composite Based on High Refractive Index Monomer Bis-Efma. SSRN Electron J 2022;134:105372. https://doi.org/10.2139/ssrn.4101073.

[41] Nassar M. The Blending Effect of Single-Shade Composite with Different Shades of Conventional Resin Composites — An In Vitro Study 2022.

[42] Yu B, Ahn JS, Lim JI, Lee YK. Influence of TiO2 nanoparticles on the optical properties of resin composites. Dent Mater 2009;25:1142–7. https://doi.org/10.1016/j.dental.2009.03.012.

[43] Wee AG, Winkelmann DA, Gozalo DJ, Ito M, Johnston WM. Color and translucency of enamel in vital maxillary central incisors. J Prosthet Dent 2022:1–7. https://doi.org/10.1016/j.prosdent.2022.01.010.

[44] Shiraishi T, Wood DJ, Shinozaki N, Van Noort R. Optical properties of base dentin ceramics for all-ceramic restorations. Dent Mater 2011;27:165–72. https://doi.org/10.1016/j.dental.2010.10.001.

[45] Valizadeh S, Mahmoudi Nahavandi A, Daryadar M, Özcan M, Hashemikamangar SS. The effect of ceramic thickness on opalescence. Clin Exp Dent Res 2020;6:693–9. https://doi.org/10.1002/cre2.325.

[46] Lee YK, Lu H, Powers JM. Measurement of opalescence of resin composites. Dent Mater 2005;21:1068–74. https://doi.org/10.1016/j.dental.2005.03.015.

[47] Fidan M. Accelerated Aging Effects on Color Change, Translucency Parameter , and Surface Hardness of Resin Composites 2022;2022.

[48] El-Rashidy AA, Abdelraouf RM, Habib NA. Effect of two artificial aging protocols on color and gloss of single-shade versus multi-shade resin composites. BMC Oral Health 2022;22:321. https://doi.org/10.1186/s12903-022-02351-7.

[49] Borges AFS. Evaluation the Color Stability and Masking Ability of Darkened Teeth Treated With Two Kinds of CAD/CAD Veneer after Thermocycling. J Dent Heal Oral Res 2022;3:1–14. https://doi.org/10.46889/jdhor.2022.3206.

[50] Ozdemir ZM, Surmelioglu D. Effects of different bleaching application durations on enamel in terms of tooth color, microhardness, and surface roughness. Color Res Appl 2022;47:204–12. https://doi.org/10.1002/col.22710.

[51] Šimunović L, Blagec T, Vrankić A, Meštrović S. Color Stability of Orthodontic Ceramic Brackets and Adhesives in Potentially Staining Beverages—In Vitro Study. Dent J 2022;10:115. https://doi.org/10.3390/dj10070115.

[52] Melgosa M, Ruiz-López J, Li C, García PA, Della Bona A, Pérez MM. Color inconstancy of natural teeth measured under white light-emitting diode illuminants. Dent Mater 2020;36:1680–90. https://doi.org/10.1016/j.dental.2020.10.001.

[53] Ruiz-Lopez J, Melgosa M, Ghinea R, Tejada-casado M, Pop-Ciutrila IS, Pérez MM. Effect of White Light-Emitting Diode Illuminants Recommended by the CIE on Colors of Dental Ceramic Materials. Appl Sci 2023;13.

[54] Seghi RR, Johnston WM, O’brien WJ. Performance Assessment of Colorimetric Devices on Dental Porcelains. J Dent Res 1989;68:1755–9. https://doi.org/10.1177/00220345890680120701.

[55] Yaqoob A. Reliability in analysing the colour attributes of human teeth with tree different protocols: visual, spectrophotometric, and digital photographic method. Int J Early Child Spec Educ 2022;14:5225–9. https://doi.org/10.9756/INTJECSE/V14I5.635.

[56] Fontes de Braganca RM, Rafael RM, André Lui F-S. Color assessment of resin composite by using cellphone images compared with a spectrophotometer 2021;46.

[57] Rizzi A, Bonanomi C, Brazzoli S, Cerutti A, Kovacs-Vajna ZM. Assessing appearance in human dental colour space. Comput Methods Biomech Biomed Eng Imaging Vis 2018;6:59–67. https://doi.org/10.1080/21681163.2016.1164079.

[58] Pop-Ciutrila IS, Ghinea R, Colosi HA, Ruiz-López J, Perez MM, Paravina RD, et al. Color compatibility between dental structures and three different types of ceramic systems. BMC Oral Health 2021;21:1–10. https://doi.org/10.1186/s12903-021-01404-7.

[59] Pandey Vimal RL, Pandey-Vimal MUC. Ancient historical scripture and color vision. Color Res Appl 2007;32:332–3. https://doi.org/10.1002/col.20323.

[60] CIE Colorimetry, CIE technical report, 4th Ed. (2018).

[61] CIE 170-1 (2006).

[62] Jost S, Ngo M, Ferrero A, Poikonen T, Pulli T, Thorseth A, and Blattner P. Determination of illuminants representing typical white light emitting diodes sources. in CIE Midterm Meeting 2017, pp. 427–432, CIE-International Commission on Illumination, 2017.

[63] MacAdam DL. Visual Sensitivities to Color Differences in Daylight. JOSA 1942;32:247–74.

[64] MacAdam DL. Specification of Small Chromaticity Differences. JOSA 1943;33:18–26.

[65] Luo MR, Rigg B. Chromaticity Discrimination Ellipses for Surface Colours. Color Res Appl 1986;11:25–46.

[66] Clarke FJ, McDonald R, and Rigg B. Modification to the jpc79 colour– difference formula. Journal of the Society of Dyers and Colourists 1984;100(4):128–132, 1984.

[67] Luo MR, Rigg B. BFD (l:c) colour-difference formula Part 1 - Development of the formula. J Soc Dye Colour 1987;103:86-94.

[68] Mcdonald R, Smith KJ. CIE94 - a new colow-difference formula *. J Soc Dye Colour 1995;111:376–9.

[69] Luo MR, Cui G, Rigg B. The development of the CIE 2000 colour-difference formula: CIEDE2000. Color Res Appl 2001;26:340–50. https://doi.org/10.1002/col.1049.

[70] Sharma G, Wu W, Dalal EN. The CIEDE2000 color-difference formula: Implementation notes, supplementary test data, and mathematical observations. Color Res Appl 2005;30:21–30. https://doi.org/10.1002/col.20070.

[71] Douglas RD, Brewer JD. Acceptability of shade differences in metal ceramic crowns. J Prosthet Dent. 1998;79:254-2603

[72] Alghazali N, Burnside G, Moallem M, Smith P, Preston A, Jarad FD. Assessment of perceptibility and acceptability of color difference of denture teeth. J Dent. 2012;40(suppl 1):e10-e17

[73] Douglas RD, Steinhauer TJ, Wee AG. Intraoral determination of the tolerance of dentists for perceptibility and acceptability of shade mis- match. J Prosthet Dent. 2007;97:200-208.

[74] Paravina RD, Ghinea R, Herrera LJ, Bona AD, Igiel C, Linninger M, et al. Color difference thresholds in dentistry. J Esthet Restor Dent 2015;27:S1–9. https://doi.org/10.1111/jerd.12149.

[75] Da Silva JD, Park SE, Weber HP, et al. Clinical performance of a newly developed spectrophotometric system on tooth color reproduction. J Prosthet Dent. 2008;99:361-368

[76] Paravina RD, Pérez MM, Ghinea R. Acceptability and perceptibility thresholds in dentistry: A comprehensive review of clinical and research applications. J Esthet Restor Dent 2019;31:103–12. https://doi.org/10.1111/jerd.12465.

[77] Perez MDM, Ghinea R, Herrera LJ, Ionescu AM, Pomares H, Pulgar R, et al. Dental ceramics: A CIEDE2000 acceptability thresholds for lightness, chroma and hue differences. J Dent 2011;39:0–7. https://doi.org/10.1016/j.jdent.2011.09.007.

[78] Technical report(E): Dentistry - guidance on color measurements., tech. rep., Geneva, Switzerland: ISO, 2016. ISO/TR 28642:2016.

[79] Rizzi A. Colour after colorimetry. Color Technol 2021;137:22–8. https://doi.org/10.1111/cote.12496.

[80] Rizzi A. What if colorimetry does not work. IS&T Int Symp Electron Imaging Sci Technol 2021;2021:1–5. https://doi.org/10.2352/ISSN.2470-1173.2021.16.COLOR-323.

[81] Arteaga Y, Marchioni D, Courtier S, Boust C, Hardeberg JY. Appearance - based evaluation of varnish removal methods in gilded surfaces. Herit Sci 2023;11:1–22. https://doi.org/10.1186/s40494-023-00868-w.

[82] Gigilashvili D, Thomas JB, Hardeberg JY, Pedersen M. Behavioral investigation of visual appearance assessment. Final Progr Proc - IS T/SID Color Imaging Conf 2018;2018-November:294–9. https://doi.org/10.2352/issn.2169-2629.2018.26.294.

[83] Gigilashvili D, Thomas JB, Hardeberg JY, Pedersen M. Translucency perception: A review. J Vis 2021;21:1–41. https://doi.org/10.1167/jov.21.8.4.

[84] Gigilashvili D, Urban P, Thomas J-B, Pedersen M, Hardeberg JY. The Impact of Optical and Geometrical Thickness on Perceived Translucency Differences. J Percept Imaging 2022;5:000501-1-000501–18. https://doi.org/10.2352/j.percept.imaging.2022.5.000501.

[85] Kubelka P, Munk F. Ein Beitrag zur Optik der Farbanstriche. Zeitschrift für technische Physik 1931;12:593-601.

[86] Kubelka P. New contributions to the optics of intensely light-scattering materials. Part I. J Opt Soc Am 1948;38:448-57. https://doi.org/10.1364/JOSA.38.000448.

[87] Saunderson JL. Calculation of the Color of Pigmented Plastics. JOSA 1942;32:727–36.

[88] Spitzer D, Ten Bosch JJ. The absorption and scattering of light in bovine and human dental enamel. Calcif Tissue Res 1975;17:129–37. https://doi.org/10.1007/BF02547285.

[89] Miyagawa Y, Powers JM, O’Brien WJ. Optical Properties of Direct Restorative Materials. J Dent Res 1981;60:890–4. https://doi.org/10.1177/00220345810600050601.

[90] Cook WD, McAree DC. Optical properties of esthetic restorative materials and natural dentition. J Biomed Mater Res 1985;19:469–88. https://doi.org/10.1002/jbm.820190502.

[91] Ragain JC, Johnston WM. Accuracy of Kubelka-Munk reflectance theory applied to human dentin and enamel. J Dent Res 2001;80:449-52. https://doi.org/10.1177/00220345010800020901.

[92] Pop-Ciutrila IS, Ghinea R, Perez Gomez MDM, Colosi HA, Dudea D, Badea M. Dentine scattering, absorption, transmittance and light reflectivity in human incisors, canines and molars. J Dent 2015;43:1116-24. https://doi.org/10.1016/j.jdent.2015.06.011.

[93] Pecho OE, Ghinea R, Ionescu AM, Cardona JC, Della Bona A, Del Mar Pérez M. Optical behavior of dental zirconia and dentin analyzed by Kubelka-Munk theory. Dent Mater 2015;31:60–7. https://doi.org/10.1016/j.dental.2014.11.012.

[94] Battersby PD, Battersby SJ. ScienceDirect Measurements and modelling of the influence of dentine colour and enamel on tooth colour. J Dent 2015;43:373–81. https://doi.org/10.1016/j.jdent.2014.11.003.

[95] Spitzer D, ten Bosch JJ. Luminescence quantum yields of sound and carious dental enamel. Calcif Tissue Res 1977;24:249–51. https://doi.org/10.1007/BF02223324.

[96] O’Brien WJ, Johnston WM, Fanian F. Double-layer Color Effects in Porcelain Systems. J Dent Res 1985;64:940-3.

[97] Campbell PM, O’brien WJ, Johnston WM. Light Scattering and Gloss of an Experimental Quartz-filled Composite. J Dent Res 1986;65:892–4. https://doi.org/10.1177/00220345860650060501.

[98] Yoshimura HN, Chimanski A, Cesar PF. Systematic approach to preparing ceramic-glass composites with high translucency for dental restorations. Dent Mater 2015;31:1188-97. https://doi.org/10.1016/j.dental.2015.06.015.

[99] Pulgar R, Lucena C, Espinar C, Pecho OE, Ruiz-López J, Della Bona A, et al. Optical and colorimetric evaluation of a multi-color polymer-infiltrated ceramic-network material. Dent Mater 2019;35:e131-9. https://doi.org/10.1016/j.dental.2019.03.010.

[100] Schabbach LM, dos Santos BC, De Bortoli LS, Fredel MC, Henriques B. Application of Kubelka-Munk model on the optical characterization of translucent dental zirconia. Mater Chem Phys 2021;258. https://doi.org/10.1016/j.matchemphys.2020.123994.

[101] Ma T, Johnston WM, Koran A. The Color Accuracy of the Kubelka-Munk Theory for Various Colorants in Maxillofacial Prosthetic Material. J Dent Res 1987;66:1438-44. https://doi.org/10.1177/00220345870660090601.

[102] Taira M, Okazaki M, Takahashi J. Studies on optical properties of two commercial visible-light-cured composite resins by diffuse reflectance measurements. J Oral Rehabil 1999;26:329-37. https://doi.org/10.1046/j.1365-2842.1999.00378.x.

[103] Fernández-Oliveras A. Characterization of dental biomaterials by means of optical methods : PhD thesis. 2014.

[104] Fernández-Oliveras A, Rubiño M, Pérez MM. Scattering and absorption properties of biomaterials for dental restorative applications. J Eur Opt Soc 2013;8:13056–69. https://doi.org/10.2971/jeos.2013.13056.

[105] Fernández-Oliveras A, Pecho OE, Rubiño M, Pérez MM. Measurements of scattering anisotropy in dental tissue and zirconia ceramic. Biophotonics Photonic Solut Better Heal Care III 2012;8427:84272C. https://doi.org/10.1117/12.921229.

[106] Stübel H.: “Die Fluoreszenz tierischer Gewebe in ultraviolettem Licht,” *Arch Ges Physiol*, vol. 142, pp. 1-14, 1921

[107] Filho H, Maia L, Araujo M, Ruellas A. Influence of optical properties of esthetic brackets (color, translucence, and fluorescence) on visual perception. Am J Orthod Dentofac. Orthop. 2012;141:460–467. doi: 10.1016/j.ajodo.2011.10.026.

[108] Lu H, Lee YK, Villalta P, Powers J, Farcia-Godoy F. Influence of the amount of UV component in daylight simulator on the color of dental composite resins. J. Prosthet. Dent. 2006;96(5):322–327.

[109] Volpato CAM, Pereira MRC, Silva FS. Fluorescence of natural teeth and restorative materials, methods for analysis and quantification: A literature review. J. Esthet. Restor. Dent., 2018;30:397–407.

[110] Matsumoto H, Kitamura S. Applications of fluorescence microscopy to studies of dental hard tissue. Front. Med. Biol. Engng, 2001;10(4):269–284.

[111] Volpato CAM *et al.*. Assessment of zirconia fluorescence after treatment with immersion in liquids, glass infiltration and aging. Ceram. Int., 2021;47:27511–27523. doi: 10.1016/j.ceramint.2021.06.175.

[112] Reis R *et al.*. Evaluation of Fluorescence of Dental Composites Using Contrast Ratios to Adjacent Tooth Structure : A pilot study. J. Esthet. Restor. Dent., 2007;19(4):199–206. doi: 10.1111/j.1708-8240.2007.00100.x.

[113] Da Silva T, De Oliveira H, Severino D, Balducci I, Huhtala M, Gonçalves S. Direct Spectrometry : A New Alternative for Measuring the Fluorescence of Composite Resins and Dental Tissues. Oper. Dent., 2014;39(4):407–415. doi: 10.2341/12-464-L.

[114] Meller C, Klein C. Fluorescence of composite resins: A comparison among properties of commercial shades. Dent Mater J 2015;34(6):754–765. doi: 10.4012/dmj.2014-219.

[115] Gamborena I, Blatz MB. Fluorescence. Mimicking nature for ultimate esthetics in implant dentistry. Quintessence Dent Technol, 2011;34:7-24.

[116] Ilie N, Hickel R. Resin composite restorative materials. Aust Dent J 2011;56:59–66. https://doi.org/10.1111/j.1834-7819.2010.01296.x.

[117] Baroudi K, Rodrigues JC. Flowable resin composites: A systematic review and clinical considerations. J Clin Diagnostic Res 2015;9:ZE18–24. https://doi.org/10.7860/JCDR/2015/12294.6129.

[118] Shaalan OO, Abou-Auf E, El Zoghby AF. Clinical evaluation of flowabal resin composite versus conventional resin composite in carious and noncarious lesions : Systematic review and meta-analysis. J Conserv Dent 2017;20;6:380-385. doi: 10.4103/JCD.JCD_226_17.

[119] Dionysopoulos D, Gerasimidou O. Wear of contemporary dental composite resin restorations: a literature review. Restor Dent Endod 2021;46:1–13. https://doi.org/10.5395/rde.2021.46.e18.

[120] Goodacre CJ, Eugene Roberts W, Munoz CA. Noncarious cervical lesions: Morphology and progression, prevalence, etiology, pathophysiology, and clinical guidelines for restoration. J Prosthodont 2023;32:e1–18. https://doi.org/10.1111/jopr.13585.

[121] Haas K, Azhar G, Wood DJ, Moharamzadeh K, van Noort R. The effects of different opacifiers on the translucency of experimental dental composite resins. Dent Mater 2017;33:e310–6. https://doi.org/10.1016/j.dental.2017.04.026.

[122] ISO 4049. Dentistry – Polymer-based Restorative Materials, International Organization for Standardization, 2009.

[123] Johnston WM, Hesse NS, Davis BK, Seghi RR. Analysis of edge-losses in reflectance measurements of pigmented maxillofacial elastomer. J Dent Res 1996;75:752-60. https://doi.org/10.1177/00220345960750020401.

[124] Gevaux L, Simonot L, Clerc R, Gerardin M, Hébert M. Evaluating edge loss in the reflectance measurement of translucent materials. Appl Opt 2020;59:8939. https://doi.org/10.1364/ao.403694.

[125] Mikhail SS, Azer SS, Johnston WM. Accuracy of Kubelka-Munk reflectance theory for dental resin composite material. Dent Mater 2012;28:729-35. https://doi.org/10.1016/j.dental.2012.03.006.

[126] Kristiansen J, Sakai M, Da Silva JD, Gil M, Ishikawa-Nagai S. Assessment of a prototype computer colour matching system to reproduce natural tooth colour on ceramic restorations. J Dent 2011;39:e45-51. https://doi.org/10.1016/j.jdent.2011.11.009.

[127] Nogueira AD, Della Bona A. The effect of a coupling medium on color and translucency of CAD-CAM ceramics. J Dent 2013;41:e18–23. https://doi.org/10.1016/j.jdent.2013.02.005.

[128] Lionel Simonot. Radiometry of Wet Surfaces: When Water Matters. IOGS – Institut d'Optique graduate School Textbook, 2023.

[129] Tejada-Casado M, Ghinea R, Perez MM, Lübbe H, Pop-Ciutrila IS, Ruiz-López J, et al. Reflectance and color prediction of dental material monolithic samples with varying thickness. Dent Mater 2022;38:622-31. https://doi.org/10.1016/j.dental.2021.12.140.

[130] Tejada-Casado M, Ghinea R, Pérez MM, Cardona JC, Ionescu AM, Lübbe H, et al. Color prediction of layered dental resin composites with varying thickness. Dent Mater 2022;38:1261-70. https://doi.org/10.1016/j.dental.2022.06.004.

[131] Tejada-Casado M. Reflectance and Colorimetric Modelling of Multilayer Bodies of Translucent Dental Materials. PhD Dissertation, University of Granada, Spain, 2023.

[132] Tejada-Casado M, Ghinea R, Pérez MM, Ruiz-lópez J, Lübbe H, Herrera LJ. Development of Thickness-Dependent Predictive Methods for the Estimation of the CIE L*a*b* Color Coordinates of Monolithic and Layered Dental Resin Composites. Materials (Basel) 2023;16.

[133] Hersch RD, Hébert M. Review of Spectral Reflectance Models for Halftone Prints : Principles , Calibration , and Prediction Accuracy. Color Res Appl 2015;40:383–97. https://doi.org/10.1002/col.21907.

[134] Hersch RD, Brichon M, Bugnon T, Amrhyn P, Crété F, Mourad S, et al. Deducing ink thickness variations by a spectral prediction model. Color Res Appl 2009;34:432–42. https://doi.org/10.1002/col.20541.

[135] Deeb R, Muselet D, Hébert M, Trémeau A., van de Weijer J. 3D color charts for camera spectral sensitivity estimation. BVMC 2017.

[136] Chandrasekhar S. Radiative Transfer. New York: Dover Publications Inc; 1960.

[137] Ishimaru A. Wave propagation and scattering in random media. New York: Academic press; 1988, Vol. 2, pp. 336-393.

[138] Stamnes K, Tsay S, Wiscombe W, Jayaweera K. Numerically stable algorithm for discrete-ordinate-method radiative transfer in multiple scattering and emitting layered media. Applied Optics 1988;27:2502-9.

[139] Elias M, Elias G. New and fast calculation for incoherent multiple scattering. J Opt Soc Am A 2002;19:894-901.

[140] Prahl SA. Light transport in tissues. PhD dissertation, University of Texas, USA; 1988.

[141] Van de Hulst HC. Multiple Light Scattering. New York: Academic Press; 1980.

[142] Fang Q, Boas DA. Monte Carlo simulation of photon migration in 3D turbid media accelerated by graphics processing units. Opt Express 2009;17:20178-90.

[143] Spitzer D, Ten Bosch JJ. A simple method for determination of the reflection coefficient at the internal surfaces of turbid slabs. Opt Commun 1973;9:311–4. https://doi.org/10.1016/0030-4018(73)90315-5.

[144] Lee YK. Influence of scattering/absorption characteristics on the color of resin composites. Dent Mater 2007;23:124-31. https://doi.org/10.1016/j.dental.2006.01.007.

[145] Mikhail SS, Schricker SR, Azer SS, Brantley WA, Johnston WM. Optical characteristics of contemporary dental composite resin materials. J Dent 2013;41:771-8. https://doi.org/10.1016/j.jdent.2013.07.001.

[146] Carney MN, Johnston WM. Appearance Differences Between Lots and Brands of Similar Shade Designations of Dental Composite Resins. J Esthet Restor Dent 2017;29:E6-14. https://doi.org/10.1111/jerd.12263.

[147] Mikhail SS, Johnston WM. In vitro optical characterization of dental resin composite aged in darkness. Color Res Appl 2020;45:345-51. https://doi.org/10.1002/col.22464.

[148] Lucena C, Ruiz-López J, Pulgar R, Della Bona A, Pérez MM. Optical behavior of one-shaded resin-based composites. Dent Mater 2021;37:840-8. https://doi.org/10.1016/j.dental.2021.02.011.

[149] Gouveia D, Yilmaz B, Cevik P, Johnston WM. Using Kubelka-Munk reflectance theory to predict optimal pink composite thickness and shade with an opaqued PEEK background for a final gingival color : An in vitro study. Dent Mater 2022;38(9):1452–8. https://doi.org/10.1016/j.dental.2022.06.027.

[150] Perez MM, Hita-Iglesias C, Ghinea R, Yebra A, Pecho OE, Ionescu AM, et al. Optical properties of supra-nano spherical filled resin composites compared to nanofilled, nano-hybrid and micro-hybrid composites. Dent Mater J 2016;35(3):353–9. https://doi.org/10.4012/dmj.2015-126.

[151] Pecho OE, Ghinea R, Navarro do Amaral EAA, Cardona JC, Della Bona A, Pérez MM. Relevant optical properties for direct restorative materials. Dent Mater 2016;32(5):e105–12. https://doi.org/10.1016/j.dental.2016.02.008.

[152] Molenaar R, ten Bosch JJ, Zijp JR. Determination of Kubelka–Munk scattering and absorption coefficients by diffuse illumination. Appl Opt 1999;38(10):2068-77. https://doi.org/10.1364/ao.38.002068.

[153] Leyva Del Rio D, Johnston WM. Optical characteristics of experimental dental composite resin materials. J Dent 2022;118:103949. https://doi.org/10.1016/j.jdent.2022.103949.

[154] Nicomedus FE, Richmond JC, Hsia JJ, Ginsberg IW, Limperis T. Geometrical Considerations and Nomenclature for Reflectance. Natl Bur Stand 1977.

[155] CIE, Absolute methods for reflection measurements; CIE Technical Report (1979).

[156] Hébert M, Optical Models for Material Appearance, IOGS – Institut d'Optique Graduate School Textbook; 2022.

[157] Kubelka P. New contributions to the optics of intensely light-scattering materials. J Opt Soc Am 1954;44:330–5. https://doi.org/10.1364/JOSA.38.000448.

[158] Mikhail SS, Johnston WM. Confirmation of theoretical colour predictions for layering dental composite materials. J Dent 2014;42:419-24. https://doi.org/10.1016/j.jdent.2014.01.008.

[159] Wang J, Lin J, Gil M, Seliger A, Da Silva JD, Ishikawa-Nagai S. Assessing the accuracy of computer color matching with a new dental porcelain shade system. J Prosthet Dent 2014;111:247-53. https://doi.org/10.1016/j.prosdent.2013.07.008.

[160] Wee AG, Chen WY, Johnston WM. Color formulation and reproduction of opaque dental ceramic. Dent Mater 2005;21:665-70. https://doi.org/10.1016/j.dental.2004.09.003.

[161] Maheu B, Letoulouzan JN, Gouesbet G. Four-flux models to solve the scattering transfer equation in terms of Lorenz-Mie parameters. Appl Opt 1984;23:3353. https://doi.org/10.1364/ao.23.003353.

[162] Wang YP, Wu Z Sen, Ren KF. Four-flux model with adjusted average crossing parameter to solve the scattering transfer equatio. Appl Opt 1989;28:24–6.

[163] Vargas WE, Niklasson GA. Forward average path-length Parameter in Four-Flux Radiative Transfer Models. Appl Opt 1997;36:3735–8.

[164] Vargas WE, Niklasson GA. Forward-scattering ratios and average pathlength parameter in radiative transfer models. J Phys Condens Matter 1997;9:9083–96. https://doi.org/10.1088/0953-8984/9/42/021.

[165] Rozé C, Girasole T, Gréhan G, Gouesbet G, Maheu B. Average crossing parameter and forward scattering ratio values in four-flux model for multiple scattering media. Opt Commun 2001;194:251–63. https://doi.org/10.1016/S0030-4018(01)01284-6.

[166] Rozé C, Girasole T, Tafforin AG. Multilayer four-flux model of scattering, emitting and absorbing media. Atmos Environ 2001;35:5125–30. https://doi.org/10.1016/S1352-2310(01)00328-4.

[167] Vargas WE, Wang J, Niklasson GA. Scattering and absorption cross sections of light diffusing materials retrieved from reflectance and transmittance spectra of collimated radiation. J Mod Opt 2020;67:974–91. https://doi.org/10.1080/09500340.2020.1801872.

[168] Vargas WE, Wang J, Niklasson GA. Effective backscattering and absorption coefficients of light diffusing materials retrieved from reflectance and transmittance spectra of diffuse radiation retrieved from reflectance and transmittance spectra of diffuse radiation. J Mod 2021;68:605–23. https://doi.org/10.1080/09500340.2021.1936244.

[169] Vargas WE, Niklasson GA. Pigment mass density and refractive index determination from optical measurements. J Phys Condens Matter 1997;9:1661–70. https://doi.org/10.1088/0953-8984/9/7/027.

[170] Jarrige R, Andraud C, Lafait J, Eveno M, Menu M, Diniz N. Determination of the complex optical index of red pigments, vermillon. O3A Opt Arts, Archit Archaeol III 2011;8084:80840D. https://doi.org/10.1117/12.893264.

[171] Vargas WE, Greenwood P, Otterstedt JE, Niklasson GA. Light scattering in pigmented coatings: Experiments and theory. Sol Energy 2000;68:553–61. https://doi.org/10.1016/s0038-092x(00)00024-4.

[172] Vargas WE. Optical properties of pigmented coatings taking into account particle interactions. J Quant Spectrosc Radiat Transf 2003;78:187–95. https://doi.org/10.1016/S0022-4073(02)00192-9.

[173] Wang L, Eldridge JI, Guo SM. Comparison of different models for the determination of the absorption and scattering coefficients of thermal barrier coatings. Acta Mater 2014;64:402–10. https://doi.org/10.1016/j.actamat.2013.10.053.

[174] Dong N, Ge J, Zhang Y. Four-flux Kubelka-Munk model of the light reflectance for printing of rough substrate. Color Imaging XIV Displaying, Process Hardcopy, Appl 2009;7241:72411I. https://doi.org/10.1117/12.804402.

[175] Bayou S, Mouzali M, Aloui F, Lecamp L, Lebaudy P. Simulation of conversion profiles inside a thick dental material photopolymerized in the presence of nanofillers. Polym J 2013;45:863–70. https://doi.org/10.1038/pj.2012.226.

[176] Rio S, Andraud C, Deniard P, Dacquin C, Delaval R, Donze S, et al. Study of the influence of crystalline phases on optical characteristics of a glass-ceramic in the visible range via simulations by the four-flux method. J Non Cryst Solids 2021;551:120446. https://doi.org/10.1016/j.jnoncrysol.2020.120446.

[177] Eymard J, Clerc R, Duveiller V, Commault B, Hébert M. Solar Energy Materials and Solar Cells Characterization of UV – Vis – NIR optical constants of encapsulant for accurate determination of absorption and backscattering losses in photovoltaics modules. Sol Energy Mater Sol Cells 2022;240:111717. https://doi.org/10.1016/j.solmat.2022.111717.

[178] Phan Van Song T, Andraud C, Ortiz Segovia M V. Implementation of the four-flux model for spectral and color prediction of 2.5D prints. Int Conf Digit Print Technol 2016:26–30.

[179] Phan Van Song T, Andraud C, Ortiz-Segovia M V. Spectral predictions of rough ink layers using a four-flux model. Final Progr Proc - IS T/SID Color Imaging Conf 2017;2017:251–7.

[180] Phan Van Song T, Andraud C, Ortiz-Segovia M V. Towards spectral prediction of 2.5D prints for soft-proofing applications. 2016 6th Int Conf Image Process Theory, Tools Appl IPTA 2016 2017. https://doi.org/10.1109/IPTA.2016.7820957.

[181] Phan Van Song T. Optical models for appearance management of printed materials, PhD dissertation 2018.

[182] D. B. Judd, Fresnel reflection of diffusely incident light, J. Natl. Bur. Standards 29 (1942): 329-332.

[183] Born M. Wolf E. Principle of optics. 7th end. Pergamon, Oxford; 1999.

[184] Henyey LG, Greenstein JL. Diffuse radiation in the galaxy. Astrophys J 1941;93:70–83.

[185] Gautheron A, Clerc R, Duveiller V, Simonot L, Montcel B, Hébert M. Light scattering in translucent layers : angular distribution and internal reflections at flat interfaces. Electron Imaging 2022;34:1–6.

[186] Barrios D, Alvarez C, Miguitama J, Gallego D, Niklasson GA. Inversion of two-flux and four-flux radiative transfer models for determining scattering and absorption coefficients for a suspended particle device. Appl Opt 2019;58:8871. https://doi.org/10.1364/ao.58.008871.

[187] Huntley JM. Comparison between four flux theory and multiple scattering theory. Appl Opt 1989;28:3268–70.

[188] Vargas WE, Niklasson GA. Applicability conditions of the Kubelka–Munk theory. Appl Opt 1997;36:5580–6. https://doi.org/10.1364/ao.36.005580.

[189] Vargas WE. Inversion methods from Kubelka – Munk. Online 2002;452:4–9.

[190] Yang L, Kruse B. Revised Kubelka – Munk theory . I . Theory. J Opt Soc Am 2004;21:1933–41.

[191] Yang L, Miklavcic SJ. Revised Kubelka–Munk theory III A general theory of light propagation in scattering and absorptive media. J Opt Soc Am A 2005;22:1866. https://doi.org/10.1364/josaa.22.001866.

[192] Edström P. Examination of the revised Kubelka-Munk theory: considerations of modeling strategies. J Opt Soc Am A 2007;24:548. https://doi.org/10.1364/josaa.24.000548.

[193] Kokhanovsky AA. Physical interpretation and accuracy of the Kubelka-Munk theory. J Phys D Appl Phys 2007;40:2210–6. https://doi.org/10.1088/0022-3727/40/7/053.

[194] Berns RS, Mohammadi M. Single-constant simplification of Kubelka-Munk turbid-media theory for paint systems - A review. Color Res Appl 2007;32:201–7. https://doi.org/10.1002/col.20309.

[195] Illés T, Mayer J, Terlaky T. Pseudoconvex optimization for a special problem of paint industry. Eur J Oper Res 1994;79:537–48. https://doi.org/10.1016/0377-2217(94)90064-7.

[196] Walowit E, McCarthy CJ, Berns RS. Spectrophotometric color matching based on two-constant kubelka-munk theory. Color Res Appl 1988;13:358–62. https://doi.org/10.1002/col.5080130606.

[197] He G, Zhou M. Colorant formulation based on new two-constant theory. Color Technol 2007;123:217–23. https://doi.org/10.1111/j.1478-4408.2007.00086.x.

[198] Bai F, Zeng H, Yi J, Liao N, Guo L. Color Matching in Paints Using a Method of Linear Programming. Color Res Appl 2016;19:375–6.

[199] Moussa A. Textile color formulation using linear programming based on Kubelka-Munk and Duncan theories. Color Res Appl 2021;46:1046–56. https://doi.org/10.1002/col.22626.

[200] Burlone DA. Formulation of Blends of Precolored Nylon Fiber. Color Res Appl 1983;8:114–20. https://doi.org/10.1002/col.5080080210.

[201] Burlone DA. Theoretical and practical aspects of selected fiber-blend color-formulation functions. Color Res. Appl. 1984; 9(4):213-219.

[202] Taufique AMN, Messinger DW. Hyperspectral pigment analysis of cultural heritage artifacts using the opaque form of Kubelka-Munk theory. In : Algorithms, Technologies, and Applications for Multispectral and Hyperspectral Imagery XXV. SPIE, 2019. p. 297-307.

[203] Moghareh Abed F. Pigment Identification of Paintings Based on Kubelka-Munk Theory and Spectral Images. PhD Dissertation 2014.

[204] Moghareh Abed F, Berns RS. Linear Modeling of Modern Artist Paints Using a Modification of the Opaque Form of Kubelka-Munk Turbid Media Theory. Color Res Appl 2017;42:308–15. https://doi.org/10.1002/col.22086.

[205] Pottier F, Gerardin M, Michelin A, Hébert M, Andraud C. Simulating the composition and structuration of coloring layers in historical painting from non-invasive spectral reflectance measurements. Comptes Rendus Phys 2018;19:599–611. https://doi.org/10.1016/j.crhy.2018.09.007.

[206] Zhao Y. Image segmentation and pigment mapping of cultural heritage based on spectral imaging. PhD thesis, Rochester Institute of Technology. 2008. https://scholarworks.rit.edu/theses/3029

[207] Kirchner E, Lans I Van Der, Ligterink F, Geldof M. Digitally reconstructing van Gogh's Field with Irises near Arles part 2 : Pigment concentration maps. Color Res Appl 2017. https://doi.org/10.1002/col.22164.

[208] Rohani AN, Pouyet E, Cossairt O, Walton M. Nonlinear unmixing of hyperspectral datasets for the study of painted works of art. Angew Chem 2018;57:10910–4. https://doi.org/10.1002/anie.201805135.

[209] Anderson RR, Parrish JA. The Optics of Human Skin. J Invest Dermatol 1981;77:13–9. https://doi.org/10.1111/1523-1747.ep12479191.

[210] Li B, Han Z, Wang Q, Yang A, Liu Y. Detection of skin defects in loquats based on grayscale features combined with reflectance, absorbance, and Kubelka–Munk spectra. Journal of Chemometrics. 2022;36(11):e3449. doi:10.1002/cem.3449

[211] Annala, L, Pölönen, I Kubelka–Munk Model and Stochastic Model Comparison in Skin Physical Parameter Retrieval. In: Tuovinen, T., Periaux, J., Neittaanmäki, P. (eds) Computational Sciences and Artificial Intelligence in Industry. Intelligent Systems, Control and Automation: Science and Engineering, vol 76. Springer, Cham. (2022). https://doi.org/10.1007/978-3-030-70787-3_10

[212] Jasinki M. Modelling of light and human skin interaction using Kubelka-Munk theory. Scientific Research of the Institute of Mathematics and Computer Science. 2011;10(1):71-81.

[213] Gevaux L, Séroul P, Gevaux L, Adnet C, Séroul P, Clerc R, et al. Three-dimensional maps of human skin properties on full face with shadows using 3-D hyperspectral imaging. J Biomed Opt 2023;24:1–14. https://doi.org/10.1117/1.JBO.24.6.066002.

[214] Gevaux L, Adnet C, Séroul P, Clerc R, Trémeau A, Perrot JL, et al. Three-dimensional Hyperspectral imaging : A new method for human face acquisition. Soc. Imaging Sci. Technol., 2018.

[215] Doi M, Ohtsuki R, Tominaga S. Spectral Estimation of Skin Color with Foundation Makeup. In: Kalviainen, H., Parkkinen, J., Kaarna, A. (eds) Image Analysis. SCIA 2005. Lecture Notes in Computer Science, vol 3540. Springer, Berlin, Heidelberg. https://doi.org/10.1007/11499145_11

[216] Doi M, Ohtsuki R, Tominaga S. Spectral estimation of made-up skin color under various conditions. In : Spectral Imaging: Eighth International Symposium on Multispectral Color Science. SPIE, 2006. p. 28-37.

[217] Roy A, Ramasubramaniam R, Gaonkar HA. Empirical relationship between Kubelka–Munk and radiative transfer coefficients for extracting optical parameters of tissues in diffusive and nondiffusive regimes. J Biomed Opt 2012;17:115006. https://doi.org/10.1117/1.jbo.17.11.115006.

[218] Mudgett PS, Richards LW. Multiple scattering calculations for technology II. J Colloid Interface Sci 1972;39:551–67. https://doi.org/10.1016/0021-9797(72)90064-1.

[219] Richmond JC. Relation of emittance to other optical properties. Journal of Research of the National Bureau of Standards Section 1963;67:217–26

[220] Yamaguchi S, Karaer O, Lee C, Sakai T, Imazato S. Color matching ability of resin composites incorporating supra-nano spherical filler producing structural color. Dent Mater 2021;37:e269–75. https://doi.org/10.1016/j.dental.2021.01.023.

[221] Azhar G, Haas K, Wood DJ, van Noort R, Moharamzadeh K. The Effects of Colored Pigments on the Translucency of Experimental Dental Resin Composites. Eur J Prosthodont Restor Dent 2019;27(1):3-9. doi: 10.1922/ejprd_01855azhar08 .

[222] Azzopardi N, Moharamzadeh K, Wood DJ, Martin N, van Noort R. Effect of resin matrix composition on the translucency of experimental dental composite resins. Dent Mater 2009;25:1564–8. https://doi.org/10.1016/j.dental.2009.07.011.

[223] Yu B, Lee YK. Differences in color, translucency and fluorescence between flowable and universal resin composites. J Dent 2008;36:840–6. https://doi.org/10.1016/j.jdent.2008.06.003.

[224] Lee YK. Opalescence of human teeth and dental esthetic restorative materials. Dent Mater J 2016;35:845–54. https://doi.org/10.4012/dmj.2016-091.

[225] Song SH, Yu B, Ahn JS, Lee YK. Opalescence and fluorescence properties of indirect and direct resin materials. Acta Odontol Scand 2008;66:236–42. https://doi.org/10.1080/00016350802208414.

[226] Duveiller V, Kim E, Locquet M, Gautheron A, Clerc R, Salomon JP, et al. Predictions of the Reflectance Factor of Translucent Layered Dental Resin Composites Using Two-Flux Models: assessing the importance of the interface reflectance parameter. CEUR Workshop Proc 2022;3271.

[227] Duveiller V, Gevaux L, Clerc R, Salomon J-P, Hébert M. Reflectance and transmittance of flowable dental resin composite predicted by the two-flux model : on the importance of analyzing the effective measurement geometry. CIC28 Proc., 2020.

[228] Simonot L, Thoury M, Delaney J. Extension of the Kubelka–Munk theory for fluorescent turbid media to a nonopaque layer on a background, J. Opt. Soc. Am. A. 2001;28(7):1349, 2011. doi: 10.1364/josaa.28.001349.

[229] O’brien WJ, Johnston WM, Fanian F, Lambert S. The Surface Roughness and Gloss of Composites. J Dent Res 1984;63:685–8. https://doi.org/10.1177/00220345840630051601.

[230] Heintze SD, Forjanic M, Rousson V. Surface roughness and gloss of dental materials as a function of force and polishing time in vitro. Dent Mater 2006;22:146–65. https://doi.org/10.1016/j.dental.2005.04.013.

[231] Johnston WM. Review of translucency determinations and applications to dental materials. J Esthet Restor Dent 2014;26:217–23. https://doi.org/10.1111/jerd.12112.

[232] Johnston VM, Ma T, Kienle BH. Translucency parameter of colorants for maxillofacial prostheses. Int J Prosthodont 1995;8:79–86

[233] Luo W, Westland S, Ellwood R, Pretty I, Cheung V. Development of a whiteness index for dentistry. J Dent 2009;37:21–6. https://doi.org/10.1016/j.jdent.2009.05.011.

[234] Luo W, Westland S, Brunton P, Ellwood R, Pretty IA, Mohan N. Comparison of the ability of different colour indices to assess changes in tooth whiteness. J Dent 2007;35:109–16. https://doi.org/10.1016/j.jdent.2006.06.006

[235] Pérez MDM, Ghinea R, Rivas MJ, Yebra A, Ionescu AM, Paravina RD, et al. Development of a customized whiteness index for dentistry based on CIELAB color space. Dent Mater 2016;32:461–7. https://doi.org/10.1016/j.dental.2015.12.008.

[236] Sullivan C, Pan Q, Westland S, Ellwood R. A yellowness index for use in dentistry. J Dent 2019;91:103244. https://doi.org/10.1016/j.jdent.2019.103244.

[237] Kobashigawa AI AC. Opalescence fillers for dental restorative composite. United States Pat 6,232, 367 2001;6.

[238] Bruce HD. Photometric method for measuring the hiding power of paints. Technology paper 306. National Bureau of Standards, 1926.

[239] Sawyer RH. Hiding power and opacity. Symposium on color. Philadelphia (PA): American Society for Testing Materials; 1941, p. 22.

[240] Gevaux L, 3D-hyperspectral imaging and optical analysis of skin for the human face, PhD dissertation, University Jean Monnet, France, 2019.